UNIVERSIDADE DE LISBOA

INSTITUTO SUPERIOR TÉCNICO

New Hydraulic Binders with Low Calcium Content

Rodrigo Manuel Lino dos Santos

Supervisor:	Doctor Ricardo Manuel Simões Bayão Horta
Co-supervisors:	Doctor Rogério Anacleto Cordeiro Colaço
	Doctor José Nuno Aguiar Canongia Lopes

Thesis approved in public session to obtain the PhD Degree in Materials Engineering
Jury final classification: Pass with Distinction

Jury

Chairperson: Chairman of the IST Scientific Board

Members of the Committee:

Doctor Franz-Josef Ulm

Doctor Ricardo Manuel Simões Bayão Horta

Doctor Manuel Luís de Magalhães Nunes da Ponte

Doctor Mário Guerreiro Silva Ferreira

Doctor Paulo Manuel Cadete Ferrão

Doctor José Nuno Aguiar Canongia Lopes

Doctor Maria de Fátima Grilo da Costa Montemor

2016

UNIVERSIDADE DE LISBOA

INSTITUTO SUPERIOR TÉCNICO

New Hydraulic Binders with Low Calcium Content

Rodrigo Manuel Lino dos Santos

Supervisor:	Doctor Ricardo Manuel Simões Bayão Horta
Co-supervisors:	Doctor Rogério Anacleto Cordeiro Colaço
	Doctor José Nuno Aguiar Canongia Lopes

Thesis approved in public session to obtain the PhD Degree in Materials Engineering
Jury final classification: Pass with Distinction

Jury

Chairperson: Chairman of the IST Scientific Board

Members of the Committee:

Doctor Franz-Josef Ulm, Professor, School of Engineering, Massachusetts Institute of Technology, USA

Doctor Ricardo Manuel Simões Bayão Horta, Jubilee Full Professor, Instituto Superior Técnico da Universidade de Lisboa

Doctor Manuel Luís de Magalhães Nunes da Ponte, Full Professor, Faculdade de Ciências e Tecnologia da Universidade Nova de Lisboa

Doctor Mário Guerreiro Silva Ferreira, Full Professor, Universidade de Aveiro

Doctor Paulo Manuel Cadete Ferrão, Full Professor, Instituto Superior Técnico da Universidade de Lisboa

Doctor José Nuno Aguiar Canongia Lopes, Associate Professor, Instituto Superior Técnico da Universidade de Lisboa

Doctor Maria de Fátima Grilo da Costa Montemor, Associate Professor, Instituto Superior Técnico da Universidade de Lisboa

2016

To Tânia and Maria

Resumo

Na presente tese são propostas e estudadas duas novas abordagens de desenvolvimento de materiais cimentícios cuja produção apresenta valores de emissões de CO_2 inferiores aos da produção de clínquer tradicional.

A primeira abordagem estudada visa o desenvolvimento de um clínquer cuja microestrutura consiste na presença de cristais de belite com morfologia dendrítica no interior de uma matriz vítrea, sendo que a morfologia dos cristais de belite é controlada através de um processo de produção específico.

A segunda abordagem foca-se na produção de materiais de natureza essencialmente amorfa, tirando-se partido da sua instabilidade para serem utilizados como ligantes hidráulicos.

O comportamento hidráulico destes materiais foi estudado, tendo-se avaliado as suas propriedades mecânicas. Foi ainda seguida a evolução da hidratação e o desenvolvimento de fases hidratadas através de técnicas de difracção de raios-X, microscopia, análise química, estrutural e termogravimétrica, e ainda por calorimetria isotérmica.

Foi também estudada a activação alcalina dos materiais amorfos produzidos e o seu impacto nas propriedades destes ligantes em hidratação.

Testou-se ainda a variação das condições de arrefecimento na produção de materiais amorfos e o seu impacto no comportamento hidráulico dos mesmos.

Por fim foram estimados valores de emissões de CO_2 de produção dos diversos ligantes hidráulicos estudados neste trabalho, comparando-se com os valores típicos de produção de um clínquer tradicional.

Abstract

In the present thesis two new approaches on the development of cementitious materials are suggested and studied, having as main purpose the reduction of the process related CO_2 emissions, when compared with the production of traditional clinker.

The first approach deals with the development of a new clinker whose microstructure consists in the presence of belite crystals with a dendritic morphology embedded in a glassy matrix, with the morphology of the dendritic crystals being controlled by the use of a specific production process.

The second approach focused in the production of almost fully amorphous materials in order to take advantage from the known instability of this type of materials to act as hydraulic binders.

The hydraulic behaviour of these materials was studied and their mechanical properties assessed. The development of the hydration and hydrated phases was followed by the techniques of X-ray diffraction, optical and electronic microscopy, chemical, structural and termogravimetric analysis and also by isothermal calorimetry.

The alkaline activation of the amorphous materials produced was also studied as well as its impact in the properties of these binders during hydration.

It was also tested the impact of the variation of cooling conditions during the production of the amorphous materials in their hydraulic behaviour.

At last, it was made an estimation of the process related CO_2 emission values for the production of the several hydraulic binders studied in this work, being these values compared with the typically considered in the production of traditional clinker.

Keywords

CO_2 emissions

Dendritic belite

Amorphous hydraulic binders

Cooling rate effect

Alkaline activation

Palavras-chave

Emissões de CO_2

Belite dendrítica

Ligantes hidráulicos amorfos

Efeito da taxa de arrefecimento

Ativação alcalina

Acknowledgements

The research disclosed in this thesis has been conducted at the Central Laboratory of the InterCement group and at Instituto Superior Técnico of Lisbon University, with the financial support from CIMPOR – Cimentos de Portugal, SGPS S.A. under the Industrial Contract CIMPOR/ADIST Nanocement 2012/2015 since February of 2012.

Firstly I would like to thank Professor Ricardo Bayão Horta for the outstanding support and countless hours of discussion and brainstorming, where no hypothesis was ever left unconsidered. Furthermore, his enthusiasm for the project has been truly inspiring, helping me keeping on track even in moments of difficulty.

I am very grateful to Professor Rogério Colaço whose guidance and teachings helped me overcome the harshest obstacles that often tend to appear in a research work. His valuable advices and fruitful discussions allowed to improve the quality of this work.

I would also like to thank Professor José Nuno Canongia Lopes who introduced me to the field of computational simulation, providing new tools of analysis to understand the behavior of these challenging materials and also for all his positive comments that added value to this work and much contributed with his always constructive point of view.

I am also thankful to Dr. Adilson Freitas, whose work in the field of computational simulation opened new perspectives in the understanding of the properties of these complex materials.

My gratitude is also directed to Professor Teresa Nunes for the conduction of the NMR experiments and her valuable comments and guidance in the analysis of the results.

I am thankful to Eng. João Pereira for the warm welcome in the central laboratory of Cimpor and for guiding me during my first steps in the cement field. He always managed to take some of its time to help me either in the planning of the laboratory experiments or in their execution.

I would also like to thank Eng. Sandra Lebreiro and Eng. Paulo Rocha who have always believed in this project and whose efforts to take this project to the next level I am deeply grateful.

I would also like to thank to all the laboratory colleagues who contributed in a daily basis for the good environment on which I have been pleased to work and with whom I ended up creating good friendships.

Finally, I would like to thank my family and specially dedicate this work to my wife Tânia, who has been a source of strength and who always encouraged me to do more and better, and to my daughter Maria who has become my main source of inspiration and motivation.

Contents

List of Figures

List of Tables

Cement nomenclature

A	Al_2O_3
Ċ	CO_2
C	CaO
F	Fe_2O_3
H	H_2O
N	Na_2O
S	SiO_2
$	SO_3

List of abbreviations

BAT	Best Available Technology
C$·2H	$CaSO_4.2H_2O$ - Gypsum
C_2S	$2CaO·SiO_2$ - Belite
C_3A	$3CaO·Al_2O_3$ - Tricalcium aluminate
C_3S	$3CaO·SiO_2$ - Alite
C_3S_2	$3CaO·2SiO_2$ - Rankinite
C_4AF	$4CaO·Al_2O_3·Fe_2O_3$ - Tetracalcium alumino-ferrite
CĊ	$CaCO_3$ – Calcium carbonate
CH	$Ca(OH)_2$ - Portlandite
CS	$CaO·SiO_2$ - Wollastonite
C-S-H	Calcium Silicate Hydrate without a well-defined stoichiometry
FTIR-ATR	Fourier Transform Infrared with Attenuated Total Reflectance
LOI	Loss On Ignition
MAS NMR	Magic Angle Spinning Nuclear Magnetic Resonance
OPC	Ordinary Portland Cement
PSD	Particle Size Distribution
SEM	Scanning Electron Microscopy
TGA	Thermogravimetric Analysis
XRD	X-Ray Diffraction

1 Scope of the Thesis

The production of cement (the component of concrete responsible for its strength when reacting with water) has been following the evolution of modern society as it provides a cost-effective, durable and strong material to nearly all types of infrastructural installations, buildings and houses [1]. As a consequence concrete has turned into the most worldwide used manufactured material, having the production of cement reached presently a world annual value of over 3 billion tons and expecting to increase to more than 4 billion tons in the next decade [2]. Although this growth is a positive factor for the economic and social development, its environmental impact is an issue that deserves particular attention, since the production of Portland cement is a very high energy intensive process, being characterized by the consumption of specific non-renewable raw materials, mainly consisting in a mix of limestone with other silicate minerals, and by the emission of high amounts of CO_2. The best available technology (BAT) for the industrial production of cement (ordinary Portland cement, also known as OPC) uses a well-established process based on the production of a clinker with high alite (C_3S) content. To produce a hydraulic material that typically contains approximately 50 to 70% of alite there are required kiln temperatures close to 1450ºC and around 1250 kg of limestone for each ton of clinker produced [3]. These thermal and compositional conditions result in CO_2 emission values that can go up to 800 kg of CO_2 per ton of cement produced. Due to these characteristics and to the large amount of cement produced worldwide, cement industry is nowadays responsible for more than 5% of the total anthropogenic CO_2 emitted [4, 5]. Knowing this, it is legitimate to say that designing and developing a hydraulic binder matching the technical, economic and workability qualities of OPC, and allowing a reduction of the ecologic footprint, namely CO_2 emissions, represents simultaneously a great challenge both to the technical research and development and to the fulfilment of the social responsibility obligations of the world cement industry. In fact, the reduction of cement production related CO_2 has been the central topic of a great number of research papers and recently the four main technological levers for the mitigation of CO_2 emissions have been identified by the World Business Council for Sustainable Development (WBCSD) and the International Energy Agency (IEA) as: 1- Thermal and electric efficiency improvement; 2- Use of alternative fuels; 3- Increase clinker substitution; 4- Development and implementation of carbon capture and storage units [6]. However, apart from these four main technological

aspects, some attention should be also driven to the remarkable research works that have been conducted in the last decades targeting the development and optimization of alternatives for traditional clinker. The search for new alternatives is an extremely challenging task since OPC is a very versatile, easy to use and durable building material. Furthermore the raw materials used are relatively cheap, widely distributed and can be found almost everywhere in the world. In addition the technology used, although still possible to be optimized, is very well developed and established all around the globe. These facts are huge obstacles to overcome and end up limiting the possibilities of development of new alternatives, since they must not only present a lower ecologic footprint but also be economically competitive and comparable in terms of mechanical properties with OPC. This demand has led to the development of the present thesis.

1.1 Objectives

Since modern plants are nowadays designed in such a way that the optimization of the energy consumption has already reached a value very close to the thermodynamic barrier imposed by the chemistry of the process with the fuels typically used [7] and further optimization will only lead to small incremental steps [8], the most direct way to impact on the CO_2 emitted in the process is to start thinking about new clinker chemistries, preferably by decreasing the amount of carbonated raw materials used in clinker production.

Driven by the need of development of a new paradigm for the production of cementitious materials, from which could result lower process related CO_2 emissions, this thesis presents two main approaches that open the way for a new family of alternative environment-friendly clinkers. The approaches studied in this thesis had as main goal the production of more environment-friendly cementitious materials by changing the chemistry of the mix of some typical raw-materials used (limestone, sand, electric furnace slag and fly-ash). A lower CO_2 emission is expected to be achieved by the reduction of the limestone included in the raw mix, decreasing the C/S molar ratio from a value of 3.2-3.3, typical in the production of traditional clinker, to a C/S molar ratio of 1.1-1.4. This region of low C/S molar ratios (1.1-1.4) in the CaO-SiO_2 diagram is not usually regarded as having potential for the production of cementitious materials. However, in the present thesis it will be demonstrated that under specific processing conditions, the resultant materials present a quite noticeable hydraulic behavior.

In the present work two different approaches were used. The objective of the first approach was to assess the possibility of a reactivity improvement of belite by promoting a dendritic growth of belite crystals within an amorphous calcium silicate matrix in a clinker with an overall C/S molar ratio equal to 1.4. These controlled morphological features are expected to improve the hydraulic activity of belite, when compared to the typical round-shaped belite crystals, due to their higher surface energy and surface area available for reaction.

The objective of the second approach was the production and hydration study of amorphous hydraulic binders with C/S molar ratios ranging from 0.8 to 1.25. In this case the hydraulic reactivity was expected to be enhanced by the known low stability and high embodied energy of amorphous materials, when compared to the corresponding predicted crystals for this region of the CaO-SiO_2 diagram, namely wollastonite.

1.2 Outline of the Thesis

The structure of this thesis consists of eleven interdependent chapters. In the first chapter, an introduction to cement industry's CO_2 emission problem is given, stressing the need for new environment friendly alternatives, which serves, in fact, as motivation basis for the work developed in this thesis, being its main objectives also presented in this chapter.

The second chapter refers to general aspects about cement, namely its production, composition and hydration behavior. An analysis of the main phases in the CaO-SiO_2 system is done, with respect to their chemistry, structures and reactivity. Some physico-chemical basis on the hydration mechanism of the main calcium silicate phases are given.

Chapter 3 introduces some suggested or already existing alternatives to OPC, with focus on high belite cements and in hydraulic binders produced from alkali activated supplementary cementitious materials (SCM's).

The fourth chapter of this thesis deals with the materials and the experimental procedures and conditions used during the development of this work.

The production and characterization of new clinkers with low calcium content are described in Chapters 5, 6, 7 and 8. Chapter 5 presents the process developed for the production of new dendritic belite clinkers as well as the characterization of the clinkers produced and their behavior upon hydration, with emphasis on the mechanical properties and structure and phase development. Chapter 6 deals with the production and characterization of amorphous

hydraulic binders of low Ca/Si molar ratio as well as with the hydration of these materials, being presented an exhaustive characterization on the amount and type of the hydration products formed. Chapter 7 introduces the alkaline activation of these amorphous hydraulic binders, presenting the study on the effect of the addition of $NaCO_3$ and $NaOH/Na_2SiO_3$ solutions in the hydration kinetics and strength development of the pastes prepared, as well as in the structural changes of the resulting hydration products. Chapter 8 presents some preliminary results about the effect of the cooling rate used in the production of the amorphous hydraulic binders in the structure and in their hydration behavior.

Chapter 9 is dedicated to the study of the process related CO_2 emissions that may result from the production of the hydraulic binders presented in this work, comparing the obtained values with the typical from the production of traditional clinker and assessing the potential of each binder to be considered as an alternative to the existing OPC.

The tenth chapter presents the general conclusions and findings of this study, while the last chapter indicates some suggestions for future work.

2 General Aspects about Cement

Cement is a finely ground complex mixture of inorganic phases, mainly constituted by clinker (calcium silicates, aluminates and aluminoferrites) and gypsum [9], which when mixed with water has the ability to set and harden due to hydration processes and chemical reactions, maintaining its mechanical strength and stability after hardening even under water [10]. This material has been studied for large decades and several advances have been achieved. However, so far, there is no alternative to Portland cement, which is the universally accepted binding material used for almost all purposes [11], assuming a crucial importance in the construction field. The following sections are dedicated to the description of the production of cement and also to its main features, such as the composition, reactivity, hydration mechanisms and hydration products.

2.1 Production of Portland Cement

The production of cement can be viewed as consisting in 4 main process stages: (i) quarrying; (ii) raw meal preparation; (iii) clinkering and (iv) grinding.

Quarries are typically located near cement plants, so that the transport related costs can be minimized. Their constitution should consist essentially in a combination of limestone and some argillaceous materials, which act as sources of CaO, SiO_2, Al_2O_3 and Fe_2O_3. These minerals are then usually intermixed together in ball mills to produce a raw meal with an overall composition around 67% CaO, 22% SiO_2, 5% Al_2O_3, 3% Fe_2O_3 and 3% of other components, and a particle size distribution with a 90 µm residue close to 15% [3]. Once the raw meal is prepared, it undergoes into a series of chemical reactions activated by temperatures that can go up to 1500ºC. The first most important reactions to occur are the decomposition of clay minerals and also the calcite decomposition to give lime and carbon dioxide (Eq. 2.1), taking place at temperatures between 600ºC and 900ºC:

Eq. 2.1 $$CaCO_3 \rightarrow CaO + CO_2$$

From this point and still below 1300ºC, some liquid phase start to form and lime combines with silica to produce belite in a slightly exothermic reaction (Eq. 2.2):

Eq. 2.2 $$2CaO + SiO_2 \rightarrow Ca_2SiO_4$$

Also some aluminate and ferrite phases are formed at these temperatures.

At higher temperatures (1300 to 1450ºC) about 20-30% of the mix consists in a liquid phase formed by a mixture of aluminate and ferrite. This melt has an important role in the clinker

nodulization by sticking the solid particles together as well as in the acceleration of alite formation by the combination of lime and belite (Eq. 2.3):

Eq. 2.3 $$Ca_2SiO_4 + CaO \rightarrow Ca_3SiO_5$$

These nodules are then cooled, stabilizing the phases formed at high temperatures and producing a clinker with a final constitution of approximately 50-70% C_3S, 15-30% C_2S, 1-15% C_3A and 5-15% C_4AF.

Ultimately the clinker nodules are ground in ball mills together with less than 5% in weight of a sulfate source, typically gypsum (C$·2H), which is added to prevent the phenomenon of "flash-setting", resulting a product that is usually called ordinary Portland cement (OPC).

Although all of these stages contribute to the process related CO_2 emission, it is the clinkering stage which generates the most representative part of the total CO_2 emitted during cement production. In this stage there are two main sources of CO_2 acting together: (i) fuel burning and (ii) decarbonation of limestone. The first source, which represents about 35% of the CO_2 emissions in the process, is related to the requirement of high process temperatures in order that all the chemical reactions can occur at an acceptable rate (specially the formation of alite – C_3S). The limestone decarbonation component represents close to 55% of the total CO_2 emitted in the process. The use of such amounts of limestone is necessary due to the chemical nature of the process, where CaO-rich phases are essentially formed and from whose depend the good hydraulic properties of OPC.

2.2 Calcium Silicate Phases

The calcium silicate phases C_3S and C_2S play a very important role in the development of strength in hydrated Portland cements. Alite is the main responsible for the initial strength development whereas belite ensures the strength growth for longer ages.

Figure 2-1 depicts the isolated contributions of pure C_3S and C_2S for the compressive strength growth trend in cement. Also shown are the contributions of C_3A and C_4AF phases, which present a very low impact on the final strength of cement.

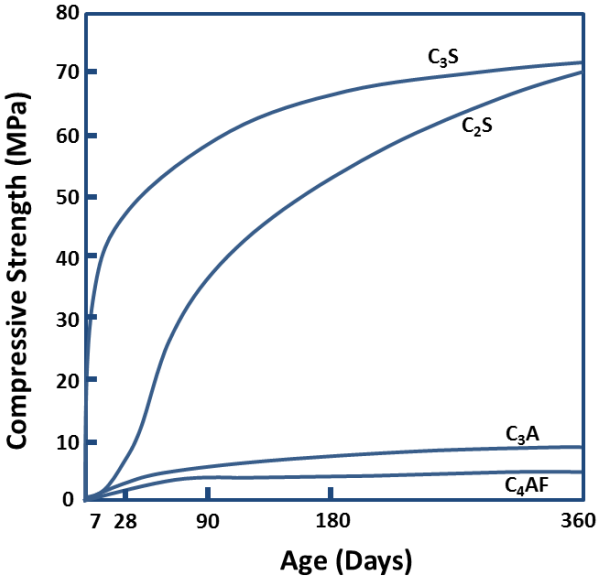

Figure 2-1. Development of strength of pure compounds. Adapted from [12].

Taking these facts into account, one can easily understand the main reason why the BAT is based on alite by considering the $CaO\text{-}SiO_2$ phase diagram (

Figure 2-2). When starting from alite (C_3S), a decrease in calcium content leads first to the formation of belite (C_2S), in one of its five allotropic forms $\alpha, \alpha'_H, \alpha'_L$, β and γ, then to rankinite (C_3S_2) and finally to wollastonite (CS), the latter with two allotropic forms α and β. It is well established in the art that belite shows a weak and slow hydraulic activity, while both rankinite and wollastonite are reported as being hydraulically inactive [3]. A brief description of the main phases present in the $CaO\text{-}SiO_2$ diagram will be done in the next sections.

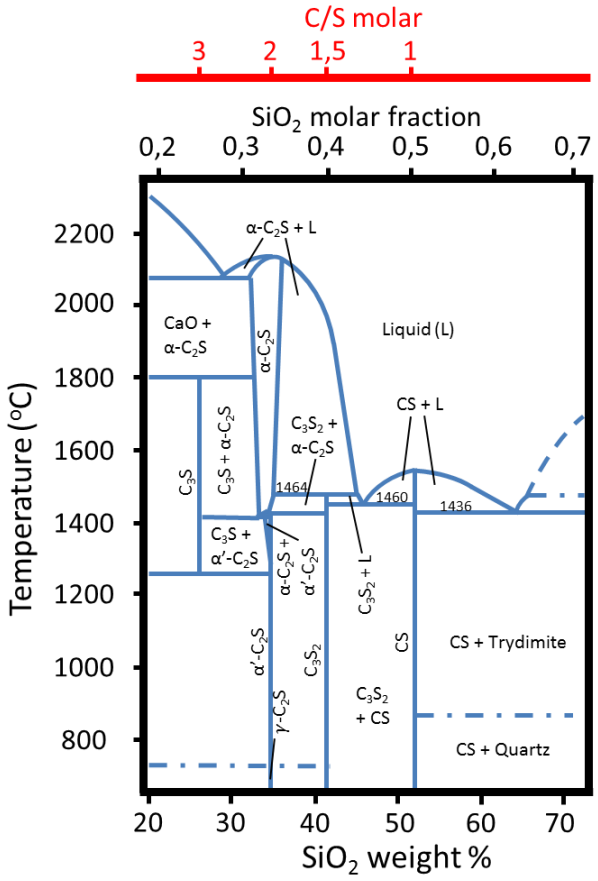

Figure 2-2. A detail of CaO-SiO_2 equilibrium phase diagram.

Usually the SiO_x structural units are referred as Q^n, with *n* increasing from 0 to 4 depending on the connectedness of the unit, as described in Table 2-1.

Table 2-1. Identification of the SiO_x structural units with respect to its Q^n connectedness.

Structural unit	Description
Q^0	Monomers of SiO_4^{4-}
Q^1	Dimers and terminal groups
Q^2	Intermediate chain groups
Q^3	Planar structures
Q^4	3-Dimensional structures

2.2.1 Alite

Alite is the chemically modified form of pure tricalcium silicate phase (Ca_3SiO_5), which is typically formed at temperatures close to 1450ºC during the clinkerization stage, by the combination of belite with lime, and is responsible for the initial strength development of OPC upon hydration. This phase appears in the CaO-SiO_2 diagram as being metastable at room temperature, occurring only for temperatures above 1250ºC. Alite presents seven different

possible polymorphic forms, with their structures and transition temperatures being schematized in Figure 2-3.

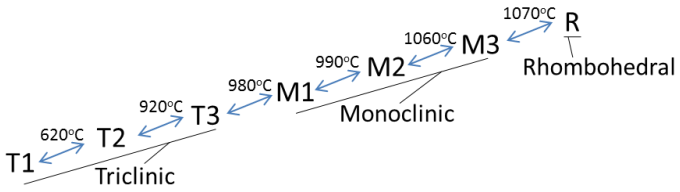

Figure 2-3. Alite polymorphs and respective transition temperatures. Adapted from [3].

Depending on the impurities contained on its structure alite can be stabilized at room temperatures in a variety of structures, being the monoclinic forms M1 and M3 the most common in industrial clinkers [13-16]. The crystal structures of the different polymorphs are similar, consisting of isolated $[SiO_4]^{4-}$ tetrahedra and two distinct Ca^{2+} positions as well as ionic O^{2-}.

Figure 2-4 presents a cut of a M3-C_3S polymorph structure modeled with a general force field developed by Freitas et al. [17], from where it is possible to observe the arrangement of the species referred. A clear distinction between free oxygen atoms and those connected to the isolated tetrahedra can be seen. In a simple approach one can say that the Alite structure consists in an arrangement of silicate Q^0 units and ionic calcium and oxygens.

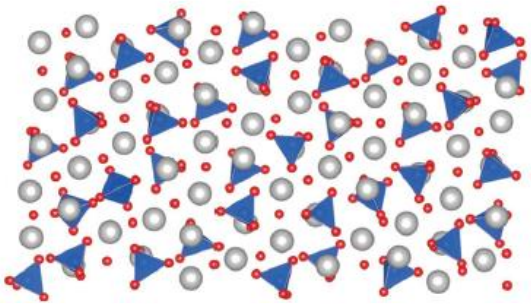

Figure 2-4. Structural detail of an alite M3 polymorph. Calcium, silicon and oxygen atoms are depicted as grey, blue and red spheres, respectively. Blue tetrahedra represent the $[SiO_4]^{4-}$ units. Adapted from [17].

2.2.2 Belite

Similarly to C_3S, belite may present several polymorphic forms. Ghosh et al. [18] referred the existence of six different polymorphs (α, α'_h, α'_l, α'_m, β and γ), however in the works performed by Gawlicki [19] and later by Corinne et al. [20], the occurrence of the α'_m polymorph was not

confirmed. From the remaining five polymorphs, the α, α'_h, α'_l and γ, in order of decreasing temperature, are stable at ordinary pressures, being the later the only polymorph which is stable at room temperature, while the β polymorph is only stable at high pressures, occurring as a metastable phase at room temperature when cooled rapidly [21].

The structures and transition temperatures for the various polymorphic forms of belite are schematized in

Figure 2-5.

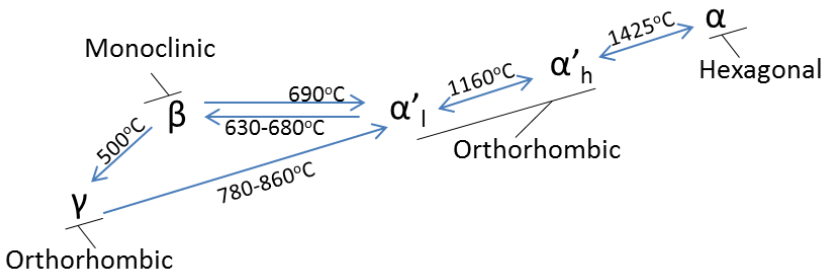

Figure 2-5. Structures and transition temperatures for C_2S. Adapted from [3].

All these structures are built from Ca^{2+} and $[SiO_4]^{4-}$ ions, being their arrangements closely similar in the α, α'_h, α'_l and β polymorphs, but different in the γ-C_2S [3].

Figure 2-6 show the structure of α-belite, which consists essentially of silicate Q^0 units, differing from alite mainly by the absence of free ionic oxygens.

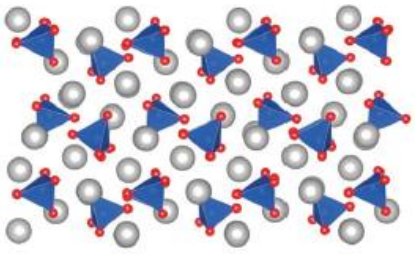

Figure 2-6. Structural detail of the α polymorph of C_2S. Calcium, silicon and oxygen atoms are depicted as grey, blue and red spheres, respectively. Blue tetrahedra represent the $[SiO_4]^{4-}$ units. Adapted from [17].

The structures of the α'_h, α'_l and β polymorphs are derived from that of α-C_2S by progressive decreases in symmetry, which arise from changes in the orientations of the $[SiO_4]^{4-}$ tetrahedra and small movements of Ca^{2+} ions. Although β-C_2S is metastable at normal pressure and temperature, this is the most commonly found in Portland cement clinkers [16, 18]. Its stability

can be achieved by a rapid cooling and/or by the presence of impurities in its structure, such as Al, Mg, Fe, B, Na, K, Ba, Mn, Cr or their combinations [3, 18, 22]. Clinker belites usually contain 4 to 6 wt% of substituent oxides, from which the most common are Al_2O_3 and Fe_2O_3 [3]. This level of substitution is typically enough to hinder the β to γ transition, thus allowing the stabilization of the more reactive polymorph over the γ-C_2S form, which has very poor hydraulic activity. When occurring, the β to γ transition can easily be detected by a phenomenon called dusting that mainly arises from the difference in density of the two forms, since the γ polymorph presents a density (2,960 $g.cm^{-3}$) 11% lower than the β polymorph (3,326 $g.cm^{-3}$), leading the β-C_2S crystals to crack into a more voluminous powder [3, 22].

C_2S β-polymorph is monoclinic and has two types of calcium ions in its structure: Ca(1) with a six-fold coordination and a Ca(2) surrounded by eight oxygens atoms. Due to this irregular coordination, there are some holes in the structure, which, however, are smaller than the ones present in the C_3S structure [11].

2.2.3 Rankinite

Rankinite, C_3S_2, melts incongruently at 1464°C and doesn't present any phase transition, existing in a well-defined structure without any polymorphic variation. Figure 2-7 depicts the structure of C_3S_2, showing an arrangement of dimeric units (Q^1 groups) of silicate tetrahedra, charge balanced by Ca^{2+} ions.

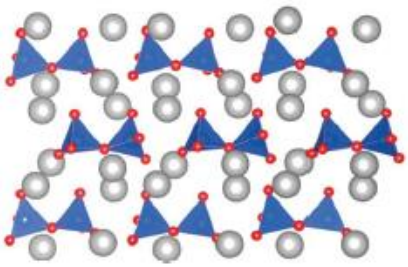

Figure 2-7. Structural detail of Rankinite. Calcium, silicon and oxygen atoms are depicted as grey, blue and red spheres, respectively. Blue tetrahedra represent the $[SiO_4]^{4-}$ units. Adapted from [17].

This phase is not usually present in Portland cement clinkers and its hydraulic activity is very low or inexistent [22].

2.2.4 Wollastonite

Wollastonite (or CS) exhibits two polymorphic forms, α-CS (pseudowollastonite) and β-CS, with the β form presenting two polytypes 1T (wollastonite) and 2M (parawollastonite). This phase melts congruently at 1544°C, with the transition between α-CS and β-CS occurring at 1125°C. Pseudowollastonite is the high temperature polymorph and rarely occurs in nature, while the other two β polymorphs are reasonably common [22]. The β to α transition is reversible but is slow in the α to β direction, being the α form easy to preserve by quenching [3].

Figure 2-8 shows the linear silicate chains that build the structure of wollastonite, which can be described as an arrangement of infinite parallel linear chains, virtually containing only Q^2 silicate units.

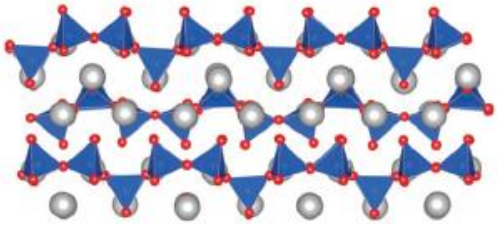

Figure 2-8. Structural detail of β-Wollastonite. Calcium, silicon and oxygen atoms are depicted as grey, blue and red spheres, respectively. Blue tetrahedra represent the $[SiO_4]^{4-}$ units. Adapted from [17].

CS is not one of the typical phases present in cements and its hydraulic behavior is known to be very poor [22].

2.3 Reactivity of Calcium Silicate Phases

As seen in the previous section not all the calcium silicate phases present appreciable hydraulic activity, thus limiting the applicability of the $CaO\text{-}SiO_2$ diagram to the region of high calcium content (> 66 wt% of CaO) when considering adequate properties of the corresponding phases for their use as cementitious materials, since apart from alite and belite no other calcium silicate phases seem to present enough potential to act itself as a hydraulic binder.

The difference of reactivity between the calcium silicate phases and even between the polymorphs of those phases has been studied by several authors and many aspects regarding

the structure of these phases and the role played by the elements present have been raised. Taylor [3] refers the importance of the basicity of the oxygen atoms in the reactivity, stating that any structural feature that draws electrons away from the oxygen atoms renders them less reactive. Furthermore this author relates the difference of reactivity between C_3S and β-C_2S with the fact that C_3S contains some oxygen atoms connected only to Ca while in β-C_2S all the oxygen atoms are connected to Si in $[SiO_4]^{4-}$ tetrahedra. Also in a recent study by Durgun et al. [16] the reactivity of alite and belite was evaluated by employing first principles calculations and a relationship with their electronic structure was found to exist, indicating that the higher reactivity of alite when compared to belite is mainly related to the reactive sites around its more ionic oxygen atoms which are loosely bound to the system. Moreover the introduction of impurities in the β-C_2S structure revealed to localize the negative charge towards the impurity site increasing its potential to react at the cost of decreasing the total number of reaction sites. Furthermore the degree of condensation was also indicated as another factor that contributes to the reactivity of calcium silicate phases [3], explaining the reason why β-C_2S is more reactive than C_3S_2 or CS, since, as it was seen in the previous section, the β-C_2S phase contains only isolated $[SiO_4]^{4-}$ tetrahedra (Q^0) where no oxygen atoms are shared with other structures (which also occurs for the C_3S structure), while both C_3S_2 and CS contain more polymerized features essentially consisting in Q^1 and Q^2 units, respectively. The difference in reactivity between γ-C_2S and β-C_2S polymorphs was recently studied by applying molecular dynamics (MD) simulations [23] and it was shown that, although the barrier energy for the surface hydration favors the γ-C_2S polymorph, the amount of sites available to react are much lower than in the β-C_2S, extinguishing the reaction almost instantaneously whereas the hydration of β-C_2S occurs for a longer period. The lower number of sites susceptible to react possibly results from the higher structural symmetry observed in the γ-C_2S polymorph. Xiuji et al. [24] even indicate another reason for the difference in reactivity between β-C_2S and γ-C_2S, suggesting that the main reason why β-C_2S possess higher hydraulic reactivity than γ-C_2S lies in the weaker Ca-O ionic bond in β-C_2S. Other factors may also play very important roles when considering the reactivity of the lower temperature polymorphs of belite, since it was observed that exsolution lamellae present in β-C_2S are preferential sites for the reaction to begin, with these lamellae boundaries often containing more reactive phases such as C_3A, which is more reactive than C_2S [3].

2.4 Hydration of Calcium Silicate Phases

The hydration process is absolutely crucial for cementitious materials. It is through this phenomenon that is possible to transform a fluid suspension into a solid material, without the need for heat or any other external processing agents and with minimal bulk volume change [25]. However only a small group of phases possess the required characteristics to set when hydrated, amongst them are some of the calcium silicates already presented in the previous sections, especially C_3S.

The potential for a given phase to act as a hydraulic binder depends not only from its reactivity with water but also on its ability to form solid hydration products, which should present very low solubility and a microstructure that can give rise to good mechanical strength, volume stability and other necessary properties [3].

In the case of Portland cement, the main constituent phases (C_2S, C_3S, C_3A and C_4AF) undergo a series of hydraulic reactions when water is added, being the most important the ones occurring with C_3S and C_2S and from which the poorly crystalline and chemically stable calcium silicate hydrate (C-S-H) is formed. Although C_3A reacts completely and very rapidly with water, the hydration products that are formed do not fully satisfy the conditions referred above, thus making the tricalcium aluminate unsuitable to act as a hydraulic binder by itself without the presence of other substances [3]. On the other hand, the C-S-H formed by the reaction of C_2S and C_3S with water meet all the criteria defined for a good hydration product, being the main responsible for the development of mechanical strength during hydration of OPC. The mechanisms of hydration as well as the respective reactions and typical hydration products are briefly described in the next paragraphs.

2.4.1 Mechanism of Hydration and Cement Hydration Products

Several studies on the mechanisms of hydration of cementing systems have been widely reported, as the understanding of these phenomena is of utmost importance for an improvement of the sustainability of concrete, allowing a better selection and proportioning of supplementary cementitious materials in the designing of new cement mixtures as well as the development of new clinkers [25-27]. The mechanism of cement hydration has been studied both by the point of view of the combined contribution of all the phases present in OPC and by the isolated study of each of those phases, especially C_3S [25, 26, 28, 29]. It is

nowadays very well accepted that the hydration of typical calcium silicate phases occur through a dissolution-precipitation process, with solubility playing a very important role in hydration of cementitious materials [27, 28, 30]. Therefore, in order for hydration to occur, the hydration products must be less soluble in water than the anhydrous phases, as it is schematically represented in Figure 2-9 for the cases of some calcium silicate phases. It is possible to observe that alite will always hydrate since the respective hydration product (C-S-H) is less soluble in the range from 0 to 36 mmol/L, value above which $Ca(OH)_2$ precipitates. The case of belite is different since, for lime concentrations above about 30 mmol/L, C_2S doesn't dissolve to form C-S-H. When considering wollastonite, Figure 2-9 shows that this phase doesn't hydrate at any CaO concentration, since it is always less soluble than C-S-H [25].

The hydration mechanism of usual cement systems, like OPC, can be described by the sequential and/or simultaneous occurrence of dissolution, nucleation and growth processes. This mechanism typically proceeds in 4 well defined steps, which can be easily identified by the use of isothermal calorimetry measurements, although the beginning and ending of these stages are still difficult to pinpoint precisely. These four stages are commonly identified as (1) initial reaction, (2) period of slow reaction, (3) acceleration period and (4) deceleration period [26], being those 4 stages shown in

Figure 2-10. The initial reaction in OPC occurs immediately upon wetting of the most hydraulically active phases, especially C_3S. At this stage major dissolution of alite takes place and an exothermic signal related to that phenomenon is observed [26].

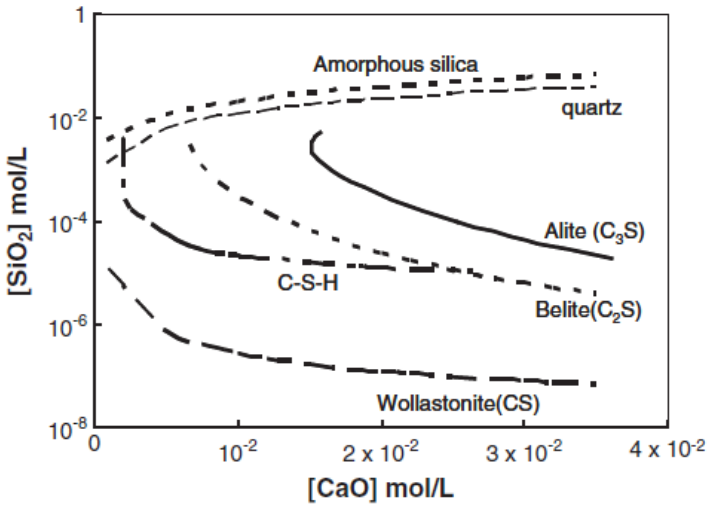

Figure 2-9. The solubility curves of silica (amorphous and quartz) and anhydrous calcium silicates (wollastonite, beta dicalcium silicate, and tricalcium silicate) are compared to the solubility of C–S–H [25].

Then the hydration process experiences a drop in the heat release (period of slow reaction), with this being related to the decrease in the dissolution rate of the dissolving phase that, in the case of alite, presents a high dependence on the concentration of the solution. Juilland et al. showed that an approach similar to the theory developed in the geochemistry field can be adopted in the analysis of the slow reaction period of alite dissolution, rejecting the theory of the formation of any protective phase and suggesting that the dissolution of the species is driven by the formation of defects, like etch pits in the surface of the grains, as long as the level of undersaturation doesn't drop below a critical value. When the concentration of CaO increases, the rate of dissolution becomes slow as the atoms may only dissolve from preformed defects. Furthermore, they also observed that defects with etch pit morphology were preferably formed under low CaO concentration conditions, whereas in lime saturated solutions the formation of steps in smooth surfaces was the main mechanism of dissolution observed [27]. Additionally in the same study the authors shown that the density of surface defects controls the rate of dissolution and thereby influence the length of the low activity period. The third stage of hydration is accompanied by a large exothermic signal in isothermal calorimetry experiments and is characterized by the initial formation of a solid interface between the solution and the hydrated product, which typically is inexistent in the beginning of the hydration process (unless in the case of pre-seeded systems [31]). The nucleation of the hydrated phase occurs preferably in pre-existing surfaces, such as in anhydrous grains of alite or other phases present. However, for the production of that interface to occur, some energy

is required, which is obtained through the supersaturation of the solution with respect to the precipitating phase. So, before the nucleation of the hydrated phase takes place, the period within only dissolution of the anhydrous phase occurs is crucial. Then, as the value of supersaturation, with respect to the hydrated phase being formed, is achieved, large enough nuclei of hydrated phase start to precipitate and further growth is observed, leading to a decrease in the free energy of the system [25]. It has been reported that only at the end of the slow reaction period it is possible to observe the presence of dimeric structures by NMR, with this suggesting that the polymerization of the silicate chains may be an important mechanism in the transition to nucleation and growth kinetics [26].

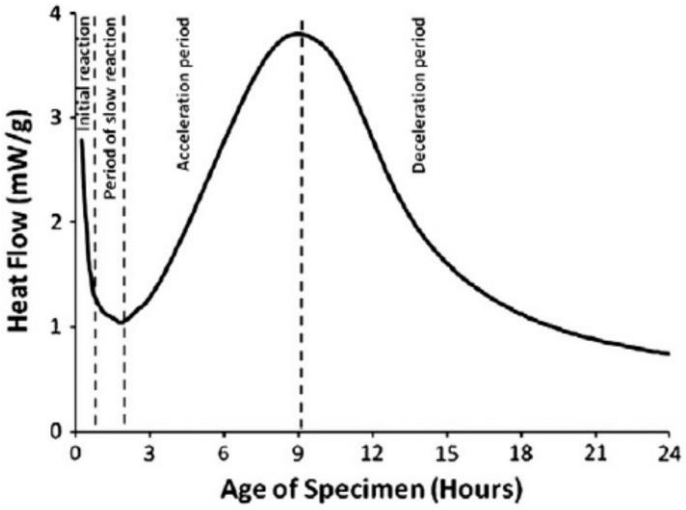

Figure 2-10. Rate of alite hydration as a function of time given by isothermal calorimetry measurements. Adapted from [26].

The final stage of hydration is a step of deceleration in the amount of the heat release that extends for a very large period and during which the slower strength development occurs. The decreasing trend in the heat release can be explained by a combination of several factors, being the most important the fact that at this point we are in the presence of a diffusion controlled process. Furthermore there are other factors contributing to the decelerating behaviour of hydration, such as the particle size, the impingement of hydrated domains or the lack of water. In the initial period of hydration, the smaller particles are rapidly dissolved, which translates in the reduction of the area available for reaction, leaving only larger particles with lower characteristic surface areas exposed. At this stage, as the hydrated phase grows from the surface of the unhydrated grains towards the available space in between, the

hydrated domains start to collide, reducing the area on which hydrated phase can deposit as well reducing the space for the formation of the hydration products. Furthermore the amount of free water ready to react also decreases, thus limiting the rate of formation of new hydrated phases and leading to a slower hydration development of the anhydrous phases.

As the hydration of high alite systems proceeds and the anhydrous phases are consequently consumed, incorporating the free water available in its structure, two major hydration products are formed, namely Portlandite and the stoichiometrically variable calcium silicate hydrate gel phase. Lea [22] suggested the equations below (Eq. 2.4 and Eq. 2.5) that described the hydration of belite and alite for any water/cement ratio at any hydration time, respectively:

Eq. 2.4 $$C_2S + (1.5+n)H \rightarrow C_{1.5+m}SH_{1+m+n} + (0.5-m)CH$$

Eq. 2.5 $$C_3S + (3+m-n)H \rightarrow C_nSH_m + (3-n)CH$$

Portlandite has a higher solubility than C-S-H, thus the calcium silicate hydrate phase is the first to be formed when alite or belite are mixed with water, with CH only precipitating when the CaO concentration rises above the critical supersaturation. This means that the amount of Portlandite formed from the hydration of C_3S or C_2S is dependent on the water/solid (w/s) ratio, being even possible to fully hydrate an alite sample without production of Portlandite, as long as the supersaturation of this phase is not achieved [25]. However, when considering the final application of cement or concrete and the typical w/s ratios used, Portlandite is usually present in C_3S hydrated systems.

2.4.2 C-S-H Models (Tobermorite and Jennite)

Calcium silicate hydrates are the main binding phases in all Portland cement-based systems with their C/S ratios varying from 1.2 to 2.3 in neat Portland cement pastes. A mean C/S value of 1.7 is usually accepted when describing the C-S-H produced from the hydration of OPC [22, 32, 33], however lower C/S values have been observed in systems of composite cements, typically containing blast furnace slag or fly-ash [3, 34, 35]. In addition to its very disperse stoichiometry (the reason why the term C-S-H is used, without implying any defined chemical

composition) this phase also presents a very poor crystalline character, being very difficult to characterize by the usual means, such as X-ray diffraction. Nevertheless, some XRD results have been obtained from synthetically prepared C-S-H samples with controlled C/S ratios [36] and some glances on the structure of C-S-H have been made with the use of NMR [37, 38], soft X-ray microscopy [39], TEM [32, 40, 41], SANS/SAXS [42], FTIR [43] or even Raman spectroscopy [44], with the information collected on the structure of this crucial hydration product revealing the existence of similarities with some structural features of mainly two natural crystalline calcium silicate hydrated phases (Tobermorite and Jennite), that have been widely used as the references from which more robust structural models of C-S-H have been constructed [40, 45, 46]. The structures of these two crystalline calcium silicate hydrate phases are well known and are schematically represented in Figure 2-11, where is possible to observe some similarities between these phases. The primary structural unit of Tobermorite consists in a layer composed of CaO polyhedral sheets sandwiched between single silicate chains, where the tetrahedra in the silicate chains typically grow in a 3n-1 units fashion, meaning that dimers are subsequently polymerized into longer chains (pentamer, then o octamer and so on…) [3, 22, 43] by the addition of repeating units of three tetrahedra, which are known as *drierketten*, where two of the tetrahedra (the pairing tetrahedra) point toward the CaO polyhedral sheet and the other tetrahedron (the bridging tetrahedron) points to the interlayer. The amount of water present in the interlayer region determines the distance between the individual layers, being known that 14Å Tobermorite contains the double of the water molecules of the 11Å Tobermorite [22]. Jennite presents a similar structure with the main difference lying in the presence of OH groups linked to the Ca atoms present in the central region of the individual layers [22].

The C/S ratio of the precursor phases also has a crucial impact in the type and properties of C-S-H, having been reported that C_3S pastes tend to produce C-S-H with higher C/S ratios than C_2S pastes [3, 47]. According to Richardson [41], as the Ca/Si ratio of the C-S-H decreases, the growth of the C-S-H particles undergo a transition from one-dimensional to two-dimensional, i.e., from long thin particles to foils, being this foil-like morphology typically associated with Tobermorite-based structures. Recent work from Uzun et al. [48] using high-energy X-ray diffraction showed a trend that indicated a transition from Tobermorite-like to Jennite-like structures with increasing C/S ratio in various C-S-H samples.

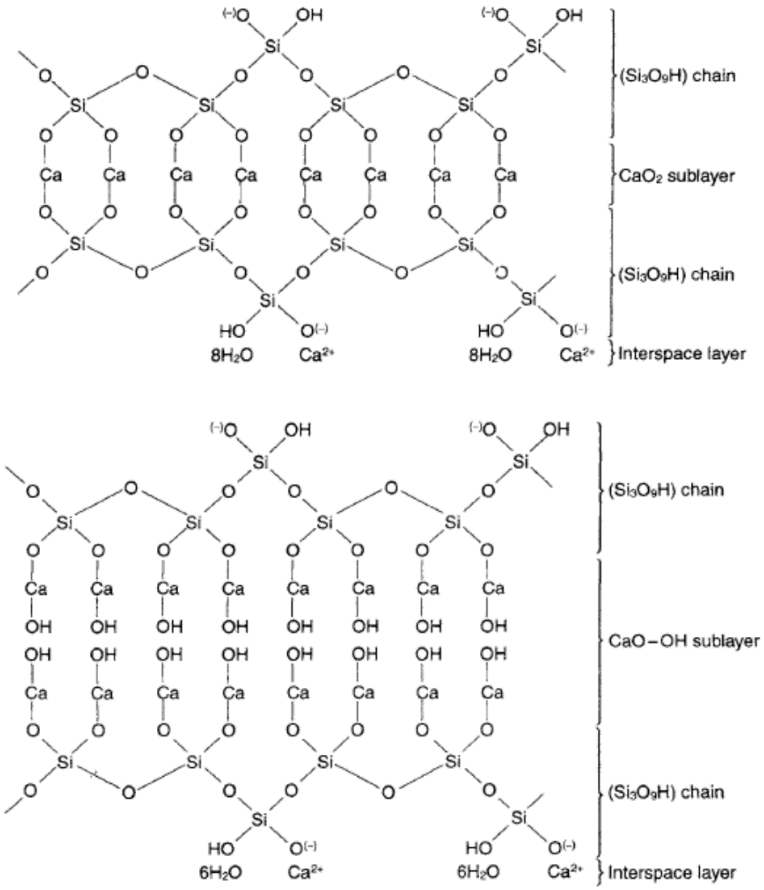

Figure 2-11. Idealized chemical structure of 1.4 Tobermorite (top) and Jennite (bottom). Adapted from [22].

Although Tobermorite ($C_5S_6H_8$) and Jennite ($C_9S_6H_{11}$) were reported to be the phases that better explain the features of the structure of C-S-H, their values of C/S ratio (0,83 and 1.5, respectively) and density (2,18 and 2,27 g/cm^3, respectively) seem to be short to justify the values typically obtained in the C-S-H formed from the hydration of OPC (C/S=1.7 and density of 2.6g/cm^3). Thus in the work of Pellenq et al.[45] it was considered a defective structure of an 11Å Tobermorite, to which neutral SiO_2 units were removed from the silicate chains in order to increase the C/S ratio, having them validated this approach by achieving values of C/S=1.65 and density of 2.56 g/cm^3 for the simulated C-S-H structure.

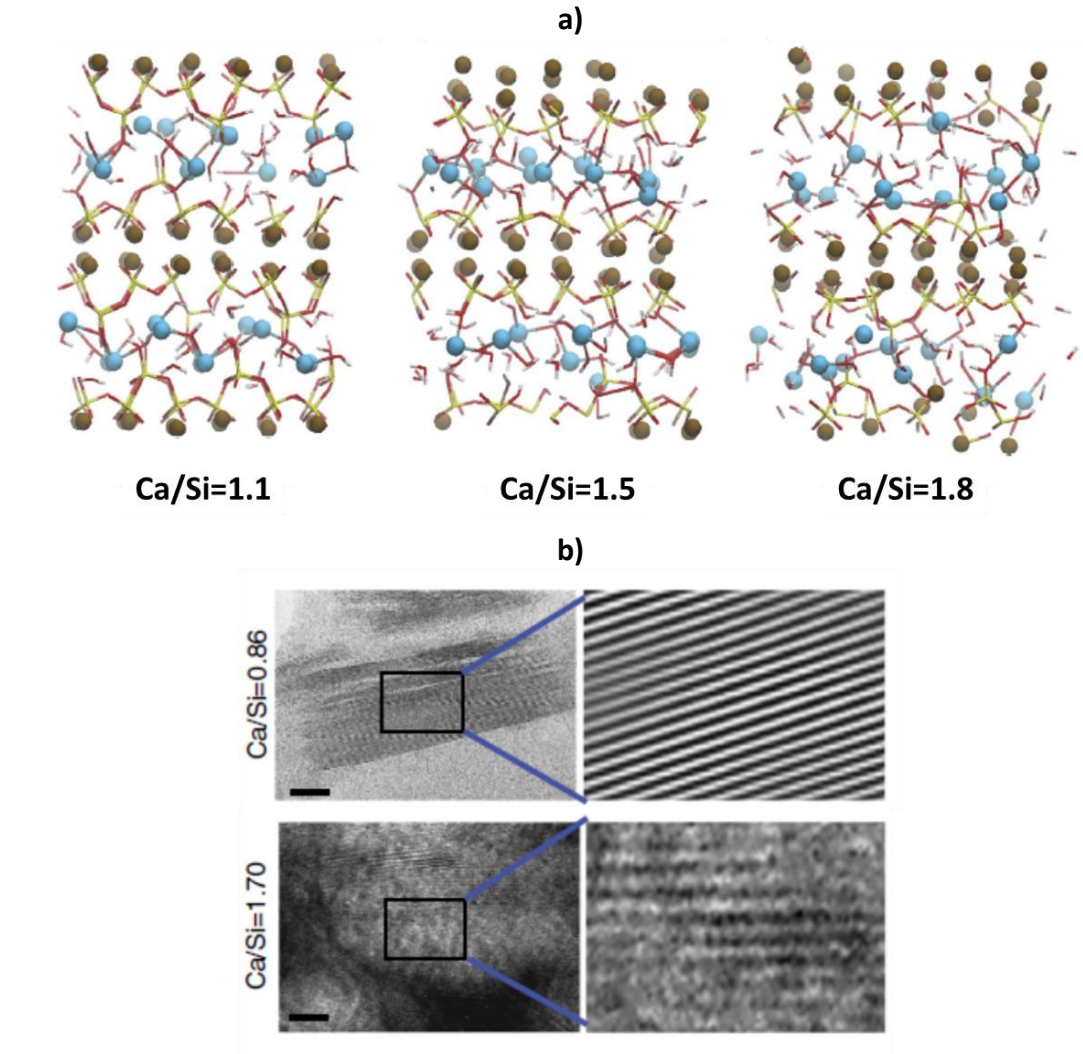

Figure 2-12. a) A molecular model proposed by Qomi et al. for C-S-H at different C/S ratios. The brown and cyan spheres represent intra- and interlayer calcium ions, respectively. Red and yellow sticks depict Si-O bonds in silicate tetrahedra. White and red sticks display hydroxyl groups and water molecules. b) TEM observation of C-S-H domains with different C/S ratios and crystallinities. The scale bar is 10nm. Adapted from [40].

This strategy was further used in a more recent study from Qomi et al. [40] on which it was revealed that as the bridging tetrahedral units are removed from the silicate chains that form the backbone of the 11Å Tobermorite, the degree of disorder also increases. Figure 2-12.a shows the effect of the increasing C/S ratio in the higher disorder of C-S-H, where for C/S=1.1 it is possible to observe well-ordered lamellar structures of silicates, while for higher C/S a more amorphous structure is formed due to the removal of more silica tetrahedral. This results seem to be in very good agreement with the observations made with TEM for samples containing domains of C-S-H with different C/S ratios (Figure 2-12.b).

This semi-crystalline nature of C-S-H was also reported in a previous study from Gartner et al. [49], where it was proposed a silicate chain based structure for C-S-H phase, that was claimed

to result as a consequence of the growth mechanism of this phase (Figure 2-13.a), containing regions of highly ordered layers that may be seen as nanocrystalline domains. Experimental evidences of this semi-crystalline nature of C-S-H were later verified by using soft X-ray microscopy [39] (Figure 2-13.b).

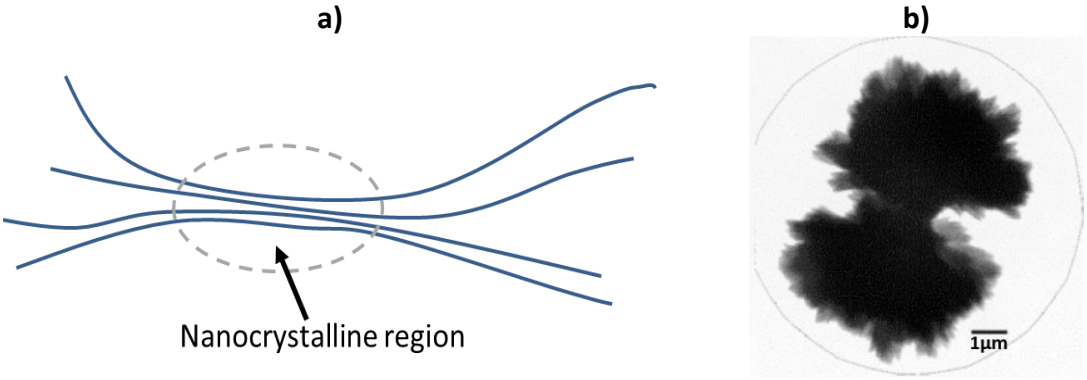

Figure 2-13. a) Schematic of the layered structure of C-S-H, with indication of nanocrystalline domains formed during growth, leading to a semi-crystalline nature of the hydration product. Adapted from [49]. b) Soft X-ray micrography of a particle in suspension formed from the reaction of silica fume with $Ca(OH)_2$. Adapted from [39].

Furthermore, Muller et al. suggested a C-S-H morphological model based on observations made by the use of H^1 NMR experiments, where different types of water were considered and quantified by measuring the signal intensity with respect to the relaxation times that are dependent on the mobility and consequently on the pore size, characteristic of each type of water present in the hydrated pastes.

Figure 2-14 shows the three different types of water considered to exist in the C-S-H structure, distinguishing between capillary water, interlayer water and structural water. Capillary water is the unbound water inside the pores that is available for reaction during hydration, while the interlayer water is held on by strong hydrogen bonding to the surface of C-S-H or by capillary forces in nanometer-scale pores. The structural water includes the water of crystallization and chemically bound, non-evaporable water that can only be extracted through the decomposition of C-S-H [50].

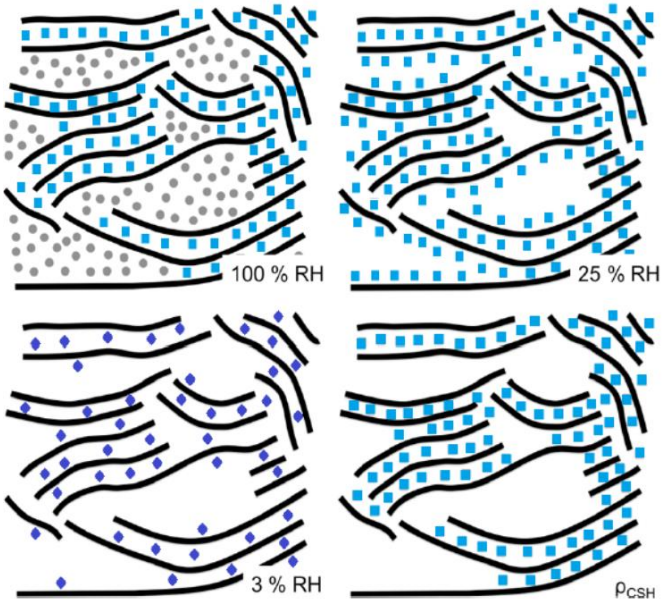

Figure 2-14. A schematic morphology of C-S-H. Capillary water is represented by grey circles, interlayer water is shown as blue squares and structural water molecules are represented as purple diamonds. Adapted from [51].

At a smaller scale, some molecular models of the C-S-H structure have been proposed, on which only structural and interlayer water are modelled together with the backbone structure of silicate chains and Ca ions. Some studies on the composition of C-S-H in various cementitious systems have shown that a correlation between the C/S and H/S ratios exist, with Richardson [46] reporting in a recent study a trend for the composition of dehydrated C-S-H pastes (i.e. without capillary water) that correlates the C/S ratio and the H/S ratio of a given C-S-H structure, as being described by Eq. 2.6:

$$\frac{H_2O}{Si} = \frac{19 \cdot \frac{Ca}{Si} - 7}{17} \qquad \textbf{Eq. 2.6}$$

Also a similar trend in the H/S vs C/S correlation has already been modelled in the work of Qomi et al. [40], which was supported by some experimental results from Cong and Kirkpatrick [37].

The results obtained from the models of Richardson [46] and Qomi et al. [40] will be considered later in this thesis for the estimation of the amount of C-S-H produced in the pastes produced in this work.

3 Alternative Solutions for Portland Cement

The search for an alternative for OPC is a very active field of investigation that has been bringing some interesting solutions to the table, always with the purpose of reducing the ecologic footprint, namely CO_2 emissions, related to the production of this material. Over the last decade, the cement industry tried to respond to this challenge using alternative fuels [7, 52, 53] or raw materials with low carbonate content that could result in decreasing the CO_2 emissions [5, 54-56]. Some approaches aim at the production of non-hydraulic binders such as the solution proposed by Solidia in the patents US 2013/0122267 A1 [57] and US/2012/0312194 A1 [58], where the binder is composed essentially by wollastonite and rankinite and it hardens through the carbonation of those phases. Still others have developed alternatives that follow non-clinker technological routes such as those described in patents US 2010/0186634 A1 [59] and US 2011/041737 A1 [60], where is described a material obtained by hydrothermal synthesis through seeding with pre-produced α-C_2S crystals. However, on a world scale, the investment of the cement industry in the existing BAT for OPC production is considerable, creating an important economic constraint to a drastic alteration of the existing technology. Thus, besides the CO_2 emissions problem, a specific issue that must be addressed in any novel hydraulic binder aiming to be an alternative to OPC is to provide a process for their production using the traditional clinker route and emitting less CO_2 than in conventional cement production. Amongst all the alternatives already referred to be able to replace or compete with OPC, it is of interest, within the scope of this thesis, to discuss some aspects regarding two specific groups of existing or suggested alternatives for Portland cement, namely (i) the ones based on high-belite content clinkers used to produce high-belite cements (HBC) and (ii) the ones containing supplementary cementitious materials (SCM's), either in mixture with OPC or in clinkerless alkali activated systems, typically based in a mix of SCM's, such as slags obtained by multiple processes, calcined clays, silica fume or fly-ash, and an alkaline activator. Amongst the alternatives referred in the second group, we will particularly focus in the systems that use highly amorphous components as starting materials.

3.1 High-Belite Cements

Recently, HBC have been proposed by some authors as an alternative to deplete CO_2 emissions [61-74]. These cements are said to save 10% of CO_2 when compared to OPC since they not only reduce the CO_2 emissions through the reduction of calcium oxide associated to the inversion of its main constituent (belite, instead of alite) but also through the fact that the clinkerization temperature is roughly 100ºC lower than for OPC, which also reduces CO_2 from fuel burning [62, 63]. In addition HBC is referred to promote better durability in concrete due to the lower amount of Portlandite formed during cement hydration, which leads to the improvement of long-term strength [61, 74]. However, the high belite content has a direct impact in the early age strength of this type of cements, since the reactivity of this phase is much slower than the observed for alite, thus resulting in inferior mechanical properties. To overcome this limitation, several approaches were studied in order to obtain hydraulic systems based on belite with improved hydraulic properties, so that a good development of mechanical strength could occur from early ages. From these approaches, 4 main strategies are usually adopted, including:

i) belite activation, typically by doping with stabilizing elements; ii) introducing more reactive phases in the clinker, such as calcium sulfoaluminate (ye'elimite – $C_4A_3\$$) in the case of belitic calcium sulfoaluminate cements; iii) designing clinker composition to produce a minimum of 15% alite; and iv) a combination of the previous strategies [63]. The following sections resume some of these approaches.

3.1.1 Stabilization of High Temperature Polymorphs (α-C_2S)

It is well known that belite presents completely different reactive behaviours depending on the polymorph formed. As it was referred in section 2.3, the reactivity of C_2S highly depends on its polymorphic form and increases in the order γ-C_2S << β-C_2S < α-C_2S [11], thus making the high temperature polymorphs (β-C_2S and α-C_2S) much more interesting than the low temperature one (γ-C_2S). In typical Portland cements, the β-C_2S polymorph is the one most commonly found, nevertheless its contribution for the development of strength only become appreciable beyond the 28 days of hydration. This is the main reason why most of the attempts to enhance HBCs hydraulic activity have used an approach that consists in bringing to room temperature the high temperature polymorphs of belite (α, α'h), leading to the

presence of metastable, more reactive forms of belite in the clinker. The stabilization of these high-temperature polymorphs at room temperature can be made by doping the clinker with some amount of activators, such as Na, K, S or Fe [64, 65, 70]. In a recent study conducted by Kacimi et al. [74] it was even proposed a belite reactivity improvement by means of the introduction of structure stabilizers (NaF and Fe_2O_3) combined with an increase of the cooling rate after clinkerization achieved by quenching in water. The obtained clinker showed to possess a hydraulic activity similar to an ordinary alite clinker. Furthermore, in a very interesting study by using in situ synchrotron X-ray powder diffraction, Cuberos et al. [62] showed that, while β-C_2S almost does not react during the first three months of hydration, the high temperature polymorphs (α'h and α) react much faster. Although, surprisingly, after one year 29 to 42wt% of unreacted α'h still existed.

3.1.2 Belite Sulfoaluminate Cements

Another group of belite based cements is the belite calcium sulfoaluminate (BCSA) cements, which are said to deplete CO_2 emissions up to 35% when compared to OPC [67, 68], however the SO_2 emissions are considerably higher [75]. These cements represent a type of ye'elimite-containing cements that have been produced in China since the 1970's under the name of "Third Cement Series" [76] and its constitution contains C_2S as main phase (40-60 wt%) and intermediate $C_4A_3\$$ contents (20-30 wt%), being the ye'elimite phase responsible for the early strength development, while belite provides good secondary hardening [67, 77].

Within this type of cements are included the BCSAF (Iron-rich Belite Calcium Sulpho-Aluminate), the BCSAA (Aluminum-rich Calcium Sulpho-Aluminate) and BACSA (Belite Alite Calcium Sulpho-Aluminate) cements, that essentially differ in the type of the secondary phases present. BCSAF clinkers also contain C_4AF apart from C_2S and $C_4A_3\$$ and are produced at 1250-1300ºC, meaning a 200^{o}C decrease when comparing to OPC, being this type of clinkers also referred to be more porous than normal Portland clinkers, rendering in a lower grinding energy. In addition they show a rapid hardening, excellent durability, self-stressing and volume stability, depending on the amount of gypsum added. Furthermore the reactivity of BCSAF clinkers was shown to be improved by the introduction of B_2O_3, which ensures the stabilization of more than 50% of C_2S in the α'h form [67, 69, 78].

BCSAA contains $C_{12}A_7$ and CA in addition to belite and ye'elimite and are produced at temperatures approximately 100°C higher than the necessary for BCSAF, requiring also higher amount of alumina-rich raw materials, such as bauxite, that are rather expensive. Nevertheless these compositions result in enhanced mechanical strengths at very early ages [68]. BACSA may contain approximately 40 wt% of belite, ~20 wt% of ye'elimite and ~20 wt% of alite, resulting in higher mechanical strengths at early ages. These cements will perform better than other BCSA cements when mixed with pozzolanic materials since the presence of alite promotes a higher basicity that will help trigger the pozzolanic reaction [77].

3.2 Using Supplementary Cementitious Materials (SCM's)

In addition to alternative cements, a very effective way of reducing the amount of CO_2 emissions related to the production of cement is the blending with other non-clinker materials that can include by-products of other industries, such as blastfurnace slags, fly ashes and silica fume, or natural and artificial pozzolans and calcined clays (metakaolin). This group of materials is commonly called as "supplementary cementitious materials" and are generally characterized by possessing a silica-rich matrix and lower calcium contents when compared to Portland cement, as it is shown in Figure 3-1. The SCM's can be mixed/interground with the Portland clinker at the cement production plant or added directly to the concrete mix as a separate material at the construction site. Some of the most commonly used SCM's are slags and fly-ash, being the reactivity of these materials typically lower than OPC and are dependent on various factors, such as the system temperature, the alkalinity of the solution, the fineness and also their composition [79]. At the early ages of hydration SCM's almost do not react, however they do contribute with the so-called "filler effect" to an increase in reactivity of the clinker phases. There are two mechanisms contributing to the this effect: i) the increase of the water to clinker ratio, as the SCM's don't produce hydrates in the initial stage of hydration, thus making more space for the hydration products of the clinker phases to grow; and ii) the creation of nucleation sites, especially in finely ground materials [79]. At later ages, and as the pH of the pore solution and the system temperature increases, the SCM's start to react, leading to the formation of hydration products richer in silicon and alumina, resulting in a more complex hydrated microstructure than the usually observed by the hydration of OPC. The addition of SCM's to Portland cements results in a reduction of the overall C/S ratio of the

system, which impacts in the hydration products formed, often resulting in the formation of C-S-H characterized by lower C/S ratios and/or by a generalized presence of Al in its structure. In fact, these two phenomena are said to be related, since Al enters preferentially bridging tetrahedra sites of the silica chain, increasing the mean chain length of the hydrates and forming C-A-S-H type gels [80]. However, even with the inclusion of aluminum in the hydrated gel, a tobermorite-like structure seems to be maintained [81]. As many SCM's have high amounts of Al, other aluminum-containing hydrated phases are frequently present, such as AFm, ettringite, strätlingite or monocarbonates [79]. Furthermore, the Portlandite formed in the hydration reaction of alite or belite in these systems, is later "consumed" by the pozzolanic material which provides a source of relatively soluble silica that further reacts with Portlandite, forming more C-S-H with low C/S ratio. Unfortunately, since many SCM's consist of X-ray amorphous compounds, its reaction degree is very difficult to follow by usual Rietveld analysis [79], even using selective dissolution methods [82].

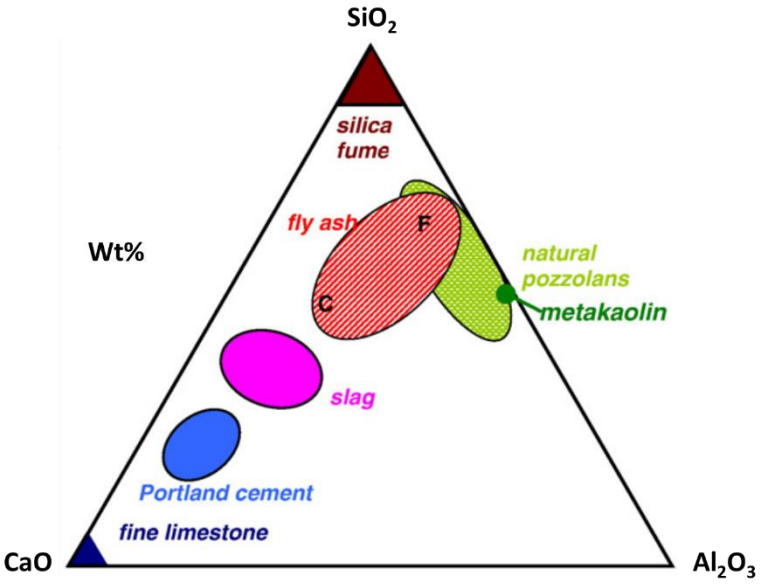

Figure 3-1. CaO-Al_2O_3-SiO_2 ternary diagram of cementitious materials. Adapted from [79].

3.2.1 Alkaline activation of SCM's

A clinker-less alternative that has deserved much attention is the alkaline activation of supplementary cementitious materials, which has been a widely studied topic in the last few decades, with many works being developed, focusing on the reactivity improvement of typical industrial slags, such as iron blast-furnace slag, steelmaking slag, phosphorous slag, copper

slag or even fly-ash [83-87]. Ground granulated blast-furnace slag (GGBFS) was the first SCM being studied with this purpose [88] and it is still being the most studied material, within the ones referred, to be activated with alkaline solutions.

According to Glukhovsky [89], the alkaline activators can be classified in six groups:

- alkalis (MOH);
- weak acid salts (M_2CO_3, M_2SO_3, M_3PO_4, MF);
- silicates ($M_2O{\cdot}nSiO_3$);
- aluminates ($M_2O{\cdot}nAl_2O_3$);
- aluminosilicates ($M_2O{\cdot}Al_2O_3{\cdot}(2\text{-}6)SiO_2$) and
- strong acid salts (M_2SO_4).

The alkaline cation M^+ work as a catalyzer in the initial phases of hydration of SiO_2- and CaO-rich materials, via cationic exchange with Ca^{2+} ions, which mechanism can be described by means of the following series of reactions [90]:

$$\equiv Si\text{-}O^- + M^+ \rightarrow \equiv Si\text{-}O\text{-}M$$

$$\equiv Si\text{-}O\text{-}M + OH^- \rightarrow \equiv Si\text{-}O\text{-}M\text{-}OH^-$$

$$\equiv Si\text{-}O\text{-}M\text{-}OH^- + Ca^{2+} \rightarrow \equiv Si\text{-}O\text{-}Ca\text{-}OH + M^+$$

This catalyzer effect will improve the kinetics of hydration of these cementitious materials which is inherently slow. It is known that a simple addition of water to GGBFS is not enough to induce a hydraulic reaction, failing these materials to develop acceptable mechanical properties at early ages on their own, only presenting hydraulic properties when suitably activated and, for that reason, GGBFS is currently used as partial replacement of Portland cement [10]. In that case the Portland cement acts as the basic component that increases the pH to a level high enough to trigger the hydraulic activity of slag [91]. If one considers fly-ash, the pH value needed to initiate the hydraulic reaction is even higher, with this difference being attributed to chemical composition and glass structure reasons [92]. The reactivity of these industrial secondary products also show a direct relation with the amount of glass content, as this is usually the active part of the material [92]. Thus, crystallized blast furnace slag has little or no value as a cementing component [83]. Moreover, it has been reported in a study by Boenisch et al. [93] that the solubility of Ca and Si specimens are sensible to the more or less crystalline networks to which they belong, revealing higher solubility when present in more

disordered environments. Furthermore, Oelkers et al. [94] refer that the Si-O bond is the strongest and slowest to break during dissolution, thus being the rate controlling step of dissolution for silicate minerals and glasses with a molar Si/O ratio above 0.28. Therefore, glasses, by presenting a lower order in the Si-O bond, are more prone to dissolve than their corresponding minerals since these bonds will also be more susceptible to break.

In addition, amorphous glassy materials show as advantage a preferred behavior when alkali activated [92] to act as cementitious materials and reveal favorable conditions to compete with OPC as standard hydraulic binders in the future. This type of cementitious systems can theoretically be used as fully replacement of OPC, as they have demonstrated to develop similar or higher mechanical strength, improved durability and also lower hydration heat development, however they are nowadays very dependent on the availability of SCM's, which tend to be not as widespread as the raw materials that are normally used for the production of OPC, as well as they are not yet included in any regulatory standard as accepted cementitious materials for building and construction purposes. Nevertheless, it was recently created a technical committee with the purpose of evaluating the conditions that would pave the basis for the development of performance-based standards that would open the way to incorporate these alkali activated materials in the construction materials category [95]. In opposition to the existing prescriptive standards that do not present enough flexibility to consider such variety of materials and activators, the design of new performance-based standards should even lead to the development of other groups of cementitious materials.

In this work the effect of alkaline activation (using a set of alkaline solutions including $NaCO_3$, Na_2SO_4 and a mixture of NaOH with Na_2SiO_3) was tested on synthetically produced amorphous hydraulic binders. The results are shown in chapter 7.

4 Materials and experimental techniques

This chapter describes the characteristics of the raw materials used in the production of the several hydraulic binders studied in this work, as well as the procedures adopted in the preparation of the samples and in all the experiments performed for the characterization of the studied samples.

4.1 Raw materials

For the production of the low calcium content hydraulic binders covered in this work, a set of raw materials typical in the cement industry were used. Four different types of raw materials were selected, namely limestone, sand, fly-ash and electric furnace slag.

Table 4-1. Chemical composition of the raw materials selected for the production of the hydraulic binders produced in this work.

	Composition (weight %)												
Raw materials	**LOI**	**SiO_2**	**Al_2O_3**	**Fe_2O_3**	**CaO**	**MgO**	**SO_3**	**K_2O**	**Na_2O**	**TiO_2**	**P_2O_5**	**MnO**	**Cr_2O_3**
Fly- Ash	4,54	57,07	23,91	8,68	3,96	1,56	0,12	1,84	0,62	---	---	---	---
Sand	0,37	97,30	1,29	0,16	0,00	0,02	0,00	0,52	0,11	---	---	---	---
Limestone	43,34	0,46	0,06	0,09	55,53	0,23	---	---	---	---	---	---	---
Slag	0	13,90	8,26	43,54	21,18	6,06	0,40	0,00	0,00	0,46	0,46	3,76	1,98

shows the composition of the raw materials selected for the production of the various low calcium content hydraulic binders produced throughout this work.

Each of the raw materials used contribute differently for the overall composition of the resulting hydraulic binder, with limestone acting as the main calcium source whereas sand is the main source of silica. Electric furnace slag and fly ash are used as correction materials, contributing to the final composition essentially as sources of iron and alumina, respectively.

Table 4-1. Chemical composition of the raw materials selected for the production of the hydraulic binders produced in this work.

	Composition (weight %)												
Raw materials	**LOI**	**SiO_2**	**Al_2O_3**	**Fe_2O_3**	**CaO**	**MgO**	**SO_3**	**K_2O**	**Na_2O**	**TiO_2**	**P_2O_5**	**MnO**	**Cr_2O_3**
Fly- Ash	4,54	57,07	23,91	8,68	3,96	1,56	0,12	1,84	0,62	---	---	---	---
Sand	0,37	97,30	1,29	0,16	0,00	0,02	0,00	0,52	0,11	---	---	---	---
Limestone	43,34	0,46	0,06	0,09	55,53	0,23	---	---	---	---	---	---	---
Slag	0	13,90	8,26	43,54	21,18	6,06	0,40	0,00	0,00	0,46	0,46	3,76	1,98

4.2 Sample preparation

The sand used as raw material in this work required previous milling before being intermixed with the other raw materials. This milling stage was performed in a ring mill, where portions of 50g of sand were ground for 2 minutes. The particle size distribution (PSD) of the raw materials used is shown in Figure 4-1.

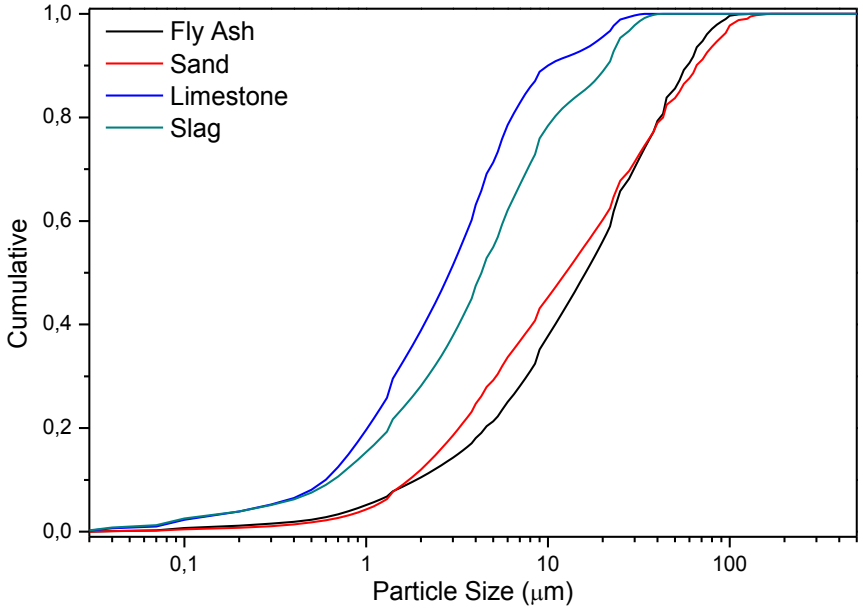

Figure 4-1. Particle Size Distribution of the raw materials used for the preparation of the raw meal, as determined by laser granulometry using ethanol as dispersing agent.

Then the raw meal further used for the production of each hydraulic binder was prepared by intermixing the raw materials, in their respective proportions, by hand, until a good degree of homogenization was achieved.

For the production of the hydraulic binders studied in this work, the raw meal undergoes specific heating and cooling cycles, which will be described in more detail in sections 5.2 and 6.1. In the end of this process a bulk material with hydraulic properties is obtained, further requiring a grinding stage so that it can be used as a binder that sets when mixed with water.

4.3 Paste preparation

Pastes were prepared by using a bench-top mixer. The water/cement (w/c) ratio used in the preparation of each pastes is specifically defined in the sections 5.2, 6.1, 7.1 and 8.1. The water to cement ratios used in this work were tested as function of the fineness of the anhydrous

materials from which the pastes were produced, in order to maintain similar paste workability, as this property is the one ultimately considered when using a hydraulic binder on its final application. The mixing time was of approximately 2 minutes for all the pastes prepared in this work. After mixing the pastes were poured into proper molds with dimensions of 20x20x40mm^3, as shown in

Figure 4-2. The molds were kept in a moist cabinet with a controlled environment off over 95% relative humidity and approximately 20^{o}C. After 7 days the paste prisms were taken from the molds and left to cure in the same moist cabinet until the age they were mechanically tested.

Figure 4-2. Prism mold used in the production of paste samples.

4.4 Laser Granulometry

Laser granulometry measurements were performed in a CILAS equipment, operating with a red 650nm laser under the Fraunhofer model approximations, and using ethanol as dispersing agent. A pre-measurement ultrasound stage of 40 seconds was used for a better disaggregation of the particles. Particle size distribution PSD analysis was essentially used as a tool for a proper preparation of the raw materials and the anhydrous hydraulic binders, where specific milling times were defined accordingly to the desired PSD of each material to be used.

4.5 Optical Microscopy

For optical microscopy observation, bulk pieces of the anhydrous as prepared samples or its respective pastes were mounted in an epoxy composite resin, which cured for 24 hours. The samples were then cut with a diamond saw in a Struers Minitom, polished with 800 and 4000 grade silicon carbide papers and finished with 9, 6, 3 and 1µm diamond spray in polishing cloth, always using an ethanol based lubricant solution from TESTA. After the polishing

procedure, the samples were cleaned in an ultrasonic bath immersed in propanol. Surface etching was performed by immerging in a Nital solution (2%v/v nitric acid in ethanol) for about 10 seconds. An Olympus BX 60 microscope with a CLEMEX camera coupled to a computer with proper software was used for samples microstructures observation.

4.6 Fourier Transform Infrared with Attenuated Total Reflectance (FTIR-ATR)

Infrared spectroscopy is a technique that allows to collect structural information from practically any type of sample, from solid to liquid and also gaseous systems. The principle of this technique is based on the vibration energies of the atoms of a molecule. An infrared spectrum is commonly obtained by exposing a sample to infrared radiation and determining what fraction of the incident radiation is absorbed at a particular energy. The energy at which any peak in an absorption spectrum appears corresponds to the frequency of a vibration of a part of a sample molecule.

For a molecule to show infrared absorptions it must possess a specific feature, i.e. the electric dipole moment of the molecule must change during the vibration. This is the selection rule for infrared spectroscopy [96].

Nowadays there are two main methods available for the acquisition of an infrared spectrum, transmission and reflectance. In this thesis a reflectance method was used, namely attenuated total reflectance (ATR). This technique utilizes the phenomenon of total internal reflection. A beam of radiation entering a crystal will undergo total internal reflection when the angle of incidence at the interface between the sample and crystal is greater than the critical angle, where the latter is a function of the refractive indices of the two surfaces. The beam penetrates a fraction of a wavelength beyond the reflecting surface and when a material that selectively absorbs radiation is in close contact with the reflecting surface, the beam loses energy at the wavelength where the material absorbs. The resultant attenuated radiation is measured and plotted as a function of wavelength by the spectrometer and gives rise to the absorption spectral characteristics of the sample [97].

In this thesis, the acquisition of the FTIR-ATR spectra was performed with a bench-top Bruker spectrometer (model Alpha) operating with an ATR module. The spectra were collected in the range from 400 to 4000 cm^{-1}, with 24 accumulations and a 4 cm^{-1} resolution.

4.7 X-Ray Difraction with Rietveld Analysis (XRD – Rietveld)

X-ray diffraction (XRD) is a widely used technique for the study of crystalline materials, allowing the identification of the crystalline phases present in a given sample and also its quantification by using the Rietveld refinement technique. This technique is very useful in the study of the hydration of cementitious materials since it enables to follow their phase development by determining the amounts of the different phases present in each system and at each hydration age. The theoretical basis for Rietveld analysis can be found in the paper of Bish and Howard [98], with its principle consisting in iteratively comparing the experimental pattern with a simulated pattern that is generated with basis on presumed amounts, crystal parameters and equipment parameters of a mixture of previously identified phases. Rietveld analysis always returns a 100% sum of the identified phases. Therefore, all the phases present must be entered into the analysis and their structures known. The presence of amorphous or unknown phases result in an overestimation of the true amounts of the crystalline phases present in the sample. However, if an amorphous phase is known to be present, this problem can be easily solved by adding a known amount of a reference standard. The amount of each phase may then be corrected by dividing its value by the ratio of the measured to true amount of standard added. The amount of amorphous phases is then calculated as the difference of the sum of the amount of all the phases to 100% [99].

In this work, diffractograms of powder samples were acquired in a X'Pert Pro (PANalytical) diffractometer using monochromatic $CuK_{\alpha 1}$ radiation (λ=1.54059 Å) and working in reflection geometry (θ/2θ). The optics configuration was a fixed divergence slit (1/2°), a fixed incident antiscatter slit (1°), a fixed diffracted anti-scatter slit (1/2°) and an X'Celerator detector, working in scanning mode with maximum active length. Data for each sample were collected from 5° to 60° (2θ). The samples were rotated during data collection at 16 rpm in order to enhance particle statistics. The X-ray tube worked at 45 kV and 40 mA.

Phase quantification was performed through Rietveld analysis using the Panalytical software Highscore Plus. An amount of 20% in weight of an internal standard of corundum (99.9% α-Al_2O_3 from Alfa Aesar) was added to each mixture in order to allow the quantification of the amorphous content.

The code of the phases used for the Rietveld refinement is given in sections 5.3.3, 6.2.2, 7.2.2, and 8.2.2 for each system studied.

For the Rietveld refinement, the background was defined by regulating the granularity and the bending factor to a degree that allow it to adjust to the amorphous hump typically present in all the samples analyzed. The generated background was used as reference in each refinement and the scale factors, cell units and the peak width W parameter were set as flexible values to perform the profile fit, resulting in goodness of fit values below 5 for all the refinements.

4.8 Solid State Nuclear Magnetic Resonance

Solid state NMR spectroscopy is a powerful technique capable of providing information about the structure of a wide range of materials including amorphous and crystalline, organic and inorganic. NMR is able to monitor the changes occurring in the atomic environment when materials change from one state of structural disorder or heterogeneity to another. To produce an NMR spectrum, a nucleus must possess a nuclear spin *I*. Nuclei with odd mass numbers (e.g. ^{29}Si and ^{27}Al) have half-integer spins (I=1/2) and are of most interest for solid state NMR [100]. When such a nucleus is placed in a strong magnetic field, the energy levels between the various spin states are split (the Zeeman interaction). The differences between the various energy levels are small compared with spectroscopies involving electronic energy states, and transitions are only possible between adjacent energy levels, with the absorption or emission of a photon in the radiofrequency range. It is the frequency of this radiation which is measured in an NMR experiment. The nuclei in different structural environments in a solid may experience slightly different magnetic fields because they are shielded by the surrounding electrons and consequently absorb photons of slightly different frequency. Since the absolute NMR frequencies are difficult to measure with sufficient accuracy, the resonance frequencies are normally reported as chemical shifts (δ) relative to an external standard compound.

In its simplest form, an NMR experiment consists of three parts: the preparation, the perturbation and the detection. The preparation of the nuclear spin system is achieved by placing it in an external magnetic field B_0, leading the system magnetic moment to precess about the B_0 axis. The response will be an average of the behavior of each individual spin. The frequency of the precession is called the Larmor frequency and is characteristic of the

particular nucleus, so that each NMR experiment is specifically tuned for the nuclide under study. The perturbation stage occurs when the sample, experiencing the external magnetic field B_0, is irradiated by a pulse of plane-polarized radiation, at the Larmor frequency, interacting with its magnetic field component and causing the equilibrium magnetization to incline with respect to the applied magnetic field. In the simplest experiment, the angle of inclination is 90º and, provided the pulse is of short duration compared with the time taken for the spin packet to spiral into the new field direction, the precession can be assumed to remain fixed at 90º. Such a pulse, which is long enough to rotate the spin packet trough 90º, is described as a π/2 pulse. The detection stage begins as the radiation field is turned off at the end of the simple 1-pulse experiment. At this point the spin system dephases in the x-y plane with a characteristic relaxation time T_2, returning to the equilibrium condition along the z-axis with a characteristic relaxation time T_1. During this process the voltage induced in the coil by the transverse magnetization is recorded as a function of time. This signal, usually called Free Induction Decay (FID) contains frequency information that can be treated by means of Fourier transformation giving a plot of amplitude vs. frequency. In order to improve the signal to noise ratio, the sample is usually irradiated with a large amount of pulses that will generate a series of individual signals being added up together to form a NMR spectrum.
Contrarily to the NMR of liquids, where the atomic motion is faster than the interaction frequency thus allowing all the nuclei in a particular environment to experience the same average magnetic field leading to the production of narrow NMR spectra, the NMR spectra of solids suffer from broadening due to various interactions between the dipole moments of the nuclei, between the quadrupole moments of quadrupolar nuclei and the electric field gradient at the nucleus, and by anisotropy of the electronic shielding at different sites in the structure. However, some of these interactions can be cancelled out or at least reduced by spinning the sample very rapidly at an angle that follows the rule $\cos\theta_m = \frac{1}{\sqrt{3}}$, i.e. 54.74º, the so-called magic angle (θ_m). This technique has the name of magic angle spinning (MAS) and is performed with a proper probe that allows the sample to rotate at the magic angle, thus removing the dipole-dipole and chemical shift anisotropy interactions, as well as the first order quadrupolar interactions, narrowing the resonance lines from spin I=1/2 and quadrupolar nuclei to better reveal spectral details [100].

In this work solid state MAS-NMR was used to follow the structural evolution of the hydraulic binders produced during hydration as well as to identify the species being formed.

Anhydrous powders of the materials produced and their corresponding dried pastes were studied by solid state NMR spectroscopy using a TecMag (Redstone)/Bruker 300 "wide bore" spectrometer equipped with a 7 mm solid-state probe operating at a Larmor frequency of 59.625 MHz for ^{29}Si observation and at 78.216 MHz for ^{27}Al observation. Anhydrous powders were used neat with particle size below 35µm, while dried paste samples were ground by hand in an agate mortar. Samples of about 200 mg were packed into 7 mm o.d. cylindrical zirconia rotors. The chemical shifts were referenced to external samples of tetrakis(trimethylsylil)silane ($Si(CH_3)_3$, δ= -9.8 ppm) for ^{29}Si and Al_2O_3 for ^{27}Al observation. The samples were analyzed neat with a total number of accumulated scans over 2000 and the spectra were collected under magic angle spinning (MAS) with a rate of about 3.5 kHz for ^{29}Si and 5.2 kHz for ^{27}Al observation. For the single pulse ^{29}Si NMR experiments, was selected a pulse length of 2.5 µs, corresponding to 50^o magnetization flip angle, and a recycling time delay of 20 s, while for the ^{27}Al NMR measurements a pulse length of 1 µs was selected, corresponding to 30^o magnetization flip angle, with a relaxation delay time of 1 s. The chemical shifts were referenced to an external sample of tetrakis(trimethylsylil)silane ($Si(CH_3)_3$, δ= -9.8 ppm).

4.9 Scanning Electron Microscopy with Energy Dispersive Spectrometry (SEM – EDS)

Sample preparation for SEM observation followed the procedure already described in section 4.5 for the optical microscopy as regards to mounting, polishing and cleaning. Additionally, to improve the conductivity of the surface, the samples were covered with a gold palladium deposition before the visualization in SEM. The images presented in this work were taken with a Hitachi S2400 SEM, operating at 20 keV. A coupled Bruker EDS probe was also used to draw composition profiles on the images collected by SEM.

4.10 Thermogravimetric Analysis (TGA)

TGA experiments were performed in an ELTRA equipment running at constant heating rates between fixed temperature steps that evolved until constant mass at the temperatures of 105, 250, 500 and 950ºC. A heating rate of 4ºC/min was applied in the first step (from room temperature to 105ºC), while in the second step (between 105ºC and 250ºC) a heating rate of 10ºC/min was used. The last two steps (from 250ºC to 500ºC and between 500ºC and 950ºC) ran at a heating rate of 15ºC/min).

TGA was used especially for the determination of the amount of bound water in hydrated clinkers. For this purpose it was considered that the weight loss between 105 and 500ºC was exclusively due to the structural water removal in the pastes prepared in this work.

4.11 Compressive Strength Test

Compressive strength tests were performed in paste prisms with dimensions 20x20x40 mm^3 in an Ibertest Autotest 400/10 equipment using standard test procedures, namely a 2,4kN/s force rate was applied during the compression tests. Three prisms per sample were tested at each age.

4.12 Drying and Stopping Hydration in Pastes

An effective way to stop hydration in cement pastes is to remove all the water available to proceed with the reaction of the anhydrous phases. This means that all the non-chemically bound water should be removed from the sample in order to stop the hydration process. Typically, in cement pastes, three types of water are present in hydrated samples: capillary water; interlayer water and structural water.

The former is largely free from physical interaction and as such is available for reaction during hydration. Therefore, this is the type of water that should be removed when arresting hydration of a paste, while the removal of the last two types of water may be undesirable, because the composition of some of the hydrated phases could be altered [50, 101]. Regarding the hydration stopping, there are several techniques that can be used, being divided in two major methods: direct drying, which involves the removal of the unbound water either by evaporation or by sublimation, and solvent exchange, which requires the sample to be

immersed in a preferably small molecular size liquid that penetrates into the smallest pores to replace the water that is still available for reaction. Amongst these techniques, the oven drying is probably the most popular and it was the one used in this work for stopping hydration in pastes, as a proper sample preparation and conservation method that allow the sample to be used in further analysis. All the paste samples used in compressive test experiments were collected after testing and dried at 105^{o}C in a muffle furnace for about 1 hour for evaporable water removal. Then these dried samples were used for the acquisition of X-Ray diffractogram, FTIR-ATR and MAS-NMR spectra, and TGA data.

The oven drying technique is referred to damage the microstructure of the sample and to remove some chemically bound water, especially when ettringite is present as hydration product [101]. However, no ettringite was identified in any of our studied systems, neither microstructure analysis was made in samples previously dried in oven.

4.13 Isothermal Calorimetry

The isothermal calorimetry technique has been widely used in the study of the mechanisms that occur during the hydration of cement, with the information collected by this technique being very useful to describe the main stages that cement pastes undergo until the formation of a rigid and perfectly solid material.

Isothermal Calorimetry measurements were conducted at the application laboratory of TAM Air Instruments – Waters Sverige AB. The samples were analyzed as received using milli-Q quality water or an alkaline solution properly provided by the author, being the paste preparation performed *ex-situ*. All experiments were performed at 25^{o}C and the heat of hydration information collected during 8 days.

5 Development of Dendritic Belite Clinkers

In this chapter it is described the production of CaO/SiO_2 - based hydraulic binders formed of dendritic belite embedded in an amorphous phase. These hydraulic binders are produced by a process involving heating the raw materials with a specified CaO/SiO_2 ratio to a temperature bellow the liquidus surface, followed by a two-step cooling ramp, in order to obtain during solidification a dendritic morphology of the crystalline phase. After milling the clinker obtained by this process, and by adding up to 25% of water, the paste sets showing mechanical resistances that went up to 4 times higher the values obtained for a reference round shape belite clinker. This result opens the possibility of developing a novel belite-based clinker that may lead to a relevant reduction of the CO_2 emissions, as compared to common alitic clinkers.

5.1 Production Concept

In this chapter, a totally different approach to the synthesis and production of low C/S ratios cements in the belitic domain is described. The approach presented here is based on the use of morphological control of the material's microstructure to enhance its hydraulic reactivity. In fact it is well known that, as the G/R ratio decreases during solidification (being G the thermal gradient and R the solidification speed), the morphology of the crystalline phase changes from granular, to columnar and finally to dendritic [102]. Dendrites, by having a much higher surface to volume ratio, increase significantly the internal energy of the system thus leading to a higher instability and, consequently, are expected to induce a higher hydraulic reactivity. On the other hand the high solidification speed that result in the formation of dendrites, also leads to the formation of amorphous structures, pretty well known in the SiO_2 based systems [103, 104]. Amorphous structures at room temperature in the $CaO.SiO_2$ system are also unstable by nature. Therefore the control of the solidification sequence and solidification conditions opens an important route for changing the reactivity of belite based cements. Thus, the focus of the approach used in the present work is to produce a hydraulic binder by using a proper microstructural control of the phases formed in the liquid + belite range of the Cao-SiO_2 system that results in enhanced hydraulic reactivity.

Although some authors have look into the impact of synthesis parameters on the clinker microstructure, such as burning conditions and cooling rate (e.g. see ref. [2], section 3.4 and 4.2, for a review), as far as the author knows, this is the first time that it is reported an approach that uses a controlled cooling path to change the phase composition of the clinker and the morphology of belite, from round shape to dendritic, order to enhance the reactivity of the clinker. We show that pastes of a clinker formed by belite with a dendritic micro-morphology embedded in an amorphous phase, presents higher compressive strengths than typical round morphology belite clinkers. This specific micromorphology, which can be produced by a process involving well defined cooling steps that enable for dendrite growth in the liquid, may be compatible with the actual clinker production technology. Therefore, we show that the micromorphological and microstructural control of the phases present in the clinker is a promising route to enhance reactivity in the liquid + belite range.

The production process designed for the development of dendritic belite clinkers will be fully described in the next sections. To evaluate the hydraulic behavior of the dendritic belite clinkers and for comparison purposes, it was also produced a reference clinker consisting mainly in round shaped belite crystals.

5.2 Materials and Processing Conditions

The raw materials used for the production of the dendritic belite clinkers were those described in section 4.1.

The raw mix proportions used for the production of dendritic belite-based hydraulic binders, with a C/S molar ratio of 1.4, and the reference clinker, with a C/S molar ratio of 2.0, as well as their final theoretical compositions are shown in Table 5-1.

Table 5-1. Raw materials composition and mixture proportions for the production of dendritic belite-based hydraulic binders, with a C/S ratio of 1.4.

	wt%/Sample		Composition (weight %)												
Raw materials	**1.4**	**2.0**	**LOI**	**SiO_2**	**Al_2O_3**	**Fe_2O_3**	**CaO**	**MgO**	**SO_3**	**K_2O**	**Na_2O**	**TiO_2**	**P_2O_5**	**MnO**	**Cr_2O_3**
Fly- Ash	4,55	4,36	4,54	57,07	23,91	8,68	3,96	1,56	0,12	1,84	0,62	---	---	---	---
Sand	24,75	18,24	0,37	97,30	1,29	0,16	0,00	0,02	0,00	0,52	0,11	---	---	---	---
Limestone	63,68	70,68	43,34	0,46	0,06	0,09	55,53	0,23	---	---	---	---	---	---	---
Slag	7,02	6,73	0	13,90	8,26	43,54	21,18	6,06	0,40	0,00	0,00	0,46	0,46	3,76	1,98
1.4 Clinker (theoretical)	100		---	38,8	2,85	5,04	50,64	0,90	0,06	0,30	0,14	0,05	0,05	0,38	0,20
2.0 Reference Clinker (theoretical)	100		---	31,26	2,77	5,05	58,27	0,93	0,06	0,26	0,14	0,05	0,05	0,38	0,20

The raw materials were mixed by hand in the proportions given in Table 5-1 in batches of 500g for each composition. Then, approximately 120g of the prepared raw meal was pressed with a force around 100kN to a disc shape with 10 cm of diameter and 1.5 cm height. The disc was then broken into four pieces and placed in platinum crucibles which were moved inside and outside the high-temperature furnace by means of a platinum crucible holder.

Two different processes were used in production of the dendritic clinker, with a molar C/S of 1.4, and the reference clinker, with a C/S of 2.0.

The full production cycle of the dendritic clinker follows the sequence shown in Figure 5-1.a), corresponding to the steps presented below:

I. Heating at a rate R_1= 25ºC/min to a temperature T_1 of 1500ºC;
II. The temperature T_1 (in the C_2S + Liquid region) was maintained constant for a period t_1= 30 min allowing the homogenization of the material;
III. The system was first cooled to a temperature T_2 = 1400ºC allowing the clinker to start the crystallization of belite, in this stage a cooling rate R_2 of approximately 40ºC/min was applied;
IV. This temperature was kept constant during a period t_2 between 1 and 20 min in which dendritic crystals were formed, being the real values of used t_2 described in Table 5-3;
V. The system was then brought to room temperature naturally in air, with an approximated cooling rate of 300ºC/min.

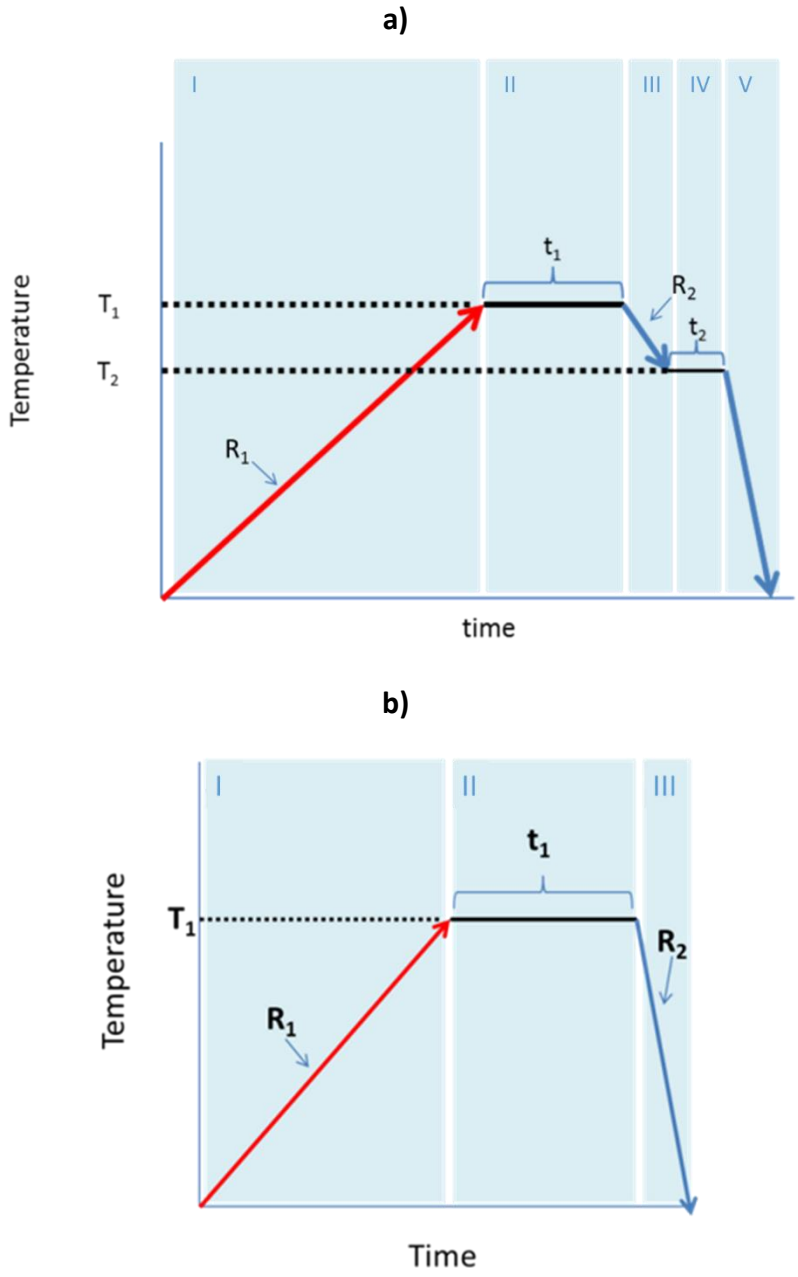

Figure 5-1. Temperature versus time diagram indicating the temperature cycle for the production of the: a) dendritic clinker and b) reference samples.

The t_2 parameter in step IV of the process described above was set to 4 different values in order to observe the effect of the time length of this step in the microstructure of the dendritic clinkers produced. Values of t_2 = 1, 2, 8 and 20 minutes were tested, resulting in the samples hereinafter designated by 1.4-1, 1.4-2, 1.4-8 and 1.4-20, respectively.

The air quenching of the hot material lead to the production of a very well defined dendritic microstructure, where the dendritic crystals are embedded in a glassy matrix.

The production cycle of the reference belite clinker comprises only three steps, since the dendritization stage is not necessary in this case, and therefore step III consisted of a single cooling to room temperature occurring naturally in air. The values of temperature T_1, heating rate R_1 and time t_1 used in the production of the reference sample were the same as the ones described in the previous procedure, while R_2 was estimated to range between -300 and -500 ^{o}C/min. Figure 5-1.b) shows the step sequence followed for the production of the reference sample.

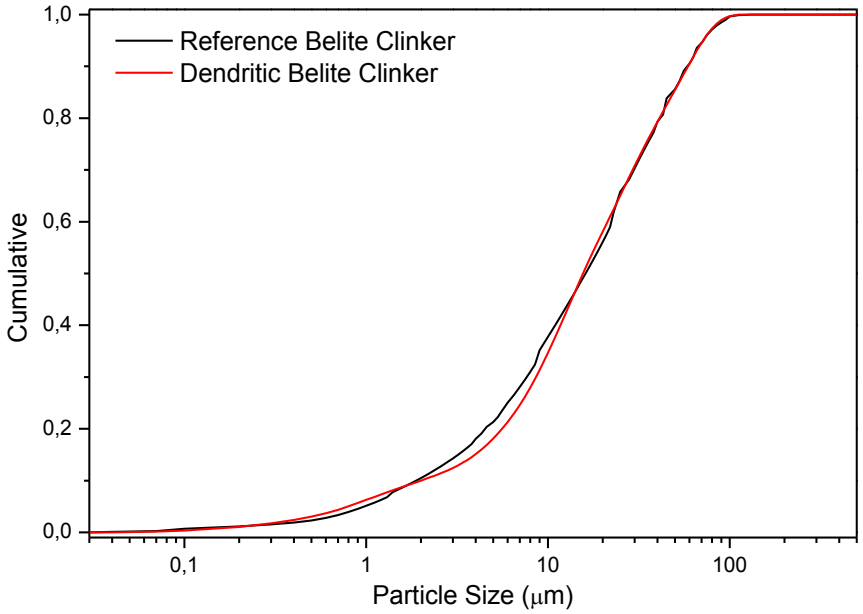

Figure 5-2. Particle size distribution obtained for the reference and dendritic belite clinkers.

The material obtained from each clinker preparation was mechanically removed from the interior of the platinum crucibles used and ground in a ring mill. The particle size distribution of the powders obtained is shown in Figure 5-2. These powders were then hydrated to a water/clinker ratio of 0.25 and poured into parallelepiped shape moulds to obtain paste samples with dimensions of 20x20x40 mm^3. The respective pastes were stored in a chamber at controlled temperature (20ºC) and humidity (90%RH) conditions. By the 7th day the parallelepipeds were taken from the mould (

Figure 4-2) and placed in the same chamber, where the cure developed till the 90 days.

5.3 Results

5.3.1 Compressive Strength

The hydraulic reactivity of the dendritic clinkers produced as described is considerably high. After a few days the pastes are hard enough to allow for manipulation without damage, and after 28 days the samples present a stone like behaviour. Compressive strength tests were performed in the pastes produced using the procedure described in section 4.11, with the results showing that the strength of these hydraulic binders can reach values 4 times higher those obtained for typical round belite clinkers, as quantitatively shown in Table 5-2.

From Table 5-2, it can be seen a growing trend in the values of compressive strength until the 90 days of hydration, with the dendritic sample presenting higher values than the reference belitic clinker.

Table 5-2. Compressive strength results for all the pastes produced in this study.

Water/ binder	Sample	Compressive Strength (MPa)		
		7 days	28 days	90 days
0.25	Reference Belite Clinker	0	0,9	2,8
	1.4 Dendritic Clinker	2,4	5,8	12,9

5.3.2 Optical microscopy and SEM-EDS

The microstructure of the anhydrous dendritic and reference belite clinkers were characterized via optical and electronic microscopy, using the experimental conditions described in sections 4.5 and 4.9, respectively, in order to assess the resulting size and shape of the crystals produced and compare it to a typical microstructure of a belitic clinker (reference sample) as well as to a clinker obtained with the BAT.

Figure 5-3 shows the microstructure typically obtained in a clinker produced by the process described above (Figure 5-3.a) and, for comparison, the typical structure of a clinker produced with the BAT (Figure 5-3.b). The differences are drastic. While the microstructure of the OPC is essentially formed of faceted alite grains and some round shape belite grains, with diameters between 10 to 30 μm, embedded in an Alumino-ferritic crystalline matrix, our clinker is formed by fine belite dendrites embedded in an amorphous matrix. The EDS analysis of the anhydrous clinker shown in Figure 5-4 (mainly on granular regions of belite because of the lack of lateral resolution of the EDS probe to solve de the dendritic composition), reveals that, as it can be expected, the C/S ratio in the belite regions is larger than the C/S ratio of the

matrix, which is essentially composed of an amorphous calcium silicate with a theoretical C/S ratio close to 1.

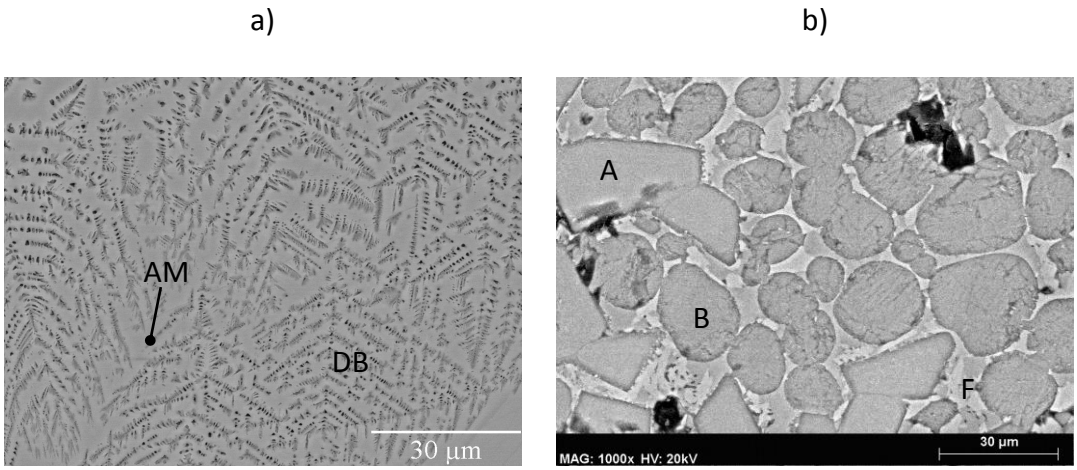

Figure 5-3. Scanning Electronic Microscopy (SEM) images of (a) a dendritic belite clinker produced according to this paper and (b) a typical OPC clinker (A- Alite, B- Belite, F- Alumino-ferritic crystalline matrix, DB- Dendritic Belite, AM – Amorphous Matrix).

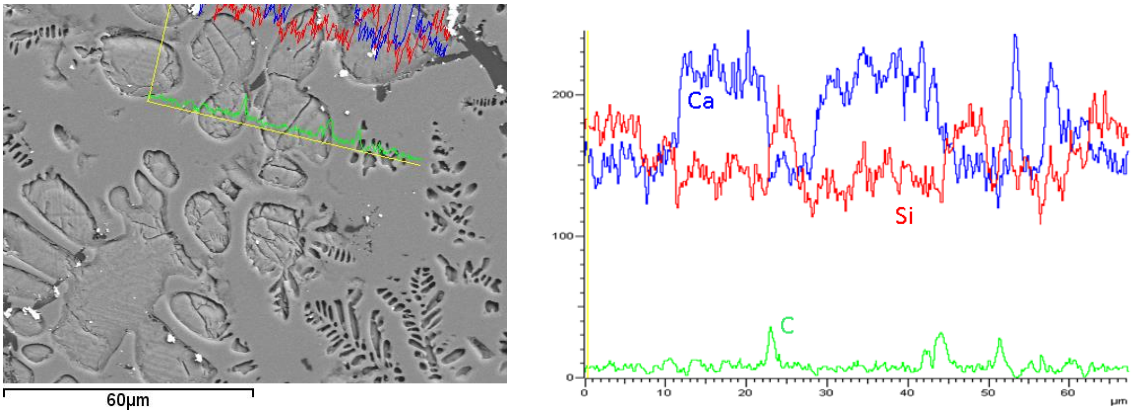

Figure 5-4. EDS line analysis of the anhydrous clinker.

Figure 5-5 shows optical microscopy images of the samples produced with t_2=1min (a), t_2=2 min (b), t_2=8 min (c) and t_2=20 min (d), as well as the reference sample with a C/S of 2 (e). It can be observed that samples produced in this time plateau range possesses a fully dendritic belitic structure, embedded in the amorphous matrix. As t_2 increases from 1 to 20, the secondary dendritic arm spacing (λ_2), defined as the distance between two consecutive secondary branches of a dendritic crystal, increases from 10 to 20 µm (Table 5-3). The reference sample, however, presents an average crystal diameter of about 40 µm.

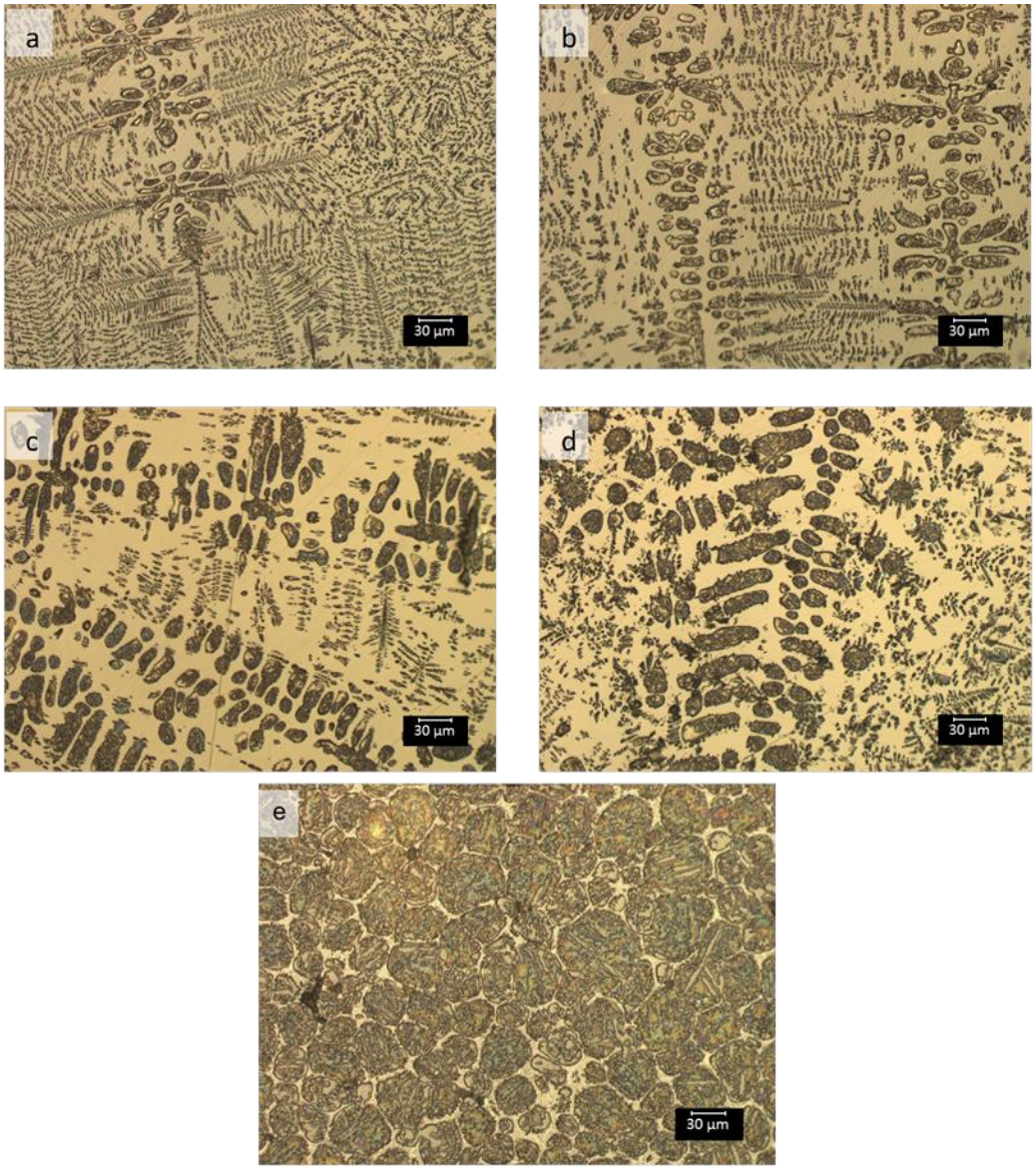

Figure 5-5. Optical microscopy images showing the microstructure of the clinkers produced with different time steps t_2 at the dendrite growing temperature T_2. a) t_2= 1 min; b) t_2= 2 min; c) t_2= 8 min and d) t_2= 20 min. e) shows the microstructure obtained for the reference sample produced.

SEM observation shows that in the presence of water an extensive hydration reaction of both crystalline and amorphous phase occurs. When mixing with water, at 28 days, the degree of reaction of the dendritic C_2S is more than one third as it results from Rietveld analysis presented in Table 5-3 and Table 5-4. In Figure 5-6, it is possible to see the dendritic shape of belite crystals in the unreacted anhydrous phase (unhydrated clinker) and a large region of hydrated clinker.

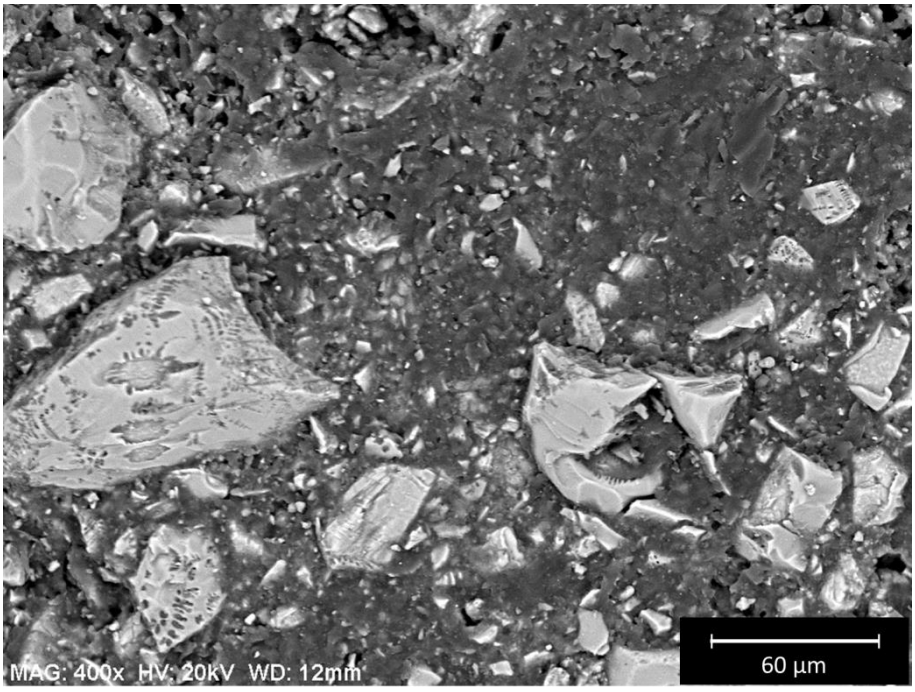

Figure 5-6. SEM observation of a paste after 28 days of hydration.

Figure 5-7 shows the SEM image of one of the pastes after 90 days of hydration with the corresponding EDS line analysis. Two distinct regions can be observed in Figure 5-7, on the left side of the image it is possible to identify some dendrites yet present in an interior layer of the unreacted clinker, while in the right side of the image a very well defined reacted region is shown. The green line that crosses the image at its center indicates the path followed by the EDS line analysis. The concentration of both calcium and silicon decreases in the hydrated region, while Al and Fe show an approximately constant profile. It is quite noticeable the change in the Ca/Si ratio as the line analysis crosses the hydration frontier, revealing a higher Ca/Si in the anhydrous region, composed by belite dendrites and unreacted amorphous matrix, and a Ca/Si close to 1 in the hydrated region, which indicates that some of the calcium present in the anhydrous clinker does not contribute for the formation of the main hydrated phase (C-S-H), incorporating other reaction products such as Monohydrocalcite or calcite during setting, however it is not present in the form of Portlandite, as it was determined by XRD (Figure 5-8).

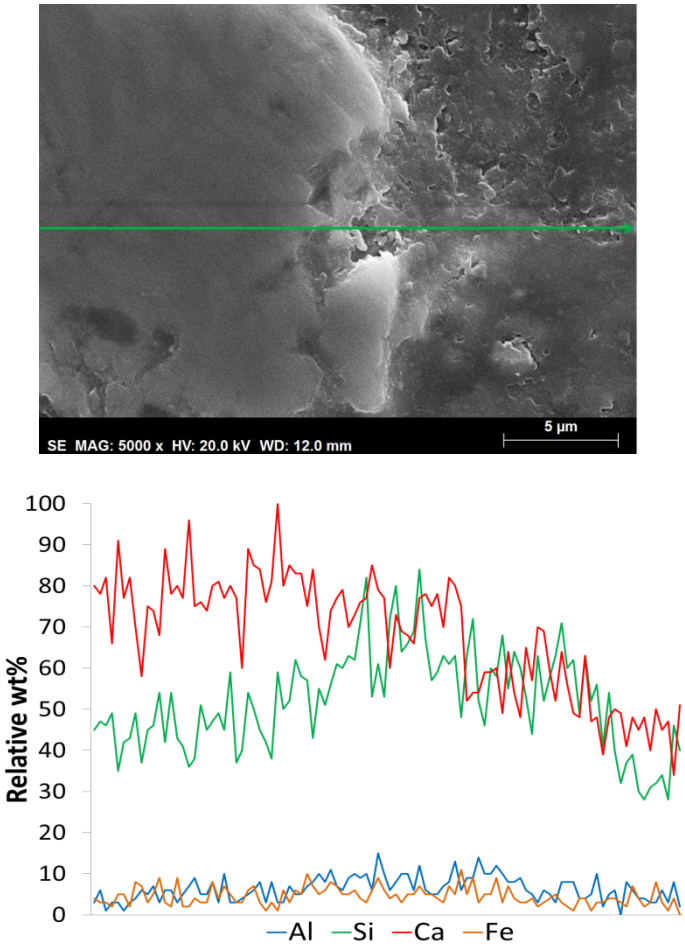

Figure 5-7. SEM image of the 1.4-1 paste after 90 days of hydration with the corresponding EDS line analysis along the green arrow.

5.3.3 XRD-Rietveld

Phase quantification of the prepared clinkers and their respective pastes was performed using XRD-Rietveld analysis in the conditions described in section 4.7. The results obtained for the anhydrous samples are shown in Table 5-3, while Table 5-4 shows the phase quantification of the pastes. Rietveld refinements were performed using the structures available from ICSD database with the following reference codes: 82994 (α'h-C_2S); 81096 (β-C_2S); 81095 (γ-C_2S); 75559 (α-Al_2O_3); 100847 (Monohydrocalcite); 40112 (Calcite) and 16695 ($CaFe_2O_4$). For comparison, the phase quantification values obtained by ^{29}Si MAS NMR for silicate phases are also presented in Table 5-3 and Table 5-4. The development of the hydrated pastes was followed by XRD until 28 days, in the case of the dendritic samples, and until the 35th day for the reference clinker, being the belite consumption, in relative weight %, determined during

this period by using the expression $\frac{C_2S_0 - C_2S_i}{C_2S_0}$, where C_2S_0 is the total C_2S weight % in the anhydrous clinker and C_2S_i is the total C_2S weight % in the hydrated paste at the time *i*.

Table 5-3. Rietveld analysis, ^{29}Si MAS NMR quantification and morphological features obtained in the clinkers produced. The samples identified as "1.4-1" and "1.4 Activation test" were obtained by the same procedure but in different batches.

	Sample	*1.4-1*	*1.4-2*	*1.4-8*	*1.4-20*	*Reference*		*1.4-1*
	t_2 (min)	1	2	8	20	---		1
	λ_2 (μm)	10	10	15	20	~40μm		10
Rietveld Wt%	**α'h-C_2S**	8,6	8,8	11,0	10,3	---		7,7
	β-C_2S	36,2	38,2	33,9	36,1	91,4	**^{29}Si MAS NMR**	34,1
	γ-C_2S	1,1	1,0	1,0	0,7	6,2	**Quantification**	3,2
	Amorphous	54,1	52,0	54,1	52,8	---	**Wt%**	54,9
	$CaFe_2O_4$	---	---	---	---	2,4		---

Table 5-4. Rietveld analysis and ^{29}Si MAS NMR quantification of the dendritic clinker pastes with 28 days and the 35 days paste of the reference sample.

		1.4-1 28 days	*1.4-2 28 days*	*1.4-8 28 days*	*1.4-20 28 days*	*Reference 35 days*		*1.4-1 28 days*
Rietveld Wt%	**α'h-C_2S**	3,4	2,3	3,3	4,2	---		3,0 [a]
	β-C_2S	28,4	27,9	31,1	28,9	83,9		31,6[a]
	γ-C_2S	0,7	0,9	0,6	1,4	5,5	**^{29}Si MAS NMR**	3,1[a]
	Amorphous	62,3	63,9	62,6	60,7	7,4	**Quantification**	57,1[a]
	Monohydrocalcite	3,1	2,0	0,7	1,9	---	**Wt%**	3,1[b]
	Calcite	2,1	3,1	1,8	3,1	1,3		2,1[b]
	$CaFeO_4$					1,9		

a – considering the values of calcite and monohydrocalcite obtained by XRD, since ^{29}Si NMR only allow the identification of silicon containing structures.
b – values obtained by XRD.

Figure 5-8 compares the XRD of the anhydrous and the 28 days hydrated samples. The first feature worth to mention is the fact that, although the main goal of the production route used in the present chapter is not the stabilization of high-temperature polymorphs of C_2S, some α-C2S actually forms, which can be seen as an advantage of this process since these polymorphs are known to possess higher hydraulic activity than β-C_2S. In fact, around 20% of the belite crystallized in the dendritic clinkers is in the form of high temperature polymorphs, but still more than 75% is in the form of β-C_2S. It can also be seen from Table 5-3 that the reference clinker sample produced contains more than 97% in weight of belite, being present mainly in the form of the β-polymorph (91,4 wt%).

Comparing the X-ray diffractograms of the anhydrous samples with the paste ones it is possible to observe an increase in the amount of amorphous phase, probably resulting from

the production of C-S-H during hydration by the consumption of belite. It is also worth to mention the absence of Portlandite in the hydrated pastes produced from these clinkers, as it is pointed out by Rietveld analysis, but in some circumstances a small amount of Monohydrocalcite can be formed during the hydraulic reaction, which tends to confirm the SEM results. The evolution of the hydration reaction was followed, both by direct SEM observation and Rietveld analysis, and the reaction degree was determined at 28 days, having been obtained values of 21,5% and 60,5% for the β-C_2S and α'h-C_2S polymorphs of sample 1.4-1, respectively.

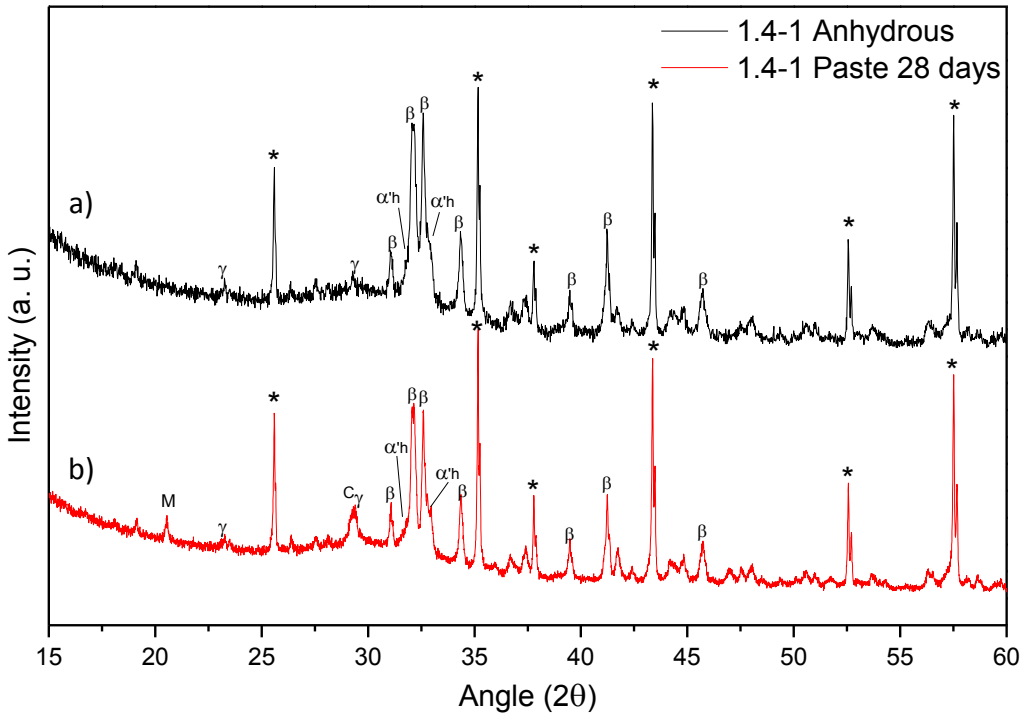

Figure 5-8. X-ray diffractogram of sample 1.4-1 anhydrous (a) and after 28 days of hydration (b). γ – gamma C_2S; β – beta C_2S; α'h – alpha'h C_2S; * - Al_2O_3 internal standard (for amorphous phase determination); M – Monohydrocalcite and C – Calcite.

5.3.4 FTIR-ATR

Figure 5-9 shows the ATR-FTIR spectra obtained for the anhydrous and the hydrated dendritic belite clinker 1.4-1 at the age of 28 days. The band at ~446 cm^{-1} appears only after hydration and is one of the most evident changes in the FTIR spectra, being assigned to Si-O-Si bending modes of C-S-H gel and is also typical of Tobermorite-like structures [43, 105-108]. The other main difference is the decrease in intensity of the band at 979 cm^{-1}, assigned to Si-O-Si

asymmetric stretching of β-C_2S [109, 110], and its further displacement to lower frequencies during hydration (~960-970 cm^{-1}), which indicates the presence of Si-O bond stretching vibrations at Q^2 sites typical of C-S-H [43, 106, 108-110]. At 497 cm^{-1} it is possible to observe, in both anhydrous and hydrated samples, the band attributed to internal deformation of SiO_4 tetrahedra [43], whereas the narrow feature at 846 cm^{-1} is related to bending vibrations of Si-O bond in belite [111-113]. The bands present at 869 cm^{-1}, 1418 cm^{-1} and 1483 cm^{-1} are assigned to the CO_3^{2-} group, where the high frequency features are related to C-O asymmetric stretching vibrations, while the low frequency band is assigned to bending vibrations of carbonate group [43, 105, 107, 108, 110]. The wide band between 600 cm^{-1} and 800 cm^{-1} , identified as (a) in Figure 5-9, is related to the presence of the amorphous phase and has been previously assigned to inter tetrahedral Si-O-Si vibrations [43, 114].

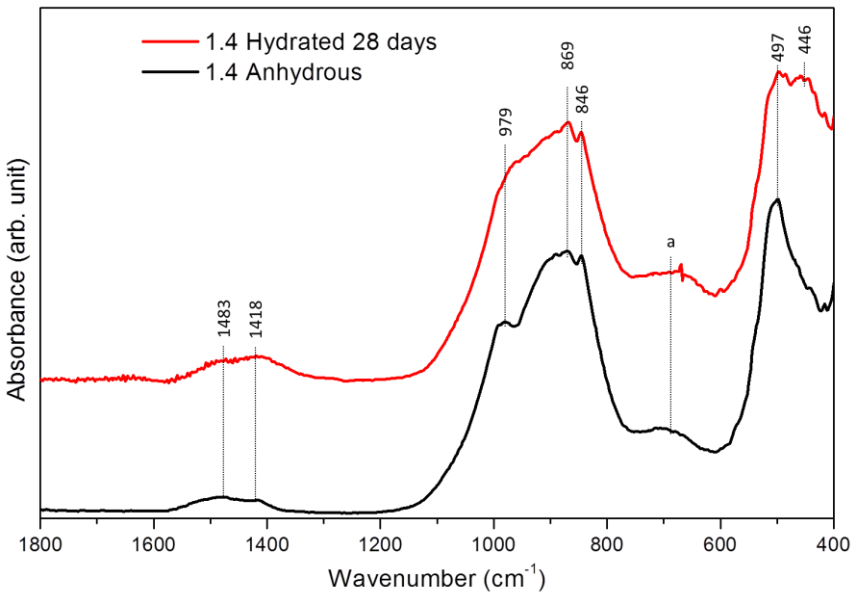

Figure 5-9. FTIR spectra of the anhydrous and hydrated 1.4-1 dendritic belite clinker.

5.3.5 ^{29}Si MAS NMR

^{29}Si MAS NMR experiments were conducted under the conditions defined in section 4.8. Figure 5-10 shows the ^{29}Si MAS-NMR spectra of the anhydrous (a) and hydrated (b) dendritic clinker. These spectra were deconvoluted using six Gaussian functions which were assigned to the major peak contributions and further considered for proper data fitting. The peak centers for the three C_2S polymorphs – α, β and γ – are known to appear near -70.7, -71.4 and -73.5 ppm [66, 115-118], respectively, and were defined accordingly for fitting. The FWHM of

each deconvoluted band was restricted to a maximum of 10 ppm in order to achieve a meaningful fitting of both amorphous and crystalline contributions in the obtained spectra. The value of FWHM defined for these deconvolutions are within the range of values used in the study of other silicate glasses [119]. The relative % areas of each fitted peak were determined and the obtained results are compiled in the pie charts of Figure 5-10 e) and f), from where it is possible to see an increase in the amount of Q^1 and Q^2 groups while Q^0 units decrease upon 28 days of hydration. Coordination degree Q^n indicates the type of structural unit on which Si element is present, as described in Table 5-5 below. The bands identified in the deconvoluted spectra of Figure 11 c) and d) as corresponding to the contribution of the different amorphous phase structural units - Q^0, Q^1 and Q^2 – have their centers around -71, -78 and -84 ppm, respectively, which are within the typical range of other studied silicate glass systems [119-121]. Figure 5-10 shows that the hydration development of these pastes gave rise to an increase in the relative intensity of the bands associated to Q^1 and Q^2 groups, these structural units are often related to the formation of calcium silicate hydrates, with their peak centered at around -79 and -85 ppm, respectively [7, 122].

The values presented in Table 5-3 and Table 5-4 for the phase quantification of sample 1.4-1, as determined by ^{29}Si MAS NMR, were calculated from the relative percentage of the areas resulting from the deconvolution of the spectra presented in Figure 5-10, considering that belite, in all the polymorphic forms present, has a fixed C_2S stoichiometry with no substitution elements and that the amorphous phase has an overall C/S molar ratio close to 1. These considerations are based on the chemical composition of the clinkers produced and in the EDS line spectra registered both for the anhydrous and for the hydrated samples. The results obtained by ^{29}Si MAS NMR are in good agreement with the phase quantification determined by XRD-Rietveld.

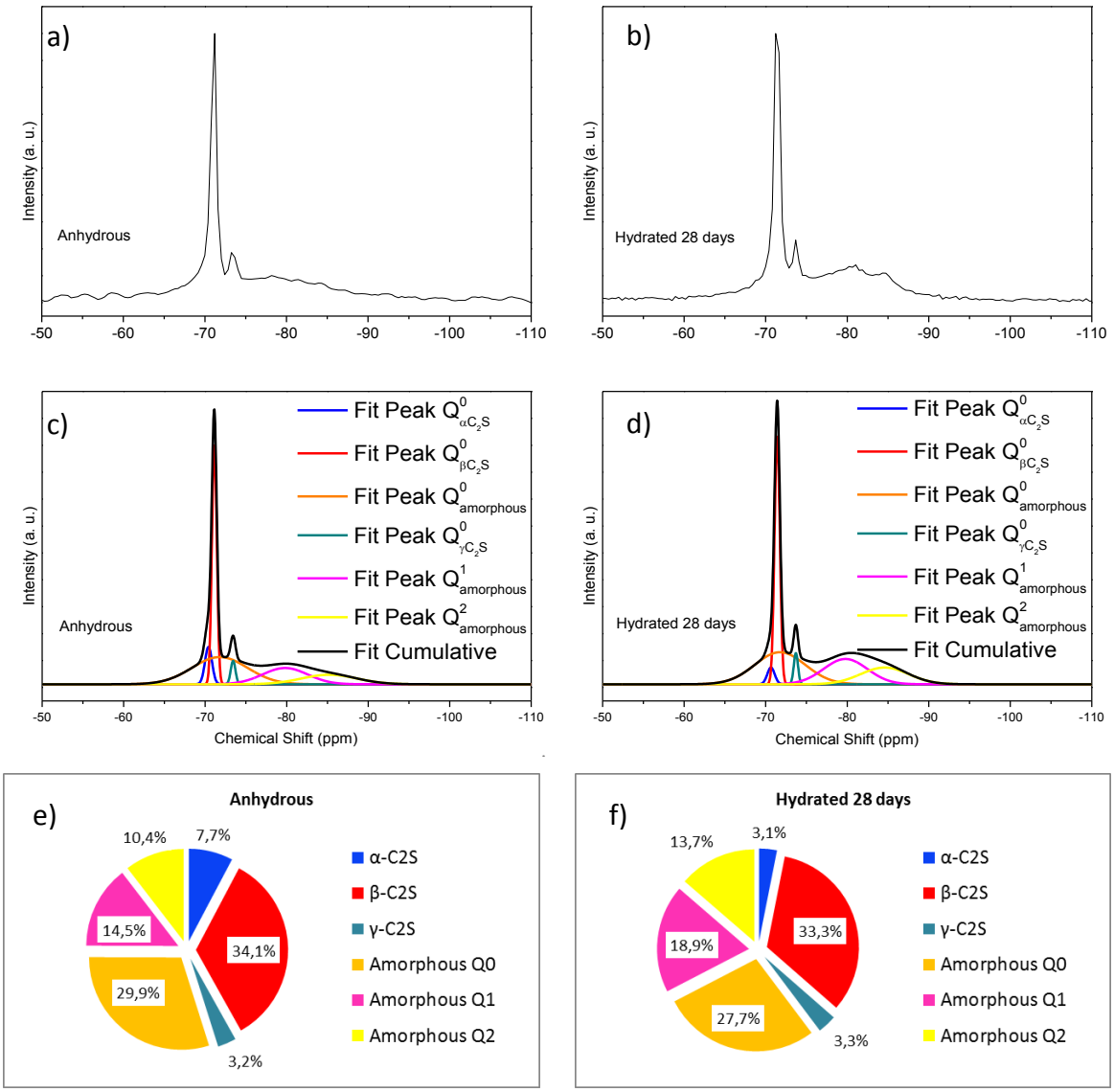

Figure 5-10. 29Si MAS-NMR spectra of the anhydrous (a) and hydrated 1.4-1 dendritic belite clinker (b) as well as their corresponding fitted spectra (c and d, respectively) with peak deconvolution. The pie charts show the relative percentage of the areas obtained after deconvolution of each band for the anhydrous (e) and the 28 days hydrated (f) samples, respectively.

Table 5-5. Structural units assignment for the ^{29}Si MAS-NMR spectra.

Structural Unit	*Description*	*Chemical Shift (ppm)*
Q^0	Monomers of SiO_4^{4-}	-66 to -74
Q^1	Dimers and terminal groups	-75 to -82
Q^2	Intermediate chain groups	-84 to -86
Q^3	Planar structures	-90 to -100
Q^4	3-dimensional structures	-103 to -115

5.4 Discussion

Results from ^{29}Si MAS NMR and XRD-Rietveld quantification indicate that more than 45% in weight of belite forms upon the cooling of a partially molten mixture characterized by an overall C/S molar ratio of 1.4. This high amount of belite formed is not quite explained by the binary CaO-SiO_2 diagram, which, for the composition studied and under equilibrium conditions, predicts the formation of only about 20% in weight of belite with the excess being liquid phase that would result in the formation of a glassy matrix with a C/S molar ratio around 1.25. In part, this phenomenon may be justified by the fast cooling stage during production, which leads to an out-of-equilibrium state. The dendritic growth of belite is also an out-of-equilibrium phenomenon, being responsible for a very effective heat releasing from the undercooled system. However, for crystallization of dendritic belite to occur in such a high amount, the diffusion of calcium needs to be strongly dislocated towards the dendritic crystals, diminishing its presence in the liquid phase that may achieve a composition with a characteristic C/S molar ratio between 1.1 and 0.8, probably with a compositional gradient decreasing in calcium content from the surface of the belitic crystals to the interior of the liquid that will end up forming the glassy matrix. The EDS line analysis obtained in the anhydrous clinker, and presented in Figure 5-4, seems to suggest the existence of this calcium compositional gradient, however further investigation would be needed to confirm this assumption. Nevertheless it is quite obvious that the resultant microstructure and the phase distribution obtained in this clinkers do not follow what is predicted under equilibrium conditions.

Figure 5-11 depicts the differences in the hydration behavior between the dendritic and the round belite clinkers produced in this work. There seems to be a good correlation between the values obtained for compressive strength and the consumption of belite in both samples, with an obvious advantage for the dendritic morphology which shows higher reaction kinetics and consequently higher compressive strength values. The difference in compressive strength between the two morphologies reaches a factor of 4 times up until the 90th day of hydration. The relative percentage of belite reacted was calculated by the results obtained by the XRD and ^{29}Si MAS NMR techniques, being the corresponding values presented in Figure 5-11.

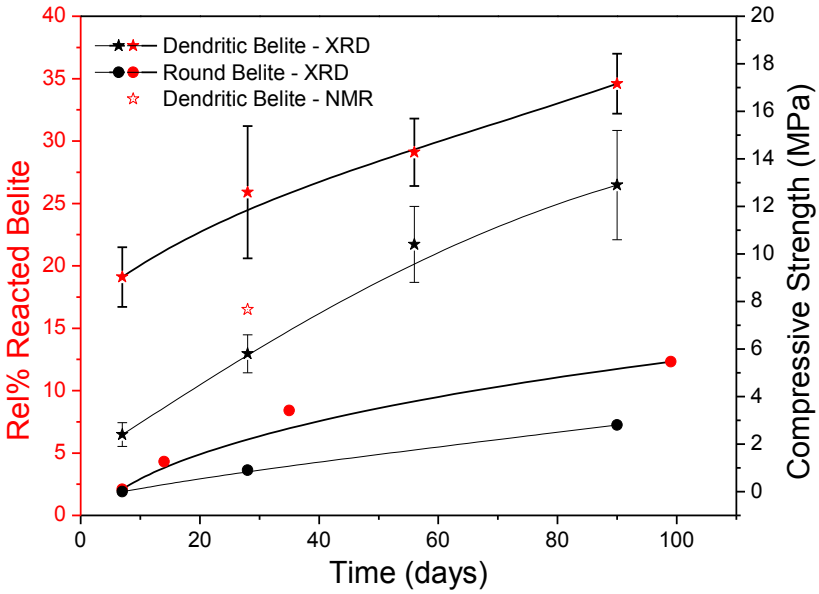

Figure 5-11. Comparison of the hydration evolution between round and dendritic belite samples. The left scale in red refers to the relative amount of reacted belite while the right scale in black shows the values of compressive strength for both crystal morphologies. The lines presented in the plot are just a guide for the eye.

Figure 5-11 clearly shows that the hydraulic reactivity of the dendritic clinker produced is considerably higher than the observed for the round shaped crystals belitic clinker. In fact, after only 7 days of hydration approximately 20% in weight of the existing belite had already reacted in the dendritic clinker, while in the same period only 2% in weight of the round belite was consumed. At 28 days of hydration, different values of reacted dendritic belite were obtained by the techniques of XRD-Rietveld (25,9%) and ^{29}Si MAS NMR (16,5%), however this discrepancy may be explained by possible uncertainties on the deconvolution of the ^{29}Si MAS NMR spectra of both the anhydrous and hydrated samples, due to a high superposition of the bands related to the amorphous and β- C_2S phase, as well as some fluctuations in the assumed composition of the amorphous phase, which changes its nature as it hydrates. Furthermore, at 90 days more than one third of the total dendritic belite reacted in contrast to the value of 12% obtained for the round belite clinker at 99 days of hydration. These results can be compared with the work developed by Cuberos et al. [62] in the analysis of belite rich clinker reaction that points to a β-C_2S reaction degree close to zero after 3 months of hydration and around 14% after 1 year, while for α'h-C_2S the reaction degree reached 60% after 1 year. However, in the present work, after 28 days the obtained reaction degrees were larger than 20% for β-C_2S and larger than 60% for α'h-C_2S, in the dendritic clinkers. These values reflected

in the mechanical properties of the pastes produced in this work, where the compressive strength of dendritic belite clinkers can go up to 4 times higher those obtained for round belite clinkers, although the grinding and water content of the paste, which play an important role in the stone setting of the binder, were not optimized.

As it can be observed from Figure 5-3 and Figure 5-5, the resulting microstructure of the clinker produced by the method described in the present work is composed of fine dendritic crystals of belite embedded in an amorphous matrix, whose dendritic arm spacing λ_2, depends to some extent of the cooling conditions (see also Table 5-3). However the enlargement of dendrites arms due to the increase of t_2 during cooling does not seem to slow the hydration process, at least for those values of t_2 and corresponding λ_2, as it is indicated by the results obtained from Rietveld analysis and shown in Table 5-3 and Table 5-4. Considering these results it can be suggested that the thinner dendritic arms (with characteristic λ_2 dimensions not higher than 20 μm) are responsible for the enhanced initial kinetics of belite hydration, while the central core from which these arms grow is seen as having a behavior similar to the round belite crystals of the reference clinker, continuing its hydration for older ages at an inferior rate. This fact ends up limiting the initial degree of hydration of belite to about one third, up to 90 days of curing, but clearly shows that it can be taken as an evidence for the important role played by the special micromorphology of theses samples, namely the ability to hydrate of the dendritic belite embedded in an unstable amorphous matrix.

Although XRD Rietveld analysis is a very powerful technique for quantitative phase determination of crystals it is not suited for amorphous phase differentiation, which turns it difficult to evaluate the consumption of the amorphous matrix of this binder and the resulting formation of C-S-H gel. Nevertheless, by the combination of this technique with FTIR and ^{29}Si MAS NMR it is possible to characterize the major transformations occurring during the hydration of the samples produced.

The FTIR spectra presented in Figure 5-9 shows the evolution of the binder structure as it hydrates for 28 days, from where it is possible to see the development of the bands related to presence of C-S-H at ~970 cm^{-1} and ~450 cm^{-1}, revealing the good hydraulic activity of belite's dendritic crystals. Furthermore, structural analysis by ^{29}Si MAS-NMR reveals an increase in the degree of Si-O-Si chains polymerization upon hydration, with the development of Q^1 and Q^2 structural units, at chemical shifts of around -79.5 and -85 ppm, respectively,

typical of the formation of C-S-H structures that is suggested to be triggered by the reaction of both belite and amorphous phase, as it is indicated by the decrease of their corresponding Q^0 signals. This behavior was also suggested by SEM observation and by the evaluation of the reaction frontier performed with EDS (Figure 5-7). It is thus unequivocal that calcium silicate hydrates are formed during the hydration of these dendritic belite clinkers. In addition, by combining the information collected by the techniques of XRD, FTIR and ^{29}Si MAS NMR, it is possible to state that the C-S-H phase formed has a highly amorphous character, since no signal of crystalline peaks was detected by X-ray diffraction.

5.5 Conclusions

In this chapter it was described the production of calcium silicate-based hydraulic binders formed by dendritic belite (containing the α'h, β and γ polymorphs) embedded in an amorphous phase. The clinker is formed by a hydraulic crystalline phase with dendritic micro-morphology (composed essentially by the α'h, β and γ polymorphs of C_2S), and an amorphous phase. The pastes produced with these clinkers revealed that dendritic β-C_2S reacted to a relative extent of more than 20% after 28 days of hydration, while α'h-C_2S presented a reaction degree over 60% for the same period. Other interesting features of these new dendritic clinkers are the production of a C-S-H with low C/S ratio, as well as the absence of portlandite upon hydration. Furthermore these same pastes developed a compressive strength 4 times higher than those obtained for a round belite rich clinker at 90 days. The results presented here strongly suggest that, due to its generalized fine dendritic micro-morphology, the reactivity of the belite crystals embedded in the amorphous silicate phase is significantly increased, even when the polymorphism of the C_2S is more than 75% of β-C_2S. These results open a new via for the development of new CaO-SiO_2 hydraulic binders which, as far the author knows, has never been exploited yet.

6 Low Calcium Content Amorphous Hydraulic Binders

This chapter is dedicated to the study of the hydraulic behavior of a series of highly amorphous calcium silicate materials produced in laboratory and contains the results of distinct but complementary works conducted in different stages of this thesis. Although different information was collected from each set of samples, the results obtained can be analyzed as whole and general conclusions taken from the several experiments performed. All the samples have in common their highly amorphous nature and their compositions can be approximately considered as being variations of an $xCaO.SiO_2$ system, where *x* stands for the C/S molar ratio, ranging from 0.8 to 1.25. The preparation of amorphous samples in this range of C/S molar ratio was intended to mimic the glassy matrix of the dendritic clinkers, whose hydraulic behavior was still not fully characterized, in part due to its amorphous nature but also due to the superposition of signals, especially in ^{29}Si MAS NMR, that result from mixed contributions of the various belite polymorphs present in the clinkers described in chapter 5.

The isolated characterization of the hydraulic behavior of these amorphous binders as exogenous[1] materials, rather than an endogenous[2] glassy matrix, is attempted through the use of a vast group of techniques.

Within the experiments performed to these glassy materials are the structure analysis by ^{29}Si MAS NMR and FTIR-ATR and the quantification of the amorphous content as determined by means of XRD-Rietveld. Also phase development was followed by XRD-Rietveld, ^{29}Si MAS NMR and FTIR-ATR, during hydration. Thermogravimetric analysis was performed in the pastes produced, allowing to estimate the amount of hydration products formed by considering a particular stoichiometry of the calcium silicate hydrates present in these materials. The relation between compressive strength and the amount of hydration products was investigated and some considerations about the mechanical properties of the hydration

[1] The term exogenous, in this context, refers to the production of the isolated glassy matrix as an individual part, without coexisting together with an embedded crystal. In this case the composition of the glassy matrix do not depend on the extent of the formation of the crystalline phase, as it was the case in the dendritic clinkers presented in chapter 5.

[2] The term endogenous, in this context, refers to the glassy matrix embedding the belite crystals formed in the particular system described in chapter 5. In that case, the amorphous phase can almost be seen as a consequence of the dendrite formation process and cannot be dissociated from the crystals that gave origin.

products and paste microstructure were inferred. The hydration behavior of the amorphous samples with lower C/S molar ratio (0.8 – 0.9) was different from the ones with C/S of 1.1 and 1.25 that shown the ability to set and harden and therefore to act by their own as hydraulic binders. However the glassy material with C/S molar ratio of 0.9 presented a pozzolanic character when mixed with clinker, as it was assessed by means of compressive strength measurements.

The results obtained in this work gave rise to a recent filing of a patent application (PCT/PT2015/000006 "Amorphous Low Calcium Content Silicate hydraulic Binders and Methods for Their Manufacturing").

6.1 Materials and processing conditions

Four new amorphous calcium silicate hydraulic binders were produced by using a combination of the raw materials described in section 4.1 in such a way that the obtained overall C/S molar ratios were 0.8, 0.9, 1.1 and 1.25. Table 6-1 shows the raw mix used in the production of these three amorphous materials and their final theoretical composition.

Table 6-1.Raw materials composition and raw-mix combinations used for the production of the amorphous hydraulic binders with C/S molar ratios ranging from 0.8 to 1.25. The respective theoretical compositions of the amorphous material produced are indicated in the bottom rows.

Sample C/S molar ratio	**1.1**	**1.25**	**0.8**	**0.9**	**Composition (wt%)**												
Raw materials	**Wt%**				**LOI**	**SiO_2**	**Al_2O_3**	**Fe_2O_3**	**CaO**	**MgO**	**SO_3**	**K_2O**	**Na_2O**	**TiO_2**	**P_2O_5**	**MnO**	**Cr_2O_3**
Fly- Ash	2,28	2,24	2,15	2,11	4,54	54,48	22,82	8,29	3,78	1,49	0,11	1,76	0,59	---	---	---	---
Sand	32,93	30,11	40,53	37,72	0,37	97,30	1,29	0,16	0,00	0,02	0,00	0,52	0,11	---	---	---	---
Limestone	62,67	65,56	55,11	57,99	43,34	0,92	0,17	0,13	54,83	0,22	0,01	0,01	0,07	---	---	---	---
Slag	2,12	2,08	2,21	2,18	0	13,90	8,26	43,54	21,18	6,06	0,40	0,00	0,00	0,46	0,46	3,76	1,98
1.1 Clinker (Sample A)	100	---	---	---	---	46,85	1,70	1,75	48,03	0,43	0,02	0,30	0,13	0,01	0,01	0,11	0,06
1.25 Clinker (Sample B)	---	100	---	---	---	43,84	1,66	1,75	51,07	0,44	0,02	0,28	0,13	0,01	0,01	0,11	0,06
0.8 Clinker (Sample C)	---	---	100	---	---	54,37	1,71	1,72	40,54	0,39	0,02	0,33	0,13	0,01	0,06	0,01	0,11
0.9 Clinker (Sample D)	---	---	---	100	---	51,63	1,68	1,72	43,31	0,40	0,02	0,32	0,13	0,01	0,01	0,11	0,06

The raw meal preparation followed the same procedure described in section 5.2, with the difference that there were considered the raw mix proportions given Table 6-1.

The production process used was similar to the one adopted in the production of the reference clinker in section 5.2 and consisted in the following steps, as also schematically exemplified in Figure 6-1:

I. Heating the raw-mix at a rate R_1= 25ºC/min to a temperature T_1 of 1500ºC;

II. The temperature T_1 (in the liquid region) was maintained constant for a period t_1= 60 min allowing the homogenization of the composition;

III. Cooling the system to room temperature naturally in air at cooling rate R_2 of approximately 300ºC/min, which can be achieved by simply removing the sample from the furnace and let it to cool in air under laboratory ambient.

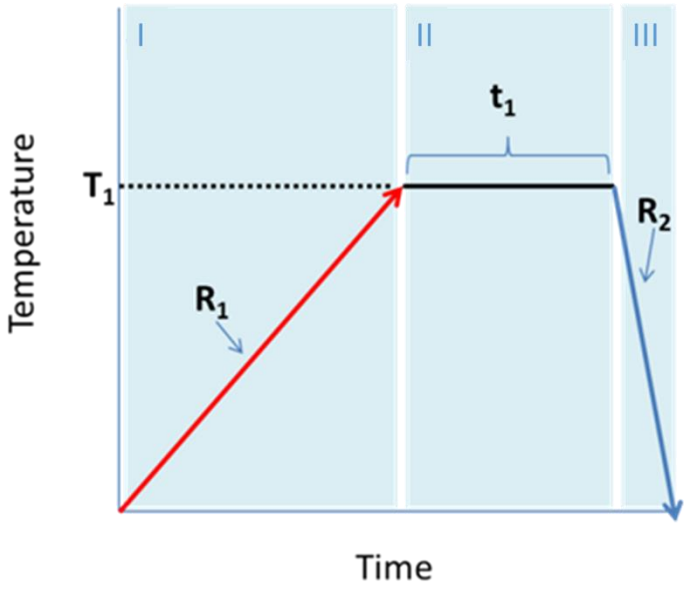

Figure 6-1. Procedure used in the production the amorphous hydraulic binders.

After air quenching, the obtained amorphous hydraulic binders were mechanically removed from the crucibles, by breaking the bulk sample in the interior and tapping its bases with a flat rigid object. The samples with C/S molar ratio of 0.8, 1.1 and 1.25 were ground in a ring mill for 180s with propanol, followed by a drying step at 50ºC in a stove for about 1h, whilst the sample with C/S molar ratio of 0.9 was ground in a ring mill for about 20s in dry conditions. None of the grinding processes introduced any changes of microstructure detectable by XRD. Particle size distribution was performed by laser granulometry using the conditions given in section 4.4, with the resulting fineness of the amorphous materials differing with the grinding process used, as schematically represented in Figure 6-2. The powders of samples A, B and C

had a particle size below 35 μm and were used to produce pastes by mixing it with water at a water/binder weight ratio of 0.375, while the coarser powders of sample D (C/S=0.9) were mixed in a water to binder ratio of 0.25. The difference in the water/binder ratios used results from the intention of keeping approximately equivalent workability conditions in each paste. Additionally, pastes prepared from a clinker sample previously ground to a fineness similar to the one of the amorphous sample with C/S of 0.9 (see Figure 6-2), were produced. The paste preparation conditions used for the reference clinker differed accordingly to the system to which it was compared, i.e., for samples A, B and D a water to binder ratio of 0.375 was used, while for the preparation of sample D it was used a water to binder ratio of 0.25 in weight. For the study of the pozzolanic effect of sample D, ten more pastes consisting in mixtures containing different clinker substitutions were prepared, according to Table 6-2. Lime and sand described in the "Raw Materials" section (section 4.1) were used as clinker substitutions, so that the obtained results of their respective compressive strength could be compared against sample D.

Table 6-2. Mixtures prepared for the study of pozzolanic behavior of sample D with C/S molar ratio of 0.9. Mixtures of lime and sand containing 50% in weight of the reference clinker were not produced.

Base Materials wt%	**Reference Clinker wt%**			
	10	***20***	***30***	***50***
Sample D	90	80	70	50
Lime	90	80	70	N.P.
Sand	90	80	70	N.P.

After mixing with water, for about 2 minutes, the pastes were poured into proper moulds with dimensions of 20x20x40 mm^3 and cured in a moisture controlled environment with a relative humidity over 95%. The prisms were demoulded at 7 days immediately before the compressive strength test. At 1 and 2 days of age the pastes didn't have gained enough consistency to be demoulded and tested. In fact, the pastes prepared with the amorphous binders of 0.8 and 0.9 C/S molar ratios didn't present any consistency at least until the 90 days of hydration.

The pastes prepared with the reference clinker were only use for comparison of their mechanical behaviour with the new amorphous hydraulic binders. The clinker main phases were estimated by XRD using Rietveld method, with the following values being obtained: C_3S~78%, C_2S~4%, C_3A~3% and C_4AF~14%. Hydration phase development and compressive

strength measurements were performed, using the conditions mentioned in section 4.11, at the ages of 7, 28 and 90 days, for samples A, B and C, so that a relationship between the evolution of hydration products and mechanical properties could be established over time.

After compressive strength testing, pieces of pastes from samples A and B, with 28 and 90 days of hydration, were ground in an agate mortar, dried at 105^{o}C and sealed in vacuum for further utilization in other characterization procedures (XRD-Rietveld, ^{29}Si MAS NMR and FTIR), with exception for the thermogravimetric analysis (TGA) on which samples with 7, 28 and 90 days were used immediately after the compressive tests in order to assess the amount of water contained in the structure of the hydrated products.

TGA experiments were conducted according to description given in section 4.10 and X-ray diffraction with corresponding Rietveld analysis were performed under the conditions referred in section 4.7, while images in scanning electron microscopy and the EDS composition profiles were collected according to section 4.9.

Anhydrous powders of the materials produced and their corresponding dried pastes were studied by ^{29}Si MAS NMR and FTIR-ATR spectroscopy using the specifications described in sections 4.8 and 4.6, respectively.

6.2 Results

Sample preparation differed in the grinding process thus leading to different particle size distributions. Figure 6-2 shows the PSD obtained for the two sets of samples studied and indicates the water/cement ratio used in the preparation of the respective pastes.

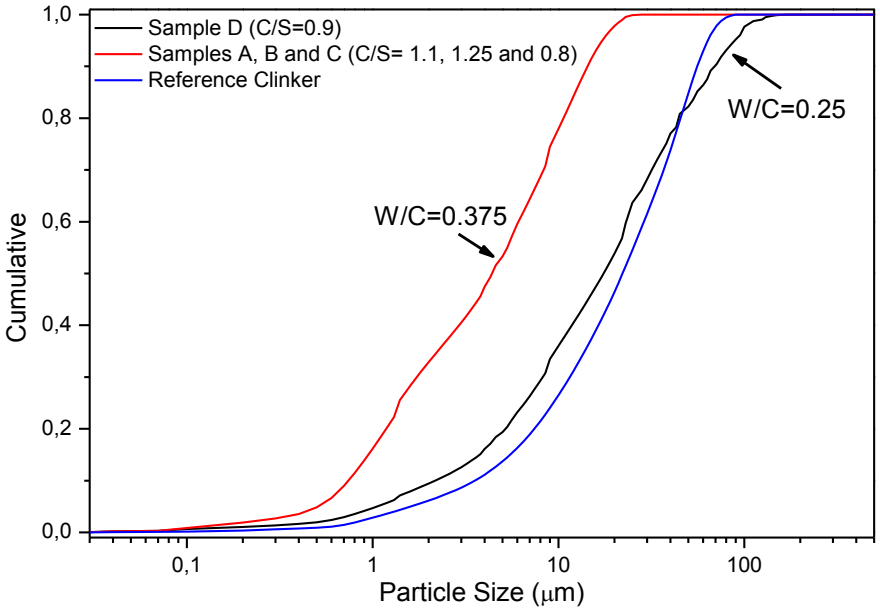

Figure 6-2. Particle size distribution (PSD) curves for the amorphous samples studied as well as for the reference clinker used. In the graph is indicated the water to cement ratio used for each system. For simplicity, only one curve is represented for samples A, B and C since they present similar PSD.

6.2.1 Compressive Strength

The development of compressive strength of pastes produced from samples A, B and C and cured in a moisture controlled environment is shown in Figure 6-3. Sample A and sample B show different compressive strength growth trends, with sample A presenting higher values at the latter ages. Sample C does not show any strength development until the 90 days of hydration, indicating a behavior completely different from samples A and B. For comparison, the compressive strength obtained for a reference clinker paste produced under the same conditions of samples A to C is also depicted in Figure 6-3.

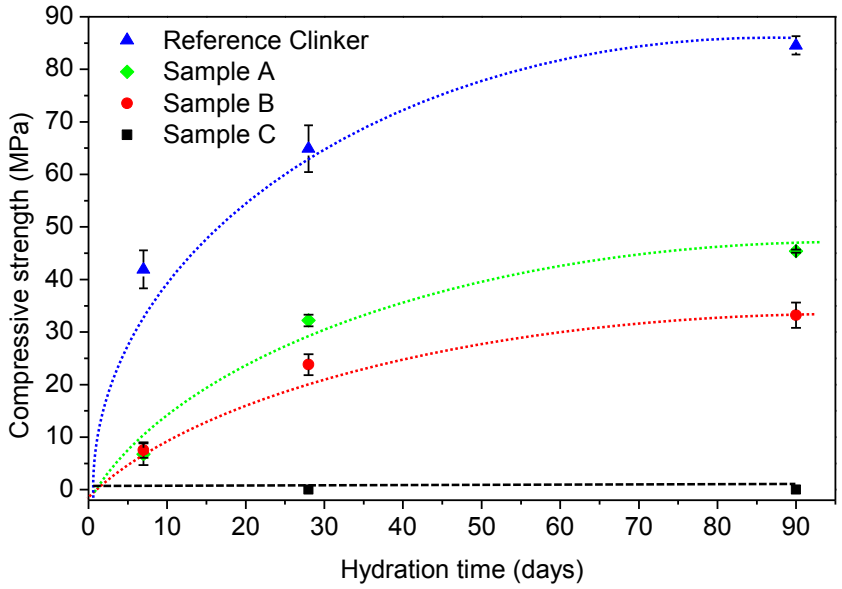

Figure 6-3. Compressive strength development of the pastes produced from samples A, B and C, as well as the clinker used as compressive strength reference. The dashed lines in the figure are just a guide to the eye. Sample C doesn't present any strength development until the 90 days of hydration. Note: water/binder = 0.375 in weight.

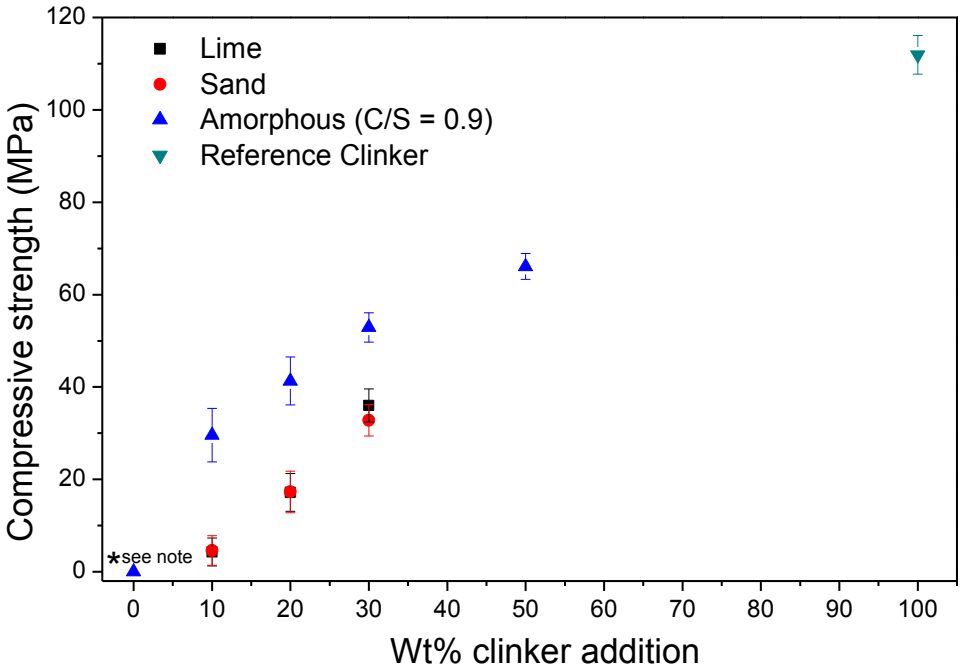

Figure 6-4. Compressive strength at 28 days for mixtures containing different additions of clinker prepared with lime, sand and the produced amorphous material with an overall C/S molar ratio of 0.9. Note: * It was not possible to test the compressive strength at 28 days of hydration of the produced amorphous material with C/S molar ratio of 0.9 since it didn't present enough consistency to be tested properly. Note: water/binder = 0.25 in weight.

Figure 6-4 presents the strength at 28 days for a series of systems with different clinker substitutions, in the proportions given in Table 6-2. The objective of this set of experiments was to assess the behavior of sample D under clinker activation, in order to detect any pozzolanic activity of this particular amorphous material with C/S molar ratio of 0.9. For comparison, there are also shown the results obtained for systems containing lime and sand with equal substitution values.

It can be seen that sample D doesn't develop any compressive strength until the 28 days of hydration, however when hydrated together with clinker, in substitutions as low as 10%, it develops appreciable strength, especially if compared with equivalent mixtures of clinker with sand or lime.

This set of experiments represent the only results available for sample D, from which only compressive strength values were collected. These results will be discussed in the discussion section of this chapter. No further characterization on these pastes was performed and the following results sections are only referred to the characterization performed in samples A, B and C.

6.2.2 XRD/Rietveld

The X-ray diffractograms of the two samples produced reveal an almost fully amorphous structure, as it can be observed in Figure 6-5 and Figure 6-6.

The XRD of the amorphous hydraulic binder of C/S equal to 1.1 (sample A) is represented in Figure 6-5, where it is shown the corresponding Rietveld analysis, indicating that only a small amount of Pseudowollastonite (5,6% in weight) was crystallized during production, whereas in Figure 6-6 the diffractogram of sample B shows an amorphization of more than 97% of the calcium silicate produced, and also the formation of some Pseudowollastonite (~3% in weight), as determined by Rietveld analysis. Diffractogram of Sample C is presented in Figure 6-7, revealing that 1.6% of Pseudowollastonite crystallized during its production.

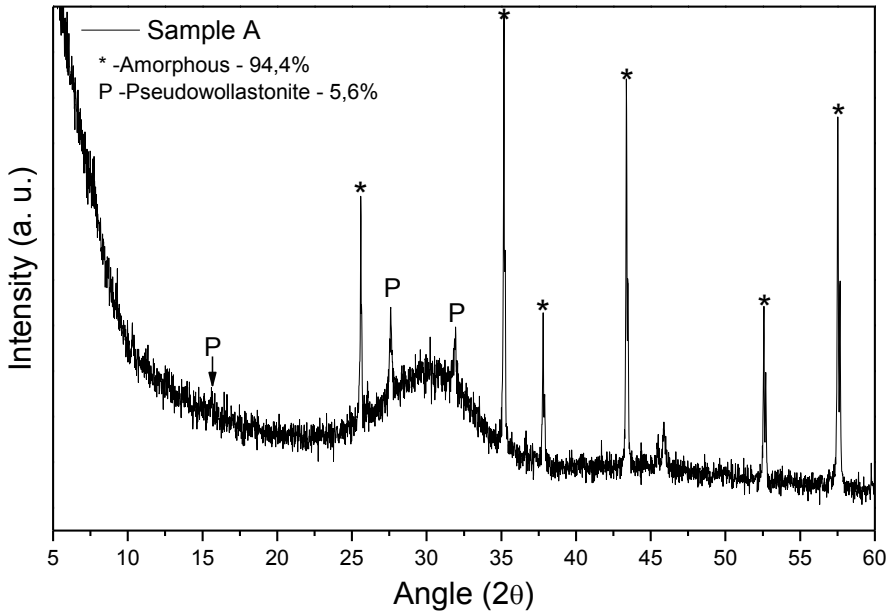

Figure 6-5. XRD of the anhydrous amorphous hydraulic binder produced with an overall C/S molar ratio of 1.1 (Sample A) with the corresponding Rietveld analysis shown in the upper left. The asterisk identifies the peaks of corundum used as internal standard to determine the amorphous content of this sample.

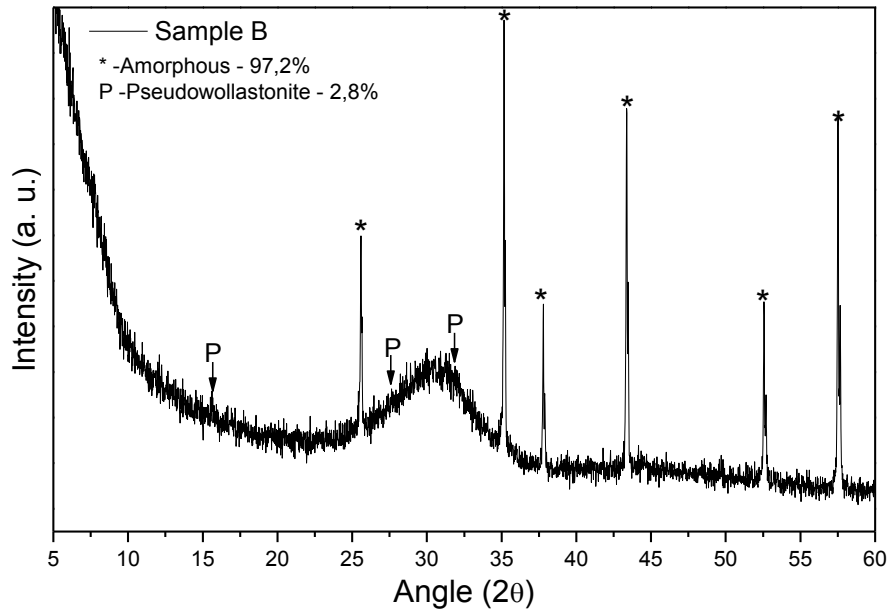

Figure 6-6. XRD of the anhydrous amorphous hydraulic binder produced with an overall C/S molar ratio of 1.25 (Sample B) with the corresponding Rietveld analysis shown in the upper left. The asterisk identifies the peaks of corundum used as internal standard to determine the amorphous content of this sample.

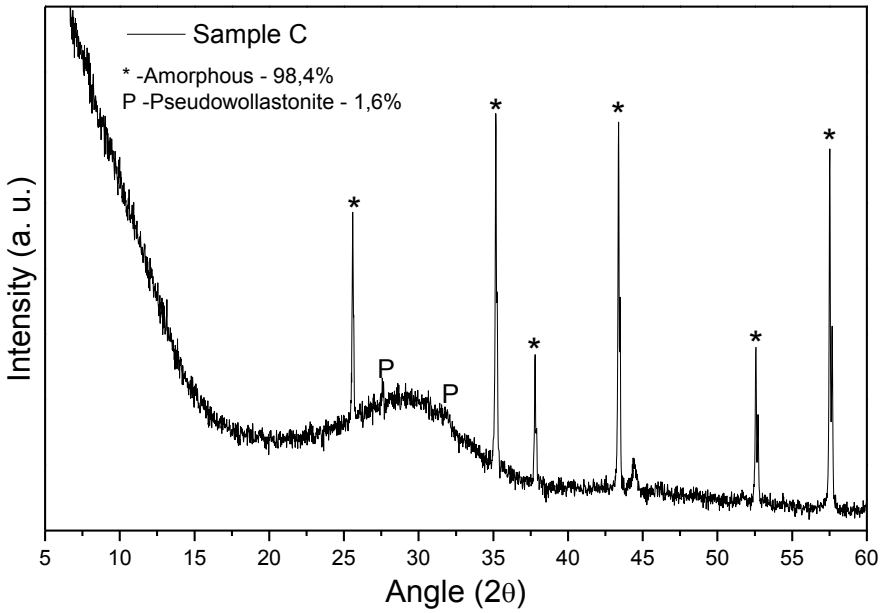

Figure 6-7. XRD of the anhydrous amorphous hydraulic binder produced with an overall C/S molar ratio of 0.8 (Sample C) with the corresponding Rietveld analysis shown in the upper left. The asterisk identifies the peaks of corundum used as internal standard to determine the amorphous content of this sample.

Figure 6-8, Figure 6-9 and Figure 6-10 depict the x-ray diffractograms of samples A, B and C as the hydration of their corresponding pastes takes place. It is possible to verify that, while in samples A and B there seems to be formed some calcium silicate hydrates with Tobermorite-like structures, sample C shows different phase development as the hydration occurs, revealing the formation of Monohydrocalcite crystals. For Rietveld fitting, the following phases were used: Tobermorite 11 Å with reference code 87690, Clinotobermorite with reference code 403090, Pseudowollastonite with reference code 87716, Aluminum oxide phase with reference code 75559 and Monohydrocalcite with the reference number 100847 from the ICSD database.

Table 6-3 summarizes the phase quantification estimated by Rietveld analysis at different ages for each sample.

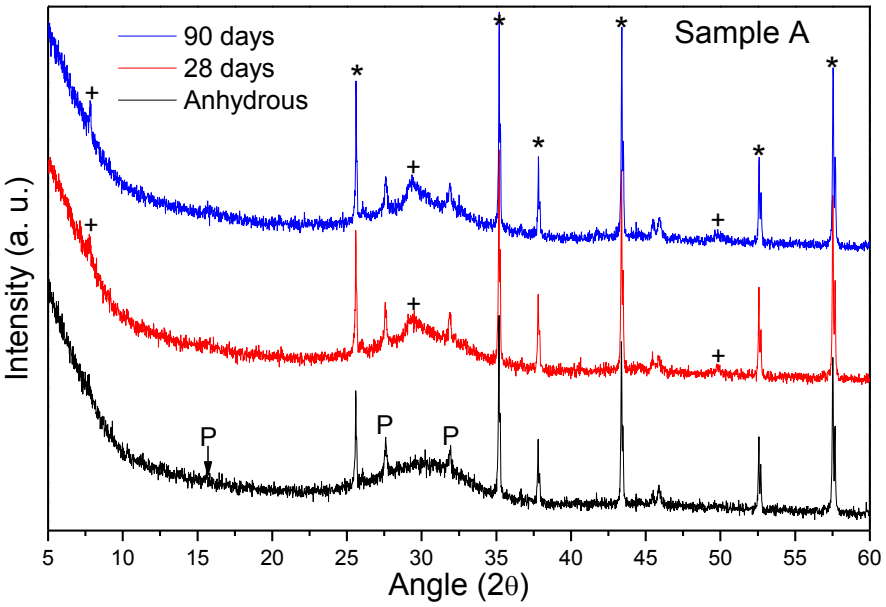

Figure 6-8. X-ray diffractograms of Sample A at different ages of hydration. The asterisk identifies the peaks of corundum used as internal standard to determine the amorphous content of this sample. + sign identifies the Tobermorite-like structures, while P denotes for Pseudowollastonite.

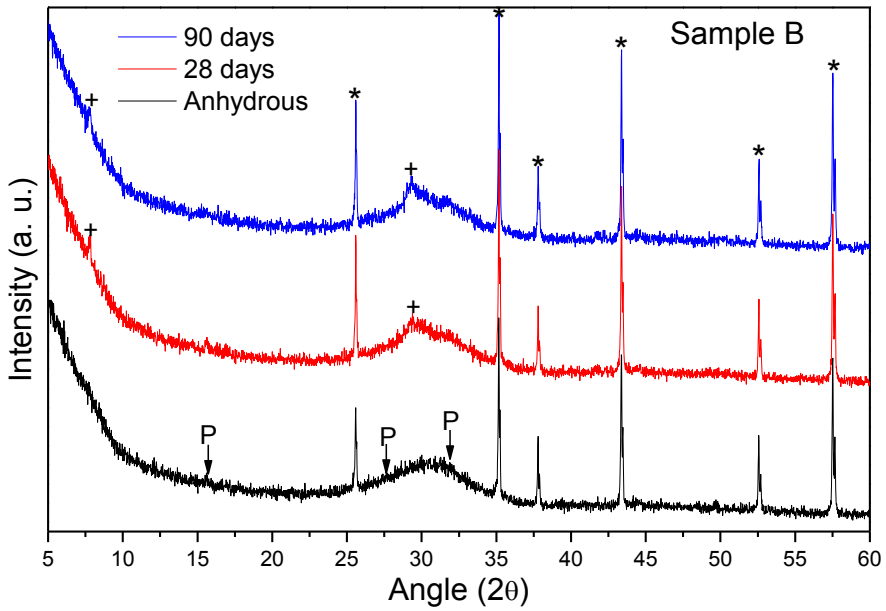

Figure 6-9. X-ray diffractograms of Sample B at different ages of hydration. The asterisk identifies the peaks of corundum used as internal standard to determine the amorphous content of this sample. + sign identifies the Tobermorite-like structures, while P denotes for Pseudowollastonite.

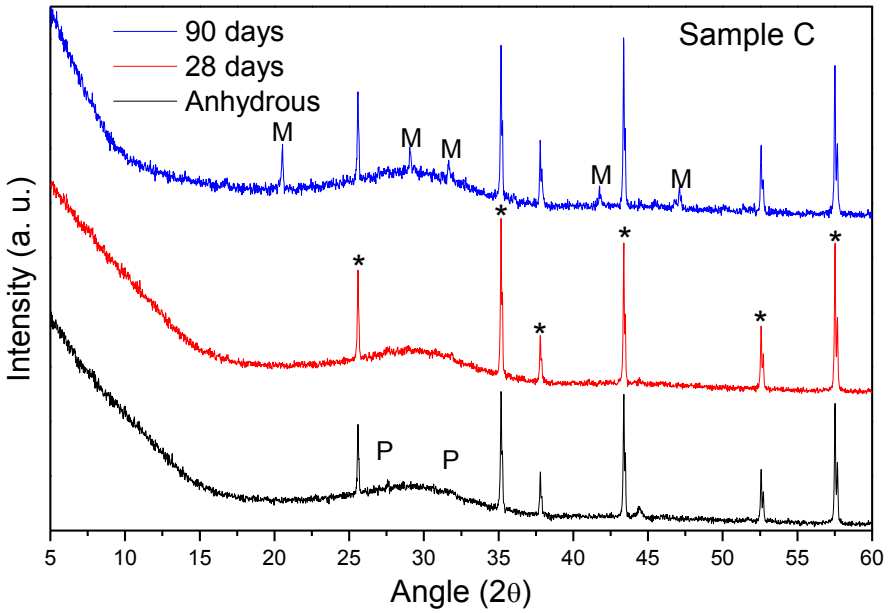

Figure 6-10. X-ray diffractograms of Sample C at different ages of hydration. The asterisk identifies the peaks of corundum used as internal standard to determine the amorphous content of this sample. P denotes for Pseudowollastonite while M indicates the peaks related to the presence of Monohydrocalcite

Table 6-3. Rietveld analysis of samples A, B and C at different hydration ages.

Samples		Rietveld Quantification (Phase wt%)				
		Amorphous	Pseudo wollastonite	Calcite	Monohydrocalcite	Tobermorite
A (C/S=1.1)	Anhydrous	94,4	5,6	---	---	---
	28 days	82,7	4,1	0,9	---	12,3
	90 days	78,4	5,1	1,2	---	15,4
B (C/S=1.25)	Anhydrous	97,2	2,8	---	---	---
	28 days	88,7	1,8	1,2	---	8,3
	90 days	84,2	2,4	2,5	---	11,1
C (C/S=0.8)	Anhydrous	98,4	1,6	---	---	---
	28 days	98,0	1,4	---	0,6	---
	90 days	86,8	1,4	---	11,8	---

6.2.3 SEM/EDS

Figure 6-11 and Figure 6-12 show SEM images of a polished anhydrous piece of sample A and a paste of sample A with 28 days of hydration, respectively. EDS line scan was performed along the indicated yellow arrows and the relative intensities for Ca and Si are presented as green and pink lines, respectively, in the upper part of the figures.

As expected, the composition of the anhydrous amorphous material appears to be very homogeneous with only small fluctuations on the Ca/Si ratio, revealing that the 60 min homogenization step is enough to ensure an approximately constant composition along the whole sample. However, sample A showed some local porosity in the bulk material as it can be seen in Figure 6-11.

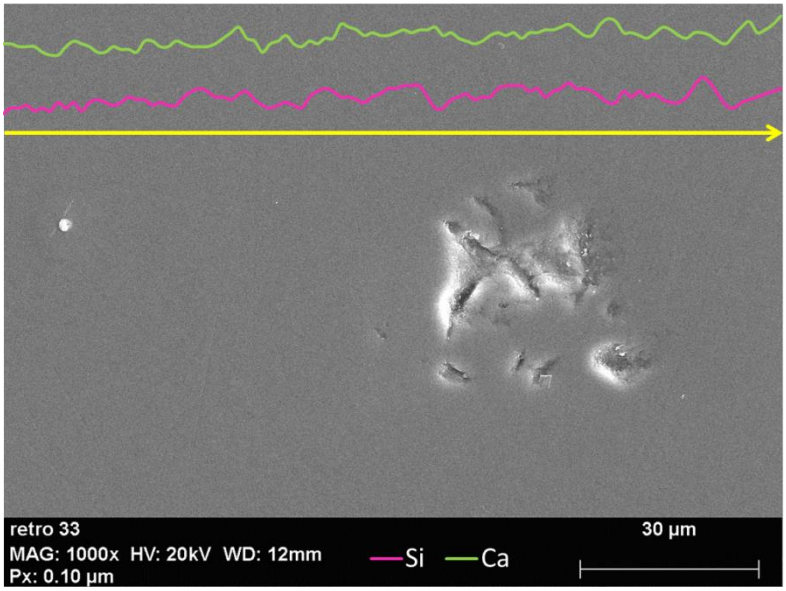

Figure 6-11. SEM image of sample A. The green and pink lines represent a relative percentage distribution of Ca and Si atoms along the yellow line, as determined by EDS.

The microstructure of the 28 days paste prepared from sample A is shown in Figure 6-12, revealing the presence of greatly dispersed hydration product interconnecting grains of unreacted amorphous phase. The EDS line scan shows that Ca and Si follow a similar trend, indicating that the overall Ca/Si ratio is kept approximately constant or, at least, without meaningful variations all over the paste, resulting in a homogeneously distributed composition within the solid solution without any other precipitates formation. This characteristic was also observed in the hydration o sample B. Small Ca or Si intensities fluctuations, only observed in pastes, are believed to be related with more or less hydrated regions, which contribute differently for the EDS signal.

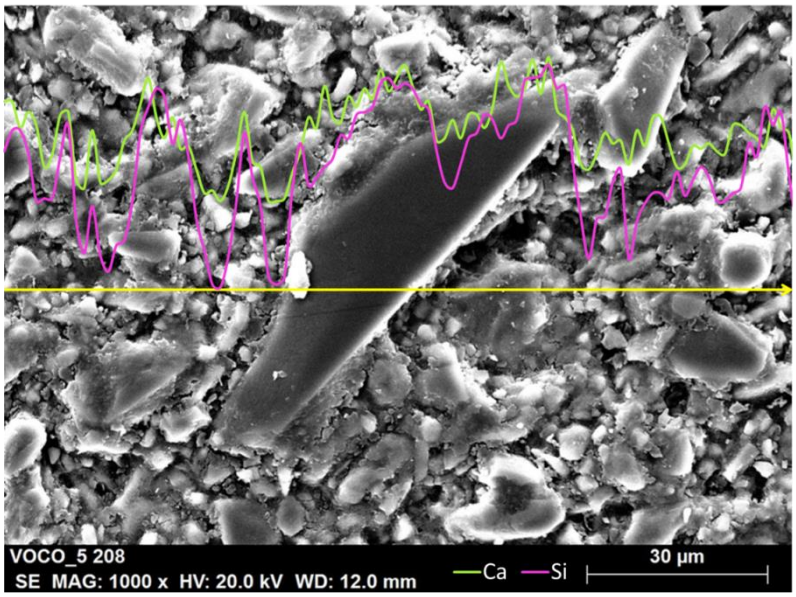

Figure 6-12. SEM image of the 28 days hydrated paste made with sample A. The green and pink lines represent the distribution of Ca and Si atoms along the yellow line, as determined by EDS.

6.2.4 ^{29}Si MAS NMR

The structural assessment of this set of amorphous materials was only performed on samples A and B, in both anhydrous and paste form, since, as it was already shown in the results obtained from XRD, these were the only samples that presented the formation of calcium silicate hydrate phases and thus were considered to be more interesting to characterize.

The acquired ^{29}Si MAS NMR spectra of the anhydrous samples A and B are shown in Figure 6-13 a) and b), respectively. The deconvolutions of the ^{29}Si NMR spectra were performed using five Gaussian functions, considering as major features the amorphous silicate contribution as well as crystalline silicate (Pseudowollastonite) contribution, which were fitted by the iterative mode of nonlinear least squares through the analysis function available in the Origin software. The FWHM of each deconvoluted signal was limited to a maximum of 10 ppm in order to achieve a significant fitting of both amorphous and crystalline spectral contributions. Such FWHM value is within the range of values used in the study of other silicate glasses [119]. The center of the bands corresponding to the Q^n units in amorphous calcium silicate materials can be found, for example, in the work of Zhang et al. [120] where Q^0, Q^1, Q^2, Q^3 and Q^4 are approximately centered at -70, -75, -82, -89 and -101 ppm, respectively, in the ^{29}Si NMR spectrum. The distribution of Q^n units, relative area (%) and the centre of each deconvoluted signal, that is the chemical shift δ, are given in Table 6-4. The peak centres considered in the

deconvolution of the spectra are in good agreement with values presented in previous studies for similar chemical systems where calcium silicates were produced and characterized [119, 120].

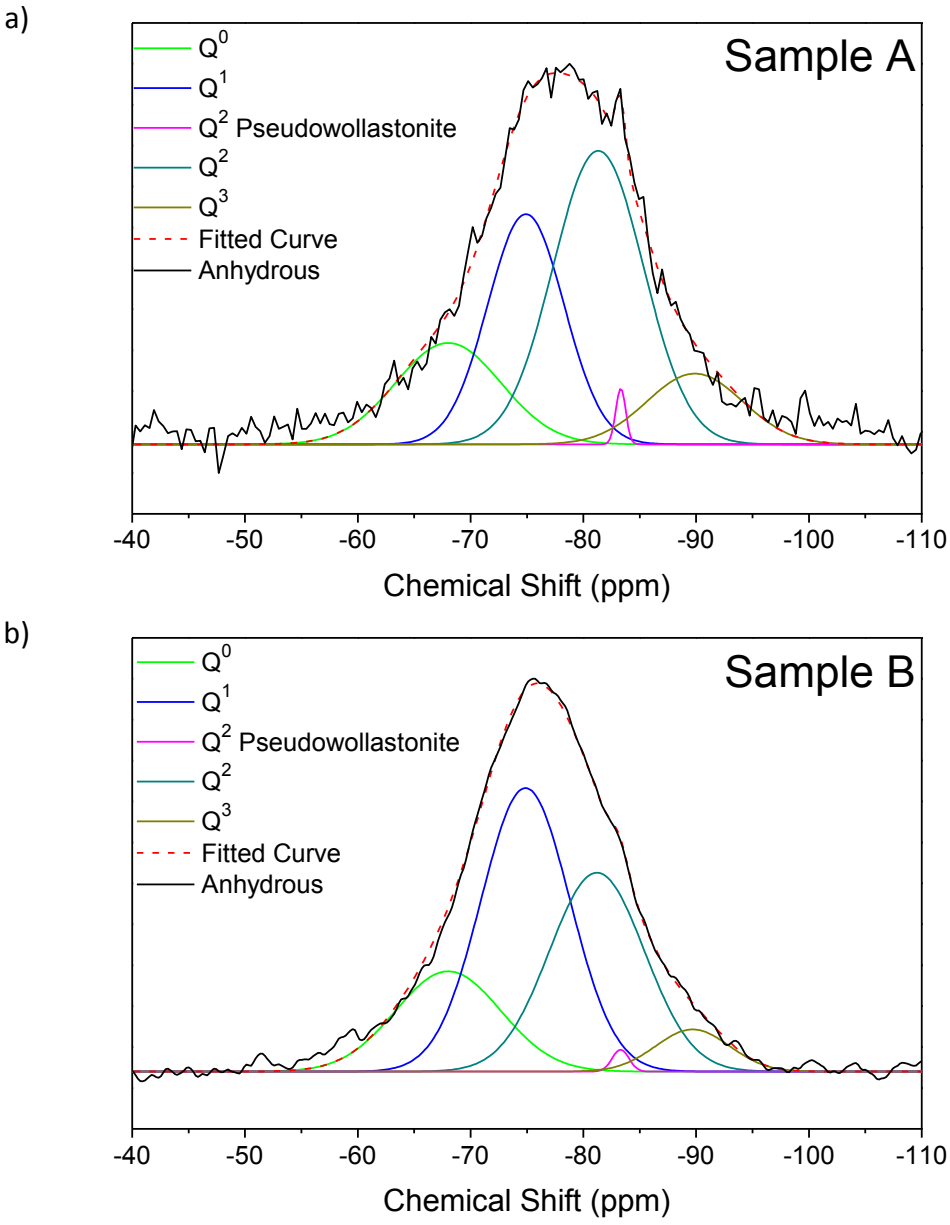

Figure 6-13. ^{29}Si MAS NMR spectra of the anhydrous samples produced and their respective deconvoluted Q^n units contributions. a) Sample A; b) Sample B.

Table 6-4. Q^n units distribution of samples A and B obtained by deconvolution of the ^{29}Si MAS NMR spectra, in Si molar basis.

Q^n units	Sample A (C/S=1.1)		Sample B (C/S=1.25)	
	Relative Area (%)	Centre (δ,ppm)	Relative Area (%)	Centre (δ,ppm)
Q^0	17.20	-68.02	18.17	-68.02
Q^1	28.30	-74.90	43.31	-74.87
Q^2	42.69	-81.32	32.53	-81.20
Q^3	10.91	-89.88	5.35	-89.68
Q^2 CS	0.90	-83.31	0.63	-83.30

It is known that the Q^2 units that compose the crystalline structure of Pseudowollastonite have a well-defined characteristic chemical shift at -83.5 ppm [37, 119], whereas the distribution of the Q^n units related to amorphous calcium-silicate structures is quite broad, going from Q^0 (monomers of SiO_4) to Q^4 (fully coordinated silicon) [120, 121, 123]. The deconvolutions of the ^{29}Si MAS NMR spectra shown in Figure 6-13 reveal that the amorphous silicate matrix of our samples does not have Q^4 units in its structure, being mainly formed by Q^1 units (dimers), in both cases, with a dispersion in the range between Q^0 and Q^3.

Figure 6-14 and Figure 6-15 show the evolution of the normalized ^{29}Si MAS NMR spectra of samples A and B, respectively, as the hydration takes place to over 90 days of curing.

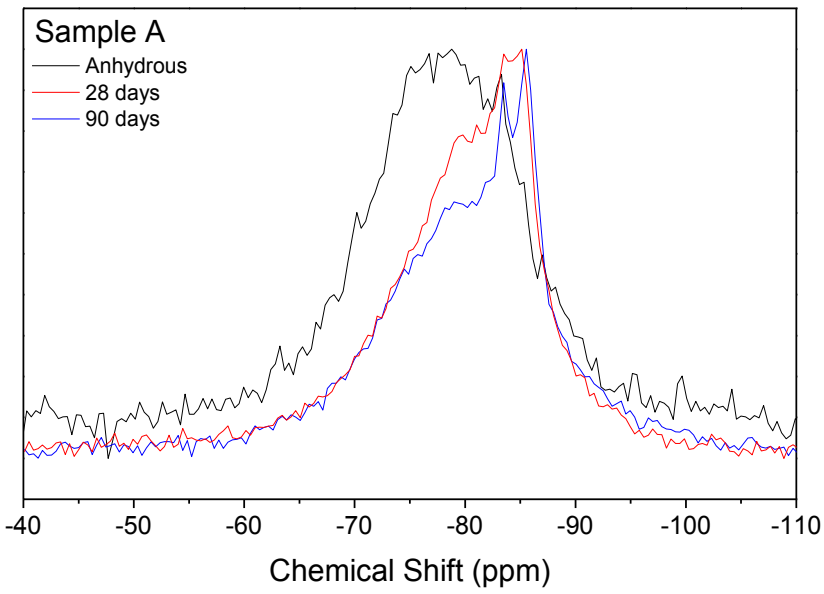

Figure 6-14. Normalized ^{29}Si MAS NMR spectra of Sample A, showing the structural evolution during hydration of pastes.

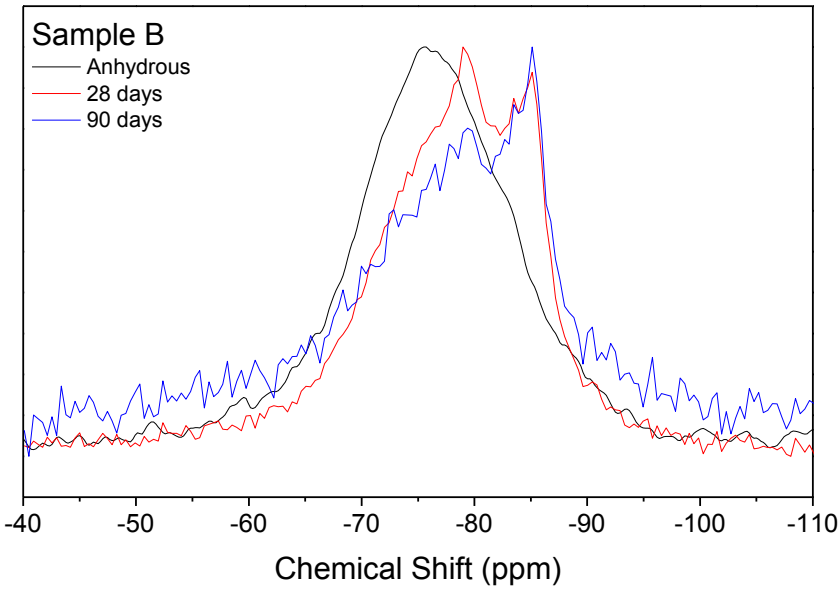

Figure 6-15. Normalized ^{29}Si MAS NMR spectra of Sample B, showing the structural evolution during hydration of pastes.

It can be seen from Figure 6-14 and Figure 6-15 that the spectra of samples A and B dislocate to more negative chemical shifts and two new bands, centered at around -79.5 and -85 ppm, emerge as a result of the hydration process, being related to the silicate hydrated structures of C-S-H, more precisely to the Q^1 and Q^2 units, respectively. It is also possible to observe that the ratio Q^2/Q^1 increases with the hydration time, indicating progressive polymerization of the hydrated structures.

6.2.5 FTIR Spectroscopy

Figure 6-16 shows the medium infrared spectra of the anhydrous samples A and B. These spectra are dominated by three main regions ranging from 400 to 550 cm^{-1}, from 600 to 750 cm^{-1} and from 800 to 1000 cm^{-1}. At the lower frequencies, both spectra are dominated by the band identified as *a* around 450-490 cm^{-1} that can be assigned to asymmetric bending of Si–O–Si bond in the SiO_4 tetrahedra [86, 114] and the small shift observed between sample A and sample B is due to their different Q^n distributions, as it was already observed in this study through ^{29}Si MAS NMR spectroscopy. The region between 600 and 750 cm^{-1} presents two distinct features, corresponding to bands *b* and *c* in Figure 6-16, where the former, at around 690 cm^{-1}, has been previously attributed to inter tetrahedral Si-O-Si vibrations of amorphous silicates [43, 114], while the latter, at 719 cm^{-1}, is more evident in sample A and is related to

the presence of Pseudowollastonite, namely to bridging Si-O-Si stretching vibrations of its three-membered rings structures [124, 125]. In the region between 800 and 1000 cm^{-1} both spectra are dominated by a wide absorption band centered at approximately 920 cm^{-1}, which is in fact a superposition of two other bands typically centered at around 900 and 950 cm^{-1}, corresponding to stretching vibrations of non-bridging Si-O in Q^1 and Q^2 units, respectively [126, 127]. The feature identified as *d* is more evident in sample B and is assigned to the stretching mode of non-bridging Si-O of isolated tetrahedra [126, 127]. The bands identified as *e* and *f* in Figure 6-16 are related to the stretching vibrations of non-bridging Si-O bonds in Pseudowollastonite [125].

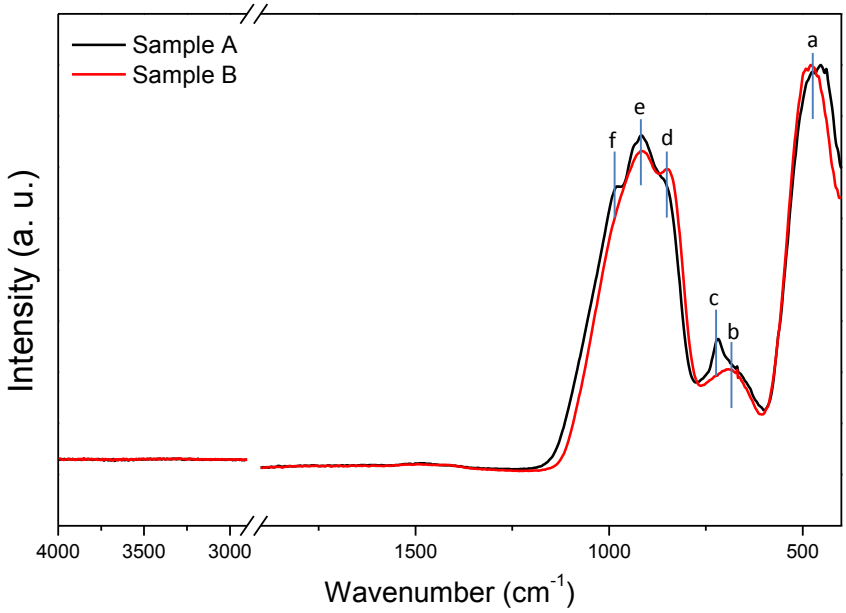

Figure 6-16. FTIR spectra of anhydrous samples A and B. Main features of both spectra are identified with letters *a* to *f*.

Figure 6-17 shows FTIR spectra of the hydration evolution of sample A (top) and sample B (bottom), revealing the development of a narrow band centered at -445 cm^{-1} in both samples as hydrations proceeds, which indicates that the hydration products being formed may present some similarities between both samples, being characterized by a local environment more organized than the precursor material, confirming the results obtained by XRD and ^{29}Si MAS NMR. This band has already been reported in previous studies to be related to Si-O-Si bending modes of C-S-H gel, being also typical of Tobermorite-like structures [43, 105-108,

128]. Along with this feature, two other bands at ~670cm and ~960 cm^{-1} also emerge upon hydration in both samples, with the first being typical of low C/S (<1.2) C-S-H gels and related to Si-O-Si bending mode, while the second is attributed to stretching vibrations of the Q^2 tetrahedra [43]. It is also observable the presence of the asymmetric stretching of CO_3^{2-} band, probably from calcite, in the range of 1400 to 1500 $cm^{-1}$and the H-O-H bending vibration of molecular water band at 1640cm^{-1} as well as the region assigned to the stretching vibrations of O-H from 2800 to 3600 cm^{-1} [43, 107].

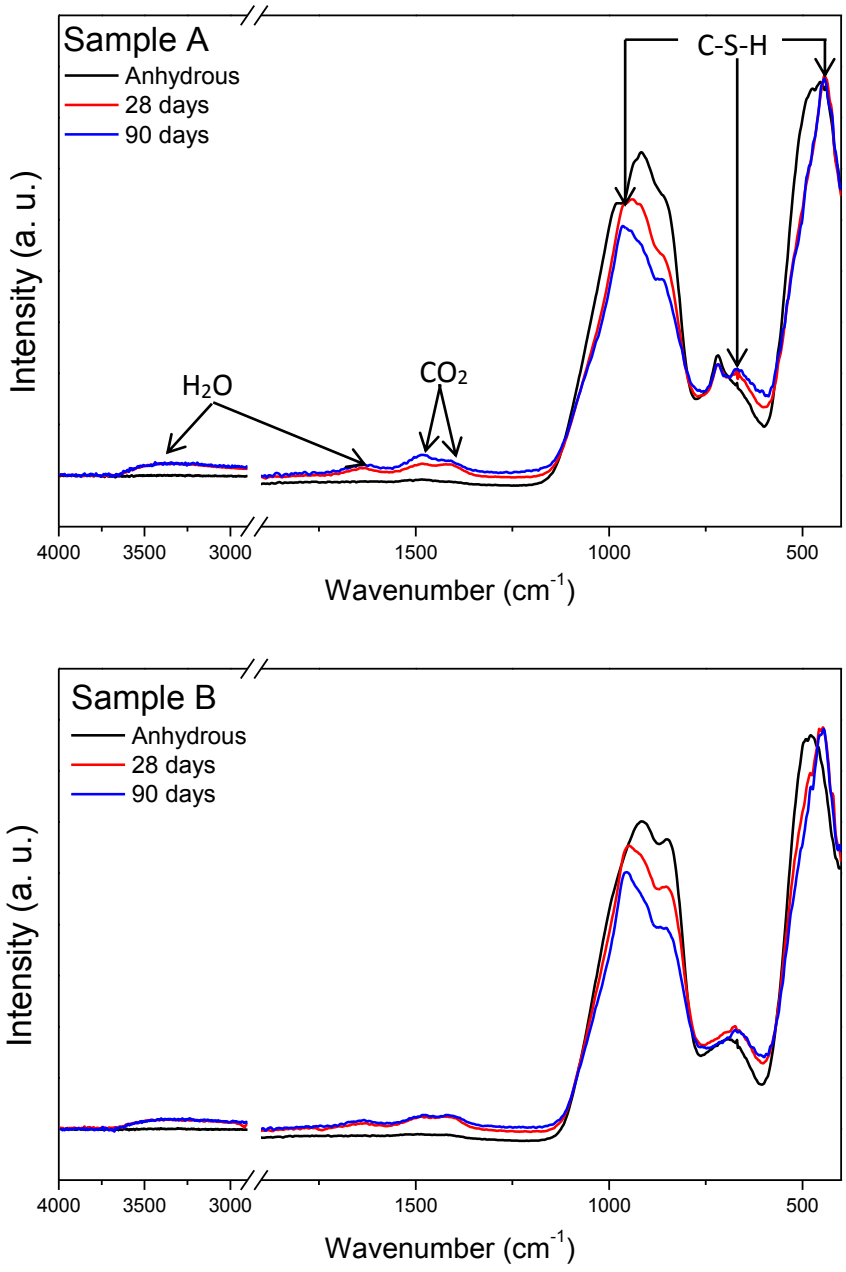

Figure 6-17. Hydration evolution of Sample A (top spectra) and Sample B (bottom spectra) followed by FTIR. In the top spectra are identified the main features occurring after hydration of both samples.

6.2.6 Thermogravimetric analysis (TGA)

The determination of the hydration products bound water through TGA followed the assumption that all the bound water (structural water) should be lost between 105 and 500ºC and knowing that no Portlandite contribution to the weight loss in this temperature range should exist. This temperature range was defined in agreement with other published studies on the water loss of C-S-H of several cement types [129-132]. Figure 6-18 shows the thermogravimetric results obtained for the pastes produced with 7, 28 and 90 days of hydration as well as plot these results against the compressive strength values obtained. The evolution of strength clearly follows the trend of the water incorporation process, which is, of course, related to the amount of hydrated products formed. The values plotted in the x axis of Figure 6-18 for the weight% of H_2O_{bound} correspond to the total sample weight loss in the temperature range between 105 and 500ºC in a dry-basis.

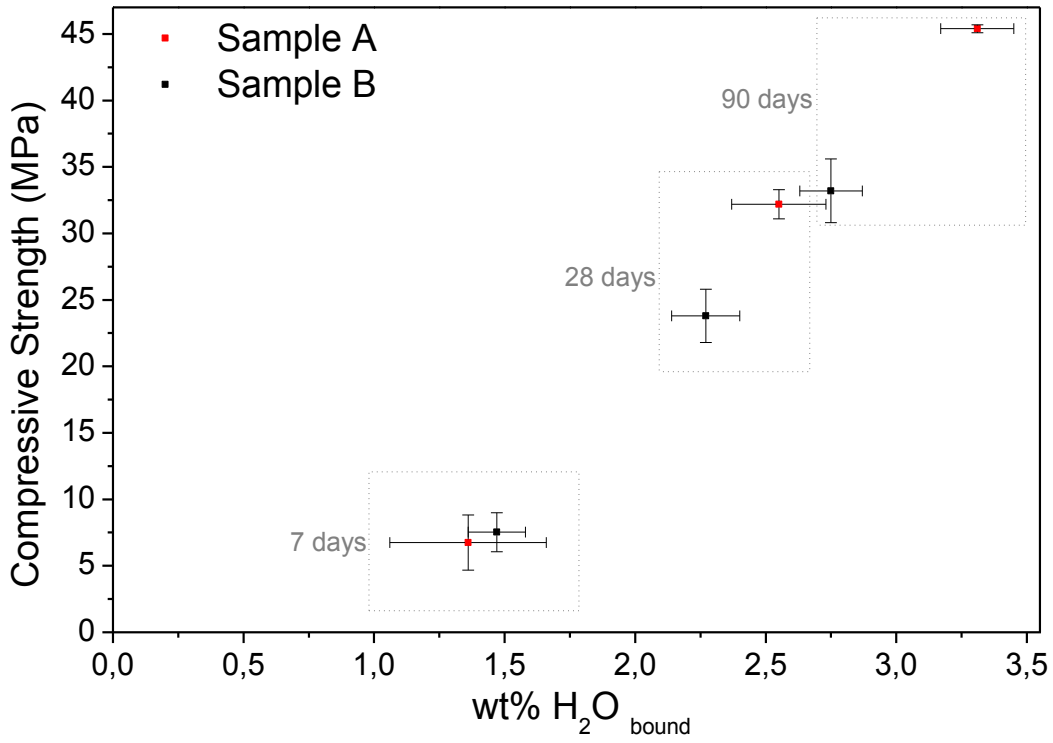

Figure 6-18. Relationship between the water incorporated in the structure of the pastes produced and the determined compressive strength. The boxes identified in the graph group the results in terms of hydration age.

6.3 Discussion

The process used to produce the amorphous exogenous materials with C/S molar ratios ranging from 0.8 to 1.25 lead to an amorphization degree close to 95% in weight, containing only small amounts of Pseudowollastonite. This fact allows to say that the general properties of the samples produced and analyzed in this work are essentially governed by their amorphous component.

The existence of crystalline Pseudowollastonite in the samples prepared indicates two possible causes:

i. The initial cooling rate is not very effective enabling the nucleation and growth of the Pseudowollastonite phase even when cooled from the liquid (*L*) region of the CaO-SiO_2 diagram indicated in Figure 6-19; or
ii. The Pseudowollastonite formed has a primary nature and results from an equilibrium, achieved in the heating stage, in the region "liquid + Pseudowollastonite" (*CS + L*) of the CaO-SiO_2 diagram indicated in Figure 6-19.

A mixed contribution had probably occurred, however, the former explanation may have contributed in a larger extent, since, in the samples produced, the majority of the Pseudowollastonite crystals observed were distributed at the surface of the clinker, thus indicating that the phenomenon of surface crystallization had probably occurred during cooling.

From Figure 6-3 and Figure 6-4 one can clearly observe distinct hydration behaviours from the amorphous samples with higher C/S molar ratios (1.1 and 1.25) when compared to the samples with lower C/S (0.8 and 0.9), as the former two samples (A and B) present strength development from at least the 7 days of hydration which tends to grow until the 90 days. Samples C and D however do not present any ability do set and harden by their selves at least until the 90 and 28 days of hydration, respectively.

Particularly sample A presents a very interesting growth trend in its mechanical properties, if it is taken into account that the compressive strength obtained was achieved by only mixing with water, with no other activators. It is possible to observe that, with exception for the very early ages, sample A follows a compressive strength development that represents about 50% of the obtained for an industrial clinker. From the comparison of the results plotted in Figure 6-3 and Figure 6-4 it can be seen the effect of the water/binder ratio in the reference clinker,

where the strength almost doubles as the value of water/binder decreases from 0.375 to 0.25. Considering this conversion factor of 2, it possible to say that Sample A presents, at 28 days of hydration, a similar compressive strength value of a mix containing 50% clinker and 50% sample D in weight. In fact sample D appears as an interesting pozzolanic material since, when combined with 50% in weight of clinker, their pastes can reach around 60% of the strength presented by a paste containing 100% clinker.

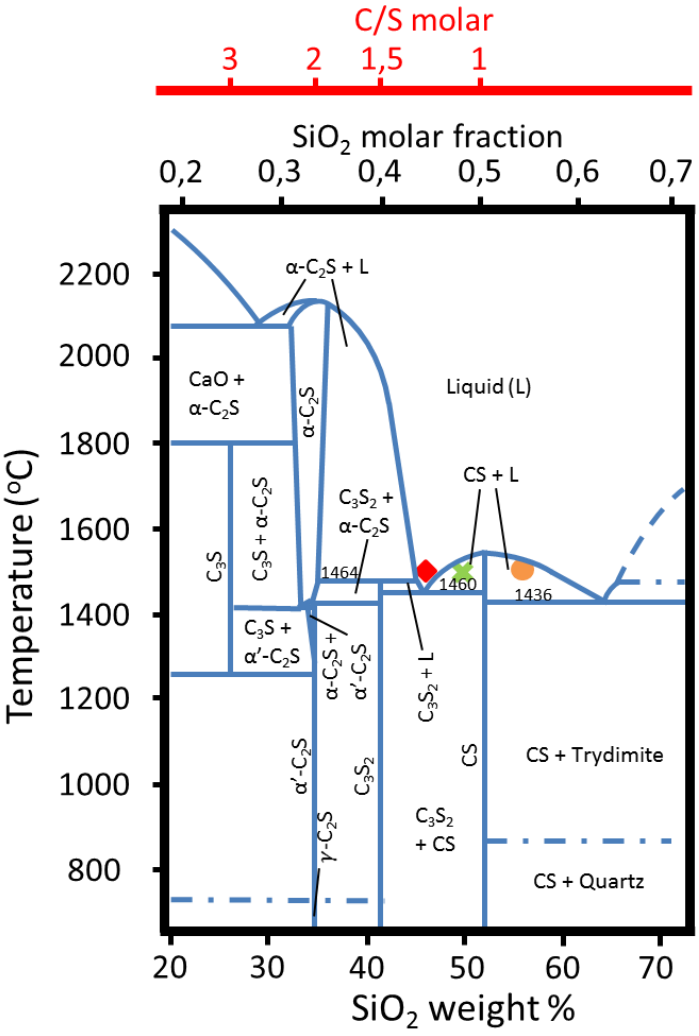

Figure 6-19. Detail of the CaO-SiO_2 diagram showing the maximum process temperature for each of the compositions produced. The green cross indicates sample A, the red diamond indicates sample B and the orange circle indicates sample C composition. The red scale on top of de diagram shows the range of C/S molar ratio.

In order to compare the results obtained in this chapter with similar hydraulic binders studied in other works, a compilation of results is presented in Table 6-5, where some details on the preparation, water to cement ratio and geometry of the samples tested are also given. These

parameters differ greatly from study to study, thus the interpretation of Table 6-5 should not be made as a direct comparison between the values presented, since the conditions on which the samples were prepared have impact on the properties obtained, but only as reference values in the perspective of the mechanical properties of the materials for their final application as hydraulic binders. As it was already seen in this work, the water to cement ratio has some impact in the compressive strength of the pastes produced, however one of the properties that is ultimately measured in practical situations is the workability of the cement paste that typically depends on the balance of two main contributions: the fineness and the water to cement ratio. As the particle size of a given cementitious system decreases, the amount of water needed to attain a constant workability increases. In this work, it was intended to maintain a constant workability of the pastes produced, so the water to cement ratio also changed with the fineness of the powders prepared. This approach was adopted with the perspective of giving a higher relevance to the practical aspect of the final cement paste application.

By a question of similarity, the compressive strength results shown are essentially referred to systems containing ground granulated blast-furnace slag (GGBFS) reported in recent works. GGBFS are mainly amorphous hydraulic binders that possess C/S ratios similar to the ones presented by the hydraulic binders produced in this work. However, GGBFS present very low compressive strength values and are typically studied as base materials for the production of alkaline activated pastes or as addition to OPC to produce mainly types II, III or V cements (according to EN 197-1 [10]). Much information can be obtained regarding their performance under alkaline activation or in combination with Portland clinker but very little information about their isolated behaviour upon hydration is still available. Nevertheless, Jin et al. [133] present a compressive strength value for a non-activated slag paste that may be used as comparison to the hydraulic binders studied in this chapter since, not only the C/S ratio (1.16) is within the range of the materials studied here but also the water to binder ratio (0.32) is close to the one used in this work (0.375). The value reported by Jin et al. [133] for the compressive strength of a non-activated slag paste is much lower at all ages than any of the hydraulic binders described in this work. Jin et al. [134], Jang et al. [135] and Tanzer et al. [136] present slag pastes with compressive strength values at 28 days similar to the ones obtained in this work, however these values were obtained under alkaline activation conditions. Nevertheless, when optimizing the activation conditions, compressive strength values of slag

pastes can go over 80 MPa at 28 days, as shown in the works of Tanzer et al. [136] and Puertas et al. [86]. These results will be further compared in the chapter 7 of the present thesis, where alkaline activation experiments were made, using an amorphous binder with a C/S molar ratio of 1.1 as base material.

As referred previously, GGBFS are often used as replacement materials in mixtures with OPC due to their good pozzolanic character.

Table 6-5 shows some compressive strength values for this type of systems, with Hoshino et al. [137] and Escalante-Garcia et al. [138] reporting strengths at 28 days of around 40 MPa for OPC pastes produced with 40%wt and 60%wt of GGBFS, respectively, which compares to the value obtained for the paste prepared in this work with 20%wt of clinker and 80%wt of amorphous sample D. However, it is important to note the higher water/binder ratio used by those two authors in their studies.

Table 6-5. Reference values for the mechanical performance of commercial slags pastes and mortars. Strength, activators used and water to binder ratios are indicated for comparison with the amorphous hydraulic binders produced in this work.

Molar C/S of Slag	Strength (MPa) 7 days	28 days	70 days	90 days	Activator	Observations	Source
1.16	~1	~6	---	~14	No activator	Pastes of 40mm cubes. W/C=0.32.	Jin et al. [133]
1.16	~21	~35	---	~45	4%$NaCO_3$	Pastes of 40mm cubes. W/C=0.32.	Jin et al. [134]
2.86	---	~28	---	---	16.7% Waterglass + 4,6% NaOH	Pastes 50mm cubes. W/C~0.39	Jang et al. [135]
1.24	~33	~44	---	---	NaOH/Na_2CO_3	Pastes of 1x1x6 cm^3 prisms W/C = 0.4	Puertas et al. [86]
1.24	~77	~84	---	---	Waterglass (SiO_2/Na_2O=1.2)	Pastes of 1x1x6 cm^3 prisms W/C = 0.44	Puertas et al. [86]
1.22	~20	~30	---	---	NaOH (2.4%Na_2O by mass of solids)	Pastes of 20mm cubes. W/C=0.35.	Tanzer et al. [136]
1.22	~70	~80	---	---	KOH Waterglass (3.6%K_2O by mass of solids. SiO_2/K_2O=1)	Pastes of 20mm cubes. W/C=0.35.	Tanzer et al. [136]
0.86	~25	~33	---	---	NaOH (2.4%Na_2O by mass of solids)	Pastes of 20mm cubes. W/C=0.35.	Tanzer et al. [136]
0.86	~60	~85	---	---	(3.6%K_2O by mass of solids. SiO_2/K_2O=1)	Pastes of 20mm cubes. W/C=0.35.	Tanzer et al. [136]
1.42	~32	~42	---	---	NaOH (2.4%Na_2O by mass of solids)	Pastes of 20mm cubes. W/C=0.35.	Tanzer et al. [136]

Molar C/S of Slag	Strength (MPa) 7 days	28 days	70 days	90 days	Activator	Observations	Source
1.42	~45	~65	---	---	(3.6%K_2O by mass of solids. SiO_2/K_2O=1)	Pastes of 20mm cubes. W/C=0.35.	Tanzer et al. [136]
1.05	~8	~13	---	~20	NaOH (6%Na_2O by mass of slag)	Mortar of 50 mm cubes. W/C=0.485.	Shi [139]
0.93	~1	~3	~3	---	Waterglass (25% by mass of solids. SiO_2/Na_2O=3.2)	EN 196-1 Mortars. W/C ~0.41.	Altan et al. [140]
0.93	~12	~16	~17	---	NaOH (8M, 4.4%Na_2O by mass of solids)	EN 196-1 Mortars. W/C ~0.41.	Altan et al. [140]
0.96	14.3	21.3	---	26.2	NaOH (4%Na_2O by mass of solids)	EN 196-1 Mortars. W/C=0.5).	Aydin et al. [141]
0.80	---	0.0	---	0.0	No activator	20x20x40 mm^3 Prisms. W/C=0.375	This work
1.10	6.8	32.2	---	45.4	No activator	20x20x40 mm^3 Prisms. W/C=0.375	This work
1.25	7.5	23.8	---	33.2	No activator	20x20x40 mm^3 Prisms. W/C=0.375	This work
1.41	~25	~41	---	---	60%wt OPC	40x40x160 mm^3 Paste. W/C=0.5	Hoshino et al. [137]
1.34	~16	~37	---	---	40%wt OPC	10x10x100mm3 Paste W/C=0.5	Escalante-Garcia et al. [138]
1.27	26.0	40.9	---	50.9	65%wt OPC	40x40x160 mm^3 Mortar W/C=0.5	Menéndez et al. [142]
0.90	---	0.0	---	---	No activator	20x20x40 mm^3 Prisms. W/C=0.25	This work
0.90	---	29.6	---	---	10%wt Clinker	20x20x40 mm^3 Prisms. W/C=0.25	This work
0.90	---	41.3	---	---	20%wt Clinker	20x20x40 mm^3 Prisms. W/C=0.25	This work
0.90	---	52.9	---	---	30%wt Clinker	20x20x40 mm^3 Prisms. W/C=0.25	This work
0.90	---	66.1	---	---	50%wt Clinker	20x20x40 mm^3 Prisms. W/C=0.25	This work

The phase development observed by XRD for the hydrated pastes are in line with their respective compressive strength results. A general feature observed for all the samples analyzed is the absence of Portlandite at all ages, which is a phenomenon already known to occur in slag-based cementitious systems, that usually are characterized by low C/S molar ratios [26]. By drawing a parallel with the hydration mechanism of crystalline calcium silicate

phases, which is related to the release of calcium and silicate ions into solution, resulting in the increase of concentration of Ca^{2+} until it reaches its maximum that may or may not exceed the $Ca(OH)_2$ saturation level, it is possible to say that, in the case of the amorphous hydraulic binders produced in this work the saturation level of $Ca(OH)_2$ doesn't seem to be exceeded at any time of the hydration process, even for the relatively low water/binder ratios used, and no Portlandite was ever identified by any of the techniques used, namely XRD or FTIR. Apart from this common point, sample C behaves very differently from samples A and B, showing the formation of Monohydrocalcite during hydration, similarly to what was observed, although in a lower extent, in the dendritic belite clinkers analyzed in chapter 5. The lack of ability to react as well as the formation of Monohydrocalcite in these cases might be related with the low solubility of the silicate matrix that presents a higher condensation degree, thus hindering the formation of hydrated calcium silicate products. However, since the solubility of Ca is higher, some Ca-based products end up forming, such as is the case of Monohydrocalcite.
Regarding the phase development of samples A and B, it was observed the formation of C-S-H gel phase with structural features resembling Tobermorite. These structures can be primarily characterized by the presence of a peak assigned to the d_{002} spacing in x-ray diffraction that is related to the interspacing of parallel sheets. It is known that three main distinct phases exist, corresponding to three degrees of hydration and to different d_{002} values, Tobermorite 9Å, Tobermorite 11Å and Tobermorite 14Å, from the least to the most hydrated form, respectively [3, 143]. In this work, the Tobermorite-like structures formed during hydration present a first peak at ~11.3Å, which indicates that the Tobermorite 11Å type is predominantly being produced.
The quantification of this phase was attempted by using XRD-Rietveld, however, since it has a semi-crystalline nature, some non-negligible errors are probably being considered in the estimations presented in Table 6-3. The applicability of XRD-Rietveld method to follow the hydration of these amorphous binders seems to be limited when compared to the analysis of crystalline systems, as is the case of OPC, where the degree of hydration can be determined by the measurement of phase consumption over time, by applying the expression:

Eq. 6.1 $$DH = 1 - Wf_{anhydrous}(t),$$

being DH the degree of hydration and $Wf_{anhydrous}(t)$ is the weight fraction of anhydrous phases determined at the time t. However, amorphous systems are more difficult to analyze by using

XRD-Rietveld method and its degree of hydration cannot be determined by simply using the expression give above (Eq. 6.1). This limitation is essentially related to the amorphous nature of the hydration products formed that present characteristic signals in XRD can be easily mistaken with the signal of the anhydrous precursors. Furthermore, the amount of C-S-H formed during hydration of a typical OPC is usually estimated as the amorphous fraction quantified by Rietveld analysis. This procedure is not suitable for the study of the hydration of amorphous cementitious materials since there are two contributions for the amorphous component in the system: anhydrous binder and C-S-H.

It was thus adopted a procedure for the determination of the amount of C-S-H supported by the combined information collected by SEM-EDS, XRD, ^{29}Si MAS NMR, FTIR and TGA and also taking into account the water/silicon ratios defined by the models developed by Richardson [46] and Qomi et al. [40] for C-S-H gels with Tobermorite-like structures.

Then, from the amount of bound water determined by TGA and by assuming the models presented in the works of Qomi et al. [40] and Richardson [46] that compute correlations between the water to silicon molar ratio (*H/S*) and the C/S molar ratio in calcium silicate hydrates, an estimation of the weight % of the C-S-H produced in the pastes prepared in this work was performed.

In this case, it was considered the Eq. 2.6: , that is disclosed in the work of Richardson [46], to define the stoichiometry of the calcium silicate hydrate formed. It is important to note that this equation is valid for the conditions of severely dried samples that include the method used in this work, i.e., a pre-drying paste preparation at 105^{o}C. As a starting point it was also assumed that the resulting C/S molar ratio of the C-S-H obtained by the hydration of samples A and B should be close to the original C/S of the precursor materials, since no other products than C-S-H were found to be produced upon hydration, and that the C-S-H formed will incorporate in its structure the minor elements present in the same proportions as they appear in the theoretical composition of each clinker. Taking into account all these considerations a final C_xSH_y stoichiometry would arise for each system considered, where *x* represents the C/S molar ratio, which is defined with the same value as the precursor material, and *y* defines the H/S molar ratio, being calculated from Eq. 2.6. Thus, in the case of sample A, for an *x* = 1.1 results a C_xSH_y stoichiometry of $C_{1.1}SH_{0.82}$, while the calculation for sample B returns a stoichiometry of $C_{1.25}SH_{0.98}$.

Calculations for the determination of the C_xSH_y weight percentage produced for each sample were then performed according to the equations below:

Eq. 6.2
$$wt\%C_xSH_y = \left(\frac{\frac{wt\%SiO_{2\,reacted}}{\left(\frac{wt\%SiO_{2\,initial}}{100}\right)} + wt\%H_2O_{bound}}{100 + wt\%H_2O_{bound}} \right) * 100$$

where

Eq. 6.3
$$wt\%SiO_{2\,reacted} = \frac{wt\%H_2O_{bound}}{(H/S) * \frac{M(H_2O)}{M(SiO_2)}}$$

and the value of $wt\%SiO_{2\,initial}$ can be taken from Table 6-1.

Table 6-6 presents the calculated average weight % of $C_{1.1}SH_{0.82}$ and $C_{1.25}SH_{0.98}$ formed in the pastes produced with samples A and B, respectively, at 7, 28 and 90 days of hydration, with an estimation of uncertainty resulting from the experimental determination of bound water.

Table 6-6.Calculated weight % of the $C_{1.1}SH_{0.7}$ and $C_{1.25}SH_{0.8}$ produced upon hydration of samples A and B, respectively, at 7, 28 and 90 days of hydration.

	Calculated wt% $C_{1.1}SH_{0.82}$ Sample A	**Calculated wt% $C_{1.25}SH_{0.98}$ Sample B**
7 days	13.0±1.3	12.6±0.9
28 days	24.1±1.6	19.4±1.1
90 days	31.0±1.2	23.4±1.0

Comparing the values presented in Table 6-3 and Table 6-6 for the amount of C_xSH_y at 28 and 90 days, it is possible to separate the hydrated products in two distinct fractions, a crystalline one and an amorphous one. The crystalline fraction can be taken directly from Rietveld analysis while the amorphous fraction can be calculated as the difference between the total C_xSH_y determined by TGA (values of Table 6-6) and the crystalline fraction obtained by Rietveld (values of Table 6-3). Figure 6-20 depicts the calculated values for the different amorphous and crystalline C-S-H fractions considered, revealing a practically even distribution between amorphous and crystalline regions of C-S-H for the hydrated amorphous binders studied.

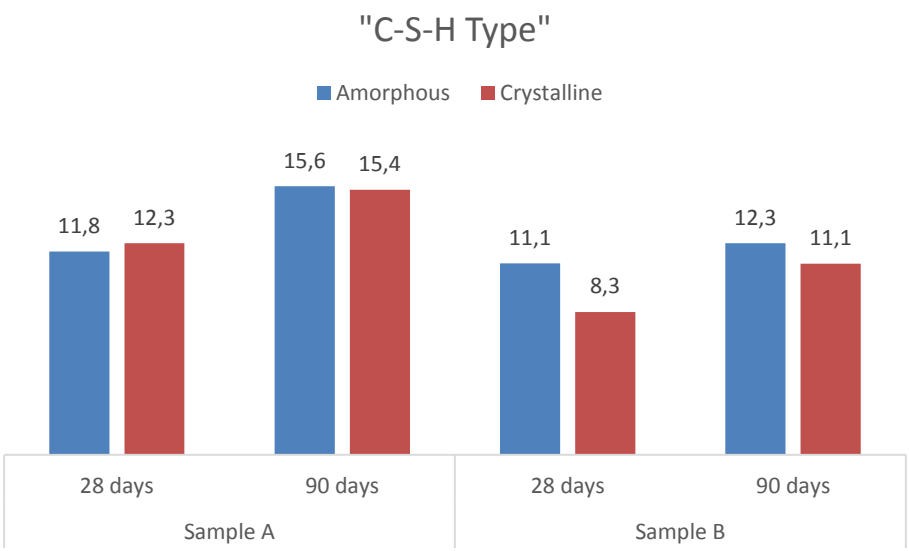

Figure 6-20. Amorphous and crystalline weight percentages of C-S-H phase calculated for sample A and sample B

^{29}Si MAS NMR revealed, as expected theoretically, a decrease in the amount of higher coordination units with increasing C/S ratio of the anhydrous samples, which is in agreement with recent molecular dynamics simulations performed by Wu et al. [144] or by Freitas et al. [17] in calcium silicate melts, as well as in a recent study by Tanzer et al. [136] for amorphous ground granulated blast-furnace slags. However the absolute values for the distribution of Q^n units in the molecular dynamics studies predict a higher polymerization degree for structures equivalent to those presented in this study in terms of C/S ratios. This difference may arise from the fact that the referred MD simulations considered only Si, Ca, Al and O atoms, whereas in the present study no pure chemical reagents were used and the resultant chemical composition show the presence of other minor elements, as it can be seen in Table 6-1. This minor elements may act as structure modifiers, which will break the structure of the glassy matrix backbone, composed essentially of an interconnected silica-based net, and thus decreasing the degree of condensation of these structures.

It can be clearly seen from the ^{29}Si MAS NMR spectra in Figure 6-14 and Figure 6-15 that, in both cases, as the hydration develops the resonances move to more negative chemical shifts, indicating an increase in the degree of polymerization achieved by the rearrangement of the least coordinated Q^n units (Q^0 and Q^1). Q^0 units are expected to be the most prone to react, in fact these isolated tetrahedra are the main motif of belite and alite crystal structures and one of the factors contributing for the hydraulic behavior of those phases, as it was referred in section 2.3. It would then be expected that sample B, which presents a lower degree of

condensation, would present higher reactivity than sample A. However, as TGA and XRD Rietveld results indicate, sample A develops higher amounts of C-S-H gel, being these results also in line with the compressive strength trend observed for the two samples. It is not yet very clear the reason why this difference occurs, however some aspects can be raised to justify the observed behavior, namely: (i) the fewer reaction sites available in sample B; (ii) a possible charge dislocation that may have been introduced by the presence of minor elements; or (iii) a higher number of nucleation sites present in sample A. Aspect (i) is given by the comparison of the chemical compositions of samples A and B (see Table 6-1), since sample A contains a higher amount of silica which translates in a higher number of possible reaction sites, although its distribution is richer in Q^n units with higher degree of polymerization. The second aspect has already been focused in section 2.3 and suggests that the impurity elements present in the structure of sample B, which, in relation to sample A, will be more concentrated in the silica-based network, therefore dislocating the negative charge towards these impurities. This charge dislocation would increase the reaction potential of those particular sites at the cost of a decrease in the number of reactive sites, thus making the reaction proceed at slower rates from the point on which the highly reactive sites extinguish. At last, the third aspect can be discussed through a comparison with slag, where it is known that the presence of a small amount of crystals (around 5% in weight) within the glass phase is beneficial to the compressive strength, since these crystals may act as nucleation sites for the hydration products to grow [3].

It is possible to observe, by the ^{29}Si MAS NMR spectra, the evidence for the formation of the C-S-H gel products by the presence of the two very well-defined peaks, at around -79 and -85 ppm, developed upon hydration. These peaks are known to be characteristic of the end-chain Q^1 groups (-79 ppm) and middle-chain Q^2 groups (-85 ppm) with non-bridging Si-O-Si linkages in C-S-H phase or Tobermorite-like structures [32, 37, 122, 145, 146]. Furthermore, considering the relative intensities of the peaks corresponding to the Q^1 and Q^2 structural units of the C-S-H formed, at approximately -79 and -85 ppm, respectively, it is possible to observe that the Q^2 component increases its contribution at longer hydration ages, thus indicating that the Tobermorite-like structures are primarily formed by short length silicate chains that continue to polymerize at later ages to produce longer silicate chains. The formation of these highly polymerized structures is very likely to be related with the development of the mechanical properties of the pastes produced in this work.

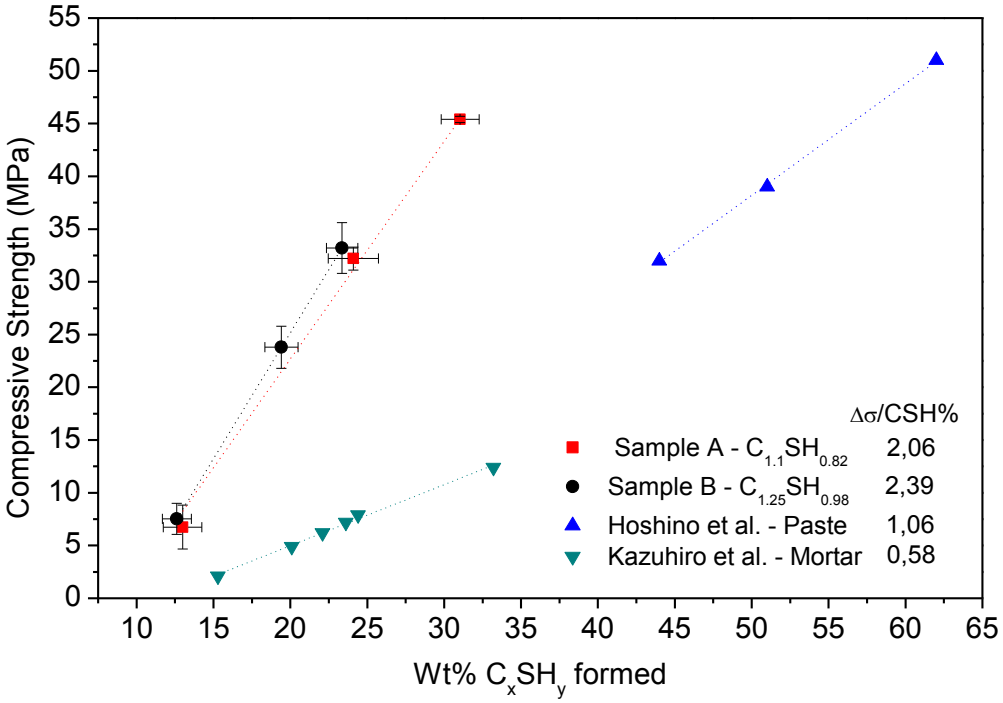

Figure 6-21. Plot of weight percentage of formed C-S-H versus the obtained compressive strength in the pastes produced in this work. Also plotted are some results obtained in the works of Hoshino et al. [137] and Kazuhiro et al. [147].The values of Δσ/ΔC-S-H% presented are related to the slope of the linear fit of each set of results.

In fact, Figure 6-21 depicts the correlation between the amount of hydrated products formed in the pastes produced from samples A and B, as well as in the studies from Hoshino et al. [137] and Kazuhiro et al. [147], and their corresponding compressive strengths. Regarding the values obtained in this work, it is clearly visible the dependence of the compressive strength on the amount of C-S-H produced, indicating that this phase is the main responsible for the mechanical properties and that possible contributions to strength due to other factors are quite small. A similar trend as already been reported in other studies such as the ones from Hoshino et al. [137] for pastes of slag and limestone blended cements or from Kazuhiro et al. [147] for mortars of low heat cements. However, considering the slope of the correlations plotted in Figure 6-21, we can see that the index $\Delta\sigma/\Delta C\text{-}S\text{-}H\%$ (where $\Delta\sigma$ is the compressive strength variation and $\Delta C\text{-}S\text{-}H\%$ is variation of the amount of hydration products in weight percentage) presents higher values for the pastes produced in this work than those obtained for other types of common cement, indicating that the hydration products formed by the hydration of samples A and B have better intrinsic mechanical properties. One of the factors

affecting these better properties may be the higher crystallinity of the calcium silicates produced, as it was observed by XRD and ^{29}Si MAS NMR and is also predicted in the work of Qomi et al. for C-S-H with low C/S [40], as well as it was determined by X-ray scattering for C/S around 1 in synthetically produced C-S-H over a range from 0.6 < C/S < 1.75 [48]. Another factor that may be contributing to these better mechanical properties is the porosity which is external to the quality of the hydration products, being related to the resulting microstructure. This factor is typically directly related to the water to solids ratio [3], which in our work was of 0.375 while in the other two studies presented for comparison a water to solids ratio of 0.5 was used, however no porosity assessment was performed in this work.

6.4 Conclusions

A series of highly amorphous calcium silicates with C/S molar ratios ranging from 0.8 to 1.25 were produced and their hydration behaviours analysed. It was shown that, even at room temperature, the amorphous materials with the highest C/S ratios (1.1 and 1.25) revealed to possess hydraulic activity which was evidenced by the development of very interesting compressive strengths.

The samples with lower C/S molar ratio (0.8 and 0.9), however, did not develop any strength until the 90 days of hydration, revealing to be inadequate to be used by their selves as hydraulic binders. Nevertheless the amorphous binder with C/S molar ratio of 0.9 exhibited pozzolanic properties when used in mixtures containing clinker, presenting compressive strengths superior to equivalent mixtures containing clinker and lime or sand.

^{29}Si MAS-NMR spectroscopy allowed to observe that the least coordinated Q^n units (Q^0 and Q^1) play a very important role in the hydration behaviour of these materials, since they appear to be very prone to convert into calcium silicate hydrated structures similar to Tobermorite, which according to the XRD results is of the 11Å type.

The combination of results from SEM-EDS, XRD, ^{29}Si MAS NMR and FTIR pointed out that these hydrated structures present a low C/S ratio and a semi-crystalline character, which is in accordance with a recent simulation study from Qomi et al. [40] that also predicts improved mechanical properties for these low C/S calcium silicate hydrates when compared to the typical $C_{1.7}SH_y$. It is somehow curious how these semi-crystalline structures form from almost fully amorphous precursor materials, diverging from the typical behaviour of Portland

cements which upon hydration dissolve their hydraulic crystalline phases (C_3S, C_3A, C_2S, etc…) to form an amorphous C-S-H gel with an average C/S of 1.7. It is also noteworthy to mention that, contrarily to normal Portland cement clinker, no Portlandite is formed upon hydration of these materials, which may indicate further improved performance in terms of durability.

The amount of C_xSH_y produced was investigated and compared to the values typically obtained for other cement systems. Although a smaller amount of hydration products was obtained for the pastes prepared in this work, when compared to the pastes prepared from slag and limestone cement blends, similar compressive strengths were obtained, indicating possible improved properties of the resultant hydration products and/or denser microstructures. It was also estimated that the C-S-H produced in these pastes have a semi-crystalline nature, divided in approximately equal fractions amorphous and crystalline regions.

Estimations on the CO_2 emissions linked to the production of these amorphous hydraulic binders indicate savings of about 30% of the raw materials related CO_2 contribution when comparing the amorphous binder of 1.1 C/S molar ratio with OPC.

It is clear, however, that an optimization of the hydraulic properties of these amorphous binders will still be needed to make them competitive with OPC. Nevertheless, as far as the author knows, this is the first time that such hydraulic binders are being studied and probably much improvement is yet to be done.

Having all these features combined, it is therefore not overoptimistic to say that the production of these novel amorphous hydraulic binders may bring to the table the possibility of development of new hydraulic binders with lower calcium content, without compromising the mechanical properties of the resultant hardened pastes.

7 Alkaline Activation of Amorphous Hydraulic Binders

In this chapter the results concerning alkaline activation of an amorphous hydraulic binder with C/S molar ratio of 1.1, similar to the one described in Chapter 6 are presented. Several alkaline solutions were used including Na_2SO_4, Na_2CO_3 and a mixture of NaOH/Na_2SiO_3 (usually known as waterglass). A mixture containing 10% of a reference clinker was also tested. The hydration evolution of the prepared pastes was monitored by compressive strength testing, XRD, FTIR, ^{29}Si and ^{27}Al MAS NMR and TGA. An estimation of the amount and type of hydration products formed was made by considering the results obtained from XRD, ^{29}Si MAS NMR and TGA. The paste prepared with a mixture of NaOH and Na_2SiO_3 revealed to develop compressive strength competitive with OPC at all ages. Upon hydration, a C-S-H phase with a semi-crystalline character was found to be the only hydration product directly formed. The amount of C-S-H produced was determined by the techniques of XRD, ^{29}Si and ^{27}Al MAS NMR and TGA and their values compared. The difference of the values obtained between the three techniques was attributed to the semi-crystalline nature of the hydration product. The crystalline and amorphous fractions of the C-S-H obtained were estimated to be roughly divided in a 50/50 proportion. The mean chain length of the calcium silicate hydrate was calculated using the data obtained by ^{29}Si MAS NMR and correlated with the information given by ^{27}Al MAS NMR. A direct dependence between the compressive strength and the weight percentage of the total C-S-H determined by TGA was established.

7.1 Materials and processing conditions

The raw-materials and theoretical composition of the amorphous hydraulic binder with C/S molar ratio of 1.1 studied in this chapter can be taken from Table 6-1. Also the production process was already referred in chapter 6, being schematically represented in Figure 6-1.

The same grinding process described in section 6.1 was used in the preparation of this hydraulic binder, with the powders obtained being used to produce pastes by mixing it with water or in solutions of alkaline activators in such a way that the water/binder weight ratio was kept constant at a value of 0.375. In the case of the alkali-activated samples, the amount of activator added was defined in order to obtain a total Na_2O content of 3% in weight, furthermore the Na_2SiO_3 commercial solution used was corrected with the addition of NaOH,

so that the Si/Na ratio would be equal to 1,2. This value of Si/Na is within the range of values studied by other authors, which have shown to be adequate in the activation of amorphous materials with a Ca/Si close to the one presented in this work [86, 148, 149]. Also pastes of 100% of reference clinker and another one consisting in a mixture containing the amorphous binder and 10% in weight of the reference clinker were prepared. The analysis of the pastes containing the reference clinker (100% and 10%) and the Na_2SO_4 activator solution were conducted as isolated experiments and only 28 and 90 days compressive strength information was collected, whereas much more detailed information was acquired from the pastes activated with Na_2CO_3 and $NaOH/Na_2SiO_3$ solutions.

The pastes were poured into proper molds with dimensions of 20x20x40 mm^3 and cured in a moisture controlled environment with a relative humidity over 95%. Hydration evolution and compressive strength measurements were performed at the ages of 7, 28 and 90 days, so that a relationship between hydration products development and mechanical properties could be established over time.

The compressive strength tests were performed according to the procedure referred in section 4.11, while XRD-Rietveld was conducted under the conditions indicated in section 4.7. Structural analysis was performed with FTIR-ATR and ^{29}Si and ^{27}Al MAS NMR spectroscopies, following the procedures given in sections 4.6 and 4.8, respectively.

The structural water content was determined by thermogravimetric analysis using the test parameters described in section 4.10, while isothermal calorimetry was performed according to the procedure given in section 4.13.

7.2 Results

7.2.1 Compressive Strength

Figure 7-1 shows the development of the compressive strength for the pastes activated with Na_2SiO_3 and Na_2CO_3 as well as for the non-activated one. It is also depicted in Figure 7-1 typical values obtained for the reference OPC clinker for comparison purposes only. The values of compressive strength obtained for the non-activated sample are very close to the ones obtained in the previous chapter, showing an increase from approximately 7 MPa at 7 days to more than 45 MPa at 90 days. The alkali-activated samples, however, evidenced a much faster

evolution trend, especially the sample activated with Na_2SiO_3 whose strength rapidly achieved a maximum plateau of 77 MPa at 28 days, surpassing the value typically obtained for an OPC clinker paste.

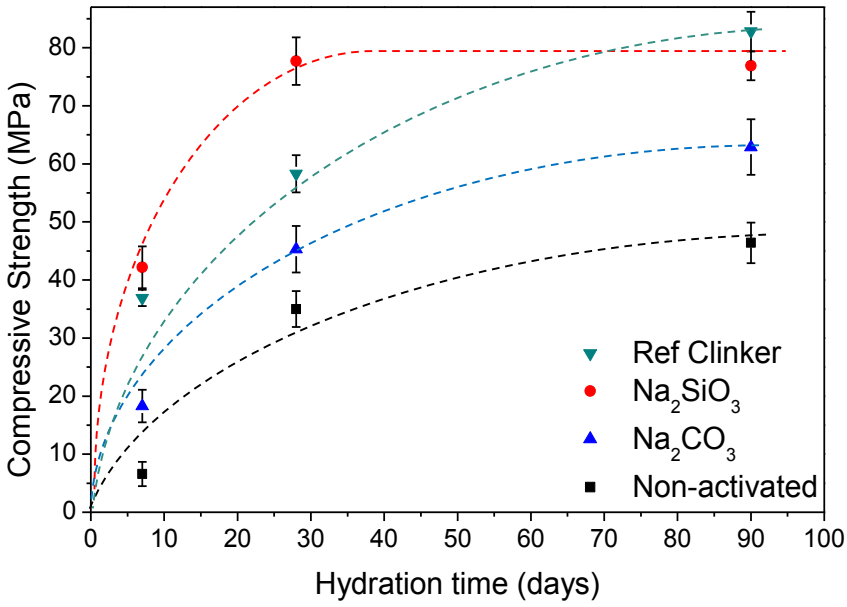

Figure 7-1. Comparison of the compressive strength development over time obtained for the non-activated paste and for the alkali-activated samples (with Na_2SiO_3 and with Na_2CO_3). Values from a reference Clinker are also depicted for comparison. The dashed lines are just a guide for the eye.

Figure 7-2 shows all the results of compressive strength obtained at 28 and 90 days, including the ones from isolated experiments, for the samples with alkaline activation as well as for the mixture containing 10% in weight of the reference OPC clinker. Also depicted are the values obtained for the reference OPC clinker. It is possible to observe that the addition of 10% in weight of the reference OPC clinker to the amorphous hydraulic binder with a C/S molar ratio of 1.1 has little effect on the development of compressive strength at 28 and 90 days, whereas the addition of the alkaline activator shows relatively high improvements in the strength, when compared to the none activated sample, reaching values that are competitive with Portland cement clinker, especially the sample activated with waterglass. Regarding the activations with Na_2CO_3 and Na_2SO_4, their effects seem to be very similar, reaching, in both cases, compressive strengths above 40 MPa at 28 days and higher than 60 MPa at 90 days.

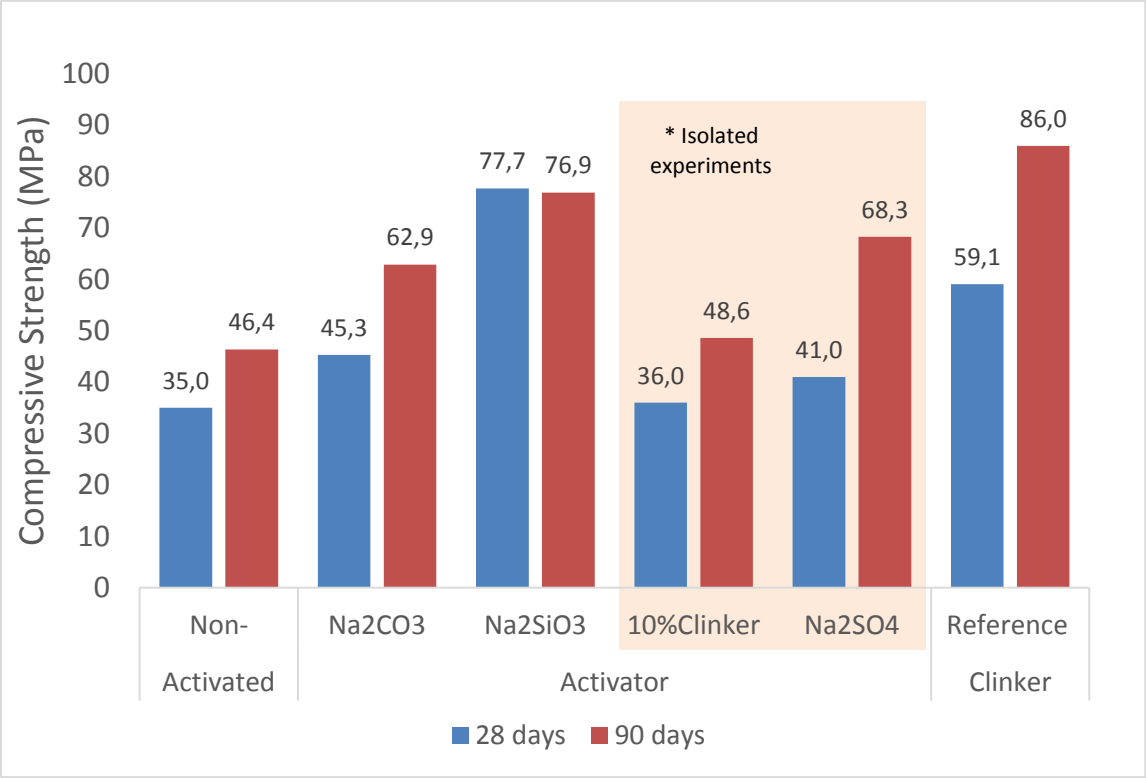

Figure 7-2. Comparison between all the compressive tests performed, including the isolated experiments (in the shaded region of the graph), with mixtures containing alkaline activators and a reference clinker, at 28 and 90 days.

7.2.2 XRD – Rietveld Analysis

The phase development of the pastes prepared with the addition of waterglass and Na_2CO_3 was followed by XRD-Rietveld analysis at 7, 28 and 90 days.

Table 7-1 shows the results obtained by quantitative XRD Rietveld analysis for the content in weight % of each phase present in the pastes produced as well as from the precursor anhydrous hydraulic binder.

The initial constitution of the hydraulic binder produced contains close to 13% of Pseudowollastonite which resulted from the thermal path of the process used to produce the amorphous binder. This value revealed to be higher than the observed in the preparation of sample with the same composition in chapter 6. The peaks assigned to this phase are identified in Figure 7-3 a), b) and c) as *P*, while the symbols + and * denote the presence of the Tobermorite-like phases and the internal standard used (Al_2O_3 – Corundum) for the amorphous fraction quantification, respectively. It was also verified that peaks related to the presence of calcite developed during the hydration of the paste activated with Na_2CO_3, being

those peaks identified in Figure 7-3 b) as *c*. For Rietveld fitting, the following phases were used: Tobermorite 11 Å with reference code 87690, Clinotobermorite with reference code 403090, Pseudowollastonite with reference code 87716, Aluminum oxide phase with reference code 75559 and Calcite with the reference code 40112 from the ICSD database.

Table 7-1. Quantitative results obtained by XRD-Rietveld analysis for the weight percentage of the phases present in the hydraulic binder produced and in the pastes prepared from it, with and without activation.

Sample		Weight %			
		Amorphous	Pseudo wollastonite	Calcite	Tobermorite
Anhydrous	Anhydrous	86,9	13,1	---	---
Non-activated	7 days	78,6	10,4	---	11,1
	28 days	76,7	8,1	---	15,1
	90 days	70,9	8,5	---	20,5
Na_2CO_3	7 days	76	7,6	2,9	13,5
	28 days	72,3	7,5	4,9	15,3
	90 days	69,5	7	5,2	18,3
Na_2SiO_3	7 days	70,4	6,2	---	23,5
	28 days	67,6	6,2	---	26,2
	90 days	64,9	6,7	---	28,3

The hydrated pastes showed to develop Tobermorite-like structures upon hydration, with the sample activated with waterglass showing the formation of appreciable higher values of these hydration products than the non-activated and the Na_2CO_3 activated pastes, indicating some correlation with the values of the compressive strength obtained.

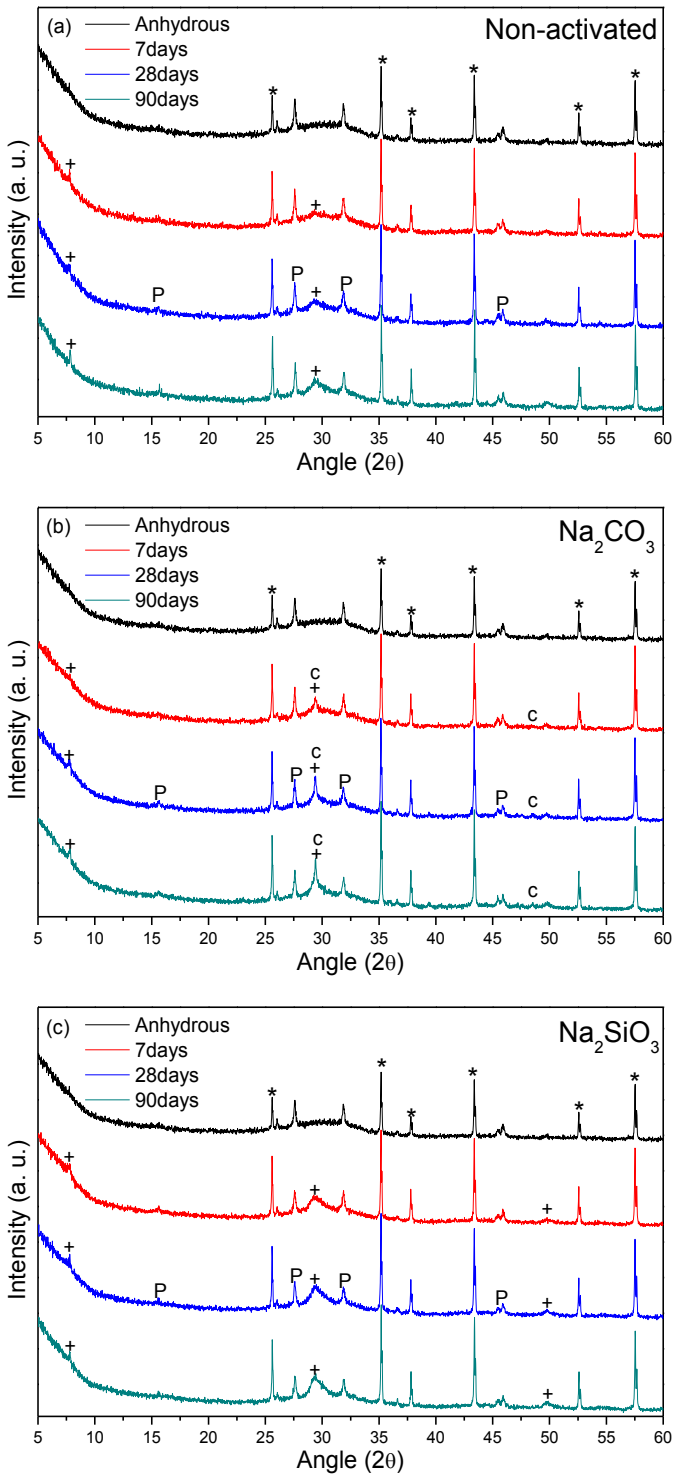

Figure 7-3. XRD results showing the phase development of the (a) non-activated sample, (b) Na_2CO_3 activated sample and (c) Na_2SiO_3 activated sample, till 90 days of hydration. P – Pseudowollastonite; c – Calcite; + - Tobermorite-like phase; * - internal standard Al_2O_3.

7.2.3 FTIR-ATR

The structural short-range order of the anhydrous sample as well as the activated pastes with 28 days of hydration was analyzed through the use of FTIR-ATR spectroscopy in order to assess the structural development upon hydration of these pastes.

Figure 7-4 shows the medium infrared spectra of the 28 days pastes produced with and without alkaline activation as well as the spectra of the anhydrous material. These spectra are essentially dominated by the presence of bands related to different modes of vibration of silica tetrahedra which compose the backbone of the amorphous anhydrous material as well as of the crystalline Pseudowollastonite and the semi-crystalline C-S-H that develops upon hydration. However, in the sample activated with Na_2CO_3, some features assigned to the presence of CO_3^{2-} group are also present, namely the signals at 1420 cm^{-1} and 875 cm^{-1} attributed to asymmetric stretch ($\nu_3[CO_3^{2-}]$) and in-plane bending ($\nu_2[CO_3^{2-}]$) vibration modes, respectively. Also the in-plane bending mode ($\nu_4[CO_3^{2-}]$) seems to be present at ~712 cm^{-1}, however it partially overlaps with the feature at 719 cm^{-1}, which is related to the presence of Pseudowollastonite, namely to bridging Si-O-Si stretching vibrations of its three-membered rings structures [124, 125]. In addition to the feature at 719cm^{-1}, Pseudowollastonite also presents a signal at 985 cm^{-1}, corresponding to the stretching vibration mode of non-bridging $Si\text{-}O^-$ [125], which is more evident in the anhydrous sample and tends to decrease after hydration. Other silicate related bands with structural information are observed in three different main regions, being the lower frequencies region dominated by the band around 450-490 cm^{-1} that can be assigned to the deformation of the SiO_4 tetrahedra [43, 86, 114, 127], while for higher wavenumbers, at around 660 cm^{-1}, it is possible to observe the band corresponding to Si-O-Si bending vibrations [43]. Another main region can be defined between 800 and 1100 cm^{-1} resulting from the combination of a group of bands assigned to symmetric and asymmetric stretching vibrations of Si-O bonds from Q^0 (~850cm^{-1}), Q^1 (~900cm^{-1}), Q^2 (~950 cm^{-1}) and Q^3 (~1100 cm^{-1}) units [43, 127]. The broad band, only present in the hydrated samples, at higher frequencies, from above 3000 to 3600 cm^{-1} is related to stretching vibrations of O–H groups in H_2O or hydroxyls with a wide range of hydrogen-bond strengths [43], probably due to the partially amorphous nature of the hydrated products formed.

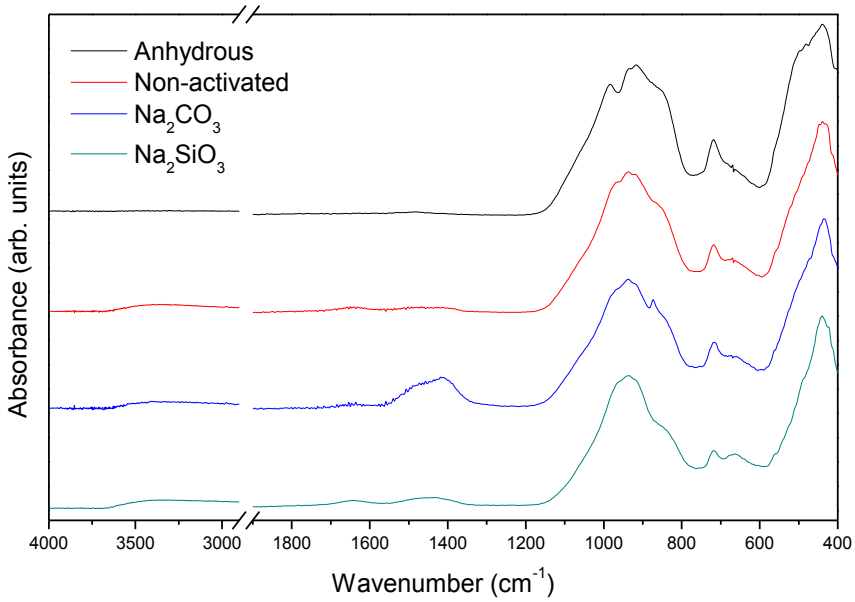

Figure 7-4. Medium infrared spectra of the anhydrous sample A and of the pastes prepared with and without alkaline activation at 28 days of hydration.

7.2.4 ^{29}Si and ^{27}Al MAS NMR

^{29}Si and ^{27}Al MAS NMR experiments were performed on the 28 days pastes and corresponding precursor material in order to collect details on the local environment of Si and Al atoms and assess the structural changes occurring due to the hydration phenomenon, namely the consumption of low coordination Q^n units of SiO_x and the formation of more polymerized units assigned to the hydration products.

Although the amount of Al_2O_3 present in this amorphous material is very low when compared to the values typically contained in other materials used for alkaline activation, such as GGBFS or fly-ash, it was examined the coordination of the existing Al in the precursor material as well as its evolution under different hydration environments.

Figure 7-5 shows the ^{29}Si MAS NMR spectra of the 28 day pastes prepared with and without alkaline activators and also the corresponding spectrum of the anhydrous hydraulic binder. The latter one can be simply characterized as comprising two distinct signals, a broader one, corresponding to the amorphous component of the sample, with chemical shifts spanning from -65 to -95 ppm and a narrow feature, at a chemical shift around -83.5 ppm, which is assigned to the presence of Pseudowollastonite (α-$Ca_3Si_3O_9$) [150]. The amorphous spectral component of the anhydrous sample has a Q^n structural unit distribution typical from calcium

metasilicate glasses, ranging from Q^0 to Q^3 groups and a negligible or inexistent amount of Q^4 units [120, 151].

For the deconvolution procedure it was considered a pure Lorentzian shape for the semi-crystalline C-S-H phase [152, 153] as well as for the Pseudowollastonite phase, while a Gaussian curve shape was found to be more adequate for the deconvolution of the unhydrated amorphous calcium silicate component [153, 154], following the same criteria applied in section 6.2.4, where a maximum FWHM of 10 ppm was considered for all the features in order to achieve a meaningful deconvolution result. The Q^n distribution values obtained after the deconvolution of the ^{29}Si MAS NMR spectra are shown in Table 7-2, while Figure 7-6 to Figure 7-9 depict graphically the deconvolution results of the anhydrous sample spectra, as well as the spectra of the 28 days hydrated pastes activated with Na_2CO_3 and Na_2SiO_3 and also the non-activated paste, respectively. Also in Table 7-2 are presented the values of mean chain length, which can be defined as the number of SiO_x units combined to form the average cluster in the C-S-H structure, calculated by the method proposed by Richardson et al. [84], using:

Eq. 7.1
$$MCL = \frac{2}{\left(\frac{Q^1}{Q^1 + Q^2}\right)}$$

where *MCL* is the mean chain length, and Q^1 and Q^2 are the silicon molar fractions related to the C-S-H phase, obtained by the deconvolution of the ^{29}Si MAS NMR spectra. It was also assumed that no Q^2(1Al) units are present in the calcium silicate hydrate structure, since the amount of alumina in the amorphous hydraulic binder is very low (see Table 6-1) and any contribution to the ^{29}Si MAS NMR spectra was considered negligible for the sake of easiness in the deconvolution process.

Table 7-2. ^{29}Si MAS NMR spectra deconvolution results and mean chain length values calculated from the method proposed by Richardson et al. [84].

Sample	Si molar %							R^2	MCL
	Q^0 amorphous	Q^1 C-S-H	Q^1 amorphous	Q^2 pseudowollastonite	Q^2 C-S-H	Q^2 amorphous	Q^3 amorphous		
Anhydrous	8,98		29,23	12,51		38,04	11,23	99,7	
Non activated	3,33	5,23	26,38	15,18	5,23	37,9	6,75	99,7	4,0
Na_2CO_3	2,57	4,81	17,51	13,83	13,41	41,04	6,83	98,9	7,6
Na_2SiO_3	1,42	11,21	12,25	14,58	18,01	37,34	5,18	99,6	5,2

Figure 7-10 shows the ^{27}Al MAS NMR spectra of the anhydrous amorphous binder as well as the pastes produced from it at 28 days of hydration. It can be seen a broad distribution of Al in both tetrahedra and pentahedral coordination in the initial anhydrous material, but no octahedral coordinated Al is visible. However, octahedral aluminum signal is present in all the pastes produced, especially in the non-activated one.

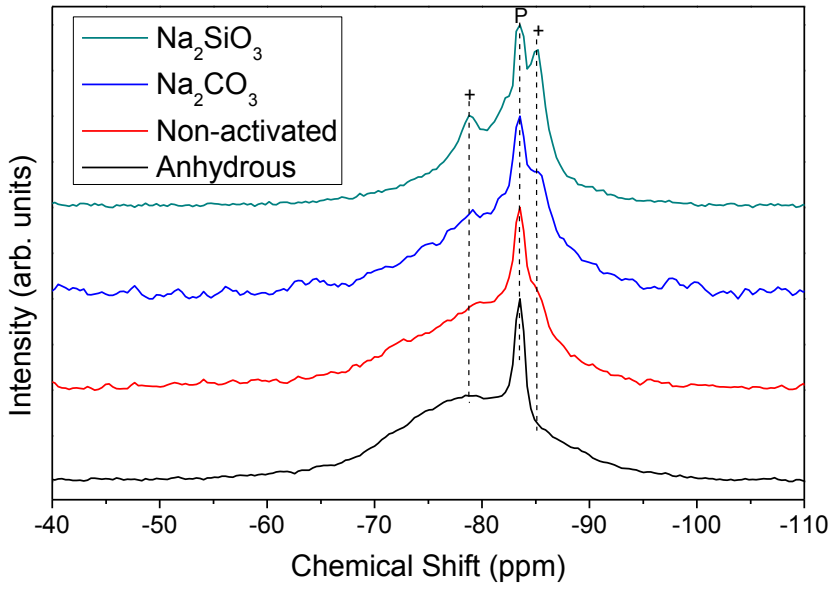

Figure 7-5. ^{29}Si MAS NMR spectra of the pastes at 28 days activated with Na_2SiO_3 (green) and Na_2CO_3 (blue), as well as the non-activated paste (red) and the corresponding precursor anhydrous material of all the pastes prepared (black). The signals corresponding to pseudowollastonite and C-S-H(I) are identified in the plot as *P* and *+*, respectively.

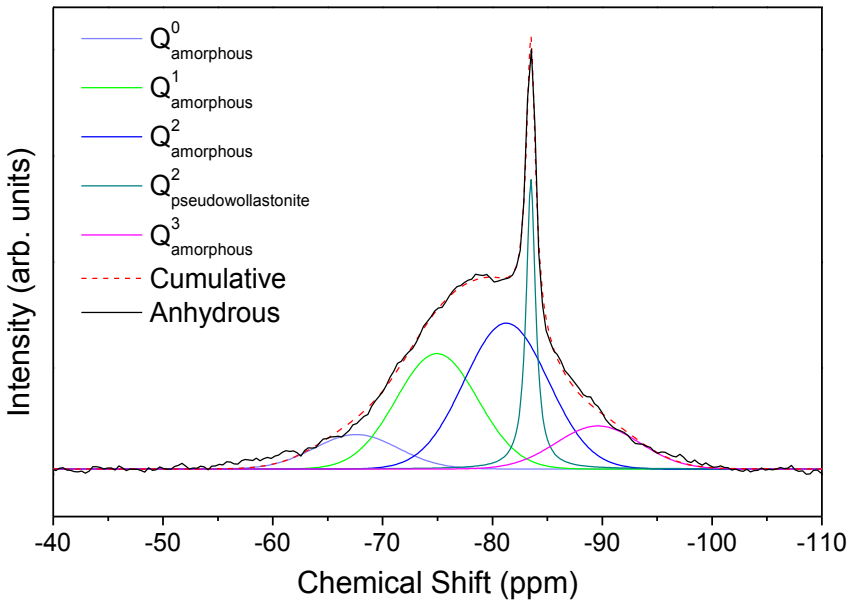

Figure 7-6. Deconvoluted ^{29}Si MAS NMR spectra of the anhydrous sample.

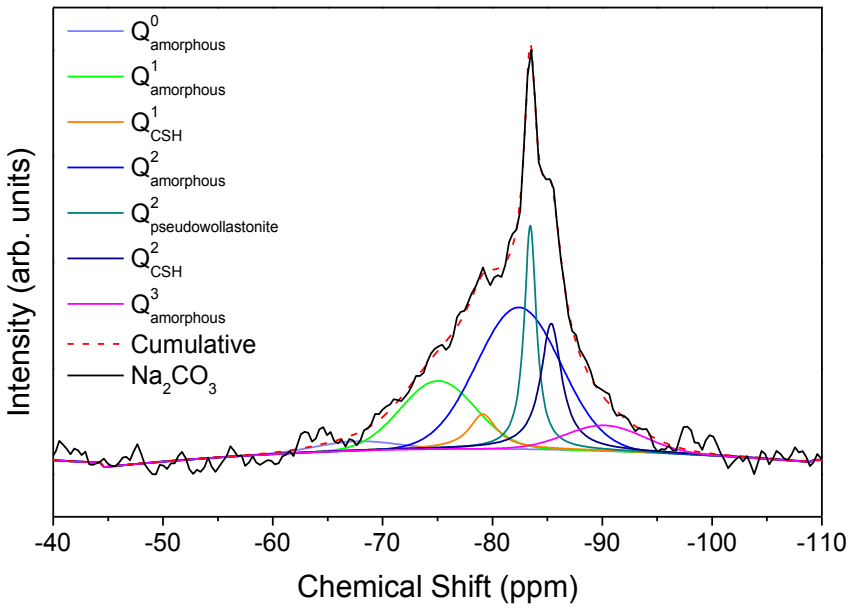

Figure 7-7. Deconvoluted ^{29}Si MAS NMR spectra of the 28 days Na_2CO_3 activated paste.

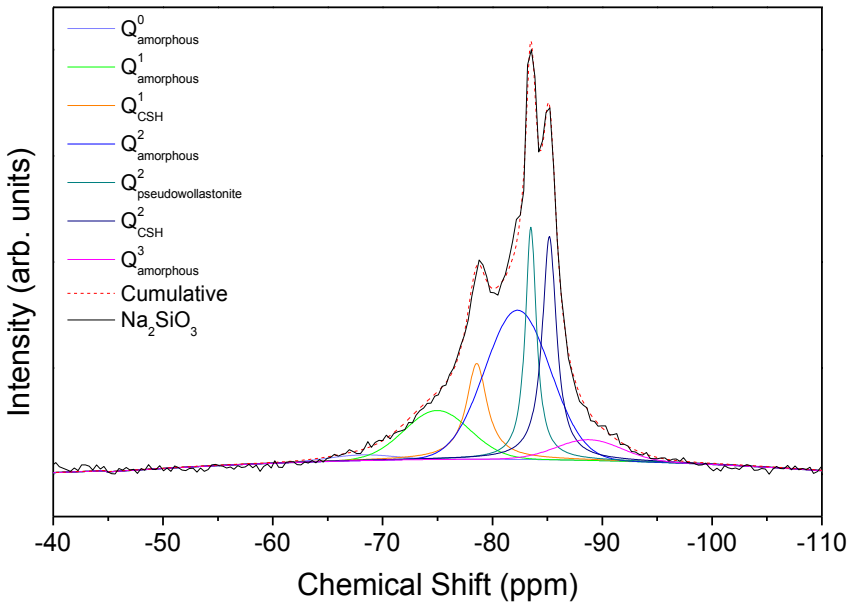

Figure 7-8. Deconvoluted ^{29}Si MAS NMR spectra of the 28 days Na_2SiO_3 activated paste.

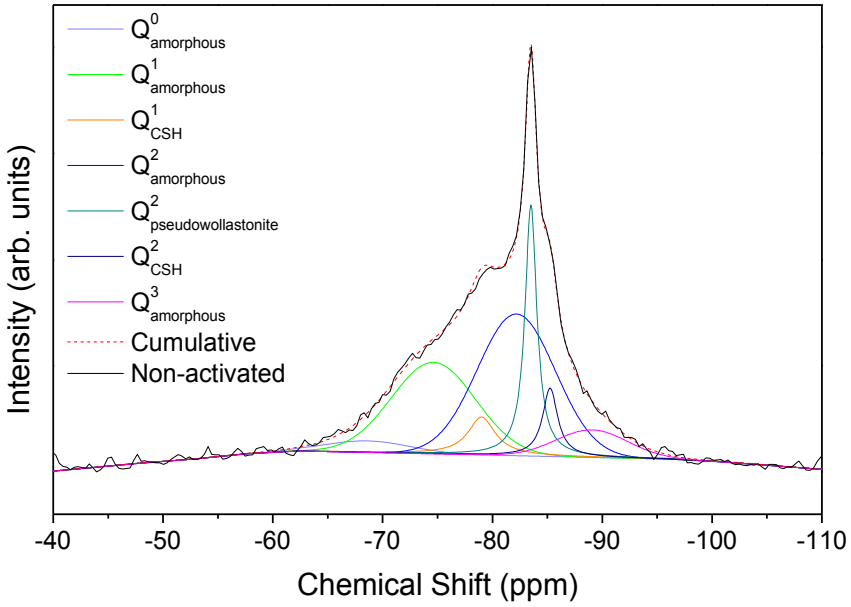

Figure 7-9. Deconvoluted ^{29}Si MAS NMR spectra of the 28 days non-activated paste.

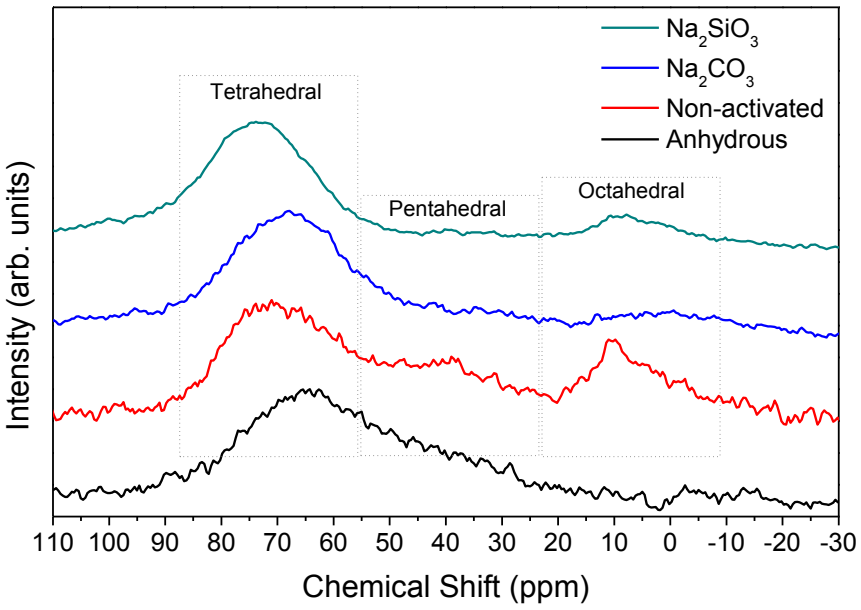

Figure 7-10. ^{27}Al MAS NMR of the anhydrous hydraulic binder and the corresponding 28 days pastes produced with and without alkaline activation. Regions corresponding to different Al coordination signals are identified in the plot as: Tetrahedral - Al[4]; Pentahedral - Al[5] and Octahedral - Al[6].

7.2.5 Thermogravimetry analysis

The pastes activated with Na_2CO_3 and waterglass, as well as the non-activated paste, were analyzed via thermogravimetry in order to determine the amount of bound water related to the hydrated phases. As the results obtained by XRD pointed out, Tobermorite-like phases seemed to be formed during hydration of these materials, as it was already observed for the amorphous hydraulic binders with C/S molar ratios of 1.1 and 1.25 studied in chapter 6, allowing us to consider that the total amount of weight loss in the temperature range from 105ºC to 500ºC would return a very good estimation of the total bound water in the pastes produced. This range of temperatures falls within the region on which the water loss of C-S-H is expected to occur, in agreement to other works where thermogravimetric studies of several cement types were performed, including in alkali activated pastes [129-132, 155, 156].

Figure 7-11 presents the values of bound water in the pastes produced as determined by TGA at the ages of 28 and 90 days. Also depicted in

Figure 7-11 are the values of bound water obtained in Samples A and B from the study presented in this work in chapter 6. It can be observed that the alkali activated samples present higher amounts of bound water when compared to the non-activated samples, which seems to be linked to the strength development registered for these cementitious systems.

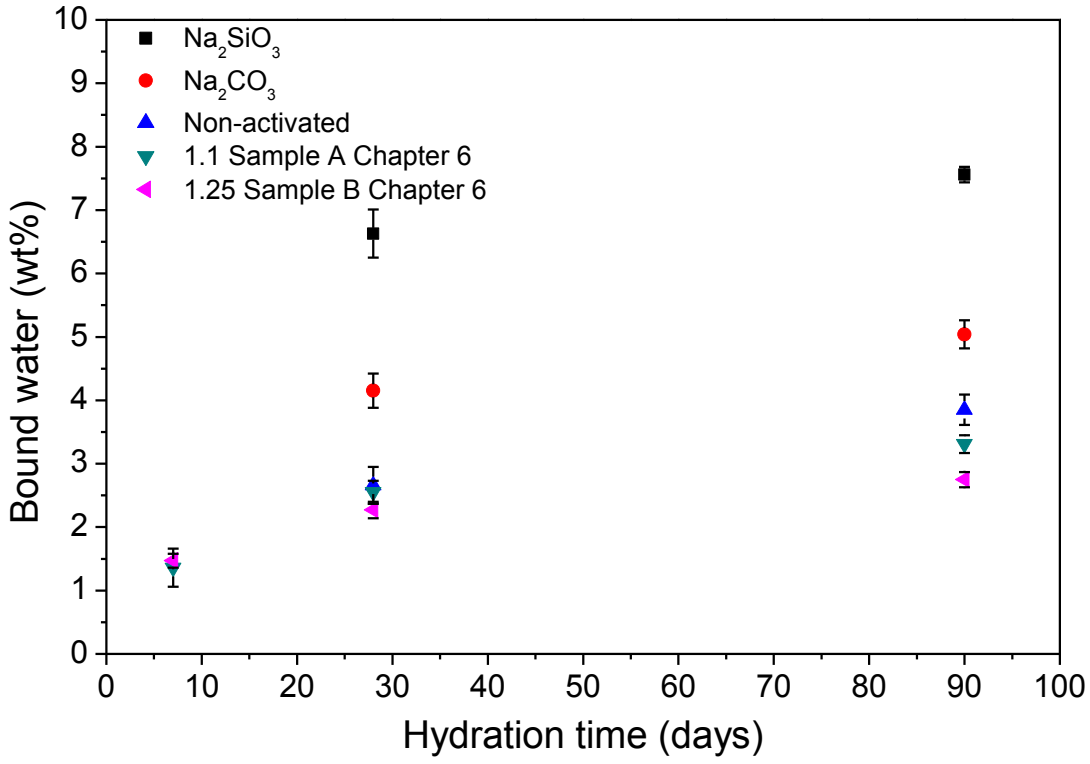

Figure 7-11. Comparison between the bound water evolution with time for the pastes prepared in this study and also for the two other pastes studied in chapter 6.

7.2.6 Isothermal Calorimetry

The pastes inserted into the vials for the calorimetric measurements were prepared using the same procedure used in the preparation of the pastes analyzed in this chapter, being this description given in section 7.1. The hydration heat evolution of three different samples is given in Figure 7-12.a).

As pastes preparation was performed ex-situ, a delay in the introduction of the samples in the equipment occurred, thus it was not possible to observe the first exothermic peaks corresponding to the wetting of slag and cement particles, neither the initial reaction period in the reference OPC sample.

Apart from the absence of the initial reaction peak, the reference OPC sample presented a typical isothermal calorimetry profile, where it can be seen the acceleration and deceleration periods corresponding to the nucleation and growth of hydration products, with the maximum of this peak occurring at around 8 hours of hydration.

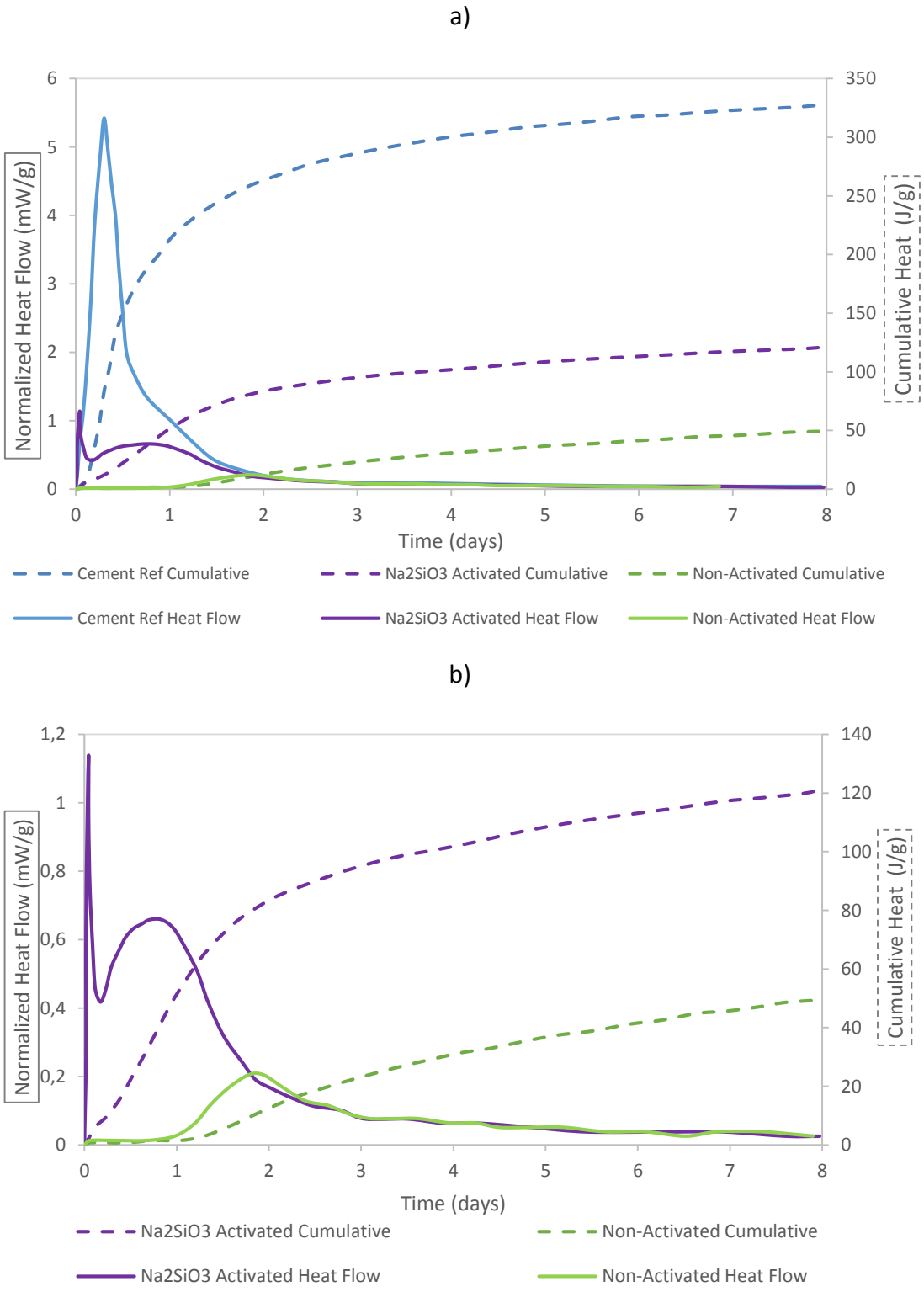

Figure 7-12. a) Comparison of the isothermal calorimetry curves obtained for the reference cement sample and the amorphous samples with sodium silicate activation and without activation. b) Detail of the Na_2SiO_3 activated and non-activated samples, rescaled to better observe the phenomena occurring during the hydration of these two samples.

Figure 7-12.b) shows the results of isothermal calorimetry obtained for the Na_2SiO_3 activated and non-activated sample in a proper scale, which allows to better analyze the hydration behavior of these samples. Regarding the non-activated sample, it was registered a dormant period that lasted for about 24 hours until some heat activity was observed. Then an increase in the heat released occurred until about 46 hours of hydration, reaching its maximum by this time. From this point a decrease in the heat flow was observed, continuing to slowly reduce its value until the 8th day. This behavior is similar to the observed in systems of water + slag, using slags characterized by C/S molar ratios values comparable with the ones used in this study [157-159].

The activated sample, however, presented a very different hydration behavior, starting from the presence of an initial reaction peak that overlaps with a broader signal that presents its maximum at approximately 20 hours of hydration, followed by a period of slow heat flow decrease.

7.3 Discussion

The compressive strength results showed that the alkaline activators played a very important role in the development of early age strength, catalyzing the hydration process. The alkaline solution prepared with commercial sodium silicate and sodium hydroxide presented a more effective impact in the hydration kinetics of this amorphous hydraulic binder with C/S molar ratio of 1.1 when compared with the solutions of sodium carbonate and sodium sulfate, which however achieved very interesting values, especially at older ages, revealing a continuous compressive strength improvement with time while the paste activated with waterglass showed a very fast compressive strength growth stabilizing its value around 77 MPa from the 28 days on. Some compressive strength values taken from literature are compiled in Table 7-3 for a better comparison of different alkaline activated slags systems already studied. There were only considered systems of activated slags in this comparison because of the bigger similarities with the amorphous material studied in this work in terms of chemical composition (specially the C/S ratio) and the very high amount of amorphous phase typically present in blast furnace slags. Other alkaline activated amorphous systems, such as the ones containing fly-ash have deserved some attention from many authors [135, 160-163], however they are chemically characterized as having high amounts of alumina in its composition (usually over

20%wt), with their reactivity and types of hydration products formed being highly dependent on the Si/Al ratio.

Table 7-3 contains also some information that was already presented in Table 6-5 since the systems described and their respective compressive strength values were considered to be appropriate to be compared with the results obtained in this study.

The values of compressive strength obtained for the activated pastes studied in this chapter are within the values presented in the literature for similar activated glassy systems, even though some differences in the water to binder ratio or in the fineness of the powders used might exist, which are factors that are known to affect the strength of alkali-activated pastes [164, 165]. However the values obtained for the non-activated pastes were found to be higher than the ones presented in the works of Jin et al. [133] and Gruskovnjak et al. [166] for non-activated slag pastes with similar water/solids ratios. This behavior may be attributed to a higher intrinsic reactivity of the amorphous calcium silicate binder produced in this work when compared to typical blast furnace slags, being this effect dissipated by the presence of alkaline activator that rapidly trigger the dissolution and nucleation and growth phenomena in these systems.

The compressive strength evolution for all the pastes produced seems to be correlated with the phase development identified by Rietveld analysis, namely with the formation of the calcium silicate hydrate phase with regions containing Tobermorite-like structures. In fact, apart from this semi-crystalline C-S-H and calcite, in the case of the sample activated with $NaCO_3$, no other hydration products were identified, although in other alkali-activated glassy systems some Gaylussite was detected, when using $NaCO_3$ activator, or even the presence of Hydrotalcite and AFm was reported [84, 149, 167-170], especially when the alkali-activating solution was composed just of sodium hydroxide or in a mixture with waterglass. However, the SCM's considered in the studies mentioned are richer in Al_2O_3 and MgO content than the systems studied in this work and in addition to the formation of the referred crystalline phases also some differences can be found in the hydrated gel since some aluminum end up being incorporated in their structures, resulting in the formation of complex C-A-S-H gels. Still in the particular case of the study developed by Richardson et al. [84], the approach of synthetically produce a glassy material with a similar GGBFS composition (with a Ca/Si = 1.1) lead to a hydrated paste containing C-S-H type I (i.e. Tobermorite-like structure) with a Ca/Si ratio very close to the precursor glassy material, as well as some Hydrotalcite, but no AFm phase was

present. Knowing this and observing the results obtained in this work, it is strongly suggested that the semi-crystalline C-S-H formed by the reaction of the amorphous hydraulic binder produced in this study would have a Ca/Si ratio close to the original values, i.e. around 1.1.

Table 7-3. Reference values for the mechanical performance of studied alkali-activated systems, including pastes prepared from commercial slags, fly ash and mixtures. Strength, activators used and water to binder ratios are indicated for comparison with the amorphous hydraulic binders produced in this work.

Molar C/S *Slag*	Strength (MPa) 7 days	28 days	90 days	Activator	Observations	Source
1.16	~1	~6	~14	No activator	Pastes of 40mm cubes. W/C=0.32.	Jin et al. [133]
1.31	13	24	---	No activator	Paste W/C=0.3	Gruskovnjak et al. [166]
1.16	~21	~35	~45	4%wt Na_2CO_3	Pastes of 40mm cubes. W/C=0.32.	Jin et al. [134]
1.24	~33	~44	---	NaOH/Na_2CO_3 (5%wt Na_2O)	Pastes of 1x1x6 mm^3 prisms W/C=0.4.	Puertas et al. [86]
1.24	~77	~84	---	Waterglass (SiO_2/Na_2O=1.2 5%wt Na_2O)	Pastes of 1x1x6 mm^3 prisms W/C=0.44.	Puertas et al. [86]
1.21	---	~80	~85	Waterglass (SiO_2/Na_2O=1 5%wt Na_2O)	Pastes of 50mm cubes W/C=0.28	Diaz et al. [149]
1.21	---	~85	~100	Waterglass (SiO_2/Na_2O=1.5 5%wt Na_2O)	Pastes of 50mm cubes W/C=0.28	Diaz et al. [149]
1.22	~20	~30	---	NaOH (2.4%Na2O by mass of solids)	Pastes of 20mm cubes. W/C=0.35.	Tanzer et al. [136]
1.44	~40	~78	---	Waterglass (SiO_2/Na_2O=2.4 5%wt Na_2O)	Pastes of 30mm diameter cylinders, 60mm height. W/C=0.23	Bernal et al. [171]
1.14	~32	~46	~56	5%wt Na_2CO_3	Pastes of 40mm cubes. W/C=0.31	Abdalqader et al. [172]
0.80	**---**	**0.0**	**0.0**	**No activator**	**20x20x40 mm3 Prisms. W/C=0.375**	**This work Chapter 6**
1.10	**6.8**	**32.2**	**45.4**	**No activator**	**20x20x40 mm3 Prisms. W/C=0.375**	**This work Chapter 6**
1.25	**7.5**	**23.8**	**33.2**	**No activator**	**20x20x40 mm3 Prisms. W/C=0.375**	**This work Chapter 6**
1.10	***6.6***	***35.0***	***46.4***	***No activator***	***20x20x40 Prisms. W/C=0.375.***	***This Chapter***
1.10	***42.2***	***77.7***	***76.9***	***Waterglass (3%wt Na_2O and SiO_2/Na_2O=1.2)***	***20x20x40 Prisms. W/C=0.375.***	***This Chapter***
1.10	***18.3***	***45.3***	***62.9***	***Na_2CO_3 (3%wt Na_2O)***	***20x20x40 Prisms. W/C=0.375.***	***This Chapter***
1.10	***---***	***41.0***	***68.3***	***Na_2SO_4 (3%wt Na_2O)***	***20x20x40 Prisms. W/C=0.375.***	***This Chapter***
1.10	***---***	***36.0***	***48.6***	***+ 10% Clinker***	***20x20x40 Prisms. W/C=0.375.***	***This Chapter***

XRD results show a peak identified as belonging to a Tobermorite-like phase at around 8º that is characteristic of the C-S-H basal lattice spacing and corresponds to a d_{001} around 11.3Å which is in agreement with the range of values presented in the work of Sun et al. [173], for a C-S-H with a Ca/Si= 1.1 and an Al_2O_3 content below 1% in weight, or in the work of Cong et al. [37], for a C-S-H with a Ca/Si of 1.32 prepared from the reaction of pure CaO with silica fume. This basal spacing value also correlates very well with the model calculated in a recent work of Richardson [46] and from which was taken the basis for the calculation of the amount of C-S-H produced in the alkali-activated pastes studied.

Regarding FTIR results, it is evident the presence of the carbonate group in the paste prepared with Na_2CO_3, whereas, in the other pastes, negligible or inexistent signal was detected for this group, which correlates very well with the phase quantification performed by Rietveld analysis where the presence of calcite was only detected in the paste activated with sodium carbonate. In fact, the amount of CO_3^{2-} added by the introduction of Na_2CO_3 in the solution explains by itself the total amount of $CaCO_3$ formed and determined by Rietveld in the 28 days paste, thus leading to believe that the presence of calcite in this paste is a direct effect of the type of activator used, since it was not identified any calcite in the other pastes.
The band present at 660 cm^{-1} seems to become better defined after 28 days of hydration, indicating a higher amount of Si-O-Si bonds, whereas the bands at 850 and 900 cm^{-1}, attributed to Q^0 and Q^1 units, present an opposite trend, thus revealing the occurrence of polymerization, through the connection of these monomers and dimers, during the hydration of the studied amorphous hydraulic binder. Furthermore, it was also detected a narrowing of the band around 490 cm^{-1} accompanied by a shift to lower frequencies, confirming the formation of more condensed tetrahedral species [170].

The results obtained by ^{29}Si MAS NMR show a decrease in the amount of Q^0 and Q^1 units upon hydration in the pastes produced, revealing that these are the preferential units to combine and form the calcium silicate hydrate. This phenomena had already been observed in the previous chapter and correlates very well with the structural information collected with FTIR in this study, however, under activation of alkaline solutions, the consumption of the Q^0 and Q^1 units occurs much faster, giving rise to the formation of a larger quantity of hydration products, as it can be seen, especially, in the pastes produced with Na_2SiO_3.

The results obtained by ^{27}Al MAS NMR show that the signal related to the presence of 4-fold coordinated aluminum narrows upon hydration in all samples, suggesting that some of the aluminum might be present in a more ordered structure such as the one of the C-S-H produced with a semi-crystalline nature resembling a Tobermorite-like structure. The presence of the signal corresponding to the octahedral aluminum is also evident in all samples, especially in the non-activated and in the waterglass activated samples, whilst the band assigned to the 5-fold coordinated aluminum is particularly visible in the non-activated sample. According to Faucon et al. [174], aluminum in tetrahedral coordination preferentially substitutes silicon in non-bridging positions when the tetrahedral sheet is formed by linear silicate chains, but as the rupture of these chains takes place by the increase of the Ca/Si ratio the redistribution of aluminum in the tetrahedral sites occurs. For even higher values of Ca/Si, Al^{3+} substitutes calcium in the interlayer space and in the octahedral sheet as 5- and 6-fold coordinated aluminum, respectively.

From this information we can correlate the results of MCL presented in Table 7-2 and propose a trend for the Ca/Si ratio obtained in the pastes produced as follows:

Non-activated > Na_2SiO_3 > Na_2CO_3, since the Ca/Si is expected to decrease with increasing MCL and therefore with increasing Al[4] presence in the C-S-H structure.

According to the recent works of Qomi et al. [40] and Richardson [46], a calcium silicate hydrate with a Ca/Si around 1.1 should have a characteristic mean chain length close to 5, which is in agreement with the results obtained in this study by deconvolution of the ^{29}Si MAS NMR spectra of the pastes prepared with water and with a solution of sodium silicate. This value is also in good agreement with both the values of MCL obtained in the work of Chen et al. [38], where a series of synthetic C-S-H phase was prepared as well as with the MCL value presented in a work of Richardson et al. [84] for the C-S-H obtained from the hydration of a synthetic glass-slag with a Ca/Si ratio of 1.1, although in this case a higher amount of alumina was present (~11,0%). Yet, the calculation of the MCL of the paste prepared with the Na_2CO_3 solution returned a value above 7, indicating the formation of a calcium silicate hydrate with a lower Ca/Si. The higher values of MCL in the activated pastes, when compared to the non-activated one, may rise from two different reasons; in the case of the paste activated with waterglass, the MCL value obtained is slightly higher than the obtained for the non-activated paste probably due to the incorporation of silicon ions from the sodium silicate solution in the C-S-H structure, whereas the higher difference in the MCL value registered in the paste

activated with Na_2CO_3 may be explained by the production of some calcite during hydration through the consumption of Ca^{2+} ions present in solution.

Isothermal calorimetry results suggest different kinetics in the formation of C-S-H species when considering the waterglass-activated and the non-activated samples. In the case of the non-activated sample, the pH in solution is not expected to be high enough to break the Si-O bonds, thus probably only dissolution of Ca^{2+} occurs in the initial period, since the Ca-O bonds are much weaker than Si-O. A slow increase in the pH of the solution is thought to occur due to the absorption of H^+ by the Si-rich framework, thus resulting in an increase of OH^- concentration that, when reaching a high enough value, may start breaking the Si-O bonds, making $[SiO_4]^{4-}$ units available to react with Ca^{2+} in solution and to form C-S-H gel [149, 157, 175]. The isothermal calorimetry profile observed for the non-activated amorphous binder is somehow different from the reported for mixtures of blast furnace slag and water, showing evidence of its hydraulic behavior in contrast to the pozzolanic nature of typical slag. While in systems containing blast furnace slag and water only a very small initial heat peak ascribed to the wetting of the slag particles is usually identified, in the case of these new amorphous hydraulic binders it can be clearly seen an exothermic broad peak after the 24 hours of hydration that is related to the onset of the production of C-S-H gel. It is the production of this C-S-H gel that further leads to the development of strength in pastes prepared with these amorphous binders and water, while pastes made from slag and water do not usually set and harden, even when cured at 50ºC [175].

Regarding the waterglass-activated sample, it was verified the occurrence of several phenomena in simultaneous as it is evidenced by the overlapping of exothermic peaks in Figure 7-12.b). The initial more intense and sharper peak is related to the production of "primary C-S-H" that is obtained by the reaction of the Ca^{2+} from the slag and the pre-dissolved $[SiO_4]^{4-}$ anions from the activator [149, 157, 175]. Also a very active period of dissolution is very likely to occur due to the action of the alkalis in solution, which increase the pH of the environment to the point where Si-O bonds are broken and $[SiO_4]^{4-}$ species are released into solution. The increase in the concentration of $[SiO_4]^{4-}$ species combined with the presence of Ca^{2+} results in the simultaneous production of more C-S-H. Actually, the end of the sharp peak coincides with the initial development of a broader heat flow signal related to the phenomena

of nucleation and posterior growth of new C-S-H phase, without being noted any induction period between the two peaks.

The information collected by ^{29}Si MAS NMR, FTIR and Isothermal Calorimetry allow the estimation of a reaction mechanism for these amorphous hydraulic binders that seems to be similar to the observed in the reaction of some aluminosilicate based SCM's. In the Figure 7-13 below it is depicted a schematic of the main stages considered to occur during the formation of the semi-crystalline C-S-H, from the reaction with water or under alkaline activation of the amorphous hydraulic binders studied in this chapter.

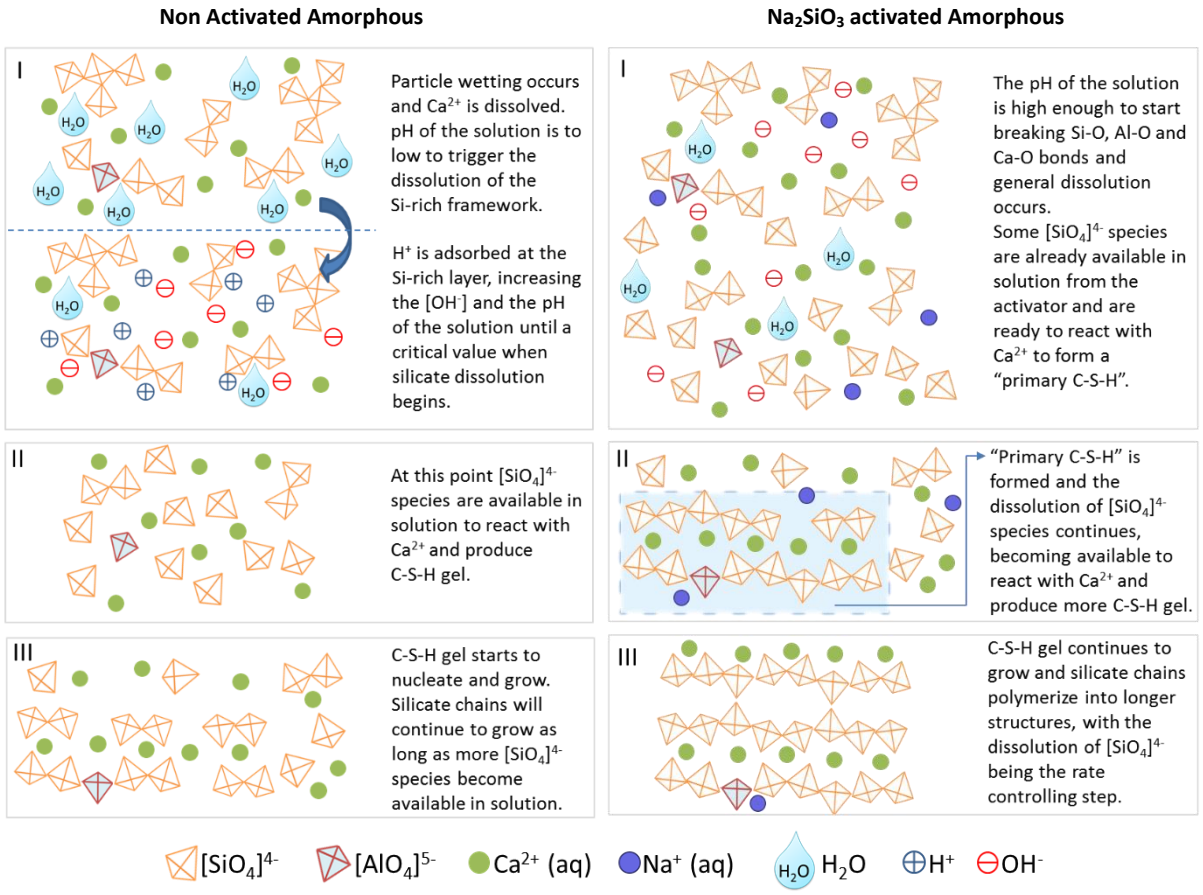

Figure 7-13. Resume of the amorphous hydraulic binders reaction mechanism. A schematic of the main stages taking place during the formation of the semi-crystalline C-S-H gel is shown. Silicon and aluminum are shown as $[SiO_4]^{4-}$ and $[AlO_4]^{5-}$ groups in their tetrahedral coordination, respectively, while calcium and sodium are represented as aqueous ionic species.

The stages represented in Figure 7-13 can be described as:

Non-activated sample:

Stage I – Initially, only wetting of the amorphous binder particles occurs. Then some dissolution of Ca^{2+} species takes place, since the Ca-O bond is much weaker than the Al-O and Si-O bonds, leaving an essentially Si-rich layer in the surface of the particles. The Si-rich layer formed may adsorb some H^+ in the water which results in the increase of OH^- and consequently the pH of the solution. When the pH of the solution achieves a critical value some Si-O bonds start to break and some $[SiO_4]^{4-}$ and $[AlO_4]^{5-}$ species become available in solution [157].

Stage II – The pH of the solution is now high enough to break the Si-O and Al-O bonds, thus $[SiO_4]^{4-}$ and $[AlO_4]^{5-}$ species become available in solution At this point only dissolution occurs and some isolated tetrahedra of $[AlO_4]^{5-}$ and $[SiO_4]^{4-}$ become available in solution. It should be noted however that the amount of Al in the amorphous hydraulic binders tested in this work is very low when compared to typical SCM's so the concentration of Al^{3+} in solution is considerably lower than the normally observed in the hydration of fly-ash or GGBFS, for instance. As the concentration of these anionic species increase, they start to react with the available Ca^{2+} and C-S-H precipitates, coinciding with the onset of the acceleration period registered by isothermal calorimetry, which occurs at around 24 hours of hydration.

Stage III – Nucleation and growth of C-S-H proceeds, with the dissolution of $[SiO_4]^{4-}$ and $[AlO_4]^{5-}$ species being the rate controlling step.

Na_2SiO_3 activated sample:

Stage I - In the case of the alkaline activation, the pH of the solution rapidly grows above the critical value and not only the Ca-O but also the Al-O and Si-O bonds are promptly broken, leading to a more abundant availability of $[SiO_4]^{4-}$ and $[AlO_4]^{5-}$ species. Furthermore, in the particular case of Na_2SiO_3 activation, the $[SiO_4]^{4-}$ species become readily available from the activator source.

Stage II – "Primary C-S-H" is formed from the reaction of the Ca^{2+} in solution with the available dissolved $[SiO_4]^{4-}$ species from the activator. This step corresponds to the first sharp peak registered in the isothermal calorimetry experiment, occurring in the first minutes of hydration. Then, as $[SiO_4]^{4-}$ and $[AlO_4]^{5-}$ species rapidly dissolve due to the activation effect, more C-S-H is produced. This second step is related to the broader peak registered in the isothermal calorimetry experiment. The formation of C-S-H now proceeds at a lower rate since

the pre-dissolved $[SiO_4]^{4-}$ species from the activator extinguished and is now dependent on the dissolution rate of the anionic species. Q^1 and Q^2 groups of begin to form in linear silica-based chains. Aluminum may occupy some positions in the linear chains, specially replacing Si in bridging sites of the *dreierketten* structure.

Stage III – The growth of C-S-H continues to occur with the formation of sandwiched structures, leading to an increase of the Q^2/Q^1 ratio as the chains become longer. Aluminum will continue to replace Si in some positions in the chains and Na^+ may also balance the charge locally and enter the structure of the hydrated products.

Taking into account the values of bound water determined by TGA for the pastes prepared in this study, it was used a methodology similar to the one applied in chapter 6 for the estimation of the amount of C-S-H produced. It was considered the Eq. 2.6, valid for the analysis of severely dried pastes, to determine the stoichiometry of the average C_xSH_y produced upon hydration, returning an *y* value of 0.82 for a fixed *x* value of 1.1, resulting in a stoichiometry of $C_{1.1}SH_{0.82}$. Then Eq. 6.2 and Eq. 6.3 were used to determine the amount of $C_{1.1}SH_{0.82}$ produced in each paste, with the values obtained being plotted against the corresponding compressive strength in Figure 7-14. Also depicted in Figure 7-14 are the values, calculated using the same methodology, from samples A and B studied in chapter 6. It can be clearly observed from Figure 7-14 that a very good correlation between the total C-S-H produced in each paste and their corresponding compressive strength exists, thus confirming that the development of strength in these pastes is strongly dependent on the production of the semi-crystalline calcium silicate hydrate phase.

In order to compare the values obtained for the weight percentage of C-S-H formed upon hydration in the pastes studied in this chapter as estimated by TGA and by XRD results, it was also estimated the amount of hydrated products formed from the results of the deconvolution of the ^{29}Si MAS NMR spectra. For this calculation the following assumptions were made:

1. the Si molar fractions, determined by deconvolution of the ^{29}Si MAS NMR spectra, assigned to the C-S-H phase were considered;
2. the stoichiometry of C_xSH_y was fixed as $C_{1.1}SH_{0.82}$, as determined by Eq. 2.6, in a similar approach to the one used for the calculation of the weight % of C-S-H using the results from TGA.

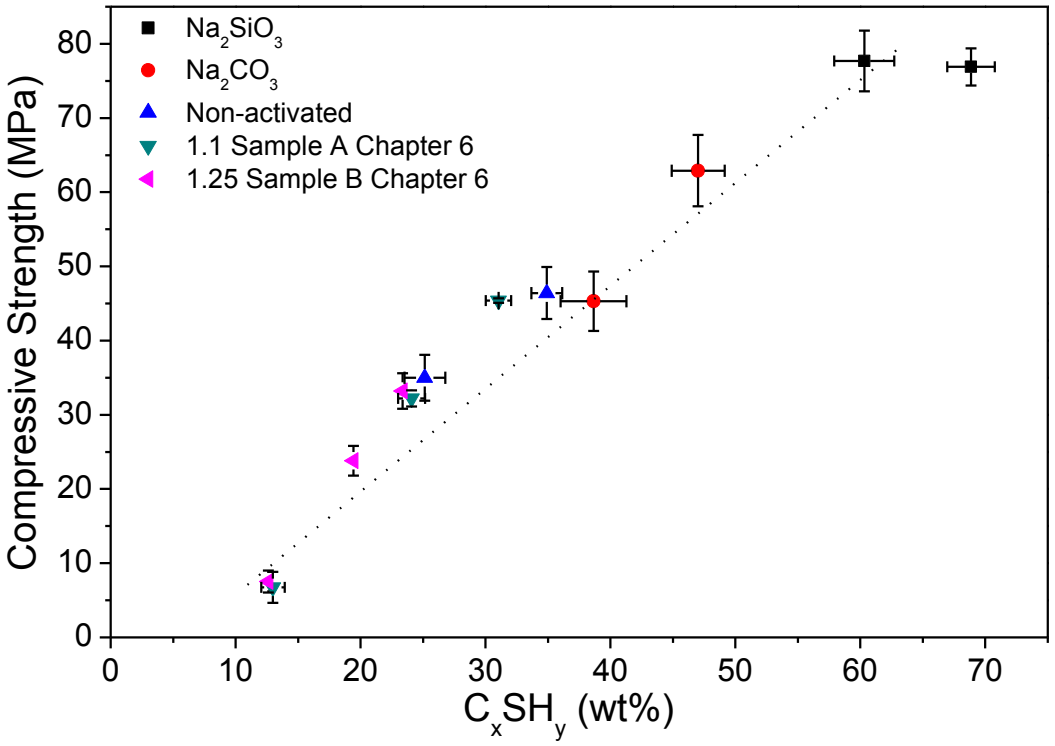

Figure 7-14. Plot of the calculated weight percentage of formed C-S-H versus the obtained compressive strength in the pastes produced in this work. Also plotted are some results obtained in a previous work from these authors. The dotted line is just a guide for the eye.

The resulting values are presented in Figure 7-15 along with the values of C-S-H weight percentages determined by XRD-Rietveld and by TGA. Also depicted in Figure 7-15 are the values calculated for the amorphous fraction of C-S-H, as the difference between the total amount of C-S-H formed (assumed to be the value corresponding to the estimation from TGA result) and the average value of the results obtained by XRD-Rietveld and ^{29}Si MAS NMR, as described by the following expression:

Eq. 7.2 $$wt\%CSH_{amorphous} = wt\%CSH_{TGA} - \left(\frac{wt\%CSH_{XRD} + wt\%CSH_{NMR}}{2} \right)$$

In the right axis of Figure 7-15 can be read the values corresponding to the relative amorphous percentages of C-S-H, which indicate amorphous fractions of C-S-H around 50% for all the pastes analyzed.

It is possible to observe from Figure 7-15 that the C-S-H weight fractions obtained by the techniques of XRD and ^{29}Si MAS NMR are very similar, however their values are much lower

than the ones obtained by TGA. This difference is thought to be related with the semi-crystalline nature of the C-S-H produced, whose constitution can be divided in a crystalline part and in an amorphous part. The crystalline fraction of the C-S-H produced should be very close to the values obtained both by ^{29}Si MAS NMR and XRD, while the value determined by TGA gives an estimation of the total amount of C-S-H present in the pastes. It is possible to observe from Figure 7-15 that the values of C-S-H obtained for the pastes of the two amorphous samples with C/S molar ratios of 1.1 studied (Sample A from chapter 6 and the non-activated sample from this chapter) are in very good agreement, as well as their corresponding compressive strength, regardless of the differences observed in the phase constitution of their respective precursor materials, namely the proportion between the glassy component and the crystalline Pseudowollastonite.

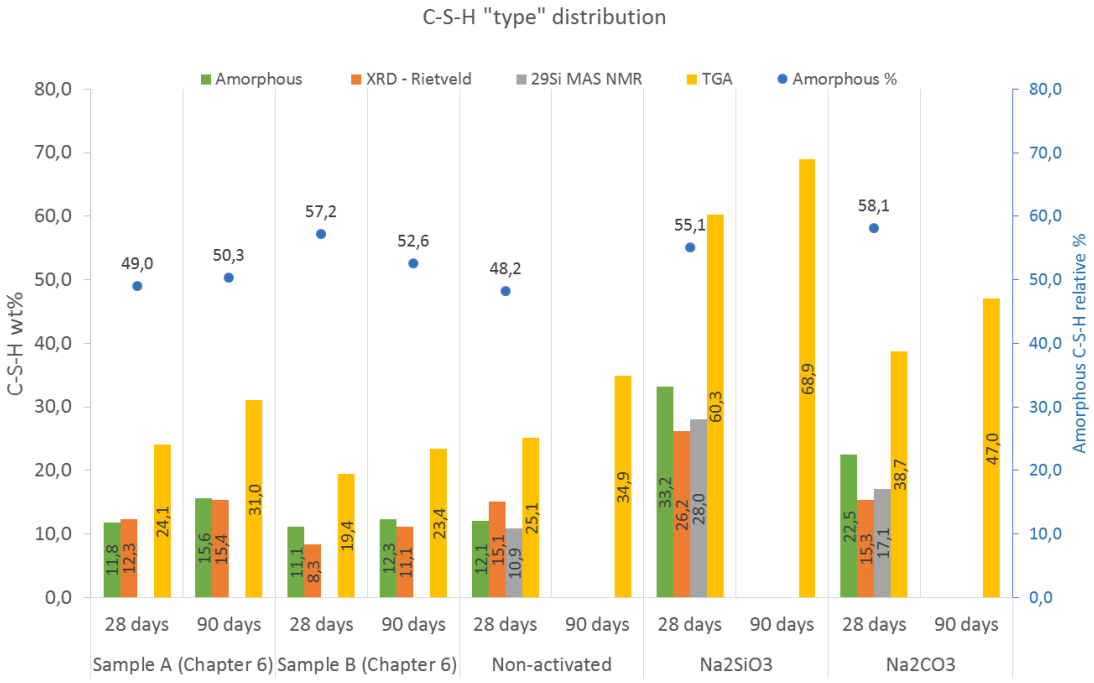

Figure 7-15. Values of C-S-H weight percentages obtained by the different techniques used in this work. The values presented for ^{29}Si MAS NMR were calculated from the corresponding Si molar fractions assigned to C-S-H. Values from TGA were calculated by assuming a $C_{1.1}SH_{0.82}$ stoichiometry, following the relation presented in the work of Richardson [46] for highly dried pastes. The values presented in the XRD column were taken directly from the Rietveld analysis results. The values of amorphous C-S-H wt% presented were estimated from Eq. 7.2. The relative percentage of the amorphous component of C-S-H is indicated as scattered blue circles.

A final remark is made with respect to the water consumption of these amorphous hydraulic binders that, due to their particularities in terms of reaction products, point to significant

reductions in water demanding in order to achieve a complete hydration. Taking $\boldsymbol{C_{1.1}SH_{0.82}}$ as the stoichiometry of the main hydration products estimated to be produced upon the hydration of the amorphous hydraulic binders with C/S molar ratio of 1.1, a water to solids ratio of 0.12 can be determined as the value with which a complete hydration can occur, in contrast with the higher values typically presented for the OPC system that ranges from 0.39 to 0.44 [176]. This translates into direct water savings in the production of concrete as well as a less porous structure is expected to be formed, leading to denser and less permeable structures that may develop better chemical resistance to a large type of aggressive environments.

In a posterior subset of experiments the activation of the endogenous amorphous phase in the dendritic clinkers (referred in chapter 5) was also attempted. Similar sample preparation and Na_2SiO_3 alkaline activation conditions were used in these experiments. A non-activated dendritic clinker reference paste was also produced. Some isolated results regarding compressive strength and phase development during hydration were acquired. The compressive strength results are plotted in Figure 7-16 together with the results already reported in chapter 5 for comparison. These results show that there is a very effective impact of the alkaline activator in the development of mechanical performance of these pastes, increasing the compressive strength by approximately a ten-fold factor at 28 days when compared to the non-activated pastes.

The phase development of these pastes was followed by XRD-Rietveld and the results obtained are compiled in Table 7-4 and Table 7-5. The former shows the results obtained for the anhydrous clinkers prepared, being possible to observe that, although the clinkers "*1.4-1*" and "*1.4 (Activation test)*" were obtained in different batches, their constitution is very similar. The latter presents the phase quantification of the respective 28 days activated and non-activated pastes prepared with the dendritic clinkers. Regarding the non-activated samples, both present similar mechanical properties and phase development, with their amorphous component increasing during hydration essentially due to the production of C-S-H gel. While in the case of the alkaline activated pastes it is possible to identify hydration products with a more crystalline character, resembling Tobermorite-like structures. This difference is certainly related to the amorphous phase activation by the presence of Na_2SiO_3, strongly indicating that the amorphous phase is responsible for the formation of semi-crystalline C-S-H, as it was also

observed in the fully amorphous binders. Furthermore, another evidence of the endogenous amorphous reaction, might be taken from the analysis of the strength development registered in the activated paste, whose substantial increase is very unlikely to be fully explained by the slight increase in belite consumption, when compared to the non-activated paste. Thus, it is possible that these hydrated dendritic clinkers might present a microstructure containing two types of C-S-H with different crystallinities and C/S ratios, with the C-S-H formed from the dendritic belite presenting a more amorphous nature and higher C/S ratios, while the endogenous amorphous phase gives rise to the production of semi-crystalline C-S-H with lower C/S molar ratios. However, this assumption will still need to be confirmed by further experiments.

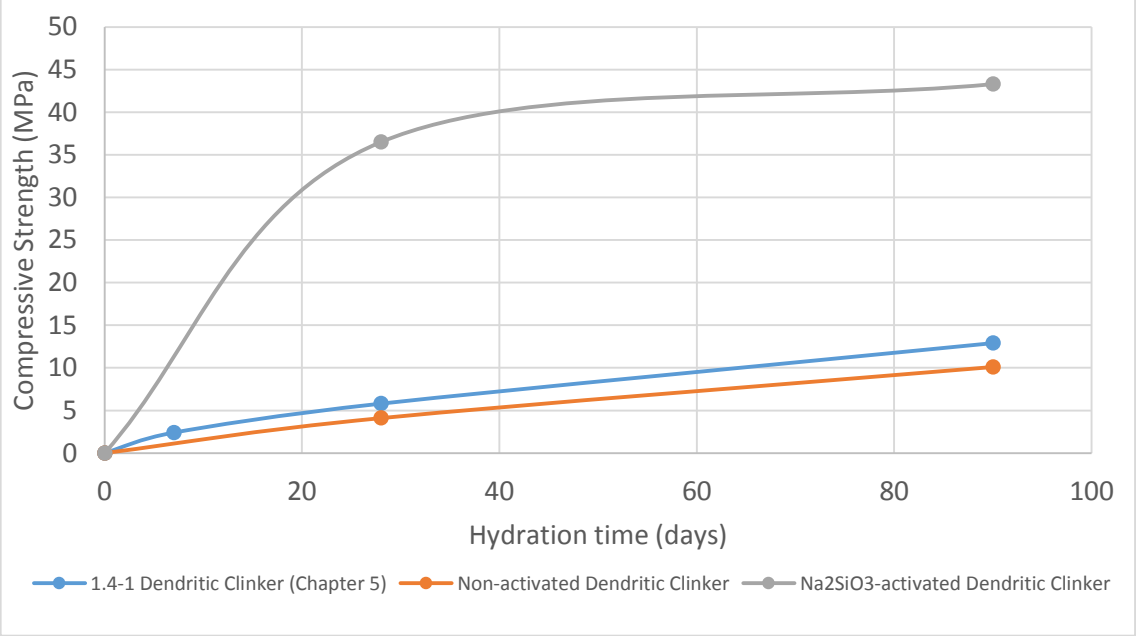

Figure 7-16. Compressive strength development obtained for the pastes produced from the dendritic belite clinkers with and without alkaline activation.

Table 7-4. Rietveld analysis and morphological features obtained in the anhydrous clinkers produced. The samples identified as "1.4-1" and "1.4 Activation test" were obtained by the same procedure but in different batches.

Sample		*1.4-1 Anhydrous*	*1.4 (Activation test) Anhydrous*
t_2 (min)		1	1
λ_2 (µm)		10	10
Rietveld Wt%	α'h-C_2S	8,6	9,9
	β-C_2S	36,2	36,0
	γ-C_2S	1,1	1,8
	Amorphous	54,1	52,3
	$CaFe_2O_4$	---	---

Table 7-5. Rietveld analysis of the dendritic clinker pastes with 28 days and the 35 days paste of the reference sample. The results presented in the last two columns refer to the dendritic clinker activation test. It is also indicated the water to binder ratio used in the preparation of the pastes.

		1.4-1 28 days	***1.4 Non-Activated 28days***	***1.4 Na_2SiO_3-Activated 28 days***
	w/b	***0.25***	***0.375***	***0.375***
Rietveld Wt%	**α'h-C_2S**	3,4	3,6	2,2
	β-C_2S	28,4	30,1	25,5
	γ-C_2S	0,7	1,6	1,0
	Amorphous	62,3	61,9	61,4
	Monohydrocalcite	3,1	1,1	0,5
	Calcite	2,1	0,8	1,3
	$CaFeO_4$			
	Tobermorite			8,0

7.4 Conclusions

Alkali-activated pastes of amorphous calcium silicate hydraulic binders were produced and found to present improved mechanical properties at all ages when compared to pastes prepared with water. The alkaline solutions increased the kinetics of the amorphous binder reaction allowing to develop initial strength competitive with typical OPC and even exceeding its results at 7 and 28 days. The addition of 10% in weight of clinker to the amorphous binder with C/S molar ratio of 1.1 did not present any considerable improvement in the strength development, thus leading to conclude that the addition of clinker in such amounts is not able to create favorable conditions for an effective activation of the amorphous hydraulic binder.

The hydration evolution of these pastes was also followed by XRD, FTIR, ^{29}Si and ^{27}Al MAS NMR and TGA. From the results obtained by these techniques, a C-S-H phase with a semi-crystalline nature was identified to be the main hydration product, with the crystalline part of this hydration product resembling Tobermorite-like structures. In addition, the development of this phase during hydration was found to be the main responsible for the mechanical properties in all the pastes prepared, with and without alkaline activation, as it is shown in Figure 7-14 where a very good correlation between these two parameters was identified.

The stoichiometry of the calcium silicate hydrate formed by the hydration of this new amorphous hydraulic binder was estimated to be around $C_{1.1}SH_{0.82}$, by using the relation between H/S and C/S proposed by Richardson in a recent study [46]. However some small differences in the stoichiometry might be present when varying the type of solution used for the hydration, as it was observed some differences in the values of mean chain length of the

C-S-H produced for the three situations studied. Pastes prepared with water revealed a lower MCL value, while the highest MCL was obtained for the pastes activated with Na_2CO_3.

The semi-crystalline nature of the C-S-H obtained lead to the determination of different weight % values by the techniques of XRD, ^{29}SI MAS NMR and TGA. The lower values obtained by XRD and ^{29}SI MAS NMR were attributed to the more crystalline fraction of the hydration product, whereas the total amount of C-S-H was considered to be the value calculated from TGA, which took into account the water weight loss between the temperatures of 105 and 500^{o}C. The amorphous fraction of the C-S-H obtained was estimated to roughly represent 50% of the total C-S-H.

The alkaline-activation experiments conducted on dendritic belite clinkers revealed a very effective impact of the Na_2SiO_3 activator in the compressive strength and phase development of the activated pastes. The initial kinetics of strength development strongly improved with the alkaline activator addition, until the 28 days of hydration, with further strength growth trend following similar rates for the non-activated and activated dendritic clinkers. Apart from a slightly higher belite consumption, the results obtained suggested that the activator triggered the reaction of the endogenous amorphous matrix of these clinkers, leading to the formation of semi-crystalline C-S-H similarly to the observed in the case of the fully amorphous binders.

8 Cooling Rate Effect on the Structure and Reactivity of Amorphous Hydraulic Binders

In this chapter the influence of the cooling conditions in some general properties of an amorphous hydraulic binder with a C/S molar ratio of 1.1 is analyzed. Four different cooling rates were tested in the production of the referred hydraulic binders and the resultant phase constitution was determined by XRD-Rietveld method with an estimative of a curve describing the "cooling rate versus final phase constitution" being attempted. The hydraulic behavior of the amorphous binders was followed through compressive strength and phase development and the differences observed were discussed. In addition, structural assessment was performed by FTIR and ^{29}SI MAS NMR spectroscopies. Hydration heat evolution of two samples obtained with distinct cooling rates was also followed by isothermal calorimetry during the first 8 days of hydration.

8.1 Materials and Experimental Conditions

For the production of the hydraulic binders studied in this chapter there were used the same raw materials already described in Table 4-1, in the proportions indicated by Table 6-1 in order to obtain a composition with a characteristic C/S molar ratio of 1.1. The production of the hydraulic binders with the composition described followed a process similar to the one presented in Figure 6-1 for all samples differing only in the cooling rate R_2 applied in step III of the process. To obtain the different cooling rates there were used four main distinct approaches: (i) allow the sample to cool inside the furnace with the door opened, which would render the slowest cooling condition, and (ii) remove the sample from the furnace and allow it to cool in air (static, non-forced), (iii) water immersion and (iv) liquid nitrogen immersion. It is important to differentiate these two last cooling conditions (water and liquid nitrogen immersion) from the usual slag granulation process where the liquid slag is directly poured into water and direct contact between water and the melt occurs. In these laboratorial processing conditions the cooling was achieved by just immerging the crucible containing the melt in water and liquid nitrogen, avoiding direct exposure of the amorphous binder to any of the tested media. The use of these cooling conditions diminishes the probability of the occurrence of any primary hydraulic reaction, keeping intact the hydraulic potential of the

produced amorphous samples, since, contrarily to granulated blast furnace slag, these amorphous materials present considerable hydraulic activity rather than only pozzolanic behavior.

The cooling rate R_2 was measured by using a type K thermocouple directly into the melt immediately after the removal of the crucibles from the interior of the furnace, in the case of the air-, water- and nitrogen-cooling experiments, while in the furnace-cooling experiment the thermocouple was only inserted into the melt after the furnace temperature reached 1350^{o}C. Figure 8-1 captures one of the moments during the measurement of the cooling rate.

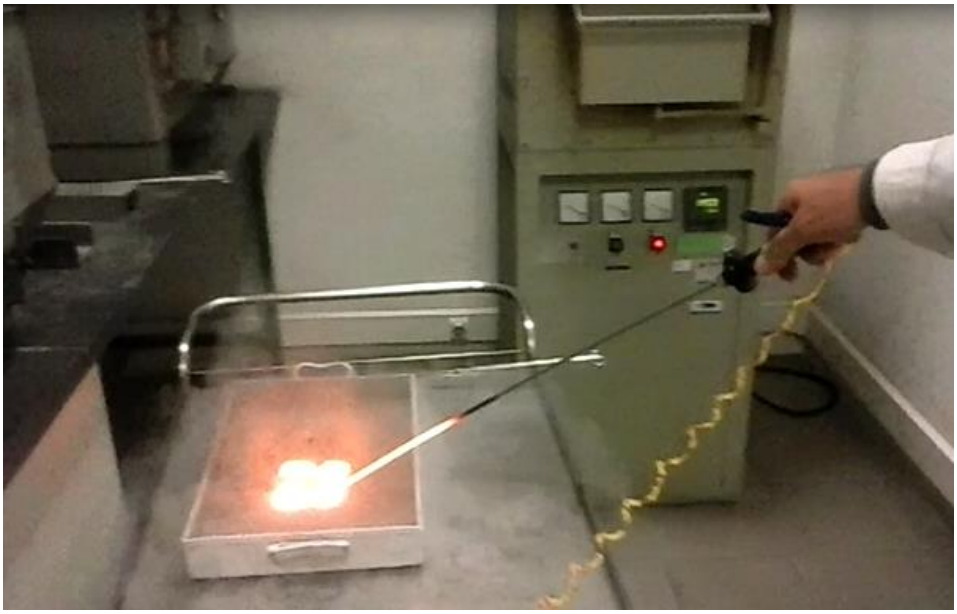

Figure 8-1. Method used for the measurement of the cooling rate during the production of the samples studied in this chapter. This particular image was recorded during the nitrogen cooling experiment.

As it was expected, the rate R_2 differed with the conditions used to cool the melts from the 1500^{o}C, being the cooling path depicted in Figure 8-2, where there are identified the cooling curves corresponding to the water-, air-, nitrogen and furnace-cooled samples.

The values of the cooling rates achieved by cooling in water, nitrogen, air and furnace conditions were estimated to be around 30, 18, 10 and 2^{o}C/s, respectively, within the temperature range between 1500^{o}C and 700^{o}C. It was estimated the 700^{o}C as the critical temperature for the amorphization of the melt, considering that below this temperature only mechanisms of solid diffusion can occur, since the reported glass transition temperature for a pure calcium metasilicate system is around 750^{o}C [177], thus being expected a limited

occurrence of any crystallization process below this temperature. The use of liquid nitrogen to cool the molten material from the 1500ºC was firstly thought as an experiment that would create the most extreme cooling condition possible and establish the ultimate case scenario of rapid cooling, however, although the equilibrium temperature of liquid nitrogen is approximately -196ºC, it didn't reveal to promote a cooling condition as effective as it was registered for water since its capacity to absorb heat is limited to a very short period. The main reason to its lack of efficiency as a cooling medium lays in the fact that, even at room temperature, its rate of evaporation is very high, reducing the time period during which heat transfer between the melt and the liquid nitrogen is made. In contrast, water is able to absorb heat at least until it reaches 100ºC, temperature at which it evaporates, allowing to constantly renew the interface between the hot surface of the crucible and the water. Therefore, the nitrogen cooling condition could be approximately compared to an attempt to cool the melt in very cold air, since the liquid effect of nitrogen is rapidly lost due to its high evaporation rate.

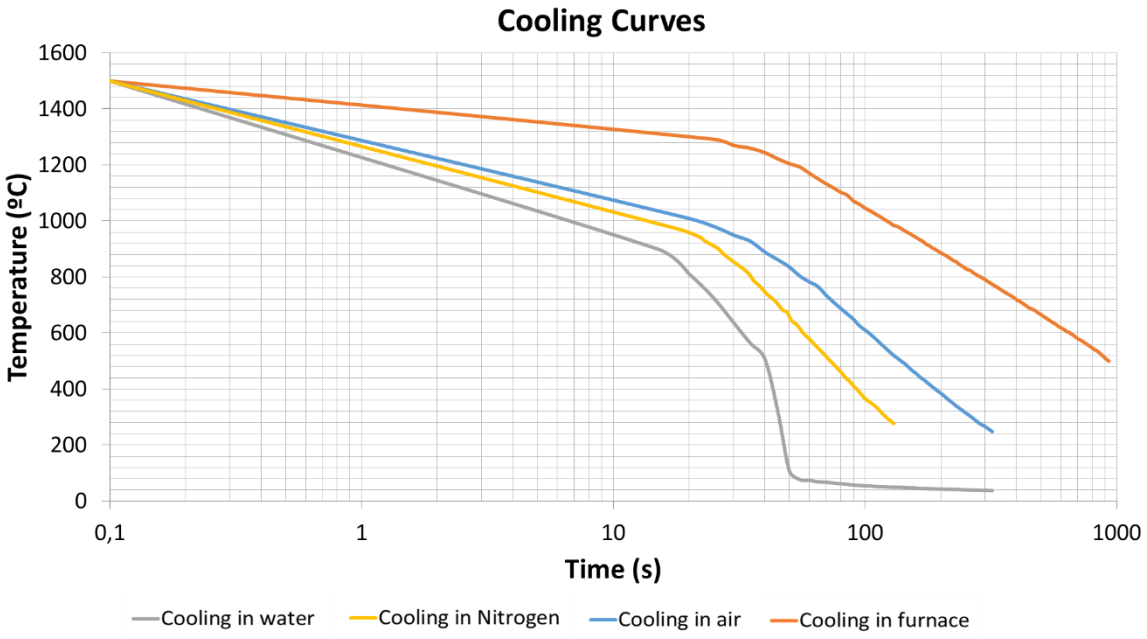

Figure 8-2. Cooling curves obtained for the different cooling environments tested in this study.

The hydraulic binders obtained were then removed from the interior of the platinum crucibles used in the production. The same grinding process described in section 6.1 was used in the preparation of these hydraulic binders, with the powders obtained being used to produce pastes by mixing it with water at a water/binder weight ratio value of 0.375. The pastes

prepared where poured in molds with cavities of 20x20x40mm^3 and left to cure under moisture and temperature controlled conditions until it was demolded at the 7 days of hydration. By this time, some of the samples were tested while the remaining samples were reintroduced in the moisture and temperature controlled chamber, being later tested at the 28 days. In this case, only one sample per age was tested.

8.2 Hydration Results

8.2.1 Compressive Strength

The compressive strength tests were performed in the pastes, prepared with the samples produced under different cooling conditions, at 7 and 28 days of hydration according to the procedure described in section 4.11.

The values obtained are plotted in Figure 8-3, where are also shown some results obtained from the samples studied in chapter 7 for comparison, since the precursor amorphous hydraulic binder possess the same theoretical chemical composition.

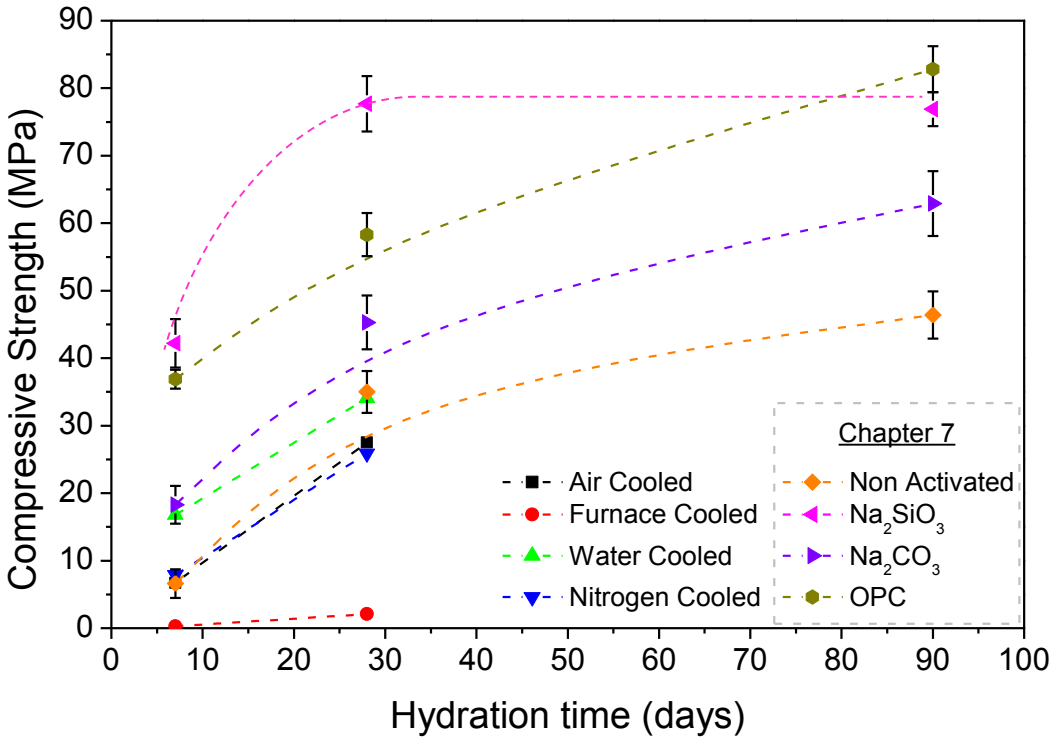

Figure 8-3. Compressive strength results at 7 and 28 days registered for the samples obtained though distinct cooling conditions. There are also plotted the values of compressive strength obtained in the samples of chapter 7 for comparison.

The compressive strength results obtained seem to indicate a relation with the cooling rates used in the production of these samples and/or with the amount of amorphous phase contained in each sample (as it can be seen in Table 8-1), with the water-cooled sample presenting higher strength, both at 7 and 28 days of hydration, when compared to the samples cooled in air and in nitrogen, which present very similar compressive strength results. The paste produced with the sample cooled inside the furnace does not show any visible strength development, presenting values below 1 MPa even after 28 days of hydration.

8.2.2 XRD – Rietveld Analysis

For Rietveld refinement, the method described in section 4.7, was used, by considering the available structures of Tobermorite 11 Å with reference code 87690 and Clinotobermorite with reference code 403090, from the ICSD database, as well as the structures of Monohydrocalcite with the code 96-901-2073, Pseudowollastonite with the code 96-900-2180, Wollastonite 2M with the code 96-901-1914, Wollastonite 1A with the code 96-901-2891, Corundum with the code 96-500-0093 and Calcite with the code 96-901-5762, from the ICDD database.

As it can be seen from both Figure 8-17 and Table 8-1, the lower cooling rate resulted from the furnace-cooling condition which lead to the formation of almost 70% in weight of Wollastonite crystals divided into three distinct polymorphs (Pseudowollastonite, Wollastonite 2M and Wollastonite 1A), while the cooling tests performed outside the furnace resulted in the crystallization of no more than 6% in weight of Pseudowollastonite. The highest cooling rate was achieved by immerging the crucibles in water, with this condition leading also to the highest amorphization of the hydraulic binder.

Figure 8-4 shows the XRD results of all the anhydrous samples produced in this study, where it can be seen the higher similarities in the constitution of the samples cooled in air, water and liquid nitrogen, whereas the sample cooled inside the furnace presents a much higher crystallinity, as expected.

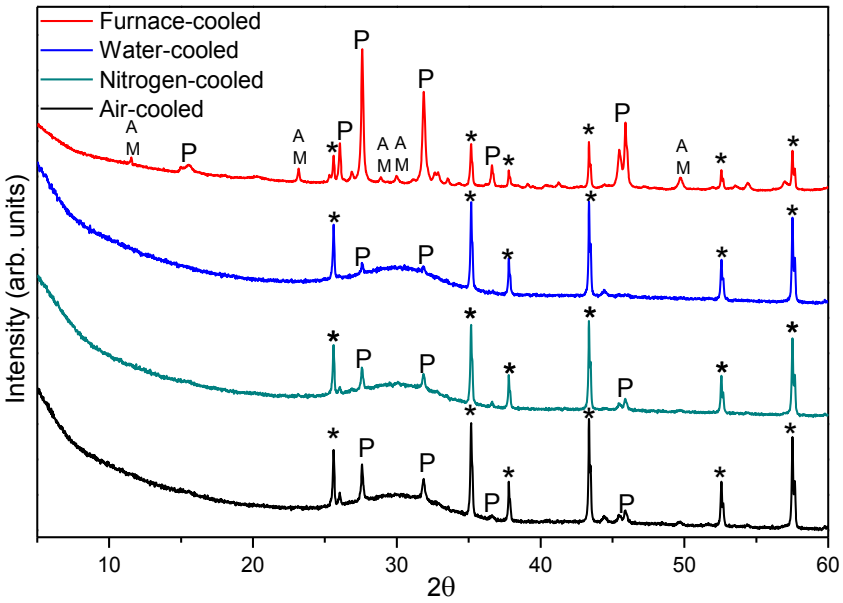

Figure 8-4. XRD results obtained for the four anhydrous samples produced in this study. A- Wollastonite 1A; M-Wollastonite 2M; P- Pseudowollastonite; *- α-$A_{l2}O_3$ used as internal standard for the determination of the amorphous phase content.

Table 8-1 shows the formation of Tobermorite-like phases as hydration proceeds in the samples cooled outside the furnace. Also small percentages (~1% in weight) of calcite were observed to be formed in the referred samples both at 7 and 28 days of hydration. The furnace-cooled sample didn't present any visible phase development at the 7th day of hydration, nevertheless, after 28 days some Monohydrocalcite was identified as well as the formation of calcite, but no Tobermorite-like phases were observed to precipitate during the hydration of this sample. In all the cases, it was not found to be formed any Portlandite.

Table 8-1. Values for the phase quantification of the anhydrous binders prepared and respective pastes produced at the ages of 7 and 28 days, as determined by XRD-Rietveld analysis.

Sample	Age	Phase wt%						
		Amorphous	Pseudo wollastonite	Tobermorite	Calcite	Wollastonite 2M	Wollastonite 1A	Monohydro calcite
Water-cooled	Anhydrous	98.4	1.6	---	---	---	---	---
	7 days	95.2	0.7	3.0	1.1	---	---	---
	28 days	91.5	0.7	6.9	0.7	---	---	---
Air-cooled	Anhydrous	93.9	6.1	---	---	---	---	---
	7 days	91.1	5.1	2.6	1.2	---	---	---
	28 days	88.5	4.6	6.2	0.7	---	---	---
Nitrogen-cooled	Anhydrous	95.4	4.6	---	---	---	---	---
	7 days	92.4	3.7	2.9	0.8	---	---	---
	28 days	92.0	2.9	4.4	0.6	---	---	---
Furnace-cooled	Anhydrous	31.9	58.7	---	---	5.2	4.2	---
	7 days	30.4	59.4	---	---	4.4	5.8	---
	28 days	32.3	54.9	---	2.3	4.3	3.2	3.0

8.2.3 Fourier Transform Infrared

For the acquisition of FTIR-ATR data it was followed the procedure indicated in section 4.6.

Figure 8-5 shows the FTIR-ATR spectra of the anhydrous samples prepared for the present study, where it can be seen the short range structural similarities between the samples cooled in water, air and nitrogen, whereas the sample cooled inside the furnace reveals a highly crystalline structure with features completely different from the ones observed in the other three samples studied. The spectra of the water-, air- and nitrogen-cooled samples seem to be dominated by three main regions of amorphous silicate species contribution plus a crystalline component assigned to the presence of Pseudowollastonite, which presents a feature at 719 cm^{-1} related to bridging Si-O-Si stretching vibrations of its three-membered rings structures [124, 125]. In addition, Pseudowollastonite also presents a signal at 985 cm^{-1}, corresponding to the stretching vibration mode of non-bridging $Si-O^-$ [125], which is better defined in the air- and nitrogen-cooled anhydrous samples and tends to decrease after hydration (see Figure 8-6 and Figure 8-8). As it was observed in the samples prepared in chapter 7, the amorphous component of these three samples can be divided in three different main regions, being the lower frequencies region dominated by the band around 450-490 cm^{-1} that can be assigned to the deformation of the SiO_4 tetrahedra [43, 86, 114, 127], while for higher wavenumbers, at around 660 cm^{-1}, it is possible to observe the band corresponding to Si-O-Si bending vibrations [43]. Another main region can be defined between 800 and 1100 cm^{-1} resulting from the combination of a group of bands assigned to symmetric and asymmetric stretching vibrations of Si-O bonds from Q^0 (~850cm^{-1}), Q^1 (~900cm^{-1}), Q^2 (~950 cm^{-1}) and Q^3 (~1100 cm^{-1}) units [43, 127, 178]. The sample obtained through furnace cooling presents several features related to the crystalline wollastonite polymorphs, including the ones already previously referred at 719 cm^{-1} and 985 cm^{-1}. In addition, the band at ~563 cm^{-1}, assigned to the bending vibrations of the O-Si-O, and the bands at ~916 cm^{-1} and ~937 cm^{-1}, attributed to the stretching vibrations of the Si-O bond in wollastonite polymorphs [179, 180], are also very well defined.

Figure 8-6 to Figure 8-9 depict the structural development upon hydration of the pastes produced with the samples cooled in air, water, nitrogen and furnace, respectively.

The group of water-, air- and nitrogen-cooled samples shows structural changes similar to the ones observed in the non-activated sample of chapter 7 as hydration takes place, being visible the narrowing of the band at very low frequencies around 430 cm^{-1}, as well as a shift to higher

wavenumbers of the band at around 915 cm^{-1} to values of ~960 cm^{-1}, indicating the development of environments with a higher polymerization degree [170]. In addition there are also visible in the hydrated samples, at around 1640 cm^{-1}, the band related to bending vibrations of hydroxyl groups [181], and at higher frequencies, from above 3000 to 3600 cm^{-1}, the broad band related to the stretching vibrations of O–H groups in H_2O or hydroxyls with a wide range of hydrogen-bond strengths [43], that result from the partially amorphous nature of the hydrated products formed. Regarding the furnace-cooled sample, no significant structural changes seem to occur upon hydration, apart from some carbonation that becomes visible at 28 days, by the presence of the features assigned to the presence of CO_3^{2-} group, namely the signals at 1420 cm^{-1} and 875 cm^{-1} attributed to asymmetric stretch ($\nu_3[CO_3^{2-}]$) and in-plane bending ($\nu_2[CO_3^{2-}]$) vibration modes, respectively. These bands related to sample carbonation are also present in the other group of samples studied in this chapter, however their magnitude is much lower.

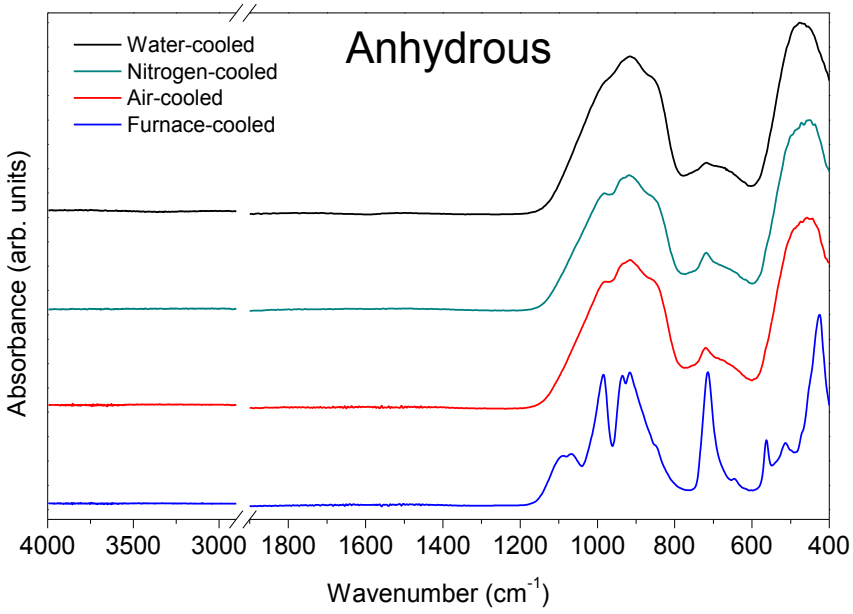

Figure 8-5. FTIR-ATR spectra of the anhydrous samples obtained with different cooling conditions

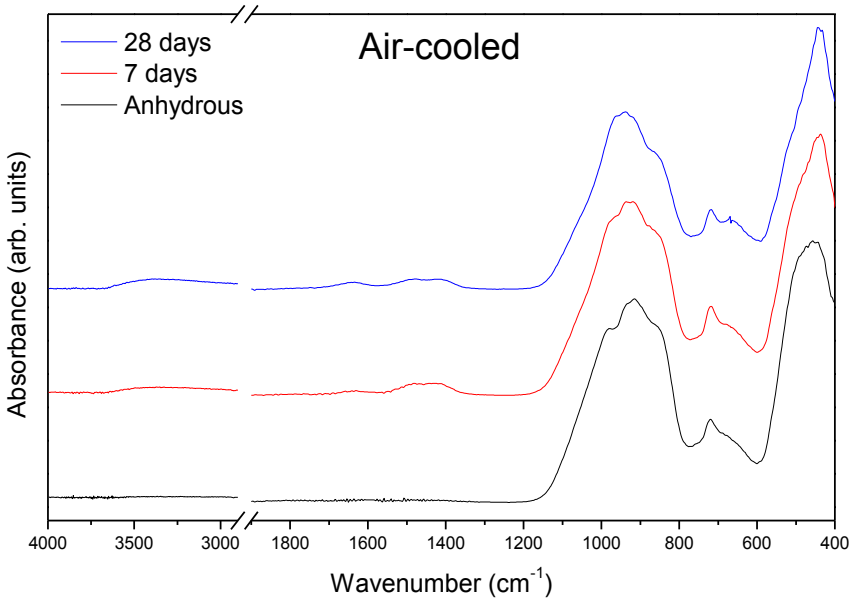

Figure 8-6. Hydration of the air-cooled sample followed by FTIR-AT until 28 days.

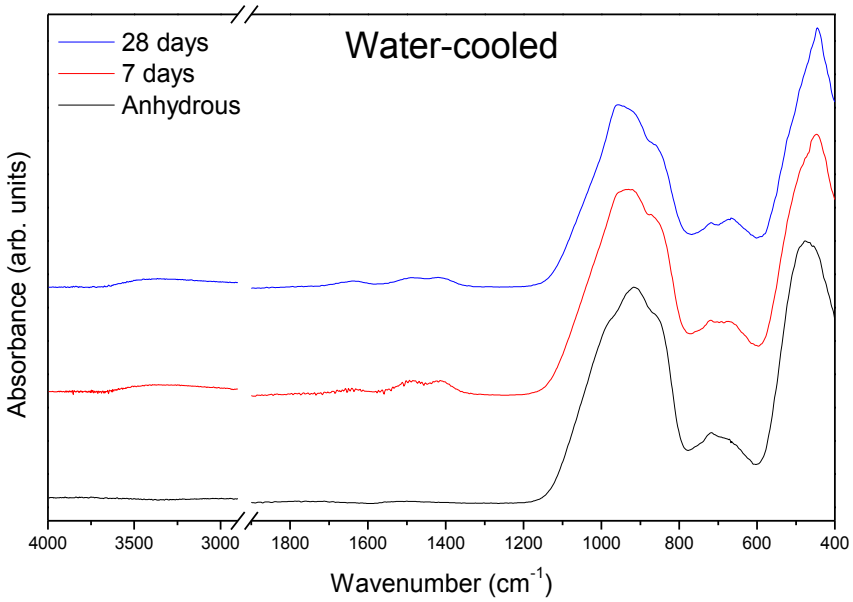

Figure 8-7. Hydration of the water-cooled sample followed by FTIR-AT until 28 days.

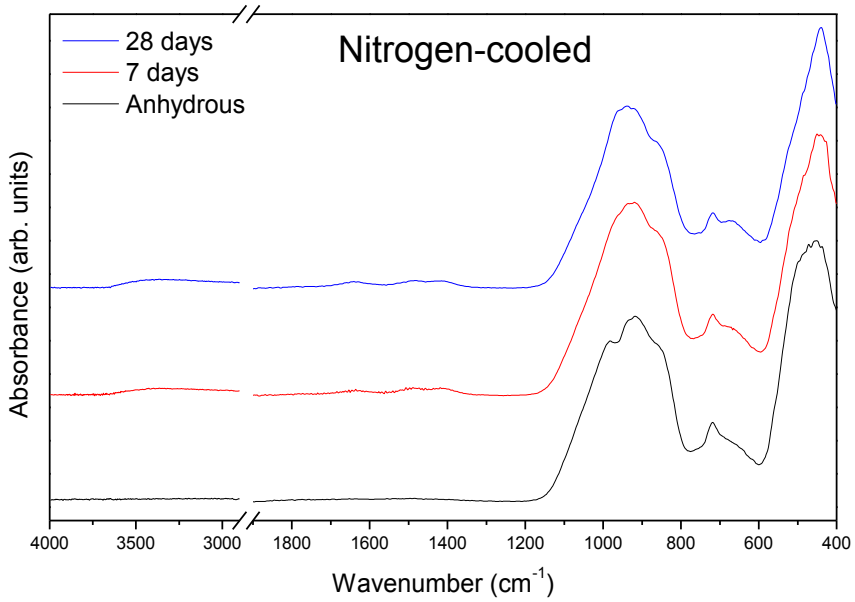

Figure 8-8. Hydration of the nitrogen-cooled sample followed by FTIR-AT until 28 days.

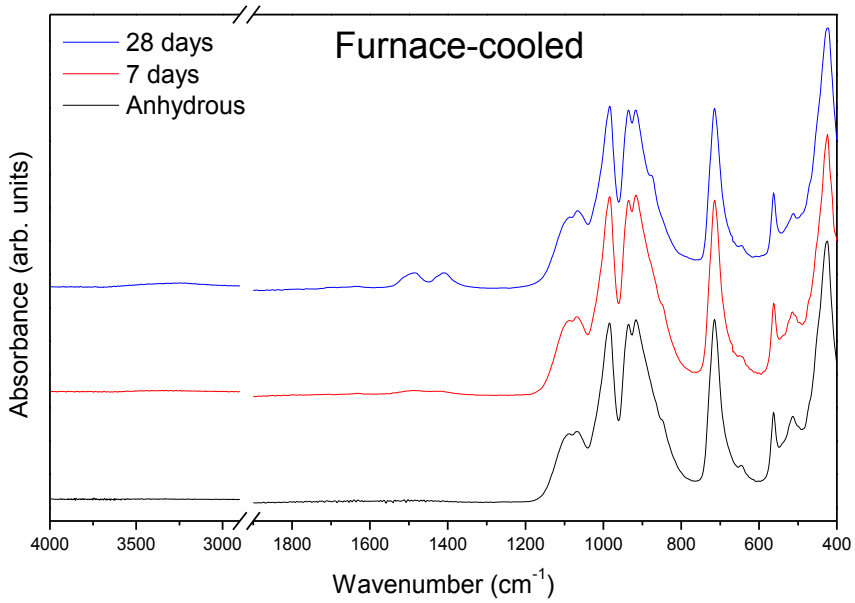

Figure 8-9. Hydration of the furnace-cooled sample followed by FTIR-AT until 28 days.

8.2.4 ^{29}Si MAS-NMR

The procedure followed for the acquisition of ^{29}Si MAS NMR spectroscopy data was the one indicated in section 4.8.

Figure 8-10 shows the ^{29}Si MAS NMR spectra of the samples obtained under water-, air- and nitrogen-cooling. The intensity of each spectra is normalized to their maxima and it is possible to observe the increasing amount of Pseudowollastonite, given by the peak at approximately

-83.5 ppm, as the cooling condition changes from water immersion to air exposure. As it was observed by XRD, no other phases were identified to be present in these samples and their respective ^{29}Si MAS NMR spectra seems to be dominated only by the amorphous component and crystalline Pseudowollastonite contributions.

The spectra presented in Figure 8-10 were deconvoluted and the Pseudowollastonite contribution was subtracted in order to determine the isolated amorphous component contribution, which was then normalized and compared amongst these samples. The resultant amorphous contribution is shown in Figure 8-11, where it is possible to observe that the main structural backbone of the amorphous component is similar for all the samples regardless of the cooling conditions applied, with the ^{29}Si MAS NMR signal being centered at chemical shifts around -78.5 ppm resulting from the high amount of Q^1 and Q^2 units, containing also some Q^0 and Q^3 species evenly distributed. The results of spectra deconvolution are shown in Table 8-2 and the distribution of Q^n units within the amorphous component is given in Table 8-3. The calculation of the amorphous and Pseudowollastonite phase's weight percentage from the ^{29}Si MAS NMR spectra was performed by considering the formation of stoichiometrically pure Pseudowollastonite ($CaSiO_3$) and the theoretical chemical composition of the sample prepared, as indicated in Table 6-1 for a sample with a C/S molar ratio of 1.1, being the values obtained in very good agreement with the ones determined by XRD-Rietveld analysis and presented in Table 8-1 for the anhydrous samples produced.

Table 8-2. ^{29}Si MAS NMR spectra deconvolution results, with indication of the molar percentage distribution of Si by the two main components of the anhydrous samples cooled in air, water and nitrogen (amorphous and Pseudowollastonite). The last two rows show the calculated values of weight percentage of the amorphous and Pseudowollastonite phases, considering the values of the Si molar % distribution.

	molar % Si (^{29}Si MAS NMR)		*wt% phase (Calculated)*	
Sample	***Amorphous***	***Pseudowollastonite***	***Amorphous***	***Pseudowollastonite***
Air-cooled	93,7	6,3	94,3	5,7
Water-cooled	98,2	1,8	98,4	1,6
Nitrogen-cooled	97,1	2,9	97,4	2,6

Table 8-3. Distribution of Q^n units in the amorphous components of the anhydrous samples produced, as determined by deconvolution of their respective ^{29}Si MAS NMR spectra.

	Amorphous component Q^n distribution			
Sample	***Q^0***	***Q^1***	***Q^2***	***Q^3***
Air-cooled	12,9	32,6	37,4	17,1
Water-cooled	13,1	33,4	38,0	15,5
Nitrogen-cooled	14,5	33,9	40,1	11,5

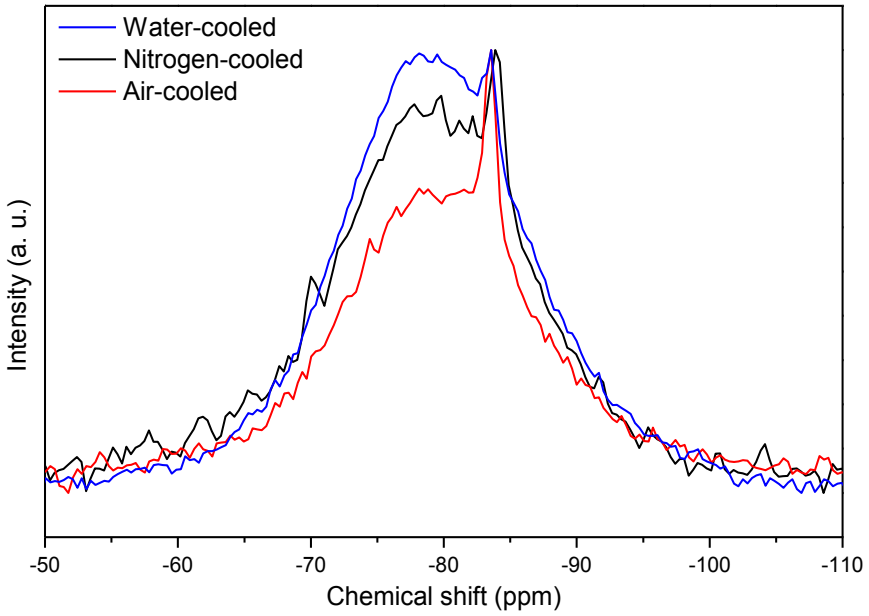

Figure 8-10. Comparison between ^{29}Si MAS NMR spectra of the anhydrous samples produced under different cooling conditions.

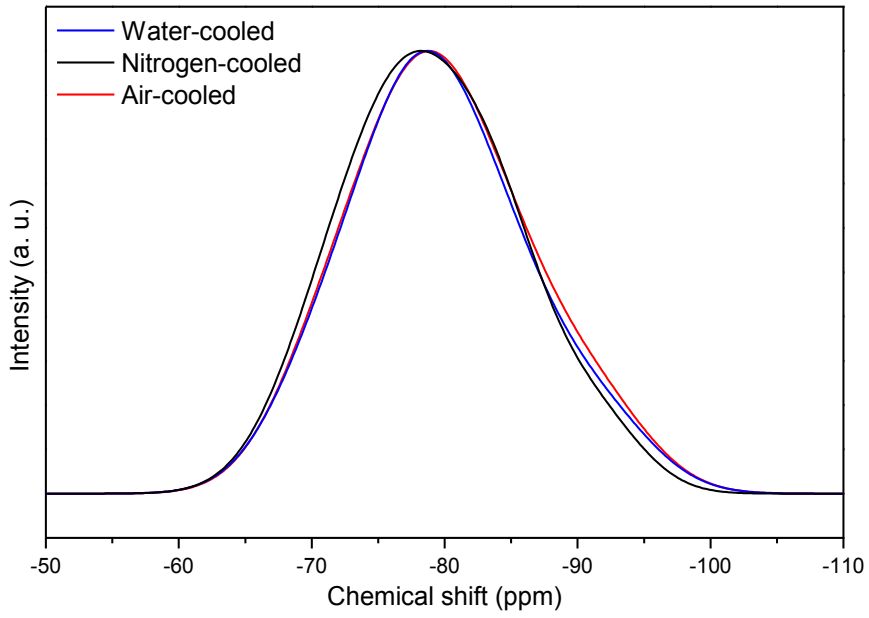

Figure 8-11. Comparison of amorphous component contribution to the ^{29}Si MAS NMR spectra of the anhydrous samples produced under different cooling conditions.

Figure 8-12 to Figure 8-14 show the structural evolution of the hydrated pastes produced with the samples cooled in water, nitrogen and air, respectively, as determined by ^{29}Si MAS NMR. It is clearly visible the formation of a shoulder around -85 ppm and, especially in the water-cooled sample, a narrow feature approximately at -79,5 ppm corresponding to the Q^2 and Q^1 units of the hydrated products formed, which, in analogy with the results of chapters 6 and 7, can be attributed to Tobermorite-like structures, with this consideration gaining some support from the XRD and FTIR results.

The overall spectra of all the samples studied seem to narrow upon hydration, mainly at the cost of a decrease in the Q^0 units that constitute the most reactive fraction amongst all the Q^n units in the silicate framework, but also due to the increase of the crystallinity of the environment that is achieved by the rearrangement of those less coordinated structural units into structures with higher polymerization degree, such as the Q^1 and Q^2 units of C-S-H.

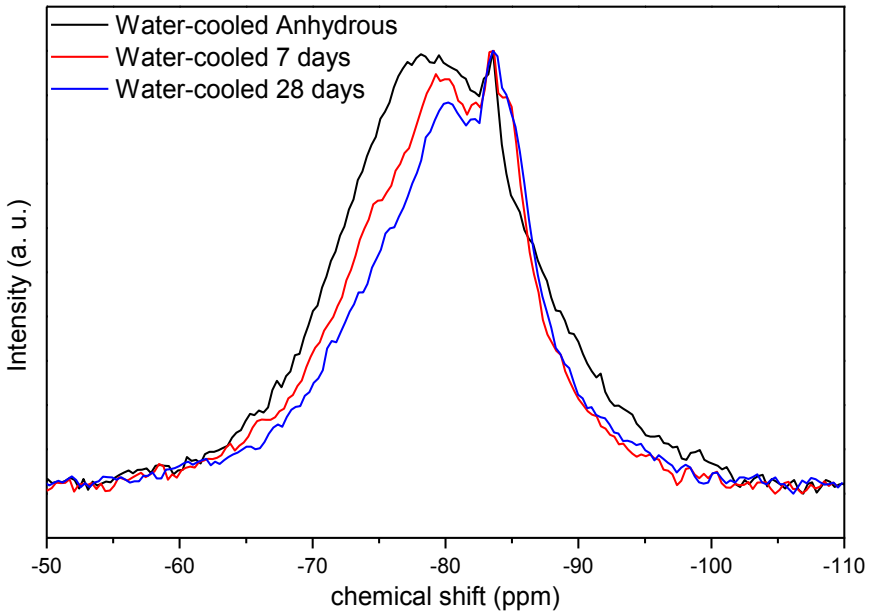

Figure 8-12. ^{29}Si MAS NMR spectra of the anhydrous water-cooled sample and its respective 7 and 28 days hydrated pastes.

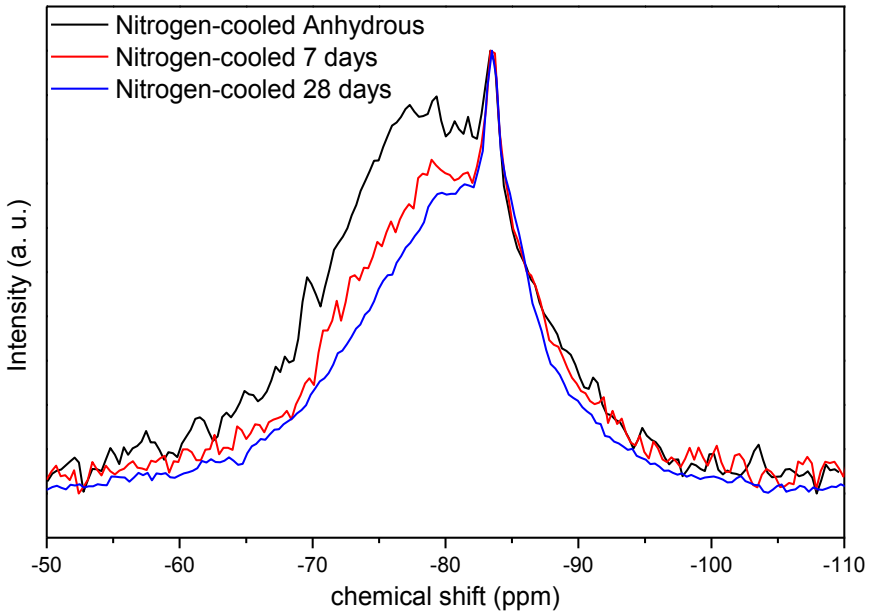

Figure 8-13. ^{29}Si MAS NMR spectra of the anhydrous nitrogen-cooled sample and its respective 7 and 28 days hydrated pastes.

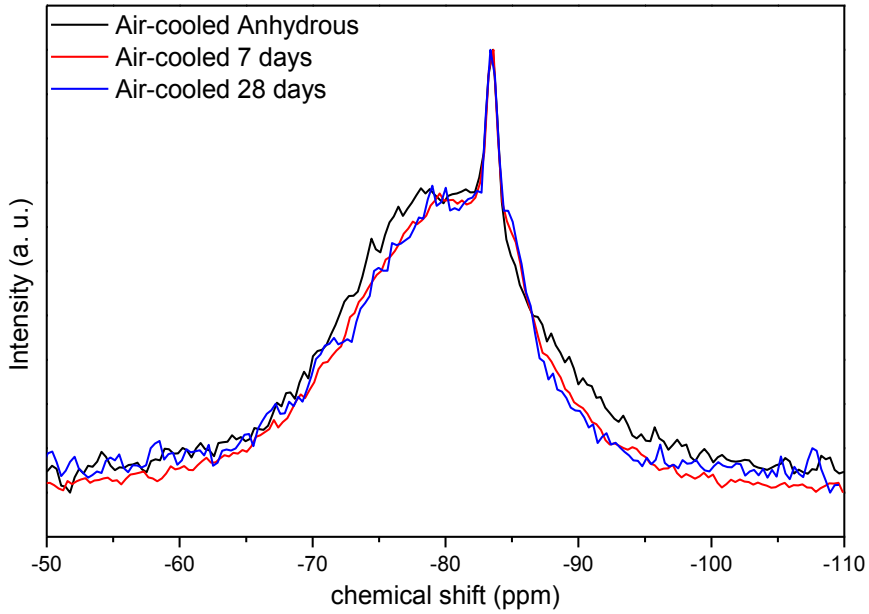

Figure 8-14. ^{29}Si MAS NMR spectra of the anhydrous air-cooled sample and its respective 7 and 28 days hydrated pastes.

8.2.5 Thermogravimetric Analysis (TGA)

The pastes produced with the mainly amorphous samples, i.e. the samples cooled outside the furnace under air, water or nitrogen conditions, were analyzed by TGA and the bound water

was determined according to the procedure referred in section 4.10, being the results obtained indicated in Table 8-4.

Table 8-4. Results obtained by TGA for the air-, water- and nitrogen-cooled samples regarding the amount of bound water and the corresponding calculated $C_{1.1}SH_{0.82}$ weight %.

	7 days				28 days			
Sample	**Bound water (wt%)**	**C/S**	**H/S**	**$C_{1.1}SH_{0.82}$ wt%**	**Bound water wt%**	**C/S**	**H/S**	**$C_{1.1}SH_{0.82}$ wt%**
Air	1,12	1,1	0,82	10,75%	2,58	1,1	0,82	24,40%
Water	1,84	1,1	0,82	17,53%	3,12	1,1	0,82	29,35%
Nitrogen	1,45	1,1	0,82	13,87%	2,5	1,1	0,82	23,66%

Figure 8-15 shows a graphical representation of the bound water results obtained from the mentioned pastes, plotting them against the respective compressive strengths and comparing with some equivalent results obtained from similar pastes produced in chapters 6 and 7 of this thesis.

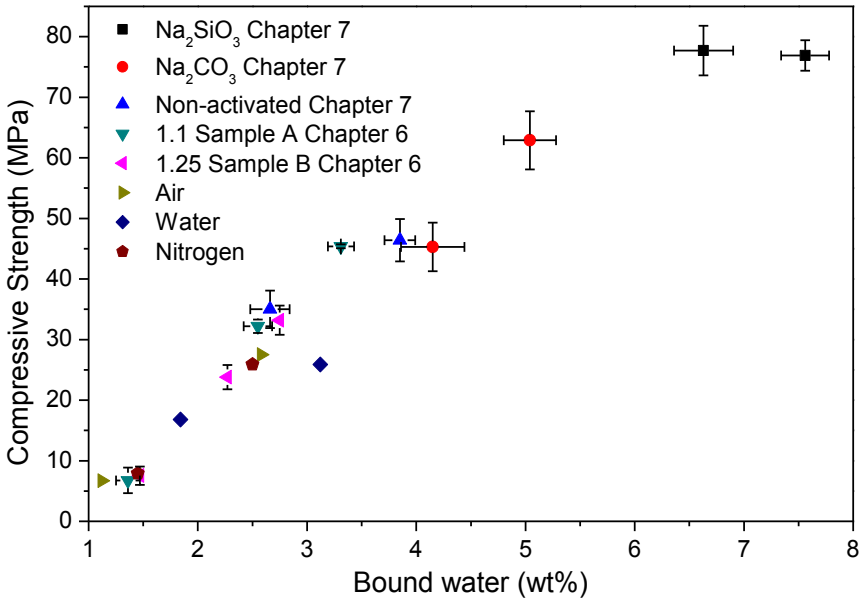

Figure 8-15. Plot of compressive strength versus bound water, as determined by TGA for the samples cooled outside the furnace under different conditions, as well as some results previously reported in chapters 6 and 7.

8.2.6 Isothermal Calorimetry

The heat of hydration of the air- and water-cooled samples was followed by isothermal calorimetry measurements, with the results obtained being plotted in Figure 8-16.a) together with the result of a reference OPC.

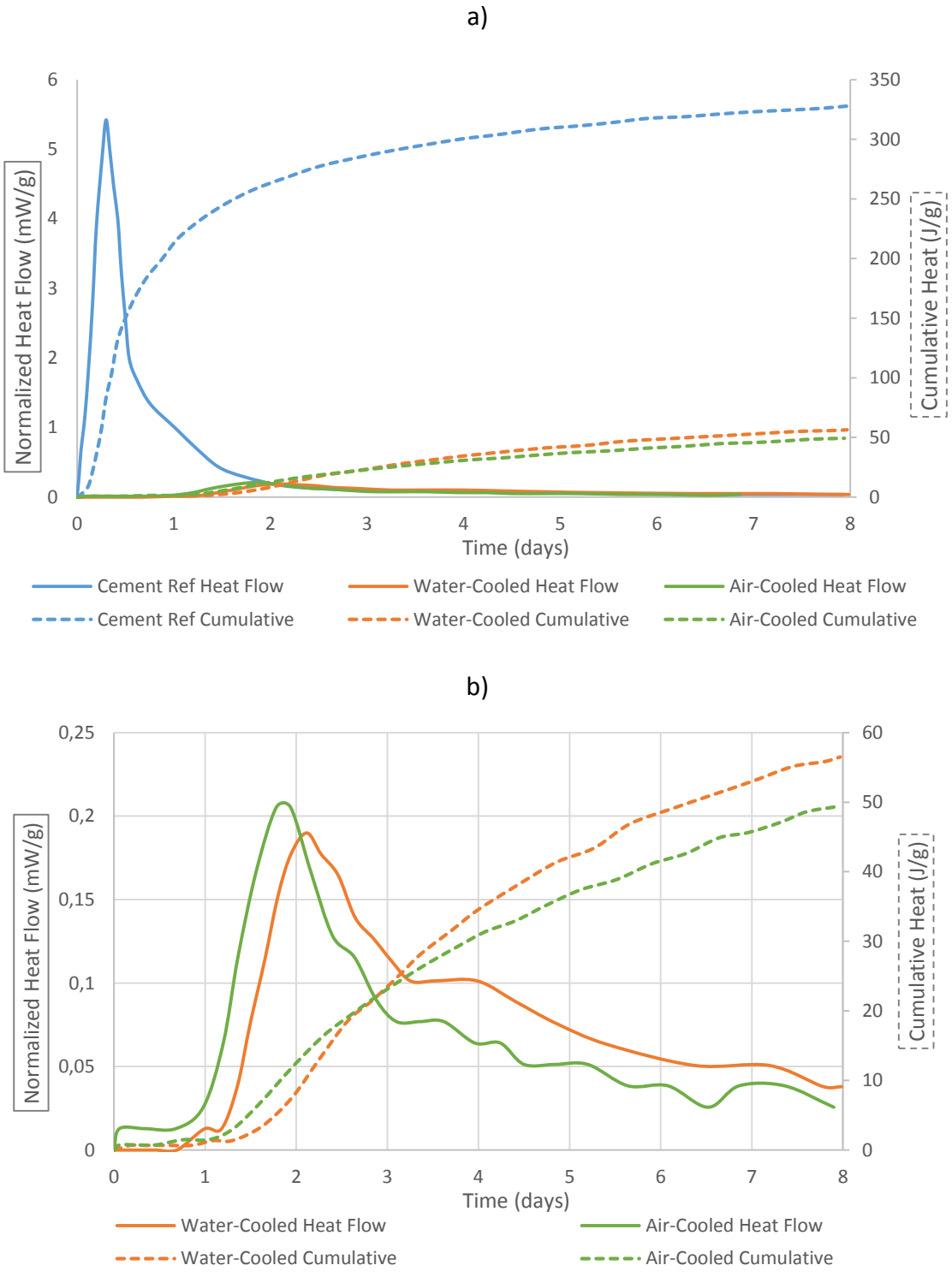

Figure 8-16. a) Comparison of the isothermal calorimetry curves obtained for the reference cement and the samples cooled in air and in water. b) Detail of the air- and water-cooled curves, rescaled to better observe the difference between these two samples.

It can be seen that, while the reference cement presents an intense and sharp peak of heat release taking place in the first 24 hours of hydration, the amorphous binders only start to show some hydration activity after the first day, reaching its maximum at around 48 hours, time by which should be formed the first hydration products, and then slowly decreasing the intensity of the heat signal. The detail shown in Figure 8-16.b) reveals that the hydration behavior measured by isothermal calorimetry is very similar for both the air- and water-cooled samples, with the water-cooled sample presenting only a slightly superior cumulative heat release at 8 days. The signal collected from these samples suggest the presence of 2 phenomena that overlap in time, being probably related to the occurrence of dissolution and hydration products formation.

8.3 Discussion

Several authors have already studied the cooling rate effect in the production of typical calcium silicate glassy materials including blast furnace slag, either experimentally [182-184] or by computational methods [185, 186], discussing its influence in their structure, crystalline phase distribution and even in the hydraulic properties of the resulting materials. It is known that the cooling rate has a direct impact on the reactivity of blast furnace slags, since it is also related to the glass content of these materials that is the main responsible for their good latent hydraulic properties [92].

It was observed by crossing the information collected from XRD and the direct measurements performed on the cooling path for each sample that increasing cooling rates resulted in the formation of higher amounts of amorphous component in the samples produced for the particular composition and processing conditions used in this study. However those differences reflect variations in the amount of glassy matrix of only 5 to 6% in weight even when changing the cooling conditions from exposure in non-forced air to partial immersion in water, i.e. varying the cooling rates from about -10 to -30 ^{o}C/s. This range of cooling rates is within the reported values for the production of fully amorphous materials in calcium silicate melts of similar compositions [187].

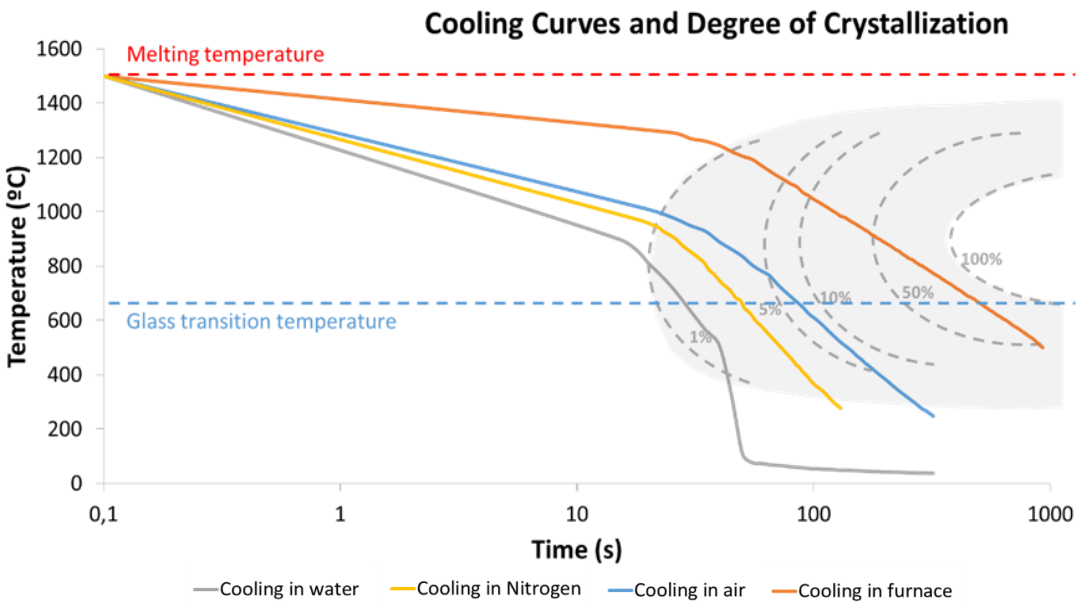

Figure 8-17. Cooling path of the samples produced in this study. It is also depicted an estimation of the crystallization curves considering the weight % of all polymorphs of wollastonite crystals formed during the production of each sample, as determined by XRD-Rietveld method.

Figure 8-17 shows the estimated crystallization curves that were obtained by combining the information taken from the cooling paths and the respective XRD analysis of the anhydrous binders. The melting and glass transition temperatures are also indicated in Figure 8-17, defining the critical temperature interval within which crystallization processes are more active. Thus, the degree of crystallization essentially depends on the cooling rate applied inside this temperature range, i.e., it depends on the time elapsed between the moment when the melt starts cooling and the point when it reaches the glass transition temperature. The dashed curves presented in Figure 8-17 indicate the amount of Wollastonite (in weight %) that resulted from each of the cooling processes used. It can be seen that limited wollastonite crystallization can be achieved when using process cooling conditions within the region defined between the water and air cooling paths. It is also worth noting that within this range of cooling rates the good hydraulic properties of the amorphous binders produced are preserved.

Compressive strength values showed some tendency to increase with higher cooling rates, and consequently with higher amount of amorphous component in the hydraulic binder. This particular effect was especially noted in the sample cooled in water that revealed a much quicker strength development when compared with the samples cooled in air or in nitrogen,

with this strength growth being felt from as soon as the 7th day of hydration, as shown in Figure 8-3. The superior mechanical performance of the paste prepared with the sample cooled in water is maintained until at least the 28 days, while the pastes prepared from the air-cooled and nitrogen-cooled samples show equivalent compressive strength at 7 and 28 days of hydration.

The phase development was followed with XRD-Rietveld analysis, which showed that the air-, water- and nitrogen-cooled samples presented an increasing formation of Tobermorite-like phases during hydration, as well as some residual amounts of calcite, being in line with the results obtained by FTIR and ^{29}Si MAS NMR.

As it was observed in chapter 7, the FTIR-ATR spectra of the highly amorphous hydraulic binders produced essentially consist in features related to silicate components, differing in degree of condensation and crystallinity, with the crystalline component arising from the presence of the only crystalline phase detected, Pseudowollastonite. With respect to the spectra of the corresponding pastes, it was observed a shift in the bending and stretching vibration modes of Si-O bonding that suggest the formation of structures with higher polymerization degree, as well as a narrowing of the lower frequency band assigned to the bending mode of the Si-O, reflecting the semi-crystalline structural arrangement of the hydration products that are formed upon hydration. Furthermore, the corresponding water signal of those hydration products formed is also visible at higher frequencies, namely by the presence of the band corresponding to the bending vibration modes of OH^- groups at around 1640cm^{-1} and also the broad signal between 3000 and 3600cm^{-1} assigned to the stretching modes of water molecules or hydroxyl groups.

^{29}Si MAS NMR show that, in the samples cooled outside the furnace, the effect of the cooling rate in the resulting structures is almost negligible for the range of cooling rates tested, revealing similar Q^n distributions. Comparable results were obtained in the study of Tan et al. [182] where the structures of sodium silicate ($Na_2Si_3O_7$) glasses, produced with cooling rates ranging from 2^{o}C/min to 500^{o}C/min, were assessed by Raman spectroscopy, presenting only a small broadening in the distribution of Q^n units, keeping the theoretical anionic equilibrium relationship of $2Q^3 \Leftrightarrow Q^2 + Q^4$, with this reaction dislocating to the right side as the cooling rate increases. Furthermore, some studies performed by computational simulation methods

in other calcium silicate glass systems had already predicted this slight Q^n distribution broadening effect caused by the increase of the cooling rate [186, 188].

From the analysis of Figure 8-15 it can be seen the existence of a direct correlation between the bound water of the pastes produced and their respective compressive strengths, indicating that the hydrated products meanwhile formed are the main responsible for the development of the good mechanical properties in these systems. The amount of hydrated products formed was then estimated by considering the premises already used in sections 6.3 and 7.3, namely by applying

Eq. 6.2 $$wt\%C_xSH_y = \left(\frac{\frac{wt\%SiO_{2\,reacted}}{\left(\frac{wt\%SiO_{2\,initial}}{100} \right)} + wt\%H_2O_{bound}}{100 + wt\%H_2O_{bound}} \right) * 100$$ and

Eq. 6.3 $$wt\%SiO_{2\,reacted} = \frac{wt\%H_2O_{bound}}{(H/S) * \frac{M(H_2O)}{M(SiO_2)}}$$

and defining a C_xSH_y stoichiometry with $x = \frac{Ca}{Si} = 1.1$ and $y = \frac{H_2O}{Si} = 0.82$, as calculated from the relation given by Richardson [46] and presented in

Eq. 2.6 $$\frac{H_2O}{Si} = \frac{19 \cdot \frac{Ca}{Si} - 7}{17}.$$

The results obtained are shown in Figure 8-18, where they are plotted against the respective compressive strength. It can be seen that the dispersion of results fall on top of very good direct linear correlation, indicating that the quality of the C_xSH_y formed by the hydration of these amorphous binders, under all the tested conditions and within the compositional range of C/S molar ratios between 1.1 and 1.25, is very similar and suggest that the final structure, density and porosity of the hardened pastes are not appreciably affected by the variations imposed in the paste preparation conditions (considering activated or non-activated pastes) or by the changes in the cooling rate in the production of the amorphous binders. However, the development of strength differ significantly especially when considering alkali activated and non-activated samples, due to the kinetic effect. Regarding the samples studied in this chapter, it is clearly seen that the sample cooled in water exhibits a formation of hydration

products higher than the verified for the samples cooled in air or in nitrogen, being in line with the observed development of mechanical properties at all ages.

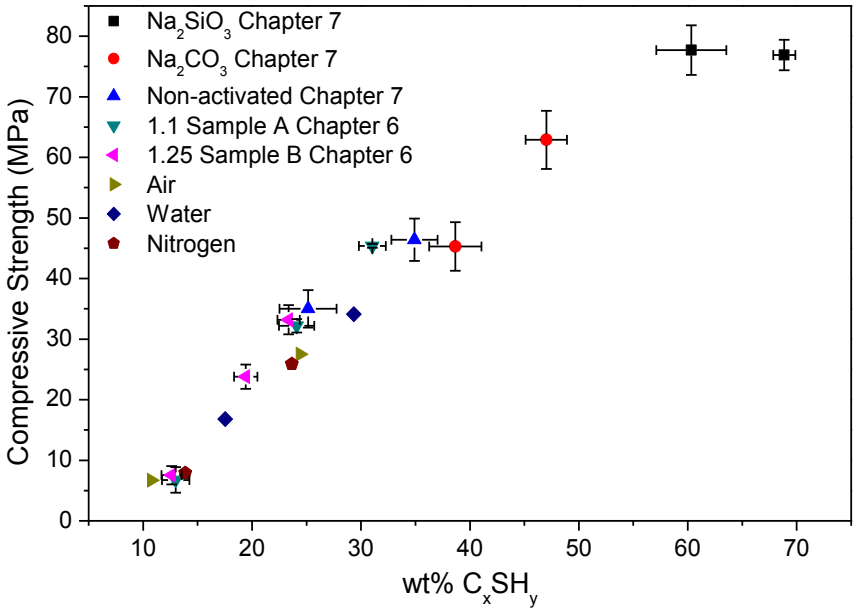

Figure 8-18. Values of calculated C_xSH_y wt% plotted against the respective compressive strengths of the pastes produced with the samples cooled outside the furnace, as well as some other results obtained in similar pastes already studied in chapters 6 and 7.

Isothermal calorimetry measurements show that the heat evolution of the amorphous samples cooled in air and in water proceed very slowly when compared to an OPC, registering some activity only after the first 24 hours. It is known that that the rate controlling step for the dissolution of glassy silicate-rich systems is the breaking of the Si-O bonds [93, 94], which present a dependence on the alkalinity of the solution. Thus the presence of $[SiO_4]^{4-}$ species in solution only become available as the pH reaches a value high enough to break the Si-O bonds in the silicate backbone. It has been reported by Shi and Day [157] that a gradual increase in the pH of the solution can occur in slag + water systems due to the absorption of H^+ by a Si-Al-rich layer that forms on the surface of the glassy particles, resulting in an increase of the OH^- concentration. It this case, due to the limited Al content, a mainly Si-rich layer is expected to form and absorb the H^+, as the Ca-O bonds are much weaker than the Si-O bonds and much of the Ca becomes readily available in the solution. Therefore, it can be inferred from the analysis of the isothermal calorimetry data obtained that this critical value of pH is achieved approximately at the end of the first day of hydration, corresponding to the instant when a heat flow signal starts to develop indicating the beginning of the dissolution process

that releases the $[SiO_4]^{4-}$ species into solution. From this moment, C-S-H products start to form, by the reaction of $[SiO_4]^{4-}$ species with the dissolved Ca^{2+}, thus leading to the occurrence of what appears to be an overlapping of two phenomena, dissolution of $[SiO_4]^{4-}$ and C-S-H formation. Furthermore, the evidences given by isothermal calorimetry indicate a more intense and earlier onset of C-S-H formation for the sample cooled in air, which could mean that the higher number of Pseudowollastonite crystals present in this sample initially triggered a more abundant and highly dispersed formation of C-S-H, since, as reported by Taylor [3], the presence of a small amount of crystals (up to 5% in weight) embedded in the glassy matrix can act as active nucleation sites for the formation of hydration products. However, the subsequent formation of C-S-H in the air-cooled sample revealed a faster decreasing trend when compared with the water-cooled sample that extended the formation of C-S-H for a longer period, translating in a higher cumulative heat of hydration at the end of the 8^{th} day. The faster decrease in the heat flow observed for the air-cooled sample may indicate that the C-S-H growth ended up being limited by the lower availability of silica-rich species in solution, which as referred previously seems to be the rate controlling factor in these glassy silicate systems. The higher cumulative heat flow observed for the water-cooled sample somehow explains its improved mechanical properties, indicating the larger formation of hydration products, as it was also confirmed by TGA measurements. In fact, the relationship between the compressive strength and the cumulative heat of hydration have already been confirmed in a study from Bentz et al. [189], where, for mortars produced with the same w/c ratio, it was found to exist a linear correlation between the compressive strength and the cumulative heat of hydration, as measured in J/g. Thus, in order to assess the reported relation, a similar exercise was performed in this work and the isothermal calorimetry and compressive strength data from the samples with a C/S molar ratio of 1.1 were considered, comprising the water-cooled and air-cooled samples of this preliminary study as well as the Na_2SiO_3 activated sample from chapter 7.

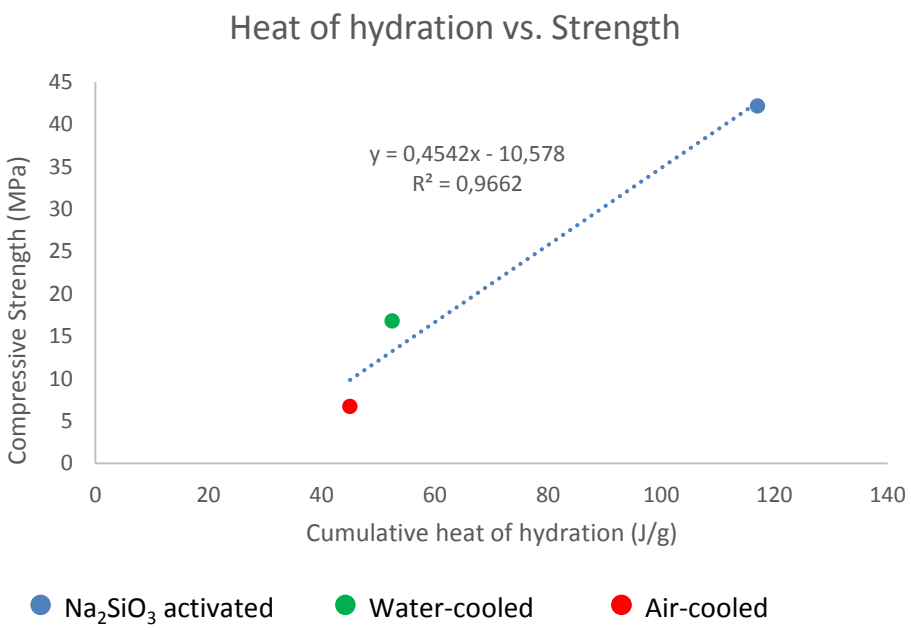

Figure 8-19. Heat of hydration versus Compressive strength plot obtained with the data taken from the water— and air-cooled samples and from the Na_2SiO_3 activated sample.

Figure 8-19 shows the plot obtained from the isothermal calorimetry and compressive strength data taken from the water- and air-cooled samples as well as from the Na_2SiO_3 activated sample studied in chapter 7.

Of course, these are preliminary results and conclusions from a 3 point plot are fragile. However a trend correlating the heat of hydration and the respective compressive strength can be perceived from Figure 8-19. The correlation factor and the linear equation are also shown in the graph, where it can be seen that the intercept presents a negative value of -10.6 MPa, which according to Bentz et al. [189] indicates that some heat release is supposed to occur prior to the beginning of the development of compressive strength, meaning that the first hydration products formed would establish a three-dimensionally connected structure that would provide the backbone for future growth and strength development.

In order to detect if the differences in hydration heat are large enough to consider the air- and the water-cooled samples two distinct cementitious materials, some more experiments will be further needed, so that the plot presented in Figure 8-19 can be completed and validated with more data.

The difference in mechanical performance registered for the sample cooled in water may be justified by its higher glass content that translates into a higher number of possible reaction sites, however, the increment observed in the compressive strength of this sample, when

compared to the samples cooled in air or in nitrogen, seems to be too large to gain fundament only on this factor, being left to explain the complete origin of the particular behavior observed in this sample. One of the possible reasons would arise from the presence of the small Pseudowollastonite crystals formed during cooling that might have acted as nucleation sites for the growth of C-S-H, but then again this explanation should also work for the other two samples (air- and nitrogen-cooled) since the amount of crystals is even higher in those cases. Furthermore, the evidences given by isothermal calorimetry indicate a more intense and earlier onset of C-S-H formation for the sample cooled in air, which could mean that the higher number of Pseudowollastonite crystals initially triggered a more abundant and highly dispersed formation of C-S-H. However the subsequent formation of C-S-H revealed a faster decrease in this sample than in the water-cooled sample that extended the formation of C-S-H for a longer period, translating in a higher cumulative heat of hydration at the 8th day. The faster decrease in the heat flow observed for the air-cooled sample may indicate that the C-S-H growth ended up being limited by the lower availability of silica-rich species in solution, since the breaking of the Si-O bonds seems to be the rate controlling factor in glassy silicate systems [93]. Additionally to the referred factors there may be also considered some structural instability effect caused by the differences of the cooling rates used during the production of the samples studied, since it is known that higher glass production cooling rates have impact in some of its properties, namely a lower density that is somehow related with an increase in the entropy of the system, which may add up some embedded energy and act as an extra driving force for breaking of Si-O, thus increasing its solubility rate for later ages. The increase in the structural distortion of glasses with increasing cooling rate was already predicted through a generic computational simulation study by applying a Lennard-Jones potential, where it was verified some bond-bond angle distortion and also an increase in the energies of the clusters that form the glass framework [185].

8.4 Conclusions

This chapter showed some preliminary results of the characterization of amorphous hydraulic binders produced under different cooling rate conditions. Four types of hydraulic binders were prepared by conducting the experiments under air, water, nitrogen and furnace cooling

conditions. As expected, the cooling rates obtained differed with the methods used and were found to decrease in the following order water>nitrogen>air>furnace.

From the four samples prepared, the one cooled inside the furnace presented a completely different phase distribution and consequently different structural features when compared to the group of samples cooled outside the furnace, namely higher amounts of crystalline Wollastonite were formed in various polymorphic forms (around 70% in weight) while the group of samples obtained through cooling outside the furnace presented less than 7% in weight of Pseudowollastonite, being constituted by a mainly amorphous structure.

These differences in crystallinity impacted in the hydraulic behavior of these samples, annulling the ability of the sample cooled inside the furnace to develop strength even at 28 days of hydration, whereas the group of samples cooled outside the furnace shown interesting mechanical performance development, especially the water-cooled sample.

The analysis of the amorphous component structure of the samples cooled in air, water and nitrogen revealed very similar Q^n units distribution although differences in cooling rates ranged from 10 to 30^{o}C/s. However, the water-cooled sample presented major differences in compressive strength values at 7 days, when compared to the samples cooled in air or in liquid nitrogen, which seem to be too large to be fully justified only by its slightly higher amount of glass phase. The results of TGA and isothermal calorimetry suggest that the improved mechanical strength registered in the water-cooled sample might outcome from the larger formation of hydration products in this sample, whereas the evidences taken from XRD-Rietveld, FTIR and ^{29}Si MAS NMR indicate that these hydration products formed possess a Tobermorite-like character, as it was also verified in other samples studied in the previous chapters.

9 CO_2 Emissions Impact and Some Technological Aspects

This chapter is dedicated to the analysis of the CO_2 emissions that may result from the production process of the several hydraulic binders studied in this work and its impact, when compared to normal OPC, in the global reduction of this greenhouse gas.

At this point, only laboratorial production of these hydraulic binders was attempted and no infrastructures were yet created or designed for the production of this type of binders in an industrial or pre-industrial pilot scale. Knowing this, the values presented in this chapter for the CO_2 emissions related to an industrial production of the hydraulic binders are just estimations and are not directly measured values obtained from any industrial trial or experiment. The values presented in this chapter were achieved through considerations based on the chemical composition differences between the raw meals used in the production of OPC clinker and in the production of the low calcium content hydraulic binders. Aditionally some considerations about the several process stages were made, namely in the stages where the heat consumption is more intense. It was estimated a global balance of heat consumption by assuming a production process of amorphous hydraulic binders via technological clinker route with some modifications on each individual stage attending to the particularities of the new raw meals chemistry.

The compressive strength results of the different hydraulic binders tested in this work were also analyzed together with their respective values of the estimated process related CO_2 emissions, and some performance and emissions indicators were designed in order to compare the different behaviors of the several pastes produced in this work as well as to directly confront the results obtained by the OPC clinker. Also target barriers of compressive strength performance were established as a function of the hydraulic binder's C/S molar ratio and their respective estimated process related CO_2 emissions, for the ages of 7, 28 and 90 days of hydration.

9.1 Estimation of the Process Related CO_2 Emissions

For the estimation of the global CO_2 emissions several considerations needed to be defined, since, as referred previously, no direct measurements were performed, neither any indicative values yet exist for this type of process.

The first and more critical premise adopted for the estimation of the process related CO_2 emissions is the assumption of the use of the same type of technology considering that the amorphous hydraulic binders are obtained through the clinker route.

Then it was also considered that the production process would contain the same type and number of stages as the ones required for the production of OPC clinker.

For the global CO_2 emissions of OPC clinker production it was considered two types of contributions: (i) CO_2 from raw-materials, that can be taken from the chemical composition of the clinkers considered and (ii) CO_2 from fuel consumption that was taken through the analysis of heat balances for estimated production processes of each of the hydraulic binders studied.

It was admitted that a 525 kg of CO_2 are emitted from raw materials in the production of one ton of OPC clinker, which corresponds to a raw-materials/clinker weight ratio of 1.55 as suggested by the reporting standards of CSI (Cement Sustainability Initiative) [190]. The contribution of the CO_2 emitted from raw materials for all the hydraulic binders produced in this work was calculated from their theoretical chemical compositions, assuming that all the CaO present in these materials was introduced in the form of $CaCO_3$, being these values summarized in Table 9-3. In addition it was considered the emission factors presented in the Table 9-2 for typical fuels used in the cement industry, distributed in a fuel mix as also indicated in the same table and whose values were collected from the 2013 sustainability report of the InterCement group [191].

Taking into account these considerations, a parallel comparison of the heat input/ouput in each stage was made, being shown in detail in Table 9-1 the five aspects considered relevant in the estimation of the heat balance of the production of an amorphous hydraulic binder with a C/S molar ratio of 1.1, which include the contribution from kiln reactions, calcination, heating of raw-meal, the heat losses by several phenomena and also the heat recovery that add up a positive contribution to the total heat consumption and has as main source the contribution from the clinker cooling.

Table 9-1. Comparison of the total heat consumption balance between the production process used for OPC clinker and an estimated process thought for the production of an amorphous hydraulic binder with a C/S molar ratio of 1.1, with a theoretical chemical composition equal to the one presented in Table 6-1. Cells highlighted in orange refer to OPC clinker process while the cells highlighted in light blue refer to the estimated production process of the amorphous hydraulic binder.

Stage	Description	Heat Value (kJ/kg)	Reaction	wt%	Heat partial (kJ/kg)	Heat total Stage (kJ/kg)	Ref.	Observations
Kiln Reactions	ΔH fusion Wollastonite	494,0	Solid → Liquid	100%	494,0	404,4	[192]	It was considered a complete fusion of raw meal with previous formation of 100% wollastonite while in the case of OPC clinker it was considered the fusion of C_3A and C_4AF by 20% in weight.
	ΔH reaction Wollastonite	-89,6	$CaO + SiO_2$ → $CaSiO_3$	100%	-89,6		[193]	
	ΔH reaction Belite	-734,0	$2CaO + SiO_2$ → Ca_2SiO_4	13%	-95,4	-318,7	[3]	
	ΔH reaction Alite	-495,0	$3CaO + SiO_2$ → Ca_3SiO_5	67%	-331,7		[3]	
	ΔH reaction C_3A	-27,0	$3CaO + Al_2O_3$ → C_3A	12%	-3,2		[3]	
	ΔH reaction C_4AF	-105,0	$4CaO+Al_2O_3+Fe_2O_3$ → C_4AF	8%	-8,4		[3]	
	ΔH fusion Aluminoferrates	600,0	Solid → Liquid	20%	120,0		[194]	
Calcination	CO_2 removal from Raw meal	1536,9	$CaCO_3$ → $CaO + CO_2$	100%	1536,9	1536,9	[3]	28.1% less energy needed to calcine the raw materials.
	CO_2 removal from Raw meal	2138,0	$CaCO_3$ → $CaO + CO_2$	100%	2138,0	2138,0	[3]	
Heating of Raw-Materials	Heating from room temperature to 1450°C	1821,7	ΔT (T_{room} - 1450°C)	100%	1821,7	1821,7	[195]	Lower fuel consumption in the heating of the raw materials as the mass of raw materials needed to produce 1 ton of clinker is reduced (1,38 ton instead of 1,55 ton)
	Heating from room temperature to 1450°C	2050,0	ΔT (T_{room} - 1450°C)	100%	2050,0	2050,0	[195]	
Heat losses	Radiation, convection preheater tower	137,9		100%	137,9	1423,1	[194]	A lower heat loss from the exit of hot gases was considered, by assuming CO_2 as the major contributor. Possibly the heat losses by radiation will also be lower since the mass of raw materials needed for the production of a ton of clinker is also reduced (1,38 ton instead of 1,55 ton).
	Radiation, convection Kiln and Cooler	224,3		100%	224,3		[194]	
	Heat lost in exit gases from preheater	464,7		100%	464,7		[194]	
	Heat lost from exit dust	68,3		100%	68,3		[194]	
	Heat lost in clinker	88,0		100%	88,0		[3]	
	Water evaporation	13,0		100%	13,0		[3]	
	Heat lost in air from cooler	427,0		100%	427,0		[3]	
	Radiation, convection preheater tower	155,2		100%	155,2	1630,7	[194]	
	Radiation, convection Kiln and Cooler	224,3		100%	224,3		[194]	
	Heat lost in exit gases from preheater	646,5		100%	646,5		[194]	
	Heat lost from exit dust	76,7		100%	76,7		[194]	
	Heat lost in clinker	88,0		100%	88,0		[3]	
	Water evaporation	13,0		100%	13,0		[3]	
	Heat lost in air from cooler	427,0		100%	427,0		[3]	
Heat Recovery	Clinker cooling	-1400,0		100%	-1400,0	-1844,4	[5]	It was considered a lower heat recovery from the cooling of CO_2 in a 70% proportion for the case of the amorphous binder. It was also eliminated the contribution from the recrystallization of the melt.
	Cooling of CO_2	-359,4		100%	-359,4		[5]	
	Cooling of water (ex. clays)	-85,0		100%	-85,0		[5]	
	Crystallization of melt	0,0		100%	0,0		[5]	
	Clinker cooling	-1400,0		100%	-1400,0	-2090,0	[5]	
	Cooling of CO_2	-500,0		100%	-500,0		[5]	
	Cooling of water (ex. clays)	-85,0		100%	-85,0		[5]	
	Crystallization of melt	-105,0		100%	-105,0		[5]	
Process Total	C/S=1.1 Amorphous			100%		3341,7		Fuel consumption is expected to be reduced in 2.0% when compared to the typical OPC Clinker production.
	Clinker OPC			100%		3410,0		
			Differential			-68,3		
			Differential %			-2,0%		

Table 9-2. Emission factors for typical fuels used in the cement industry. A fuel mix example taken from the InterCement sustainability report of 2013 is also indicated.

Fuel type	$kgCO_2/GJ$	Reference	Fuel Mix (%)	Reference
Petcoke	92.8±2.1	[190]	86	[191]
Waste Oil	74.2±5.6		7	
Solvents	73.8±14.9			
Animal Meal	89.2±6.5		7	

Table 9-3 summarizes the values of CO_2 emissions from the two major contributions of the estimated processes considered for the production of the low-calcium content hydraulic binders referred along this work. Detailed information of the considerations made for the production processes of the hydraulic binders with C/S molar ratios of 2.0, 1.4 and 1.25, listed in the Table 9-3, can be found in the annexes section, where similar analysis to the performed for the amorphous hydraulic binder with C/S molar ratio of 1.1 (see Table 9-1) were conducted.

Table 9-3. Summary of the estimated overall CO_2 emissions that may result from the production of the hydraulic binders mentioned in this work. The raw materials and the fuel contributions are indicated separately as well as the overall CO_2 emissions value for each case.

	Raw Materials		Fuel		Total	
	$kgCO_2$/ton clinker	Differential	$kgCO_2$/ton clinker	Differential	$kgCO_2$/ton clinker	Differential
OPC Clinker	525,0	--- ---	311,1	--- ---	836,1	--- ---
2.0 Belite Clinker	457,8	-67,2 *-12,8%*	243,7	-67,4 *-21,7%*	701,5	-134,6 *-16,1%*
1.4 Dendritic Clinker	397,9	-127,1 *-24,2%*	259,7	-51,4 *-16,5%*	657,6	-178,5 *-21,3%*
1.25 Amorphous Clinker	401,3	-123,7 *-23,6%*	317,6	6,5 *2,1%*	718,9	-117,2 *-14,0%*
1.1 Amorphous Clinker	377,4	-147,6 *-28,1%*	304,9	-6,2 *-2,0%*	682,3	-153,8 *-18,4%*

9.2 Discussion

It can be seen from Table 9-3 that all the alternative production processes of low-calcium hydraulic binders covered in this work present lower total CO_2 emissions when compared to the existing OPC clinker production process. However, as seen in previous chapters of this work, none of the hydraulic binders, by their own action, present mechanical strength

developments capable to be competitive with OPC. Nevertheless, some alkali-activated pastes produced with amorphous hydraulic binders with molar C/S ratios of 1.1 have shown very interesting mechanical behaviors, developing compressive strengths higher than OPC even from the early ages of hydration. In order to assess a relation between the CO_2 emissions resultant from the production of a given hydraulic binder and their respective compressive strength at all ages two indicators were defined, being their results shown in the last two sets of rows in Table 9-4. The former is the *CO_2/MPa factor* that is described as the ratio between the process related emissions of a given hydraulic binder and the corresponding compressive strength at each age, i.e, $CO_2 / MPa_{i,xdays} = \frac{CO_2 emissions_i}{CSV_{i,xdays}}$ where $CO_2 emissions_i$ is the process related CO_2 emissions of the hydraulic binder *i* (in kg CO_2/ ton clinker) and $CSV_{i,xdays}$ is the compressive strength value (in MPa) obtained by the hydraulic binder *i* at *x* days of hydration. The latter indicator is the compressive strength target values (*CSTV*) that are also depicted in Figure 9-1 for each hydraulic binder tested in this work and can be defined as the value to which a *CO_2/MPa factor* equivalent to the obtained by the OPC clinker at the same age is achieved if taken into consideration the CO_2 emissions related to the production processes of each hydraulic binder, i.e, the *CSTV* of a given hydraulic binder was calculated according to the following expression:

$$CSTV_{i,xdays} = \frac{CO_2 emissions_i}{CO_2 / MPa_{OPC,xdays}}$$

Where $CSTV_{i,xdays}$ is the compressive strength target value (in MPa) of the hydraulic binder *i* at *x* days of hydration, $CO_2 emissions_i$ is the process related CO_2 emissions of the hydraulic binder *i* (in kg CO_2/ ton clinker) and $CO_2 / MPa_{OPC,xdays}$ is the *CO_2/MPa factor* obtained by OPC clinker at x days of hydration. In the particular case of OPC the values of the *CO_2/MPa factor* taken as reference for the 7, 28 and 90 days of hydration were, respectively, 23, 14 and 10 kg of CO_2 per MPa obtained in paste prepared with one ton of clinker. This indicator served as benchmark for all the other hydraulic binders, representing the efficiency of CO_2 used per unit of compressive strength gained, hence its use in the definition of the compressive strength target values for all the hydraulic binders.

The parallel comparison between the production processes of OPC clinker and the amorphous hydraulic binder with C/S molar ratio of 1.1, shown in Table 9-1, indicates that a reduction of nearly 2% in the process heat with advantage for the amorphous hydraulic binder. This reduction translates into a decrease of CO_2 emissions due to fuel consumption of about 6.2 kg per ton of clinker, as shown in Table 9-3, considering the fuel mix presented in Table 9-2 and respective emission factors. However, when adding up the contribution from the reduction of CO_2 that is emitted through the calcination of raw materials, the global CO_2 emissions reduction in the process can go over 150 kg per ton of hydraulic binder, when compared to OPC clinker, as it can be taken from Table 9-3 above, which translates in a reduction of the process related CO_2 emissions of more than 18% in weight. When analyzing these values together with the corresponding compressive strengths obtained in pastes through the consideration of the *CO_2/MPa factor*, as shown in Table 9-4, it can be seen that, even for different cooling conditions used, within the range of -10 to -30 $^oC/s$ (air to water-cooling conditions), the values of the *CO_2/MPa factor* obtained for the 28 days of hydration are very similar, although at 7 days the water-cooled sample presents some advantage. It is also possible to observe from Table 9-3 that the *CO_2/MPa factor* values of the amorphous hydraulic binders with C/S molar ratio of 1.1 present a consistent decrease from ~100 to ~20 as the age of hydration goes from 7 to 28 days, reaching values of around 15 for 90 days of hydration. The values of *CO_2/MPa factor* presented by these binders, especially at 28 and 90 days, do not fall too far from the ones presented by OPC clinker, however they are yet not competitive with this binder. Amongst the pastes prepared from the hydraulic binders with C/S molar ratio of 1.1, the worst case appears for the furnace-cooled sample, with very high *CO_2/MPa factor* values both at 7 and 28 days, revealing that the control of the cooling conditions during the production of the amorphous low-calcium hydraulic binders is of extreme importance, since the calcium silicate phases that crystallized under lower cooling rates do not present hydraulic ability, diminishing the quality of the hydraulic binders obtained.

Table 9-4. Resume of the compressive strength values obtained by the pastes produced along this work, their respective estimated process related CO_2 emissions and the calculated values of the *CO_2/MPa factor* and Compressive Strength Target Values.

Chapter referred	Water/ binder	Sample description	Molar C/S	CO_2 Process emissions ($kgCO_2$/ton clinker)	Strength (MPa)			*CO_2/MPa factor*			Compressive Strength Target Values (*CSTV*)		
					7 days	28 days	90 days	7 days	28 days	90 days	Target 7 days	Target 28 days	Target 90 days
6 to 8		**Reference Clinker**	3,2	836,1	36,9	58,3	82,8	23	14	10	36,9	58,3	82,8
5		**Non-activated Dendritic Belite**	1,4	657,6		4,1			160				
5		**Na_2SiO_3 activated Dendritic Belite**	1,4	657,6		37,8			17		29,0	45,9	65,1
6		**Sample B Amorphous 1.25**	1,25	718,9	7,5	23,8	33,2	96	30	22	31,7	50,1	71,2
6		**Sample A Amorphous 1.1**	1,1	682,3	6,8	32,2	45,4	100	21	15	30,1	47,6	67,6
7		**Non-Activated Amorphous**	1,1	682,3	6,6	35	46,4	103	19	15	30,1	47,6	67,6
7	**0.375**	**Na_2SiO_3 activated Amorphous**	1,1	682,3	42,2	77,7	76,9	16	9	9	30,1	47,6	67,6
7		**Na_2CO_3 activated Amorphous**	1,1	682,3	18,3	45,3	62,9	37	15	11	30,1	47,6	67,6
7		**Na_2SO_4 activated Amorphous**	1,1	682,3		41	68,3		17	10	30,1	47,6	67,6
8		**Water-Cooled**	1,1	682,3	16,8	34,1		41	20		30,1	47,6	67,6
8		**Air-Cooled**	1,1	682,3	6,7	27,5		102	25		30,1	47,6	67,6
8		**Liquid Nitrogen-Cooled**	1,1	682,3	7,9	25,9		86	26		30,1	47,6	67,6
8		**Furnace-Cooled**	1,1	682,3	0,3	2,1		2274	325		30,1	47,6	67,6
6		**Reference Clinker**	3,2	836,1		111,9			7			111,9	
5	**0.25**	**Reference Belite Clinker**	2	701,5	0	0,9	2,8		779	251	31,0	48,9	69,5
5		**Dendritic Belite**	1,4	657,6	2,4	5,8	12,9	274	113	51	29,0	45,9	65,1

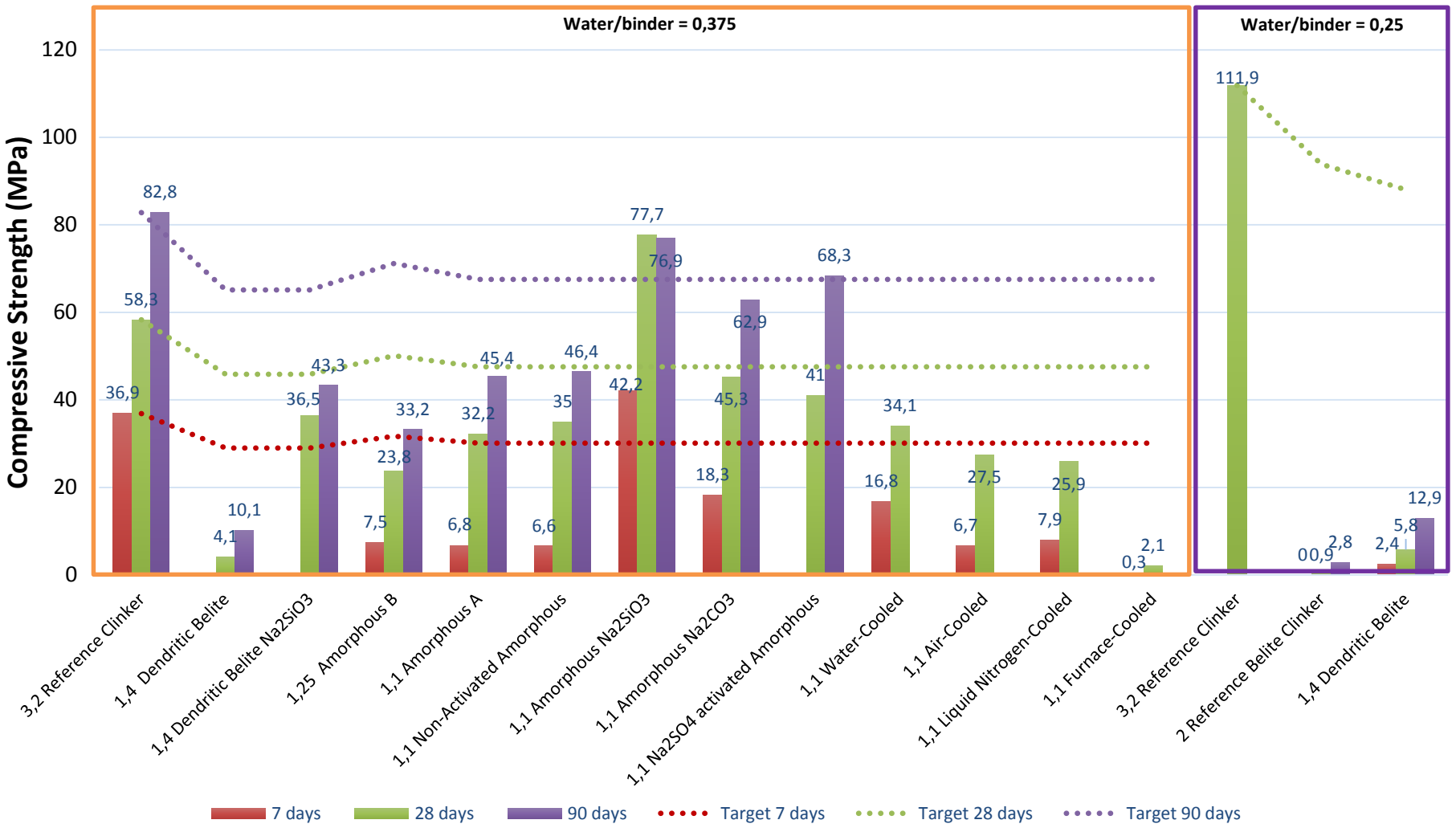

Figure 9-1. Compressive strength results summary for all the pastes referred along this work. The results at 7, 28 and 90 days of hydration are plotted and also the compressive strength values of OPC Clinker are indicated for comparison. The dashed lines correspond to the compressive strength target values at each day for all the binders produced, taking as reference the *CO_2/MPa factor* obtained for the OPC clinker at each hydration age and the process related CO_2 emissions of each hydraulic binder.

On the other hand, the best case identified in the pastes produced refer to the sodium silicate activated samples, which present lower *CO_2/MPa factor* values than the ones presented by OPC clinker even at the early ages, further maintaining its competitive values for longer ages. Also the pastes prepared with sodium carbonate and sodium sulfate seem to present competitive values with the reference clinker when considering the same indicator, with the Na_2SO_4-activated sample presenting a compressive strength slightly higher than the *CSTV* calculated for this hydraulic binder at 90 days, as it can be seen in Figure 9-1.

It should be noted that it was not considered the CO_2 emissions related with the production of any of the alkaline solutions used in the preparation of the pastes and only the CO_2 reduction attributed to the production process of the base hydraulic binders was taken into account. However, as reference, the production of sodium silicate was referred by McLellan et al. [196] to release approximately 350kg of CO_2/ton Na_2SiO_3, and, therefore, any effect in the *CO_2/MPa factor* values would be mandatorily positive, since any mix of this activator with the hydraulic binder of C/S molar ratio of 1.1 is expected to result in a decrease of the overall process related CO_2 emissions (considered to be fixed at a value of 682,3 kgCO_2/ton clinker).

The pastes prepared with the amorphous binders with CS molar ratio of 1.25 present a slightly better performance than the pastes made with the binder with C/S molar ratio of 1.1 at 7 days, however this behaviour is lost at the 28 and 90 days, which combined with higher process related CO_2 emissions result in higher CO_2/MPa factor values. Thus, also this group of hydraulic binders fail to be competitive with OPC clinkers on their own, however no tests have yet been performed in order to assess the mechanical behaviour of this type of hydraulic binders under alkaline activation.

The dendritic belite clinkers with C/S molar ratio of 1.4 fall outside the group of the mainly amorphous hydraulic binders, having as primary features the very fine micromorphology of their belite crystals, which represent the most active part of these clinkers and also the main advantage over the typical round belite clinkers that were shown to possess a slower hydraulic reaction when compared with the dendritic ones. This improvement in the reactivity kinetics had some impact in the mechanical performance of these clinkers, developing compressive strengths higher than the observed for the round belite clinkers at all ages, which combined with lower estimated process related CO_2 emissions translated in lower values of the CO_2/MPa indicator. Nevertheless the mechanical performance of the pastes prepared with dendritic belite clinkers is way below the desired values to be competitive with OPC clinker. An

explanation to the low performance of the dendritic belite clinkers might be found in glass part of these clinkers, since the amorphous matrix that embed the dendritic crystals is thought to be hydraulically inactive, being characterized by C/S molar ratios around 1.0 with some fluctuations in its composition that is suggested to have a gradient profile with regions richer in Ca closer to the surface of the dendritic belite crystals. These amorphous regions richer in Ca should have a theoretical composition corresponding to the eutectic valley, shown in the $CaO\text{-}SiO_2$ diagram of Figure 2-2 for the C/S=1.4 composition, i.e. a C/S ratio around 1.25, resulting that, away from the periphery of the dendritic crystals and towards the interior of the glassy matrix an amorphous calcium silicate with a C/S molar ratio around 0.8 is very likely to be formed. As it was seen in chapter 6, such low C/S amorphous materials do not present any hydraulic behaviour, thus limiting the contribution to the development of strength to the crystalline dendritic part that only represents as much as 50% in weight of the clinker. It should also be noted that the hydration products formed in both situations (dendritic clinkers with C/S=1.4 and amorphous calcium silicate with C/S=0.8) contained Monohydrocalcite, which was not found in any other paste tested, suggesting that effectively part of the dendritic clinker might be constituted by an amorphous region with C/S molar ratio around 0.8.

Further tests made with these dendritic clinkers with C/S molar ratio of 1.4 under Na_2SiO_3 activation indicated that its glassy matrix, if submitted to higher alkaline environments, can dissolve and contribute to the development of strength together with an enhanced reactivity of the belite dendritic crystals. Nevertheless, the compressive strength values obtained by the Na_2SiO_3-activated dendritic clinkers are much lower than the obtained by the activated amorphous binders with C/S of 1.1 (37,8 vs. 77,7 MPa at 28 days, respectively), which also translates into higher *CO_2/MPa* values.

9.3 Conclusions

Table 9-4 summarizes the most important aspects regarding mechanical performance and individual CO_2 process related emissions for all the pastes prepared from the hydraulic binders produced and studied in this work. From the analysis of the results shown in this table it is possible to conclude that the generality of the estimated process related CO2 emissions for all the materials studied fall below the values presented by the BAT for the production of OPC clinker, however, in terms of mechanical performance, only the paste prepared with the

amorphous hydraulic binder with a C/S molar ratio of 1.1 mixed with a Na_2SiO_3 activator showed to be competitive with OPC clinker, presenting lower CO_2/MPa values at all ages. Also the paste produced with the same binder and mixed with Na_2SO_4 showed a slightly better CO_2/MPa value than OPC clinker but only after 90 days of hydration.

Considering the estimated process related CO_2 emissions of the Na_2SiO_3-activated amorphous hydraulic binder, it is possible to observe that approximately 20% in weight of CO_2 can be saved, when compared to the production of OPC clinker, without disregarding the mechanical performance of these hydraulic binders. It was also possible to observe that the activation with Na_2SiO_3 had very different efficiency when applied to the dendritic clinkers with a C/S of 1.4 or when used in amorphous hydraulic binders with a C/S ratio of 1.1, resulting better in the latter case, as it can be seen both in Table 9-4 and Figure 9-1. This phenomenon is thought to occur due to the differences in the constitution of these hydraulic binders in terms relative percentage of amorphous phase but also due to differences in the glass matrix composition, which might present a higher degree of condensation in the case of the dendritic clinker.

All the other pastes prepared during this work failed to be mechanically competitive with OPC clinker under the same preparation conditions. Nevertheless it was possible to identify an optimal C/S molar ratio value at 1.1 that allow the production of the better performing amorphous hydraulic binder amongst the series of compositions studied, showing to develop approximately half the mechanical strength registered for an OPC clinker at 28 and 90 days.

Of course that limited chemical composition variation was tested and the effect of the minor elements in the reactivity and mechanical behavior of such group of amorphous hydraulic materials is yet left open to investigate. For example it is known in literature that, in the case of GGBFS, Al_2O_3 contents above 13% in weight tend to increase early strength and also other oxides such as MgO or P_2O_5 might induce variable effects [3].

A final remark should be done regarding the technological aspects inherent to the production of the referred hydraulic binders since although it was considered the use of the clinker route as a technologically viable and adequate solution to produce these highly amorphous hydraulic binders, it is expected that the industrial production of these type of clinkers will present technical challenges that are far from being addressed presently. It is clear that the question of the stabilization of such an acidic melt and the need for a relatively high cooling speed, may be incompatible with the state of the art of rotary kiln cement production, raising

some concerns about the adequate type of refractory lining to be used or on the ideal architecture of the cooler, although it is not yet known if any major transformations will have to necessarily be made to the existing industrial installations in order to adapt the process to the production of these amorphous hydraulic binders. Nevertheless, other approaches, such as the processes recently patented by Paul Wurth SA [197, 198] or by Primetals Technologies Austria GmbH [199] for slag granulation at high cooling speeds, with energy recovery, may also be a possible route for the industrial production of these binders. In any case it would be desirable to take advantage from the existing equipment and to implement a process that can run continuously in controlled conditions.

10 General conclusions

The work developed in the present thesis dealt with the production of new environmentally friendly hydraulic binders with low calcium content, having as main purpose the reduction of the process related CO_2 emissions, when compared with the production of OPC clinker. Two conceptual approaches were tested and evaluated, with the first being related with the morphological control of belite crystals within a glassy matrix of a clinker, while the second approach focused in the production of almost fully amorphous materials in order to take advantage from the known instability of this type of materials to act as hydraulic binders.

Some advances were achieved along the conduction of the present work considering the general objective proposed in this thesis. In fact, as far as the author knows, these are the first results reported on the study of such low calcium content hydraulic binders using these approaches, with these first findings opening the possibility of a future development of new environmentally friendly hydraulic binders.

The different approaches used resulted in the production of different products with distinct hydraulic behaviors, being the main conclusions of this study described in the next sections.

10.1 Dendritic Belite Clinkers

A process was designed specifically for the production of dendritic belite clinkers, consisting in a two cooling step sequence, where the first step was intended to induce the growth of the dendritic structures while the second cooling step served to stabilize and “freeze” the obtained structures. The morphological control of dendritic structures was achieved by varying the time of the first cooling step, with larger times resulting in the thickening of the dendritic arms formed, however, for the compositions tested, the formation of dendritic belite crystals was limited to an extent of about 50% in weight, with the remaining consisting in a glassy matrix phase of variable composition.

The hydraulic behavior of these dendritic belite clinkers was tested against a reference belite clinker with round shaped belite crystals. Even though these dendritic clinkers are only constituted by approximately 50% in weight of belite crystals, it was shown that they possess a faster reaction with water than the reference clinker, at least until the 90 days of hydration.

They also present a faster compressive strength development, which resulted in compressive strength values that went over 4 times the ones observed for the reference belite clinker, as shown in Figure 5 11.

The increase in strength is suggested to be related with the formation of calcium silicate hydrates that, according to the information collected by EDS, presents a low C/S ratio. Evidences for the formation of such C-S-H structures were found through the conduction of FTIR and ^{29}Si MAS NMR experiments, while XRD was only able to quantify an increase of the amorphous component as hydration of the dendritic clinkers took place. Due to the amorphous nature of these hydration products, the structural analysis techniques of FTIR and ^{29}Si MAS NMR revealed to be very useful complementing the information acquired by XRD, since their sensibility allows the detection of the very short range order of the developing hydrated silicate structures.

Regarding the activation test performed to the dendritic clinker using a mixed solution of NaOH and Na_2SiO_3, it was seen that the impact of this activator was very effective in the development of strength at least until the 28 days of hydration, with the activated paste presenting values of compressive strength approximately 10 times higher than the obtained for a paste prepared under the same conditions but without activator solution. It could be seen by XDR-Rietveld analysis the occurrence of an increase in the belite reactivity in the case of the activated paste, which, however, didn't seem to be high enough to ensure the formation of all the hydrated products and to justify the differences observed in terms of mechanical performance. This fact, suggests that the paper of the amorphous matrix of these dendritic clinkers should not be neglected under these conditions of alkali-activation, where the value of pH is high enough to break the silicate network. Thus, it is thought that the semi-crystalline C-S-H structures formed under alkaline activation of the dendritic clinkers may have their origin in the dissolution of the calcium silicate amorphous matrix due to the higher pH in the solution, greatly contributing to the improved mechanical performance of the activated dendritic clinker when compared to the non-activation condition.

As it was seen, the estimated process related CO_2 emission values for the production of the studied dendritic belite clinkers are lower than the typically observed for OPC clinkers, however the mechanical performance of these clinkers is yet too low to be considered competitive with OPC clinker and even in the alkali-activated situation, these clinkers still present *CO_2/MPa* values far from the desired to be closely compared with OPC clinker.

10.2 Amorphous Hydraulic Binders

The production of the amorphous hydraulic binders was conceptually thought to take benefit from the known high instability of these materials due to the fact that these materials are typically obtained under non-equilibrium conditions that usually consist in using high cooling rates during their production. In fact the main production process developed for the production of the amorphous hydraulic binders consisted in a sequence of steps that include the melting of the raw materials, followed by a quench in non-forced air. However, other cooling conditions were tested, namely water-, liquid nitrogen- and furnace-cooling, being observed that, depending on the cooling rate used in the production of these amorphous hydraulic binders, the amount of crystalline phases also differed, presenting higher amounts of crystalline phases (typically wollastonite forms) as the cooling rate decreased. Yet, small differences in the compressive strength values were found, when analyzing the mechanical properties of pastes prepared with clinkers obtained under cooling rate conditions ranging from around -10 to -30^{o}C/s, where the extent of crystalline wollastonite do not exceed the 10% in weight. This means that the process conditions can vary within this interval without compromising the mechanical properties of the amorphous hydraulic binders. A schematic of the range of suitable operational conditions for the production of highly amorphous hydraulic binders is shown in Figure 10-1. As referred in chapter 8 the most critical step in the amorphization of the hydraulic binders is the temperature region between the corresponding melting temperature and glass transition temperature for the composition used, with this aspect being also indicated in Figure 10-1.

The phase development characterization of the hydrated pastes produced by mixing the amorphous hydraulic binders with water indicated to exist an optimum C/S molar ratio in terms of reactivity, being maximized at the value of 1.1. Higher C/S ratios (1.25) ended up resulting in less reactive materials that developed lower compressive strength than the samples with C/S molar ratio of 1.1. Furthermore, amorphous samples with C/S molar ratios of 0.8 and 0.9 were also tested in this work, with both presenting complete absence of hydraulic properties. However the sample with C/S molar ratio of 0.9 presented a pozzolanic character when mixed with OPC, which acted as an activator that triggered its dissolution by increasing the pH value and therefore bringing into solution larger amounts of $[SiO_4]^{4-}$ species

that would react with the dissolved Ca^{2+} ions and promote the formation of hydrated products.

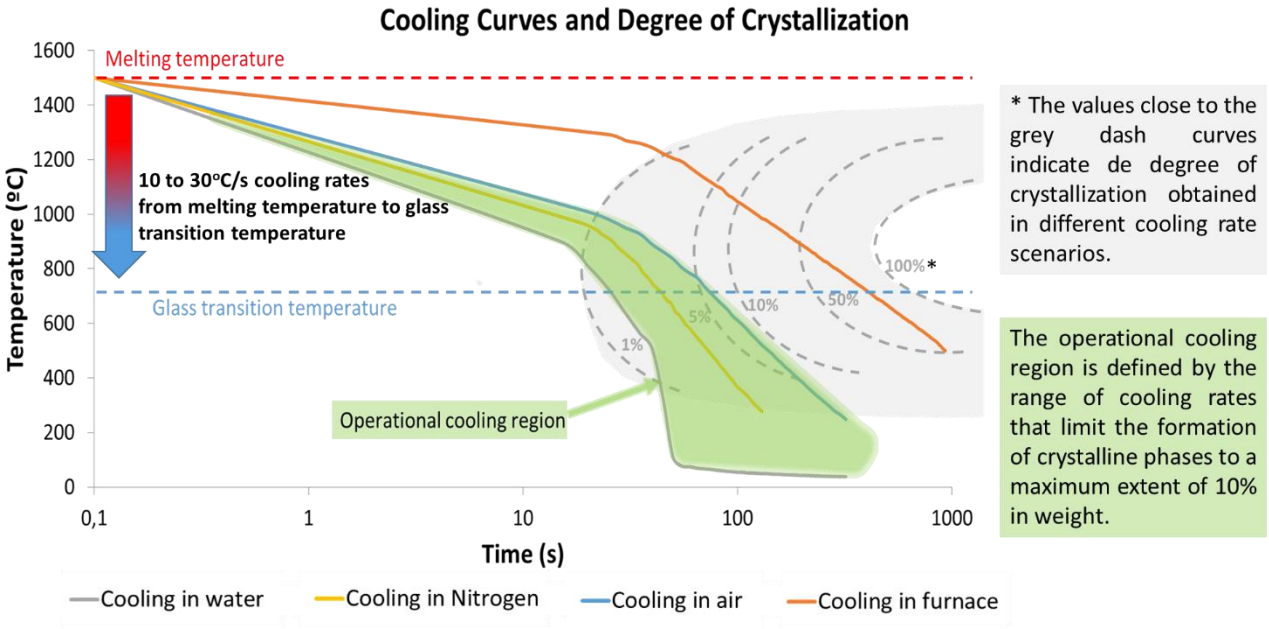

Figure 10-1. Resume of the ideal process conditions and characteristics of the hydraulic binders produced. Operational range of cooling rates is identified as well as the resulting typical range of crystal weight percentage values acceptable in the production of the amorphous hydraulic binders with C/S molar ratio of 1.1.

It was seen that the hydration of these amorphous materials occurs without the formation of other products than C-S-H, indicating that the stoichiometry of the resultant hydrated phases should be very close to the initially present in the precursor anhydrous materials. In the case of the amorphous hydraulic binder with a C/S molar ratio of 1.1 a stoichiometry of $\boldsymbol{C_{1.1}SH_{0.82}}$ was estimated. Considering this stoichiometry and since no other hydration products are formed, it was determined that in order to achieve complete hydration of these materials only 12% in weight of water is needed, significantly differing from the values typically reported for OPC that range from 0.39 to 0.44 and translating into direct water savings in the production of concrete as well as less porous structures are expected to be formed, leading to denser and less permeable hydrated structures that may develop better chemical resistance to a large type of aggressive environments.

Contrarily to the C-S-H products formed during the hydration of the dendritic clinkers, the amorphous hydraulic binders give rise to more crystalline calcium silicate hydrates containing

regions of Tobermorite-like structures that can be identified by ^{29}Si MAS NMR and FTIR but also by XRD.

The alkaline activation of these amorphous hydraulic binders resulted in an increase in the compressive strength of the respective pastes from the early ages and showed that, under these conditions, these hydraulic binders can be competitive with OPC clinker even in terms of mechanical performance. This faster gain in strength seems to be achieved by a larger formation of hydration products, which however maintain their semi-crystalline nature and are comparable to the hydration products formed in non-activated pastes. The kinetic effect is related to the use of alkaline solutions that trigger the dissolution of the silicate amorphous matrix that represent the overall backbone of these hydraulic binders, with the sodium silicate solution indicating greater impact as activator than the solutions containing Na_2CO_3 or Na_2SO_4. Isothermal calorimetry showed that activated pastes produced with these amorphous hydraulic binders release only approximately one third of the heat when compared with pastes prepared with OPC, indicating that, in some specific applications, some benefit can be taken from the use of these hydraulic binders systems.

The mechanism of reaction of these amorphous hydraulic binders can be compared to the described for GGBFS, where the dissolution of $[SiO_4]^{4-}$ species acts as the rate controlling step. It was observed that the less coordinated units (Q^0 and Q^1) play an important role in the reactivity of the amorphous hydraulic binders since these are the most readily available species to react and form hydration products. The dissolution of $[SiO_4]^{4-}$ species depend on the pH of the solution, thus the activation with alkaline solutions result in a faster development of strength in these pastes due to the increase in the amount of calcium silicate hydrates produced. However there seem to exist other factors influencing the nucleation and growth of C-S-H and consequently the development of strength, namely the existence of small crystals in low percentages within the amorphous matrix that may act as C-S-H nucleation sites, as well as the excess of energy contained in the net of the glass induced by severe cooling during production.

At last, a comparison between the production process of OPC clinker and an estimated production process of the several amorphous hydraulic binders tested in this work was made, with the estimation of the process related CO_2 emissions being favorable to the production of these amorphous hydraulic binders, mainly due to the large reduction in the CO_2 contribution from the raw materials. However, the assessment of the compressive strength of the tested

amorphous hydraulic binders revealed that these materials only become competitive with OPC when using alkaline activation, in special when adding sodium silicate solution. In this case, the pastes prepared from a mixture containing Na_2SiO_3 and NaOH and an amorphous calcium silicate hydraulic binder with a C/S molar ratio of 1.1 revealed a potential of CO_2 reduction of approximately 20% in weight, without disregarding the mechanical performances that may even surpass the ones registered for OPC clinker from the early ages on.

The results obtained in this work raised good perspectives into the development of a new group of hydraulic binders that might be able to compete with the existing OPC clinker in the future.

If the good mechanical properties of these hydraulic binders are confirmed by further tests, several benefits could be taken from both the process and the product characteristics. The next section will focus on each of these aspects (process and product), resuming the main Strengths and Opportunities of each aspect but also their related Weaknesses and Threats.

10.3 SWOT Analysis

Taking as basis all the information collected during this work, a resumed SWOT analysis of both the process and product (special focus was made on the amorphous hydraulic binder with C/S molar ratio of 1.1) was conducted in order to stress the main points of divergence between the present BAT and the process and products developed and tested along this work. Some of the points presented below were already discussed in this work while others will require further tests and evaluation to be fully confirmed.

10.3.1 Process Related Aspects

The strengths and weaknesses of the process were analyzed taking into account the different process characteristics, such as the use of a different raw materials mix, the presence of almost 100% of liquid phase in the kiln or the fact that less pure limestone will be required in the production of these new amorphous hydraulic binders. Also the opportunities and threats regarding the implementation of this new process were discussed.

10.3.1.1 Strengths

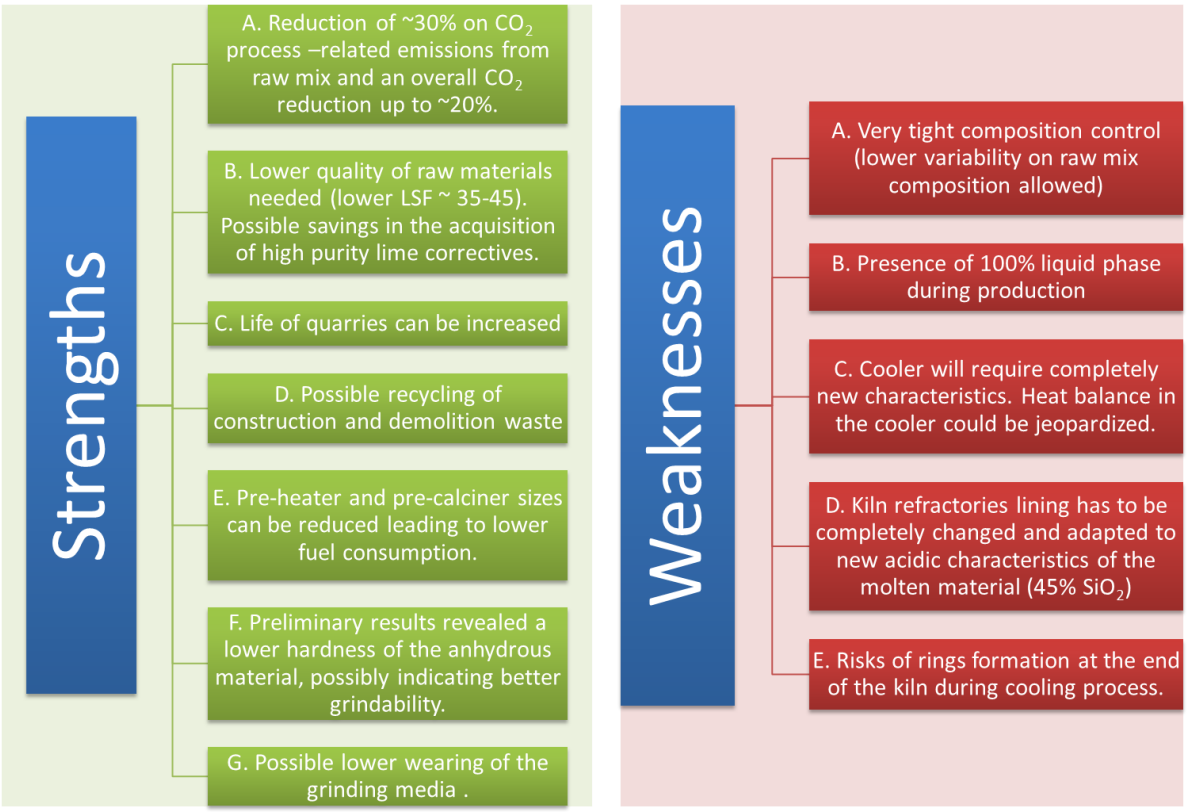

Figure 10-2. Strengths and Weaknesses analysis of the proposed production process.

Following the numbering of Figure 10-2, the topics presented are discussed below.

A. As seen in the previous chapter, the reduction of CO_2 emissions related to the raw materials mix used in the case of the production of the amorphous hydraulic binder with C/S molar ratio of 1.1 can reach values around 30% for the compositions tested. When combined with the heat balance from the process the overall CO_2 savings go up to 20% in weight. Of course that limited compositional variations were yet tested and further experiments may even indicate higher CO_2 savings.

B. Since the amount of calcium needed for the production of these amorphous binders is lower, the requirements regarding the quality of limestone may also decrease. In fact, the value of the lime saturation factor (LSF) corresponding to the raw meal used in the production of these amorphous hydraulic binders is only of around 45 while the production of OPC clinker requires values of LSF close to 100. One of the costs of production of OPC clinker is related to the acquisition of high purity limestone that sometimes has to be added to the raw mix in order to increase the levels of calcium in the

mixture. This problem would be reduced, if not eliminated, in the case of the production of the hydraulic binders with the compositions proposed in this work.

C. Another positive impact would be the increase of the lifetime of the existing quarries, since, as the quality requirements of the limestone would decrease, the amount of usable raw materials would increase, which would result in possible significant savings to cement companies. This factor would be very important to the strategy of cement companies since the use of own resources could be further optimized.

D. The use of construction and demolition waste may also be a hypothesis to consider in the production of amorphous hydraulic binders, as long as those wastes possess an overall chemical composition capable of being added to the raw mix.

E. The lower loss on ignition of the raw meal used also represents a lower mass of circulating materials inside the circuit, which means that an adjustment should be made regarding the size of the pre-heater and calciner in order to reduce the amount of heat supplied to that lower mass of circulating material. This would impact positively in terms of CO_2 emissions, as it was seen in chapter 9.

F and **G.** Preliminary hardness tests performed by using nanoindentation indicate lower hardness of the amorphous binders when compared to OPC clinker, which may indicate better grindability and, consequently, less wearing of the grinding elements.

10.3.1.2 Weaknesses

Using the sequence referred in Figure 10-2, the topics presented are discussed below.

A. Considering the compositions used in the production of the several amorphous binders, a tight chemical composition control of the raw meal should be necessary, however other compositions will be further tested in order to assess the need for such a tight composition control. Future improvements in the raw mix design might eliminate this concern.

B, **C**, **D** and **E.** As it was already referred in this work, the production process of amorphous materials involve the complete fusion of the raw materials, which may represent a serious problem to the adaptation of the OPC clinker kiln to the process proposed here. Several aspects should be revised, starting from the inclination of the kiln and extending to the type of refractory lining used to protect the interior of kiln. The more acidic melt, due to the presence of higher amounts of silica, represents a threat to the usual alumina based

refractory lining, creating the risk of alumina-silica reaction during production. Also the cooler would have to be re-thought in order to ensure a homogeneous cooling to all the incandescent liquid mass leaving the kiln at a sufficiently fast rate so that a glassy material ca be obtained. The excess of cooled air should not return back to the kiln in order to avoid the risk of formation of rings at the end of the kiln.

10.3.1.3 Opportunities

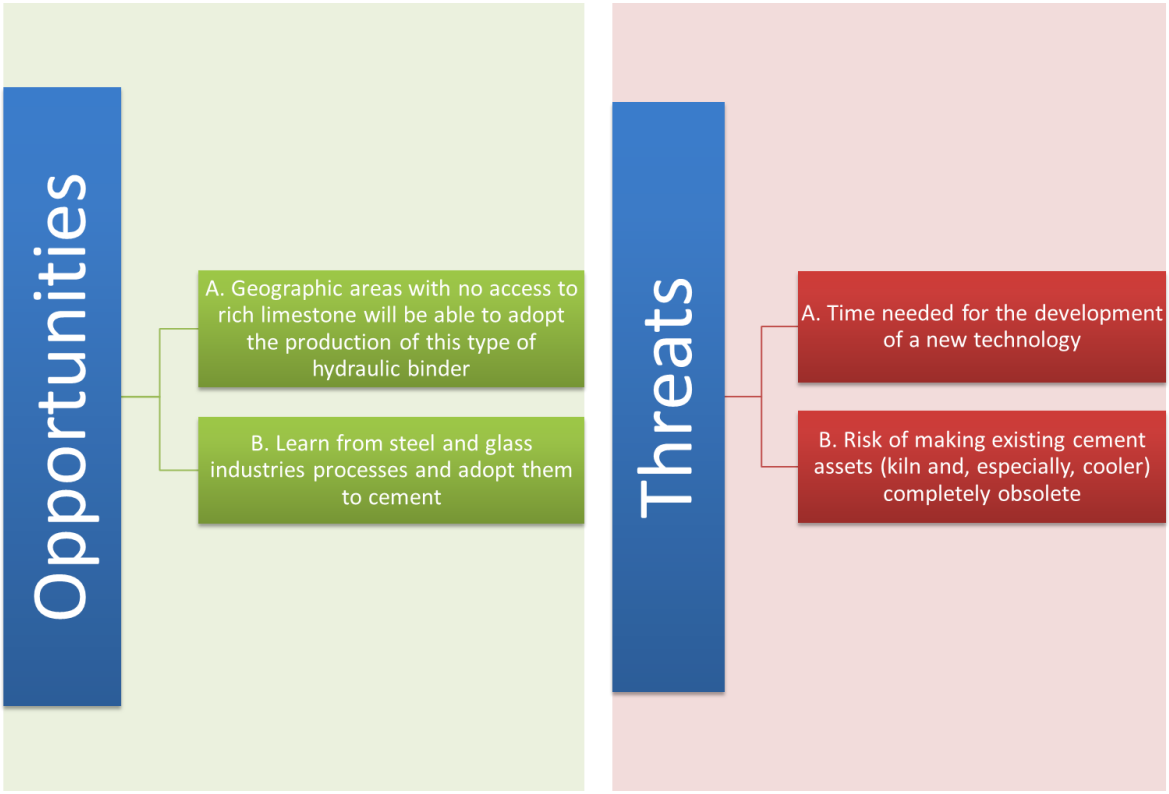

Figure 10-3. Opportunities and Threats analysis of the proposed production process.

From the sequence of topics listed in Figure 10-3, a discussion is made below.

A. The lower requirements of the limestone quality may also create new opportunities for the cement companies to find locations for new plants where before didn't existed viability due to the lack of high quality limestone resources.

B. Other industries, such as the steelmaking or the glass industry already have well-developed processes consisting in the melting and cooling of large masses of material. It could be beneficial to learn from those industries where all the important parameters needed to control have already been studied. Furthermore the existing technological

solutions used in these industries may also be adopted to the production of the new amorphous hydraulic binders.

10.3.1.4 Threats

The discussion of the topics referred in Figure 10-3 regarding the threats to the new process proposed is made below.

A. The development of a new technology is always a time consuming process that, depending on the number of adjustments to the existing technology, can possibly take several years to accomplish, as well as large amounts of capital investment will be needed to achieve a final technological solution.

B. If the number of adjustments needed to adapt the present technology are too big, there is always the risk of turning obsolete the existing assets, especially the kiln and the cooler.

10.3.2 Product Related Aspects

The main properties presented by these amorphous hydraulic binders were considered and are here analyzed as strengths and weaknesses, regarding its applicability and possible uses. Also, opportunities and threats for these new products are identified and discussed below.

10.3.2.1 Strengths

The topics identified as strengths in Figure 10-4 are discussed below, following the sequence presented.

A. It was seen by isothermal calorimetry that the heat of hydration of these amorphous hydraulic binders is only about one sixth of the registered for OPC, going up to one third in the case of using an alkaline activator. This characteristic makes this group of alternative binders attractive to be used in specific applications where a low heat of hydration is required without compromising the initial compressive strengths.

B. Preliminary results using nanoindentation tests in pastes prepared with these amorphous hydraulic binders suggest the formation of high-density C-S-H products, which is related to their low C/S ratio and to their arrangement in Tobermorite-like structures.

C. It was estimated a significant reduction in the amount of water necessary to fully hydrate these new hydraulic binders when compared to OPC clinker, which can result in less porous hydrated structures, enhancing the mechanical properties and also the resistance to chemically aggressive environments that could emerge as a positive consequence of the lower permeability through the hardened paste.

D. The anhydrous amorphous hydraulic binders present lower density than OPC clinker, which may be an advantage during the hydration process since the volume changes that might occur will be lower, resulting in a reduction of the probability of cracks development.

E. As it was seen, the hydration of these new low-calcium hydraulic binders proceeds in the absence of Portlandite, eliminating the problem of Portlandite carbonation due to the atmospheric CO_2 uptake that may result in structural damage due to local expansion in the sites where carbonation occurs.

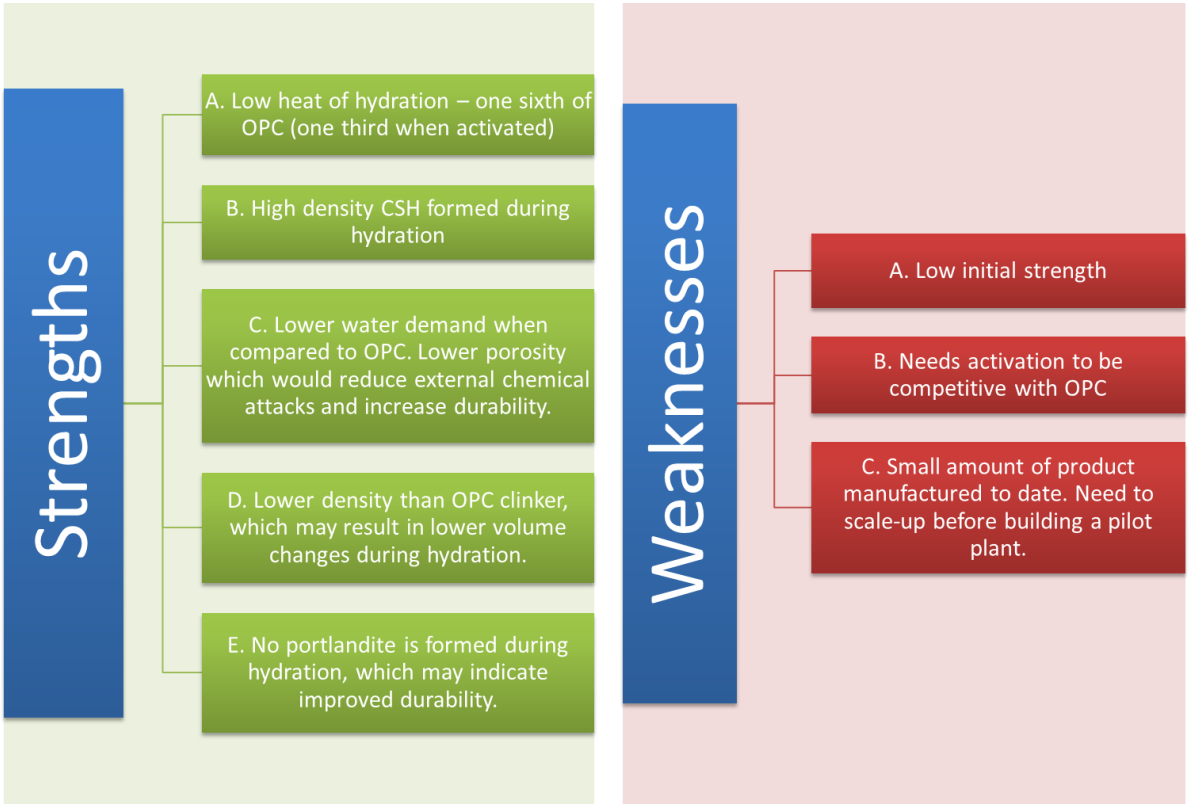

Figure 10-4. Strengths and Weaknesses of the new amorphous hydraulic materials developed in this work.

10.3.2.2 Weaknesses

Following the order of the topics presented in Figure 10-4, a discussion of the weaknesses of these new hydraulic binders is made below.

A and **B.** The compressive strength at the early ages of the pastes prepared with these new amorphous binders revealed to be considerably low when compared to OPC, only achieving interesting values at longer times of hydration. This fact makes necessary the use of an alkaline activator in order to attain mechanical performances competitive with OPC, which will represent additional costs for the production of an alternative hydraulic binder solution.

C. Until now, only small portions of these amorphous binders were produced, which has limited the scope of tests possible to perform to these materials. A larger production of these binders will be needed in order to fully characterize and optimize the product before proceeding into a transition to a pilot plant. A previous scale-up production should be tested, using a production process approximated to the idealized for the pilot plant.

10.3.2.3 Opportunities

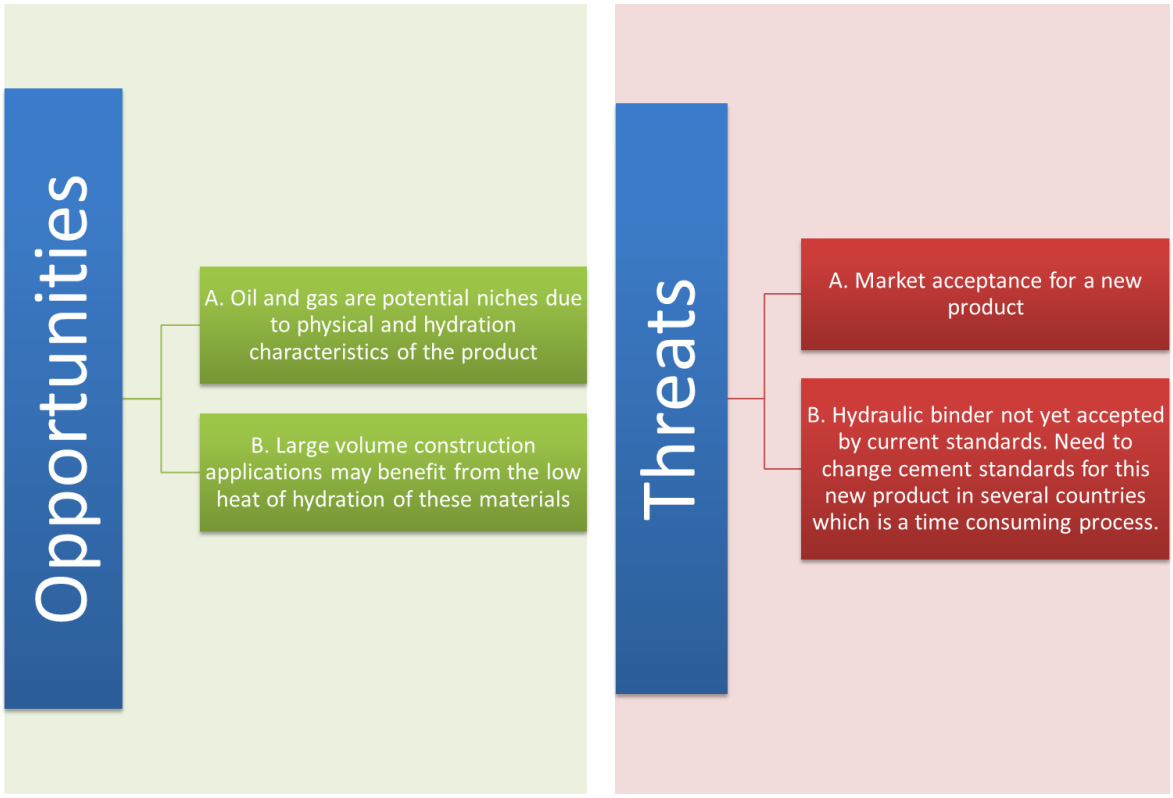

Figure 10-5. Opportunities and Threats considered for the new amorphous hydraulic materials developed in this work.

The points referred in Figure 10-5 as opportunities for the implementation in the market of these new amorphous binders are discussed below, following the same numbering as presented.

A. Some of the properties developed during the hydration of these new amorphous binders are considered as highly beneficial for some market niches where the specifications of the required materials are quite unique. In the case of oil and gas industries, the main requirements include low volume changes, low permeability, chemical durability and high stability. The latter point is very important and is highly dependent on the type of hydrated phases being formed. In the specific application of high temperature wells, where the temperatures of cement use can go above the 100^{o}C, the Tobermorite-like structures happen to be more stable than typical C-S-H with C/S ratios between 1.5 and 2.0, turning these amorphous hydraulic binders into a possible very interesting alternative to typical class G and H oil well cement.

B. Another interesting possible application would be the use of these binders in large volume constructions where a low heat of hydration is required. One alternative typically used is the addition of ice to the water with which is prepared the concrete, resulting in slower hydration rates and limiting the heat released from the hydration reactions to a non-dangerous value that will inhibit the occurrence of fractures due to thermal expansions. With the use of these new amorphous binders, the heat released would be intrinsically controlled, taking advantage from their low heat of hydration, ensuring improved mechanical performance even at the early ages.

10.3.2.4 Threats

The two aspects referred in Figure 10-5 as threats to these new hydraulic binders are discussed below.

A. OPC is a widely used construction material for the most generic purposes. Its position in the market is highly consolidated, which turns very difficult for any alternative solution to enter this market with the aim of replacing OPC even in very specific applications. Of course that further tests are still needed to confirm the aptness of these new binders to act as a reliable alternative solution to OPC, however when/if the good hydraulic

properties of these materials are confirmed, many work will still have to be done in order to introduce these new materials into the market.

B. The particularities presented by these hydraulic binders are outside the scope of any of the existing standards that regulate the characteristics and component constitution of construction materials. New performance-based standards should be developed in order to accept different alternative solutions to be used as construction materials. Such standards differ from region to region and the need to change cement standards to these new materials will be a time consuming process.

11 Future Work

The first results obtained on the development of these new low-calcium hydraulic binders have brought the knowledge on these materials to a point where many other questions raise and to which some attention should be directed in future work.

Also some efforts should be done in order to overcome the limitations that, so far, have turned impossible a large production of these hydraulic binders, restricting the types and amount of tests that can be performed with the samples produced in laboratory.

It is thus important to develop work following three different perspectives that encompass (i) the exploration of the potential that still exists regarding the development of the dendritic and (ii) amorphous hydraulic binders from a fundamental point of view, and (iii) the development of a primary scale-up of the production process before the transition to the pilot plant, with further optimization of the production parameters as well as the assessment of the properties of the resultant low C/S hydraulic binders.

The first two perspectives may still be optimized in terms of chemical composition tuning or in terms of process conditions. One of the aspects that still needs some investigation is the exploration of the suitability of other raw materials in the production of these new binders, as well as the assessment of a wider compositional range, with particular interest to the study of the impact in the increase of alumina, iron and magnesium weight percentages in the reactivity and hydraulic properties of these binders, as well as in the processing conditions, especially in the melting temperature and in the acidity of the melt. It is also of interest to optimize the granulometry and the respective water to binder relation in order to enhance the mechanical properties of the pastes produced with these binders.

Apart from these lines of development there are also some fundamental questions that were left open to answer with the execution of this work and will require further investigation. Regarding the first topic mentioned, it is necessary to study the mechanism of dendrite formation in these ceramic systems in order to increase the knowledge of the development of these structures to a level close to the already existing for metallic systems. Adding to this topic it is still necessary to study the feasibility of a general stabilization of the high temperature polymorphs of belite (α-C_2S) in the dendritic crystals as well as to understand the reason for the low reactivity of the endogenous amorphous matrix phase, aiming at an

improvement of its hydraulic behavior in order to obtain global enhanced hydraulic properties on these dendritic clinkers.

Considering the second topic, it is still unclear the mechanism of reaction of the amorphous hydraulic binders as well as the true chemical composition and mechanical properties of the hydration products formed. These questions may be answered in further work by the use of several techniques, including TEM with EDS quantification, nanoindentation and porosimetry by MIP or BET.

The use of TEM will allow to identify the semi-crystalline nature and extension of the hydrated products formed, providing also more detailed and direct information on the composition of such hydration products, which, so far, was only obtained by indirect measurements and estimated under some considerations.

Nanoindentation will allow to evaluate at a local scale the mechanical properties of the hydration products formed and also information crossing can be done with the use of SEM in order to obtain some chemomechanical insights on these products.

It is also necessary to assess the grindability or brittleness of the anhydrous hydraulic binders, with the use of nanoindentation, by determining the coefficient factor H/M where H is the indentation hardness and M is the indentation modulus.

The porosity of the resultant pastes should also be evaluated with the use of MIP or BET techniques, which will allow to take some information about the hydrated structure and also some insights on the density of the hydration products formed.

Considering the already used technique of isothermal calorimetry, it would be also valuable to determine the hydration process activation energy of the amorphous binders produced under different cooling conditions in order to evaluate the impact of the embedded energy in the reactivity and in the hydraulic properties of these materials.

Parallel to the experimental work, some computational studies are also being conducted in order to better understand the structural features of the amorphous binders and to determine the reason for their highly reactive nature.

In addition to the more fundamental characterization, it is clear that further development will still be needed in order to assess the properties of the studied hydraulic binders under real conditions and of course a larger scale production is an essential step to achieve this goal. The study of these aspects refer to the third line of work that is necessary to develop.

It will thus be crucial to identify and select an adequate existing process that can ensure the production of several kilos or even a ton of the low-calcium hydraulic binders studied in this work. This process should present technological characteristics that desirably should be compatible with the BAT for OPC clinker. One of the identified processes that may possess these requirements is the one recently presented by Paul Wurth SA [197] that aim at the granulation of molten slag with recovery of some thermal energy from the cooling stage, that is achieved by the immersion of steel spheres into the molten slag.

All the parameters of the process should be studied in a larger scale production, from the chemistry of the raw materials used to the thermal conditions of the production process. Furthermore it will be necessary to assess optimum granulometry conditions and water to binder ratios in order to potentiate the hydraulic properties of these binders.

A large production of these hydraulic materials would be essential to allow the execution of tests that would confirm, on a larger scale, the properties that until now were only assessed at a laboratorial scale. These tests would include the evaluation of the chemical, physical, mechanical as well as durability performance of these low C/S hydraulic binders, by the means that are currently used to assess the properties of OPC.

Also, it would be necessary to evaluate the activation conditions of these binders, especially the amorphous ones, and the workability of their respective pastes in a larger scale. Regarding this stage, it will be important to identify the most suitable type of activator and on which conditions (solution or solid) should the activators be added to the hydraulic binders, since it will be determinant to their future commercialization as well as to the final application of these products.

Of course that all of these optimization works should be run in parallel with a study on the economic viability of the solutions adopted.

Bibliography

1. Knut O. Kjellsen, M.G., Åsa Nilsson, *CO_2 uptake during the concrete life cycle: The CO_2 Balance of Concrete in a Life Cycle Perspective*. 2005, Norden - Nordic Innovation Centre.
2. Schneider, M., et al., *Sustainable cement production—present and future.* Cement and Concrete Research, 2011. **41**(7): p. 642-650.
3. Taylor, H.F.W., *Cement Chemistry*. 2nd ed. 1997: Thomas Telford.
4. McCaffrey, R., *Climate change and the cement industry.* GCL Magazine, 2002(Environmental Special Issue).
5. Hasanbeigi, A., L. Price, and E. Lin, *Emerging energy-efficiency and CO_2 emission-reduction technologies for cement and concrete production: A technical review.* Renewable and Sustainable Energy Reviews, 2012. **16**(8): p. 6220-6238.
6. WBCSD and IEA, *Cement Technology Roadmap 2009 - Carbon Emissions Reductions up to 2050*. 2009.
7. Damtoft, J.S., et al., *Sustainable development and climate change initiatives.* Cement and Concrete Research, 2008. **38**(2): p. 115-127.
8. Scrivener, K.L., *Options for the future of cement.* The Indian Concrete Journal, 2014. **88**(7): p. 11-21.
9. Ridi, F., E. Fratini, and P. Baglioni, *Cement: A two thousand year old nano-colloid.* Journal of Colloid and Interface Science, 2011. **357**(2): p. 255-264.
10. CEN, *Cement - Part 1: Composition, specifications and conformity criteria for common cements*. 2011.
11. Ghosh, S.N., *Cement and Concrete Science and Technology*. 1991: ABI Books Pvt. Limited.
12. Zhang, Y.M. and T.J. Napier-Munn, *Effects of particle size distribution, surface area and chemical composition on Portland cement strength.* Powder Technology, 1995. **83**(3): p. 245-252.
13. Dunstetter, F., M.N. de Noirfontaine, and M. Courtial, *Polymorphism of tricalcium silicate, the major compound of Portland cement clinker: 1. Structural data: review and unified analysis.* Cement and Concrete Research, 2006. **36**(1): p. 39-53.
14. De Noirfontaine, M.-N., et al., *Tricalcium silicate Ca3SiO5 superstructure analysis: a route towards the structure of the M1 polymorph.* Zeitschrift für Kristallographie, 2012. **227**(2): p. 102-112.
15. Manzano, H., et al., *Impact of Chemical Impurities on the Crystalline Cement Clinker Phases Determined by Atomistic Simulations.* Crystal Growth & Design, 2011. **11**(7): p. 2964-2972.
16. Durgun, E., et al., *Understanding and Controlling the Reactivity of the Calcium Silicate phases from First*

Principles. Chemistry of Materials, 2012. **24**(7): p. 1262-1267.
17. Freitas, A.A., et al., *From lime to silica and alumina: systematic modeling of cement clinkers using a general force-field.* Physical Chemistry Chemical Physics, 2015. **17**(28): p. 18477-18494.
18. Ghosh, S., et al., *The chemistry of dicalcium silicate mineral.* Journal of Materials Science, 1979. **14**(7): p. 1554-1566.
19. Gawlicki, M., *Studies of calcium orthosilicate polymorphism by differential thermal analysis.* Journal of thermal analysis, 1987. **32**(6): p. 1723-1725.
20. Remy, C., D. Andrault, and M. Madon, *High-Temperature, High-Pressure X-ray Investigation of Dicalcium Silicate.* Journal of the American Ceramic Society, 1997. **80**(4): p. 851-860.
21. Fukuda, K. and D. Kurokawa, *Morphology of α' H -Ca 2 SiO 4 Solid Solution Crystals.* Journal of the American Ceramic Society, 2010. **93**(2): p. 353-355.
22. Lea, F.M. and C.H. Desch, *Lea's Chemistry of Cement and Concrete*. 4th ed. 2003: Elsevier Ltd.
23. Wang, Q., et al., *Hydration Mechanism of Reactive and Passive Dicalcium Silicate Polymorphs from Molecular Simulations.* The Journal of Physical Chemistry C, 2015. **119**(34): p. 19869-19875.
24. Feng, X., X. Min, and C. Tao, *Study on the structure and characteristic of dicalcium silicate with quantum chemistry calculations.* Cement and Concrete Research, 1994. **24**(7): p. 1311-1316.
25. Scrivener, K.L. and A. Nonat, *Hydration of cementitious materials, present and future.* Cement and Concrete Research, 2011. **41**(7): p. 651-665.
26. Bullard, J.W., et al., *Mechanisms of cement hydration.* Cement and Concrete Research, 2011. **41**(12): p. 1208-1223.
27. Juilland, P., et al., *Dissolution theory applied to the induction period in alite hydration.* Cement and Concrete Research, 2010. **40**(6): p. 831-844.
28. Nonat, A., *Interactions between chemical evolution (hydration) and physical evolution (setting) in the case of tricalcium silicate.* Materials and Structures, 1994. **27**(4): p. 187-195.
29. Preece, S.J., J. Billingham, and A.C. King, *On the initial stages of cement hydration.* Journal of Engineering Mathematics, 2001. **40**(1): p. 43-58.
30. Gartner, E.M. and D.E. Macphee, *A physico-chemical basis for novel cementitious binders.* Cement and Concrete Research, 2011. **41**(7): p. 736-749.
31. Alizadeh, R., et al., *Hydration of tricalcium silicate in the presence of synthetic calcium-silicate-hydrate.* Journal of Materials Chemistry, 2009. **19**(42): p. 7937-7946.
32. Richardson, I.G., *The nature of C-S-H in hardened cements.* Cement and Concrete Research, 1999. **29**(8): p. 1131-1147.

33. Barnes, P. and J. Bensted, *Structure and Performance of Cements, Second Edition*. 2002: Taylor & Francis.
34. Taylor, R., I.G. Richardson, and R.M.D. Brydson, *Composition and microstructure of 20-year-old ordinary Portland cement–ground granulated blast-furnace slag blends containing 0 to 100% slag.* Cement and Concrete Research, 2010. **40**(7): p. 971-983.
35. Narmluk, M. and T. Nawa, *Effect of fly ash on the kinetics of Portland cement hydration at different curing temperatures.* Cement and Concrete Research, 2011. **41**(6): p. 579-589.
36. He, Y., et al., *Effect of calcium–silicon ratio on microstructure and nanostructure of calcium silicate hydrate synthesized by reaction of fumed silica and calcium oxide at room temperature.* Materials and Structures, 2014. **47**(1-2): p. 311-322.
37. Cong, X. and R.J. Kirkpatrick, *29Si MAS NMR study of the structure of calcium silicate hydrate.* Advanced Cement Based Materials, 1996. **3**(3–4): p. 144-156.
38. Chen, J.J., et al., *Solubility and structure of calcium silicate hydrate.* Cement and Concrete Research, 2004. **34**(9): p. 1499-1519.
39. Gartner, E.M., K.E. Kurtis, and P.J.M. Monteiro, *Proposed mechanism of C-S-H growth tested by soft X-ray microscopy*. 2000.
40. Abdolhosseini Qomi, M.J., et al., *Combinatorial molecular optimization of cement hydrates.* Nat Commun, 2014. **5**.
41. Richardson, I.G., *Tobermorite/jennite- and tobermorite/calcium hydroxide-based models for the structure of C-S-H: applicability to hardened pastes of tricalcium silicate, β-dicalcium silicate, Portland cement, and blends of Portland cement with blast-furnace slag, metakaolin, or silica fume.* Cement and Concrete Research, 2004. **34**(9): p. 1733-1777.
42. Allen, A.J., J.J. Thomas, and H.M. Jennings, *Composition and density of nanoscale calcium–silicate–hydrate in cement.* Nature Materials, 2007. **6**(4): p. 311-316.
43. Yu, P., et al., *Structure of Calcium Silicate Hydrate (C-S-H): Near-, Mid-, and Far-Infrared Spectroscopy.* Journal of the American Ceramic Society, 1999. **82**(3): p. 742-748.
44. Kirkpatrick, R.J., et al., *Raman spectroscopy of C-S-H, tobermorite, and jennite.* Advanced Cement Based Materials, 1997. **5**(3): p. 93-99.
45. Pellenq, R.J.-M., et al., *A realistic molecular model of cement hydrates.* Proceedings of the National Academy of Sciences, 2009. **106**(38): p. 16102-16107.
46. Richardson, I.G., *Model structures for C-(A)-S-H(I.* Acta Crystallographica Section B, 2014. **70**(6): p. 903-923.
47. Papatzani, S., K. Paine, and J. Calabria-Holley, *A comprehensive review of the models on the nanostructure of calcium silicate hydrates.* Construction and Building Materials, 2015. **74**: p. 219-234.

48. Soyer-Uzun, S., et al., *Compositional Evolution of Calcium Silicate Hydrate (C–S–H) Structures by Total X-Ray Scattering.* Journal of the American Ceramic Society, 2012. **95**(2): p. 793-798.
49. Gartner, E.M., *A proposed mechanism for the growth of C□S□H during the hydration of tricalcium silicate.* Cement and Concrete Research, 1997. **27**(5): p. 665-672.
50. Zhang, J. and G.W. Scherer, *Comparison of methods for arresting hydration of cement.* Cement and Concrete Research, 2011. **41**(10): p. 1024-1036.
51. Muller, A.C.A., et al., *Use of bench-top NMR to measure the density, composition and desorption isotherm of C–S–H in cement paste.* Microporous and Mesoporous Materials, 2013. **178**(0): p. 99-103.
52. Renó, M.L.G., et al., *Exergy analyses in cement production applying waste fuel and mineralizer.* Energy Conversion and Management, 2013. **75**(0): p. 98-104.
53. Strazza, C., et al., *Resource productivity enhancement as means for promoting cleaner production: analysis of co-incineration in cement plants through a life cycle approach.* Journal of Cleaner Production, 2011. **19**(14): p. 1615-1621.
54. Iacobescu, R.I., et al., *Valorisation of electric arc furnace steel slag as raw material for low energy belite cements.* Journal of Hazardous Materials, 2011. **196**(0): p. 287-294.
55. Reddy, A.S., R.K. Pradhan, and S. Chandra, *Utilization of Basic Oxygen Furnace (BOF) slag in the production of a hydraulic cement binder.* International Journal of Mineral Processing, 2006. **79**(2): p. 98-105.
56. Hilton, R.G., *Use of stabilized EAFD as a raw material in the production of a portland cement clinker*. 1998, Google Patents.
57. Riman, R.E., et al., *Bonding element, bonding matrix and composite material having the bonding element, and method of manufacturing thereof*. 2013, Google Patents.
58. Riman, R.E., et al., *Synthetic formulations and methods of manufacturing and using thereof*. 2012, Google Patents.
59. Beuchle, G., et al., *Single-phase hydraulic binder, methods for the production thereof and structural material produced therewith*. 2010, Google Patents.
60. Beuchle, G., et al., *Single-phase hydraulic binder, methods for the production thereof and building material produced therewith*. 2011, Google Patents.
61. Chatterjee, A.K., *High belite cements—Present status and future technological options: Part I.* Cement and Concrete Research, 1996. **26**(8): p. 1213-1225.
62. Cuberos, A.J.M., et al., *Phase development in conventional and active belite cement pastes by Rietveld analysis and chemical constraints.* Cement and Concrete Research, 2009. **39**(10): p. 833-842.

63. Morsli, K., *Preparación y Caracterización de Nuevos Cementos Portland Belíticos*, in *Departamento de Química Inorgánica, Cristalografía y Mineralogía*. 2007, Universidad de Málaga.
64. Morsli, K., et al., *Quantitative Phase Analysis of Laboratory-Active Belite Clinkers by Synchrotron Powder Diffraction.* Journal of the American Ceramic Society, 2007. **90**(10): p. 3205-3212.
65. Morsli, K., et al., *Mineralogical phase analysis of alkali and sulfate bearing belite rich laboratory clinkers.* Cement and Concrete Research, 2007. **37**(5): p. 639-646.
66. Raupp-Pereira, F., et al., *New waste based clinkers: Belite and lime formulations.* Cement and Concrete Research, 2008. **38**(4): p. 511-521.
67. Cuberos, A.J.M., et al., *Active Iron-Rich Belite Sulfoaluminate Cements: Clinkering and Hydration.* Environmental Science & Technology, 2010. **44**(17): p. 6855-6862.
68. Martín-Sedeño, M.C., et al., *Aluminum-rich belite sulfoaluminate cements: Clinkering and early age hydration.* Cement and Concrete Research, 2010. **40**(3): p. 359-369.
69. Cuesta, A., et al., *Reactive belite stabilization mechanisms by boron-bearing dopants.* Cement and Concrete Research, 2012. **42**(4): p. 598-606.
70. Tang, F.J., *Cement containing activated belite*. 1996, Google Patents.
71. Glasser, F.P. and L. Zhang, *High-performance cement matrices based on calcium sulfoaluminate-belite compositions.* Cement and Concrete Research, 2001. **31**(12): p. 1881-1886.
72. Quillin, K., *Performance of belite-sulfoaluminate cements.* Cement and Concrete Research, 2001. **31**(9): p. 1341-1349.
73. Janotka, I., et al., *Performance of sulphoaluminate-belite cement with high $C_4A_3\$$ content.* Ceram.-Silik., 2007. **51**(2): p. 74-81.
74. Kacimi, L., et al., *Synthesis of belite cement clinker of high hydraulic reactivity.* Cement and Concrete Research, 2009. **39**(7): p. 559-565.
75. Shi, C., A.F. Jiménez, and A. Palomo, *New cements for the 21st century: The pursuit of an alternative to Portland cement.* Cement and Concrete Research, 2011. **41**(7): p. 750-763.
76. Zhang, L., M. Su, and Y. Wang, *Development of the use of sulfo- and ferroaluminate cements in China.* Advances in Cement Research, 1999. **11**(1): p. 15-21.
77. Pinazo, G.Á., *Active sulpho-belite cements. Hydration mechanisms and mechanical properties*, in *Departamento de Química Inorgánica, Cristalografia y Mineralogía*. 2015, Universidad de Málaga.
78. Gartner, E. and G. Li, *High belite-containing sulfoaluminous clinker, method for the production and the*

use thereof for preparing hydraulic binders. 2006, Google Patents.
79. Lothenbach, B., K. Scrivener, and R.D. Hooton, *Supplementary cementitious materials.* Cement and Concrete Research, 2011. **41**(12): p. 1244-1256.
80. Richardson, I.G. and G.W. Groves, *The incorporation of minor and trace elements into calcium silicate hydrate (C□S□H) gel in hardened cement pastes.* Cement and Concrete Research, 1993. **23**(1): p. 131-138.
81. Pardal, X., I. Pochard, and A. Nonat, *Experimental study of Si–Al substitution in calcium-silicate-hydrate (C-S-H) prepared under equilibrium conditions.* Cement and Concrete Research, 2009. **39**(8): p. 637-643.
82. Haha, M.B., K. De Weerdt, and B. Lothenbach, *Quantification of the degree of reaction of fly ash.* Cement and Concrete Research, 2010. **40**(11): p. 1620-1629.
83. Shi, C. and J. Qian, *High performance cementing materials from industrial slags — a review.* Resources, Conservation and Recycling, 2000. **29**(3): p. 195-207.
84. Richardson, I.G., et al., *The characterization of hardened alkali-activated blast-furnace slag pastes and the nature of the calcium silicate hydrate (C-S-H) phase.* Cement and Concrete Research, 1994. **24**(5): p. 813-829.
85. Puertas, F., et al., *Alkali-activated fly ash/slag cements: Strength behaviour and hydration products.* Cement and Concrete Research, 2000. **30**(10): p. 1625-1632.
86. Puertas, F. and M. Torres-Carrasco, *Use of glass waste as an activator in the preparation of alkali-activated slag. Mechanical strength and paste characterisation.* Cement and Concrete Research, 2014. **57**(0): p. 95-104.
87. Palomo, A., M.W. Grutzeck, and M.T. Blanco, *Alkali-activated fly ashes: A cement for the future.* Cement and Concrete Research, 1999. **29**(8): p. 1323-1329.
88. Purdon, A.O., *The action of alkalis on blast-furnace slag.* Journal of the Society of Chemical Industry - Transactions and Communications, 1940. **59**: p. 191-202.
89. Glukhovsky, V.D., G.S. Rostovskaya, and G.V. Rumyna. *High Strength Slag Alkaline Cements*. in *7th International Congress on the Chemistry of Cement*. 1980.
90. Palomo, A., et al., *A review on alkaline activation: new analytical perspectives.* Materiales de Construccion, 2014. **64**(315).
91. Murgier, S., H. Zanni, and D. Gouvenot, *Blast furnace slag cement: a 29Si and 27Al NMR study.* Comptes Rendus Chimie, 2004. **7**(3-4): p. 389-394.
92. Li, D., et al., *The activation and hydration of glassy cementitious materials.* Cement and Concrete Research, 2002. **32**(7): p. 1145-1152.
93. Wolff-Boenisch, D., S.R. Gislason, and E.H. Oelkers, *The effect of crystallinity on dissolution rates and CO2 consumption capacity of silicates.* Geochimica et Cosmochimica Acta, 2006. **70**(4): p. 858-870.

94. Oelkers, E.H., *General kinetic description of multioxide silicate mineral and glass dissolution.* Geochimica et Cosmochimica Acta, 2001. **65**(21): p. 3703-3719.
95. *Alkali Activated Materials*. 1 ed. RILEM State-of-the-Art Reports. 2014: Springer Netherlands. 388.
96. Stuart, B.H., *Introduction*, in *Infrared Spectroscopy: Fundamentals and Applications*. 2005, John Wiley & Sons, Ltd. p. 1-13.
97. Stuart, B.H., *Experimental Methods*, in *Infrared Spectroscopy: Fundamentals and Applications*. 2005, John Wiley & Sons, Ltd. p. 15-44.
98. Bish, D.L. and S.A. Howard, *Quantitative phase analysis using the Rietveld method.* Journal of Applied Crystallography, 1988. **21**(2): p. 86-91.
99. Scrivener, K.L., et al., *Quantitative study of Portland cement hydration by X-ray diffraction/Rietveld analysis and independent methods.* Cement and Concrete Research, 2004. **34**(9): p. 1541-1547.
100. MacKenzie, K.J.D. and M.E. Smith, *Multinuclear Solid-State Nuclear Magnetic Resonance of Inorganic Materials*. 2002: Elsevier Science.
101. Collier, N.C., et al., *The influence of water removal techniques on the composition and microstructure of hardened cement pastes.* Cement and Concrete Research, 2008. **38**(6): p. 737-744.
102. Kurz, W. and D.J. Fisher, *Fundamentals of solidification*. 1986: Trans Tech Publications.
103. Shelby, J.E., *Introduction to Glass Science and Technology*. 2005, Royal Society of Chemistry. p. 26-48.
104. Varshneya, A.K., *Fundamentals of Inorganic Glasses*. 1994: Academic Press.
105. Mostafa, N.Y., E.A. Kishar, and S.A. Abo-El-Enein, *FTIR study and cation exchange capacity of Fe3+- and Mg2+-substituted calcium silicate hydrates.* Journal of Alloys and Compounds, 2009. **473**(1–2): p. 538-542.
106. Stepkowska, E.T., et al., *Hydration products in two aged cement pastes.* Journal of Thermal Analysis and Calorimetry, 2005. **82**(3): p. 731-739.
107. García-Lodeiro, I., et al., *FTIR study of the sol–gel synthesis of cementitious gels: C–S–H and N–A–S–H.* Journal of Sol-Gel Science and Technology, 2008. **45**(1): p. 63-72.
108. García Lodeiro, I., et al., *Effect of alkalis on fresh C–S–H gels. FTIR analysis.* Cement and Concrete Research, 2009. **39**(3): p. 147-153.
109. de Paiva, L.B. and F.A. Rodrigues, *Early-hydration of β-Ca2SiO4 followed by FTIR/ATR spectroscopy.* Journal of Materials Science, 2004. **39**(18): p. 5841-5843.
110. Mendes, A., et al., *NMR, XRD, IR and synchrotron NEXAFS spectroscopic studies of OPC and OPC/slag cement paste hydrates.* Materials and Structures, 2011. **44**(10): p. 1773-1791.

111. Gandolfi, M.G., et al., *Apatite formation on bioactive calcium-silicate cements for dentistry affects surface topography and human marrow stromal cells proliferation.* Dental Materials, 2010. **26**(10): p. 974-992.
112. Taddei, P., et al., *Vibrational study on the bioactivity of Portland cement-based materials for endodontic use.* Journal of Molecular Structure, 2009. **924–926**(0): p. 548-554.
113. Shuguang, H. and Z. Ming, *The microstructure and chemical bonds of β-C2S under the high energy ball grinding function.* Journal of Wuhan University of Technology-Mater. Sci. Ed., 2006. **21**(1): p. 150-153.
114. De Sousa Meneses, D., M. Malki, and P. Echegut, *Optical and structural properties of calcium silicate glasses.* Journal of Non-Crystalline Solids, 2006. **352**(50–51): p. 5301-5308.
115. Pérez, G., et al., *Structural characterization of C-S-H gel through an improved deconvolution analysis of NMR spectra.* Journal of Materials Science, 2014. **49**(1): p. 142-152.
116. Grimmer, A.R., et al., *High-resolution solid-state 29Si NMR of polymorphs of Ca2SiO4.* Cement and Concrete Research, 1985. **15**(3): p. 467-473.
117. Hong, S.-H. and J.F. Young, *Hydration Kinetics and Phase Stability of Dicalcium Silicate Synthesized by the Pechini Process.* Journal of the American Ceramic Society, 1999. **82**(7): p. 1681-1686.
118. Johansson, K., et al., *Kinetics of the hydration reactions in the cement paste with mechanochemically modified cement 29Si magic-angle-spinning NMR study.* Cement and Concrete Research, 1999. **29**(10): p. 1575-1581.
119. Schneider, J., et al., *29Si MAS-NMR studies of Q n structural units in metasilicate glasses and their nucleating ability.* Journal of Non-Crystalline Solids, 2000. **273**(1): p. 8-18.
120. Zhang, P., P.J. Grandinetti, and J.F. Stebbins, *Anionic Species Determination in CaSiO3 Glass Using Two-Dimensional 29Si NMR.* The Journal of Physical Chemistry B, 1997. **101**(20): p. 4004-4008.
121. Eden, M., *NMR studies of oxide-based glasses.* Annual Reports Section "C" (Physical Chemistry), 2012. **108**(1): p. 177-221.
122. Brunet, F., et al., *Characterization by solid-state NMR and selective dissolution techniques of anhydrous and hydrated CEM V cement pastes.* Cement and Concrete Research, 2010. **40**(2): p. 208-219.
123. MacKenzie, K.J.D. and M.E. Smith, *Multinuclear solid-state NMR of inorganic materials*. Vol. 6. 2010, Amsterdam; Boston (Mass.); London: Pergamon.
124. Paluszkiewicz, C., et al., *Structure and bioactivity studies of new polysiloxane-derived materials for orthopedic applications.* Journal of Molecular Structure, 2006. **792–793**(0): p. 176-181.

125. Paluszkiewicz, C., et al., *Nucleation of hydroxyapatite layer on wollastonite material surface: FTIR studies.* Vibrational Spectroscopy, 2008. **48**(2): p. 263-268.
126. Lecomte, I., et al., *(Micro)-structural comparison between geopolymers, alkali-activated slag cement and Portland cement.* Journal of the European Ceramic Society, 2006. **26**(16): p. 3789-3797.
127. MacDonald, S.A., et al., *Dispersion analysis of FTIR reflection measurements in silicate glasses.* Journal of Non-Crystalline Solids, 2000. **275**(1–2): p. 72-82.
128. Santos, R.L., et al., *Microstructural control and hydration of novel micro-dendritic clinkers with CaO–SiO2=1.4.* Cement and Concrete Research, 2015. **76**(0): p. 212-221.
129. Alarcon-Ruiz, L., et al., *The use of thermal analysis in assessing the effect of temperature on a cement paste.* Cement and Concrete Research, 2005. **35**(3): p. 609-613.
130. Vedalakshmi, R., et al., *Quantification of hydrated cement products of blended cements in low and medium strength concrete using TG and DTA technique.* Thermochimica Acta, 2003. **407**(1–2): p. 49-60.
131. Esteves, L.P., *On the hydration of water-entrained cement–silica systems: Combined SEM, XRD and thermal analysis in cement pastes.* Thermochimica Acta, 2011. **518**(1–2): p. 27-35.
132. Morandeau, A., M. Thiéry, and P. Dangla, *Investigation of the carbonation mechanism of CH and C-S-H in terms of kinetics, microstructure changes and moisture properties.* Cement and Concrete Research, 2013. **56**: p. 153-170.
133. Jin, F., K. Gu, and A. Al-Tabbaa, *Strength and hydration properties of reactive MgO-activated ground granulated blastfurnace slag paste.* Cement and Concrete Composites, 2015. **57**: p. 8-16.
134. Jin, F. and A. Al-Tabbaa, *Strength and drying shrinkage of slag paste activated by sodium carbonate and reactive MgO.* Construction and Building Materials, 2015. **81**: p. 58-65.
135. Jang, J.G., N.K. Lee, and H.K. Lee, *Fresh and hardened properties of alkali-activated fly ash/slag pastes with superplasticizers.* Construction and Building Materials, 2014. **50**(0): p. 169-176.
136. Tänzer, R., A. Buchwald, and D. Stephan, *Effect of slag chemistry on the hydration of alkali-activated blast-furnace slag.* Materials and Structures, 2015. **48**(3): p. 629-641.
137. Hoshino, S., K. Yamada, and H. Hirao, *XRD/Rietveld Analysis of the Hydration and Strength Development of Slag and Limestone Blended Cement.* Journal of Advanced Concrete Technology, 2006. **4**(3): p. 357-367.
138. Escalante-Garcıá, J.I. and J.H. Sharp, *The microstructure and mechanical properties of blended cements hydrated at various temperatures.* Cement and Concrete Research, 2001. **31**(5): p. 695-702.

139. Shi, C., *Strength, pore structure and permeability of alkali-activated slag mortars.* Cement and Concrete Research, 1996. **26**(12): p. 1789-1799.
140. Altan, E. and S.T. Erdoğan, *Alkali activation of a slag at ambient and elevated temperatures.* Cement and Concrete Composites, 2012. **34**(2): p. 131-139.
141. Aydın, S. and B. Baradan, *Effect of activator type and content on properties of alkali-activated slag mortars.* Composites Part B: Engineering, 2014. **57**(0): p. 166-172.
142. Menéndez, G., V. Bonavetti, and E.F. Irassar, *Strength development of ternary blended cement with limestone filler and blast-furnace slag.* Cement and Concrete Composites, 2003. **25**(1): p. 61-67.
143. Merlino, S., E. Bonaccorsi, and T. Armbruster, *The real structure of tobermorite 11Å: normal and anomalous forms, OD character and polytypic modifications.* European Journal of Mineralogy, 2001. **13**(3): p. 577-590.
144. Wu, Y.-q., C. Dai, and G.-c. Jiang, *Local structure of calcium silicate melts from classical molecular dynamics simulation and a newly constructed thermodynamic model.* Transactions of Nonferrous Metals Society of China, 2014. **24**(5): p. 1488-1499.
145. Houston, J., R. Maxwell, and S. Carroll, *Transformation of meta-stable calcium silicate hydrates to tobermorite: reaction kinetics and molecular structure from XRD and NMR spectroscopy.* Geochemical Transactions, 2009. **10**(1): p. 1.
146. Cong, X., et al., *29Si and 17O NMR investigation of the structure of some crystalline calcium silicate hydrates.* Advanced Cement Based Materials, 1996. **3**(3): p. 133-143.
147. Mori, K., et al., *Hydration properties and compressive strength development of Low Heat Cement.* Journal of Physics and Chemistry of Solids, 2012. **73**(11): p. 1274-1277.
148. Wang, S.-D. and K.L. Scrivener, *29Si and 27Al NMR study of alkali-activated slag.* Cement and Concrete Research, 2003. **33**(5): p. 769-774.
149. Burciaga-Díaz, O. and J.I. Escalante-García, *Structure, Mechanisms of Reaction, and Strength of an Alkali-Activated Blast-Furnace Slag.* Journal of the American Ceramic Society, 2013. **96**(12): p. 3939-3948.
150. Hansen, M.R., H.J. Jakobsen, and J. Skibsted, *29Si chemical shift anisotropies in calcium silicates from high-field 29Si MAS NMR spectroscopy.* Inorganic chemistry, 2003. **42**(7): p. 2368.
151. Lin, C.-C., et al., *Elasticity and structure of the compounds in the wollastonite (CaSiO3)–Na2SiO3 system: from amorphous to crystalline state.* Journal of Materials Science: Materials in Medicine, 2015. **26**(1): p. 1-14.
152. Le Saoût, G., et al., *Hydration Degree of Alkali-Activated Slags: A 29Si NMR Study.* Journal of the American Ceramic Society, 2011. **94**(12): p. 4541-4547.
153. Schneider, J., M.A. Cincotto, and H. Panepucci, *29Si and 27Al high-resolution NMR characterization of calcium*

silicate hydrate phases in activated blast-furnace slag pastes. Cement and Concrete Research, 2001. **31**(7): p. 993-1001.
154. Kenneth, J.D.M. and E.S. Mark, *Chapter 4 29Si NMR*, in *Pergamon Materials Series*, J.D.M. Kenneth and E.S. Mark, Editors. 2002, Pergamon. p. 201-268.
155. Ismail, I., et al., *Drying-induced changes in the structure of alkali-activated pastes.* Journal of Materials Science, 2013. **48**(9): p. 3566-3577.
156. Palacios, M. and F. Puertas, *Effect of Carbonation on Alkali-Activated Slag Paste.* Journal of the American Ceramic Society, 2006. **89**(10): p. 3211-3221.
157. Shi, C. and R.L. Day, *A calorimetric study of early hydration of alkali-slag cements.* Cement and Concrete Research, 1995. **25**(6): p. 1333-1346.
158. Hubler, M.H., J.J. Thomas, and H.M. Jennings, *Influence of nucleation seeding on the hydration kinetics and compressive strength of alkali activated slag paste*. 2011.
159. Gebregziabiher, B.S., R. Thomas, and S. Peethamparan, *Very early-age reaction kinetics and microstructural development in alkali-activated slag.* Cement and Concrete Composites, 2015. **55**: p. 91-102.
160. Criado, M., A. Fernández-Jiménez, and A. Palomo, *Alkali activation of fly ash: Effect of the SiO2/Na2O ratio: Part I: FTIR study.* Microporous and Mesoporous Materials, 2007. **106**(1–3): p. 180-191.
161. Criado, M., et al., *Effect of the SiO2/Na2O ratio on the alkali activation of fly ash. Part II: 29Si MAS-NMR Survey.* Microporous and Mesoporous Materials, 2008. **109**(1–3): p. 525-534.
162. Criado, M., A. Fernández-Jiménez, and A. Palomo, *Alkali activation of fly ash. Part III: Effect of curing conditions on reaction and its graphical description.* Fuel, 2010. **89**(11): p. 3185-3192.
163. Jeon, D., et al., *Microstructural and strength improvements through the use of Na2CO3 in a cementless Ca(OH)2-activated Class F fly ash system.* Cement and Concrete Research, 2015. **67**: p. 215-225.
164. Wang, S.D., K.L. Scrivener, and P.L. Pratt, *Factors affecting the strength of alkali-activated slag.* Cement and Concrete Research, 1994. **24**(6): p. 1033-1043.
165. Brough, A.R. and A. Atkinson, *Sodium silicate-based, alkali-activated slag mortars: Part I. Strength, hydration and microstructure.* Cement and Concrete Research, 2002. **32**(6): p. 865-879.
166. Gruskovnjak, A., et al., *Hydration of alkali-activated slag: comparison with ordinary Portland cement.* Advances in Cement Research, 2006. **18**(3): p. 119-128.
167. Wang, S.-D. and K.L. Scrivener, *Hydration products of alkali activated slag cement.* Cement and Concrete Research, 1995. **25**(3): p. 561-571.

168. Pacheco-Torgal, F., J. Castro-Gomes, and S. Jalali, *Alkali-activated binders: A review: Part 1. Historical background, terminology, reaction mechanisms and hydration products.* Construction and Building Materials, 2008. **22**(7): p. 1305-1314.
169. Chen, W. and H.J.H. Brouwers, *The hydration of slag, part 1: reaction models for alkali-activated slag.* Journal of Materials Science, 2007. **42**(2): p. 428-443.
170. Fernández-Jiménez, A., et al., *Structure of Calcium Silicate Hydrates Formed in Alkaline-Activated Slag: Influence of the Type of Alkaline Activator.* 2003.
171. Bernal, S.A., et al., *Performance at high temperature of alkali-activated slag pastes produced with silica fume and rice husk ash based activators.* 2015. 2015.
172. Abdalqader, A.F., F. Jin, and A. Al-Tabbaa, *Development of greener alkali-activated cement: utilisation of sodium carbonate for activating slag and fly ash mixtures.* Journal of Cleaner Production, 2015.
173. Sun, G.K., J.F. Young, and R.J. Kirkpatrick, *The role of Al in C–S–H: NMR, XRD, and compositional results for precipitated samples.* Cement and Concrete Research, 2006. **36**(1): p. 18-29.
174. Faucon, P., et al., *Aluminum Incorporation in Calcium Silicate Hydrates (C–S–H) Depending on Their Ca/Si Ratio.* The Journal of Physical Chemistry B, 1999. **103**(37): p. 7796-7802.
175. Shi, C., D. Roy, and P. Krivenko, *Alkali-Activated Cements and Concretes*. 2006: Taylor & Francis.
176. Brouwers, H.J.H., *The work of Powers and Brownyard revisited: Part 1.* Cement and Concrete Research, 2004. **34**(9): p. 1697-1716.
177. Fokin, V.M., et al., *Nonstoichiometric crystallization of lithium metasilicate–calcium metasilicate glasses. Part 1 — Crystal nucleation and growth rates.* Journal of Non-Crystalline Solids, 2013. **362**: p. 56-64.
178. Thompson, S.P., et al., *Fine-grained amorphous calcium silicate CaSiO3 from vacuum dried sol–gel – Production, characterisation and thermal behaviour.* Journal of Non-Crystalline Solids, 2012. **358**(5): p. 885-892.
179. Joanna, P., et al., *A novel ceramic material with medical application.* Processing and Application of Ceramics, 2008. **2**(1): p. 19-22.
180. Ismail, H., R. Shamsudin, and M.A. Abdul Hamid, *Effect of autoclaving and sintering on the formation of β-wollastonite.* Materials Science and Engineering: C, 2016. **58**: p. 1077-1081.
181. Wang, S., et al., *Influence of inorganic admixtures on the 11 Å-tobermorite formation prepared from steel slags: XRD and FTIR analysis.* Construction and Building Materials, 2014. **60**: p. 42-47.

182. Tan, J., et al., *The effect of cooling rate on the structure of sodium silicate glass.* Materials Science and Engineering: B, 2004. **106**(3): p. 295-299.
183. Gan, L., et al., *Continuous cooling crystallization kinetics of a molten blast furnace slag.* Journal of Non-Crystalline Solids, 2012. **358**(1): p. 20-24.
184. Tossavainen, M., et al., *Characteristics of steel slag under different cooling conditions.* Waste Management, 2007. **27**(10): p. 1335-1344.
185. Vollmayr, K., W. Kob, and K. Binder, *How do the properties of a glass depend on the cooling rate? A computer simulation study of a Lennard-Jones system.* The Journal of Chemical Physics, 1996. **105**(11): p. 4714-4728.
186. Tilocca, A., *Cooling rate and size effects on the medium-range structure of multicomponent oxide glasses simulated by molecular dynamics.* J Chem Phys, 2013. **139**(11): p. 114501.
187. Weston, R. and P. Rogers, *The growth of calcium metasilicate polymorphs from supercooled melts and glasses.* Mineralogical Magazine, 1978. **4**(2): p. 325-35.
188. Du, J. and Y. Xiang, *Effect of strontium substitution on the structure, ionic diffusion and dynamic properties of 45S5 Bioactive glasses.* Journal of Non-Crystalline Solids, 2012. **358**(8): p. 1059-1071.
189. Bentz, D.P., et al., *Relating Compressive Strength to Heat Release in Mortars.* Advances in Civil Engineering Materials, 2012. **1**(1): p. 1-14.
190. (WBCSD), C.S.I.C.o.t.W.B.C.f.S.D., *CO_2 and Energy Accounting and Reporting Standard for the Cement Industry*. 2011.
191. InterCement, *InterCement Sustainability Report*. 2013.
192. Lange, R.A., J.J. De Yoreo, and A. Navrotsky, *Scanning calorimetric measurement of heat capacity during incongruent melting of diopside.* Am Mineral, 1991. **76**: p. 904-912.
193. Zhu, H., R.C. Newton, and O.J. Kleppa, *Enthalpy of formation of wollastonite (CaSiO3) and anorthite (CaAl2Si2O8) by experimental phase equilibrium measurements and high-temperature solution colorimetry.* American Mineralogist, 1994. **79**(1-2): p. 134-144.
194. Martins, I. and I.-T.P.-P.a.P. Engineering, *Audit to Kiln 7 of Alhandra's Plant (Portugal) - Internal Report*. 2014, InterCement.
195. Consulting, H.M.a., *Holderbank Cement Engineering Book - Materials Technology II*. 2000.
196. McLellan, B.C., et al., *Costs and carbon emissions for geopolymer pastes in comparison to ordinary portland cement.* Journal of Cleaner Production, 2011. **19**(9-10): p. 1080-1090.
197. Kappes;, H. and D. Michels, *Dry Slag Granulation with Energy Recovery: Operation of Full Scale Pilot Plant*, in *METEC and 2nd ESTAD*. 2015: Dusseldorf.

198. Solvi, M., et al., *Dry granulation of metallurgical slag*. 2013, Google Patents.
199. Featherstone, W.B., *Slag granulation system and method of operation*. 2015, Google Patents.

List of Publications

❖ *Papers*

- Freitas, A.A., **Santos, R.L.**, Colaço, R., Bayão Horta, R. and Canongia Lopes, J.N., *From Lime to Silica and Alumina: Systematic Modeling of Cement Clinkers using a General Force-Field.* Physical Chemistry Chemical Physics, 2015. *17*(28): p. 18477-18494.
- **Santos, R.L.**, Bayão Horta, R., Pereira, J., Nunes, T.G., Rocha, P., Canongia Lopes, J.N. and Colaço, R., *Microstructural control and hydration of novel micro-dendritic clinkers with $CaO/SiO_2 = 1,4$*. Cement and Concrete Research, 2015. *76*: p. 212-221.
- **Santos, R.L.**, Bayão Horta, R., Pereira, J., Nunes, T.G., Rocha, P., Canongia Lopes, J.N. and Colaço, R., *Novel high-resistance clinkers with $1.25 < CaO/SiO_2 < 1.10$: production route and preliminary hydration characterization*. Cement and Concrete Research, 2016. 85: p. 39-47.
- **Santos, R.L.**, Bayão Horta, R., Pereira, J., Nunes, T.G., Rocha, P., Canongia Lopes, J.N. and Colaço, R., *Alkali-activation of high-resistance low-calcium silicate hydraulic binders* (Submitted).

❖ *Patents*

- Dendritic belite based hydraulic binders and methods for their manufacturing; R. Bayão Horta, **Rodrigo L. Santos**, J. Pereira, P. Rocha, S. Lebreiro, J. N. Canongia Lopes, R. Colaço. IST DDR 130319, January 2015. PCT/PT2015/000005.
- Amorphous low-calcium content silicate hydraulic binders and methods for their manufacturing; R. Bayão Horta, **Rodrigo L. Santos**, J. Pereira, P. Rocha, S. Lebreiro, J. N. Canongia Lopes, R. Colaço. IST DDR 130319, January 2015. PCT/PT2015/000006.

Annexes

1st. Heat Balance of an Estimated Production Process of a Clinker with a C/S Molar Ratio of 2.0 (Reference Belite Clinker)

Stage	Description	Heat Value (kJ/kg)	Reaction	wt%	Heat partial (kJ/kg)	Heat total Stage (kJ/kg)	Ref.	Observations
Kiln Reactions	ΔH reaction Belite	-734,0	$2CaO + SiO_2 \rightarrow Ca_2SiO_4$			-734,0	[3]	It was considered the formation of 100% belite while in the case of OPC clinker it was considered the fusion of C_3A and C_4AF by 20% in weight.
	ΔH reaction Belite	-734,0	$2CaO + SiO_2 \rightarrow Ca_2SiO_4$	13%	-95,4	-318,7	[3]	
	ΔH reaction Alite	-495,0	$3CaO + SiO_2 \rightarrow Ca_3SiO_5$	67%	-331,7		[3]	
	ΔH reaction C_3A	-27,0	$3CaO + Al_2O_3 \rightarrow C_3A$	12%	-3,2		[3]	
	ΔH reaction C_4AF	-105,0	$4CaO+Al_2O_3+Fe_2O_3 \rightarrow C_4AF$	8%	-8,4		[3]	
	ΔH fusion Aluminoferrates	600,0	Solid → Liquid	20%	120,0		[194]	
Calcination	CO_2 removal from Raw meal	1864,3	$CaCO_3 \rightarrow CaO + CO_2$	100%	1864,3	1864,3	[3]	12.8% less energy needed to calcine the raw materials.
	CO_2 removal from Raw meal	2138,0	$CaCO_3 \rightarrow CaO + CO_2$	100%	2138,0	2138,0	[3]	
Heating of Raw-Materials	Heating from room temperature to 1450ºC	1928,1	ΔT (T_{room} - 1450ºC)	100%	1928,1	1928,1	[195]	Lower fuel consumption in the heating of the raw materials as the mass of raw materials needed to produce 1 ton of clinker is reduced (1,46 ton instead of 1,55 ton)
	Heating from room temperature to 1450ºC	2050,0	ΔT (T_{room} - 1450ºC)	100%	2050,0	2050,0	[195]	
Heat losses	Radiation, convection preheater tower	146,0		100%	146,0	1534,2	[194]	A lower heat loss from the exit of hot gases was considered, by assuming CO_2 as the major contributor. Possibly the heat losses by radiation will also be lower since the mass of raw materials needed for the production of a ton of clinker is also reduced (1,46 ton instead of 1,55 ton).
	Radiation, convection Kiln and Cooler	224,3		100%	224,3		[194]	
	Heat lost in exit gases from preheater	563,7		100%	563,7		[194]	
	Heat lost from exit dust	72,1		100%	72,1		[194]	
	Heat lost in clinker	88,0		100%	88,0		[3]	
	Water evaporation	13,0		100%	13,0		[3]	
	Heat lost in air from cooler	427,0		100%	427,0		[3]	
	Radiation, convection preheater tower	155,2		100%	155,2	1630,7	[194]	
	Radiation, convection Kiln and Cooler	224,3		100%	224,3		[194]	
	Heat lost in exit gases from preheater	646,5		100%	646,5		[194]	
	Heat lost from exit dust	76,7		100%	76,7		[194]	
	Heat lost in clinker	88,0		100%	88,0		[3]	
	Water evaporation	13,0		100%	13,0		[3]	
	Heat lost in air from cooler	427,0		100%	427,0		[3]	
Heat Recovery	Clinker cooling	-1400,0		100%	-1400,0	-1921,0	[5]	It was considered a lower heat recovery from the cooling of CO_2 in a 87.2% proportion for the case of the amorphous binder. It was also eliminated the contribution from the recrystallization of the melt.
	Cooling of CO_2	-436,0		100%	-436,0		[5]	
	Cooling of water (ex. clays)	-85,0		100%	-85,0		[5]	
	Crystallization of melt	0,0		100%	0,0		[5]	
	Clinker cooling	-1400,0		100%	-1400,0	-2090,0	[5]	
	Cooling of CO_2	-500,0		100%	-500,0		[5]	
	Cooling of water (ex. clays)	-85,0		100%	-85,0		[5]	
	Crystallization of melt	-105,0		100%	-105,0		[5]	
Process Total	Reference Belite Clinker			100%		2671,5		Fuel consumption is expected to be reduced in 21.7% when compared to the typical OPC Clinker production.
	Clinker OPC			100%		3410,0		
			Differential			-738,4		
			Differential %			-21,7%		

2nd. Heat Balance of an Estimated Production Process of a Clinker with a C/S Molar Ratio of 1.4 (Dendritic Belite Clinker)

Stage	Description	Heat Value (kJ/kg)	Reaction	wt%	Heat partial (kJ/kg)	Heat total Stage (kJ/kg)	Ref.	Observations
Kiln Reactions	ΔH fusion Wollastonite	494,0	Solid → Liquid	50%	247,0	-209,6	[192]	It was considered the formation of 100% belite while in the case of OPC clinker it was considered the fusion of C_3A and C_4AF by 20% in weight.
	ΔH reaction Wollastonite	-89,6	$CaO + SiO_2 \rightarrow CaSiO_3$	100%	-89,6		[193]	
	ΔH reaction Belite	-734,0	$2CaO + SiO_2 \rightarrow Ca_2SiO_4$	50%	-367,0		[3]	
	ΔH reaction Belite	-734,0	$2CaO + SiO_2 \rightarrow Ca_2SiO_4$	13%	-95,4	-318,7	[3]	
	ΔH reaction Alite	-495,0	$3CaO + SiO_2 \rightarrow Ca_3SiO_5$	67%	-331,7		[3]	
	ΔH reaction C_3A	-27,0	$3CaO + Al_2O_3 \rightarrow C_3A$	12%	-3,2		[3]	
	ΔH reaction C_4AF	-105,0	$4CaO+Al_2O_3+Fe_2O_3 \rightarrow C_4AF$	8%	-8,4		[3]	
	ΔH fusion Aluminoferrates	600,0	Solid → Liquid	20%	120,0		[194]	
Calcination	CO_2 removal from Raw meal	1620,4	$CaCO_3 \rightarrow CaO + CO_2$	100%	1620,4	1620,4	[3]	24.2% less energy needed to calcine the raw materials.
	CO_2 removal from Raw meal	2138,0	$CaCO_3 \rightarrow CaO + CO_2$	100%	2138,0	2138,0	[3]	
Heating of Raw-Materials	Heating from room temperature to 1450ºC	1848,8	ΔT (T_{room} - 1450ºC)	100%	1848,8	1848,8	[195]	Lower fuel consumption in the heating of the raw materials as the mass of raw materials needed to produce 1 ton of clinker is reduced (1,40 ton instead of 1,55 ton)
	Heating from room temperature to 1450ºC	2050,0	ΔT (T_{room} - 1450ºC)	100%	2050,0	2050,0	[195]	
Heat losses	Radiation, convection preheater tower	140,0		100%	146,0	1534,2	[194]	A lower heat loss from the exit of hot gases was considered, by assuming CO_2 as the major contributor. Possibly the heat losses by radiation will also be lower since the mass of raw materials needed for the production of a ton of clinker is also reduced (1,40 ton instead of 1,55 ton).
	Radiation, convection Kiln and Cooler	224,3		100%	224,3		[194]	
	Heat lost in exit gases from preheater	490,0		100%	490,0		[194]	
	Heat lost from exit dust	69,2		100%	69,2		[194]	
	Heat lost in clinker	88,0		100%	88,0		[3]	
	Water evaporation	13,0		100%	13,0		[3]	
	Heat lost in air from cooler	427,0		100%	427,0		[3]	
	Radiation, convection preheater tower	155,2		100%	155,2	1630,7	[194]	
	Radiation, convection Kiln and Cooler	224,3		100%	224,3		[194]	
	Heat lost in exit gases from preheater	646,5		100%	646,5		[194]	
	Heat lost from exit dust	76,7		100%	76,7		[194]	
	Heat lost in clinker	88,0		100%	88,0		[3]	
	Water evaporation	13,0		100%	13,0		[3]	
	Heat lost in air from cooler	427,0		100%	427,0		[3]	
Heat Recovery	Clinker cooling	-1400,0		100%	-1400,0	-1864,0	[5]	It was considered a lower heat recovery from the cooling of CO_2 in a 75.8% proportion for the case of the amorphous binder. It was also eliminated the contribution from the recrystallization of the melt.
	Cooling of CO_2	-379,0		100%	-379,0		[5]	
	Cooling of water (ex. clays)	-85,0		100%	-85,0		[5]	
	Crystallization of melt	0,0		100%	0,0		[5]	
	Clinker cooling	-1400,0		100%	-1400,0	-2090,0	[5]	
	Cooling of CO_2	-500,0		100%	-500,0		[5]	
	Cooling of water (ex. clays)	-85,0		100%	-85,0		[5]	
	Crystallization of melt	-105,0		100%	-105,0		[5]	
Process Total	Reference Belite Clinker			100%		2847,1		Fuel consumption is expected to be reduced in 16.5% when compared to the typical OPC Clinker production.
	Clinker OPC			100%		3410,0		
			Differential			-562,9		
			Differential %			-16,5%		

3rd. Heat Balance of an Estimated Production Process of a Clinker with a C/S Molar Ratio of 1.25 (Amorphous Binder)

Stage	Description	Heat Value (kJ/kg)	Reaction	wt%	Heat partial (kJ/kg)	Heat total Stage (kJ/kg)	Ref.	Observations
Kiln Reactions	ΔH fusion Wollastonite	494,0	Solid → Liquid	100%	494,0	404,4	[192]	It was considered the formation of 100% belite while in the case of OPC clinker it was considered the fusion of C_3A and C_4AF by 20% in weight.
	ΔH reaction Wollastonite	-89,6	$CaO + SiO_2 \rightarrow CaSiO_3$	100%	-89,6		[193]	
	ΔH reaction Belite	-734,0	$2CaO + SiO_2 \rightarrow Ca_2SiO_4$	13%	-95,4	-318,7	[3]	
	ΔH reaction Alite	-495,0	$3CaO + SiO_2 \rightarrow Ca_3SiO_5$	67%	-331,7		[3]	
	ΔH reaction C_3A	-27,0	$3CaO + Al_2O_3 \rightarrow C_3A$	12%	-3,2		[3]	
	ΔH reaction C_4AF	-105,0	$4CaO+Al_2O_3+Fe_2O_3 \rightarrow C_4AF$	8%	-8,4		[3]	
	ΔH fusion Aluminoferrates	600,0	Solid → Liquid	20%	120,0		[194]	
Calcination	CO_2 removal from Raw meal	1634,2	$CaCO_3 \rightarrow CaO + CO_2$	100%	1634,2	1634,2	[3]	23.6% less energy needed to calcine the raw materials.
	CO_2 removal from Raw meal	2138,0	$CaCO_3 \rightarrow CaO + CO_2$	100%	2138,0	2138,0	[3]	
Heating of Raw-Materials	Heating from room temperature to 1450ºC	1853,3	ΔT (T_{room} - 1450ºC)	100%	1853,3	1853,3	[195]	Lower fuel consumption in the heating of the raw materials as the mass of raw materials needed to produce 1 ton of clinker is reduced (1,40 ton instead of 1,55 ton)
	Heating from room temperature to 1450ºC	2050,0	ΔT (T_{room} - 1450ºC)	100%	2050,0	2050,0	[195]	
Heat losses	Radiation, convection preheater tower	140,3		100%	140,3	1456,1	[194]	A lower heat loss from the exit of hot gases was considered, by assuming CO_2 as the major contributor. Possibly the heat losses by radiation will also be lower since the mass of raw materials needed for the production of a ton of clinker is also reduced (1,40 ton instead of 1,55 ton).
	Radiation, convection Kiln and Cooler	224,3		100%	224,3		[194]	
	Heat lost in exit gases from preheater	494,2		100%	494,2		[194]	
	Heat lost from exit dust	69,3		100%	69,3		[194]	
	Heat lost in clinker	88,0		100%	88,0		[3]	
	Water evaporation	13,0		100%	13,0		[3]	
	Heat lost in air from cooler	427,0		100%	427,0		[3]	
	Radiation, convection preheater tower	155,2		100%	155,2	1630,7	[194]	
	Radiation, convection Kiln and Cooler	224,3		100%	224,3		[194]	
	Heat lost in exit gases from preheater	646,5		100%	646,5		[194]	
	Heat lost from exit dust	76,7		100%	76,7		[194]	
	Heat lost in clinker	88,0		100%	88,0		[3]	
	Water evaporation	13,0		100%	13,0		[3]	
	Heat lost in air from cooler	427,0		100%	427,0		[3]	
Heat Recovery	Clinker cooling	-1400,0		100%	-1400,0	-1867,2	[5]	It was considered a lower heat recovery from the cooling of CO_2 in a 76.4% proportion for the case of the amorphous binder. It was also eliminated the contribution from the recrystallization of the melt.
	Cooling of CO_2	-382,2		100%	-382,2		[5]	
	Cooling of water (ex. clays)	-85,0		100%	-85,0		[5]	
	Crystallization of melt	0,0		100%	0,0		[5]	
	Clinker cooling	-1400,0		100%	-1400,0	-2090,0	[5]	
	Cooling of CO_2	-500,0		100%	-500,0		[5]	
	Cooling of water (ex. clays)	-85,0		100%	-85,0		[5]	
	Crystallization of melt	-105,0		100%	-105,0		[5]	
Process Total	Reference Belite Clinker			100%		3480,9		Fuel consumption is expected to be increased in 2.1% when compared to the typical OPC Clinker production.
	Clinker OPC			100%		3410,0		
			Differential			70,9		
			Differential %			2,1%		